UNIVERSITY OF SOUTHAMPTON

Faculty of Engineering and Physical Sciences

School of Chemistry

Characterisation and Application of Weakly Coordinating Solvents for the Electrodeposition of Semiconductors

by

Alexander William Griffiths Black

Thesis for the degree of Doctor of Philosophy

July 2022

UNIVERSITY OF SOUTHAMPTON

ABSTRACT

FACULTY OF ENGINEERING AND PHYSICAL SCIENCES

School of Chemistry

Thesis for the degree of Doctor of Philosophy

Characterisation and Application of Weakly Coordinating Solvents for the Electrodeposition of Semiconductors

Alexander William Griffiths Black

Weakly coordinating solvents, such as dichloromethane, have been shown to be attractive for the electrodeposition of functional p-block alloy and compound semiconductors for application to electronic devices. Weakly coordinating solvents are of interest for the electrodeposition of p-block elements since they do not interact strongly with solute molecules and will not disrupt the speciation of labile p-block element complexes. Dichloromethane is commonly used as a weakly coordinating solvent but is volatile. In this thesis, alternative weakly coordinating solvents were identified and electrochemically characterised in order to improve understanding of electrochemistry in weakly coordinating solvents. They were then applied to the electrodeposition of metals and semiconductors at elevated temperatures to achieve electrodeposits with improved material properties.

Weakly coordinating solvents can be defined and identified using solvent descriptors. Here, a set of solvent selection criteria were identified using Kamlet and Taft's $\pi*$, α and β parameters. Suitable solvents should be polar ($\pi* \geq 0.55$), aprotic ($\alpha \leq 0.2$) and weakly coordinating ($\beta \leq 0.2$). With this criteria, five candidate solvents were identified: trifluorotoluene, o-dichlorobenzene, p-fluorotoluene, chlorobenzene and 1,2-dichloroethane. The solvents were characterised and compared to dichloromethane with a suite of measurements including electrolyte potential window, conductivity, and double-layer capacitance, as well as the electrochemistry of the model redox couples decamethylferrocene and cobaltocenium hexafluorophosphate. The measurements indicated that ion pairing was a determining feature in weakly coordinating solvents. o-dichlorobenzene (oDCB) and 1,2-dichloroethane (DCE) were chosen as the most promising solvents for application to electrodeposition because of their polarity.

In order to understand the nature of electrodeposition in oDCB and DCE, the electrochemistry of the metal precursors $[N^nBu_4][SbCl_4]$, $[N^nBu_4][BiCl_4]$ and $[N^nBu_4]_2[TeCl_6]$ were then studied using macro- and microelectrodes, and the electrochemical quartz crystal microbalance. The voltammograms indicated that the $Sb^{3+/0}$ and $Bi^{3+/0}$ broadly displayed simple deposition and stripping processes. Similarly the quartz

crystal microbalance showed mass gain and ensuing mass loss with a high Faradaic efficiency. The microelectrodes were used to measure the redox potential and diffusion coefficient of the precursors. The electrochemistry of $[N^nBu_4]_2[TeCl_6]$ was found to be more complex. The deposition of Te appeared kinetically limited in DCE and there was also evidence to suggest the cathodic stripping of deposited Te to form Te^{2-}, along with subsequent chemical reactions. Sb, Bi and Te were successfully electrodeposited onto TiN substrates from oDCB and DCE. The resulting deposits were characterised using scanning electron microscopy, energy dispersive X-ray spectroscopy, X-ray diffraction and Raman spectroscopy. It was found that Sb grew amorphously at room temperature, but that Bi and Te were crystalline.

Further to this, the co-electrodeposition of antimony telluride and bismuth telluride onto TiN was attempted. Deposits were collected at several potentials and it was possible to electrodeposit stoichiometric Sb_2Te_3 from electrolytes containing 1.5 mM $[N^nBu_4][SbCl_4]$ and 3 mM $[N^nBu_4]_2[TeCl_6]$ in oDCB, and 1.75 mM $[N^nBu_4][SbCl_4]$ and 3 mM $[N^nBu_4]_2[TeCl_6]$ in DCE. Deposition of Bi_2Te_3 from both solvents was also successful, with baths composed of 2 mM $[N^nBu_4][BiCl_4]$ and 3 mM $[N^nBu_4]_2[TeCl_6]$ for oDCB, and 2.5 mM $[N^nBu_4][BiCl_4]$ and 3 mM $[N^nBu_4]_2[TeCl_6]$ for DCE. Characterisation of the deposits with scanning electron microscopy, energy dispersive X-ray spectroscopy and X-ray diffraction showed that the deposits were nanocrystalline.

Finally, the effect of temperature on electrochemistry in oDCB and DCE was studied. Its influence was initially explored with measurements of the redox potential and diffusion coefficient of decamethylferrocene and cobaltocenium hexafluorophosphate as a function of temperature. Sb was then electrodeposited at various temperatures between 25 °C and 140 °C. Scanning electron microscopy indicated that the deposits became smoother and more uniform with increasing temperature. Additionally, X-ray diffraction and Raman spectroscopy showed that Sb deposited in a crystalline form at temperatures above 120 °C, rather than amorphously at lower temperatures. Attempts at the electrodeposition of antimony telluride showed similar improvements in the properties of the deposit, but the composition was no longer stoichiometric.

Table of Contents

List of Figures

List of Tables

DECLARATION OF AUTHORSHIP

Alexander W. Black

Characterisation and Application of Weakly Coordinating Solvents for the Electrodeposition of Semiconductors

I declare that this thesis and the work presented in it is my own and has been generated by me as the result of my own original research.

I confirm that:

1. This work was done wholly or mainly while in candidature for a research degree at this University;
2. Where any part of this thesis has previously been submitted for a degree or any other qualification at this University or any other institution, this has been clearly stated;
3. Where I have consulted the published work of others, this is always clearly attributed;
4. Where I have quoted from the work of others, the source is always given. With the exception of such quotations, this thesis is entirely my own work;
5. I have acknowledged all main sources of help;
6. Where the thesis is based on work done by myself jointly with others, I have made clear exactly what was done by others and what I have contributed myself;
7. Parts of this work have been published as:

A. W. Black and P. N. Bartlett, Selection and Characterisation of Weakly Coordinating Solvents for Semiconductor Electrodeposition, *Phys. Chem. Chem. Phys.*, 2022, **22**, 8093-8103.

A. W. Black, W. Zhang, G. Reid, P. N. Bartlett, Diffusion in Weakly Coordinating Solvents, *Electrochim. Acta*, 2022, DOI: 10.1016/j.electacta.2022.140720.

Signed:

Date:

Acknowledgements

First and foremost I must thank my supervisor Prof. Phil Bartlett for all of his support and advice throughout this project. He was a source of infinite knowledge who helped turn my ideas into useful experiments and without whom this work would never have been possible. I am very grateful to him for giving me the opportunity to complete my PhD at the University of Southampton.

I would also like to thank all the members, past and present, of the Bartlett group and the ADEPT project for welcoming me to Southampton and teaching me so much. I am especially grateful to Dr David Cook and Dr Gabriela Kissling for turning me into a functioning scientist. As well as Dr Simon Reeves, Dr Lingcong Meng and Dr Shibin Thomas for all of their interesting and helpful discussions, and Dr Almudena Marti-Morant, Beth Bowden and Dr Jo Corsi for their friendship. I also owe thanks to Dr Wenjian Zhang for rapid and reliable provision of dried and purified solvents and reagents, and Dr Yasir Noori for the preparation of substrates for electrodeposition.

I want to thank my parents and Stephen for always taking an interest in my work and for their encouragement in pursuing science too. Finally, last but by no means least, I will always be grateful to Ella for her support during the completion of my PhD, the writing of this thesis, and for making the last few years in Southampton so enjoyable. Your dedication is inspirational, and your presence made this work so much easier than it might have otherwise been.

List of Terms and Symbols

A Area of electrode, m^2

CR Charge rate parameter, $\mathrm{mC\,cm^{-2}\,min^{-1}}$

D_O Diffusion coefficient of oxidised species, $\mathrm{cm^2\,s^{-1}}$

D_R Diffusion coefficient of reduced species, $\mathrm{cm^2\,s^{-1}}$

D Diffusion coefficient, $\mathrm{cm^2\,s^{-1}}$

$E_{1/2}$ Half-wave potential, V

$E_{1/4}$ First quartile potential, V

$E_{3/4}$ Third quartile potential, V

E_T Potential shift associated with the Thompson effect, V

$E_{\mathrm{a,D}}$ Activation energy of diffusion, $\mathrm{J\,mol^{-1}}$

$E_{\mathrm{a},\eta}$ Activation energy of viscosity, $\mathrm{J\,mol^{-1}}$

E_a Electrolyte anodic limit, V

E_c Electrolyte cathodic limit, V

E_rc Redox couple potential shift, V

E_tlj Potential shift associated with thermal liquid junction potential, V

E_window Electrolyte potential window, V

E Potential, V

K_A Association constant for ion pairing, $\mathrm{dm^3\,mol^{-1}}$

K_D Dissociation constant for ion pairing, $\mathrm{mol\,dm^{-3}}$

N_A Avogadro's number, $\mathrm{mol^{-1}}$

Q Charge, C

R_u Uncompensated resistance, Ω

T_b Boiling point, K, °C

T_c Critical temperature, K, °C

T Temperature, K, °C

V_{McG} McGowan volume, $cm^3\ mol^{-1}$

V_{crs} Crystallographic volume, $Å^3$

V_m Molar volume, $cm^3\ mol^{-1}$

V_{vDW} van der Waals volume, $cm^3\ mol^{-1}$

ΔG_f Free energy of formation, $J\ mol^{-1}$

ΔG_{lat} Lattice energy, $J\ mol^{-1}$

ΔG_{soln} Free energy of solution, $J\ mol^{-1}$

ΔG_{solv} Free energy of solvation, $J\ mol^{-1}$

ΔS_{rc} Entropy change of redox couple, $J\ K^{-1}\ mol^{-1}$

Λ_m^0 Limiting molar conductivity, $S\ cm^2\ mol^{-1}$

Λ_m Molar conductivity, $S\ cm^2\ mol^{-1}$

α Transfer coefficient

α Kamlet and Taft hydrogen bond donation parameter

α Polarisability, cm^3

β Kamlet and Taft hydrogen bond acceptor parameter

ϵ_0 Permittivity of free space, $F\,m^{-1}$

ϵ_{op} Optical dielectric constant

ϵ_r Dielectric constant

η_0 Pure solvent viscosity, Pa s

η_r Relative viscosity

η Viscosity, Pa s

κ Specific conductivity, $S\ cm^{-1}$

$\lambda_{\pm}^{0}$ Limiting ionic conductivity, $\mathrm{S\,cm^2\,mol^{-1}}$

F Faraday constant, $\mathrm{C\,mol^{-1}}$

R Gas constant, $\mathrm{J\,K^{-1}\,mol^{-1}}$

n Number of transferred electrons

μ Dipole moment, D

ν Potential scan rate, $\mathrm{V\,s^{-1}}$

π^* Kamlet and Tafts' polarity parameter

ρ Density, $\mathrm{g\,cm^{-3}}$

τ_{D} Debye relaxation time, s

τ_{L} Longitudinal relaxation time, s

a^{TM} Coordination ability index

a Radius of microelectrode, cm

c Concentration of electroactive species in the bulk, M

d Ion solvent distance, m

e Elementary charge, C

f_{HS} Hard sphere friction factor, $\mathrm{kg\,s^{-1}}$

f_{P} Perrin correction friction factor

f_{tot} Total friction factor, $\mathrm{kg\,s^{-1}}$

g_{K} Kirkwood correlation parameter

i_{L} Mass transport limited current, A

i_{p} Peak current, A

i Current, A

j Current density, $\mathrm{A\,cm^{-2}}$

k_s' Standard heterogeneous rate constant, $\mathrm{cm\,s^{-1}}$

k_{B} Boltzmann constant, $\mathrm{J\,K^{-1}}$

n Refractive index

p_c Critical pressure, Pa

p_v Vapour pressure, Pa

p Pressure, MPa

r_{McG} McGowan radius, m

r_S Stokes radius, m

r_{crs} Crystallographic radius, m

r_{solv} Solvent radius, m

r_{vDW} van der Waals radius, m

r Radius of electrode, m

$z^{\pm}$ Ionic charge

List of Abbreviations

ACN Acetonitrile

AN Gutmann's acceptor number

CB Chlorobenzene

Cc Cobaltocene

Cp Cyclopentadienyl anion

crs Crystallographic

DCE 1,2-dichloroethane

DCM Dichloromethane

DME Dimethoxyethane

DMF N,N-Dimethylformamide

DMFc Decamethylferrocene

DMSO Dimethyl sulphoxide

DN Gutmann's donor number

EG Ethylene glycol

EPA Electron Pair Acceptor

EPD Electron Pair Donor

HBA Hydrogen Bond Acceptor

HBD Hydrogen Bond Donor

KT Kamlet and Taft

LFER Linear Free Energy Relationship

McG McGowan

o.e. Oxidation efficiency

oDCB o-dichlorobenene

PC Propylene carbonate

pFT p-fluorotoluene

scDFM Supercritical difluoromethane

SCF Supercritical Fluid

TFT Trifluorotoluene

THF Tetrahydrofuran

tlj Thermal liquid junction

vDW van der Waals

WCS Weakly coordinating solvent

1

Introduction

1.1. Solute-Solvent Interactions

To make an electrolyte, a salt, A_yB_x composed of ions aA^{x+} and bB^{y-} must be dissolved in a solvent. Fig. 1.1 shows the free energy processes associated with solution formation, where ΔG_L is the lattice energy, ΔG_{soln} is the free energy change of solution and ΔG_{solv} is the free energy change upon solvation, also described as hydration.

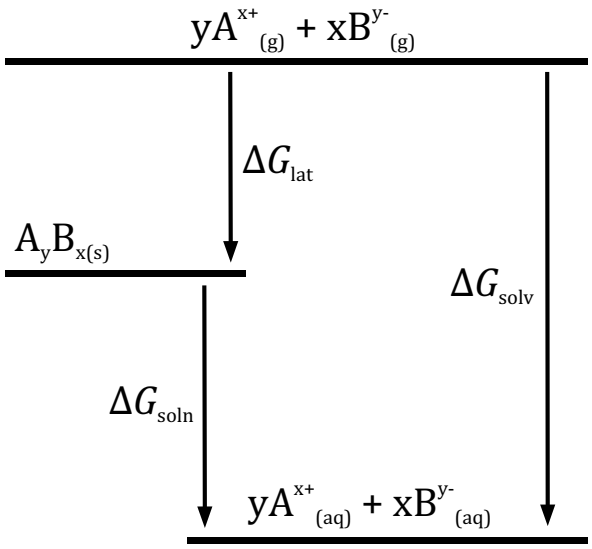

Figure 1.1: Generalised Born-Haber cycle of electrolyte formation.

Once in solution, the ion is surrounded by solvent molecules in a solvation shell. The dipolar solvent molecules orient themselves according to the charge on the ion and there is an energy of interaction between the solvent and the solute, described in general terms as 'intermolecular forces'. These interactions between a solute and its solvent are broadly composed of non-specific and specific interactions. Non-specific interactions are electrostatic in nature and involve the entire solute molecule equally. Specific interactions are concerned with particular moieties on the molecules. There is also a cavitation energy

associated with disrupting the solvent structure and forming a cavity for the entry of the solute.

Non-specific interactions are composed of various types which have a differing dependence on the distance, d, between the two interacting particles. They are present in all solutions between the solvent molecules, and between the solvent and solute also. These are summarised in Table 1.1 for two particles in fixed positions.[1]

Type of force	Internuclear distance function
Ion-ion	d^{-1}
Ion-dipole	d^{-2}
Ion-induced dipole	d^{-4}
Dipole-dipole	d^{-6}
Dipole-induced dipole	d^{-6}
Instantaneous-induced dipole	d^{-6}

Table 1.1: Forces involved in ion solvation.

Below shows the potential energy of interaction, U_{ij}, between two particles, i and j for the types of interaction in Table 1.1. Those in Eqns. (1.4), (1.5) and (1.6) are also known as Keesom, Debye and London forces respectively. Collectively they are referred to as van der Waals forces.[1,2] ϵ_0 is the permittivity of free space, z is the charge on the ion, e is the elementary charge, ϵ_r is the dielectric constant of the liquid, μ is the dipole moment of the species, θ is the angle of the point charge relative to the the dipole, α is the polarisability, k_B is Boltzmann's constant, T is the absolute temperature, and I is the ionisation potential.

ion-ion:
$$U_\mathrm{ij} = \frac{1}{4\pi\epsilon_0}\frac{z_\mathrm{i} z_\mathrm{j} e^2}{\epsilon_\mathrm{r} d} \tag{1.1}$$

ion-dipole:
$$U_\mathrm{ij} = -\frac{1}{4\pi\epsilon_0}\frac{z_\mathrm{i} e \mu_\mathrm{j}}{d^2}\cos\theta \tag{1.2}$$

ion-induced dipole:
$$U_\mathrm{ij} = -\frac{1}{(4\pi\epsilon_0)^2}\frac{(z_\mathrm{i} e)^2 \alpha_\mathrm{j}}{2d^4} \tag{1.3}$$

dipole-dipole:
$$U_\mathrm{ij} = -\frac{1}{(4\pi\epsilon_0)^2}\frac{2\mu_\mathrm{i}^2\mu_\mathrm{j}^2}{3k_\mathrm{B}Td^6} \tag{1.4}$$

dipole-induced dipole:
$$U_\mathrm{ij} = -\frac{1}{(4\pi\epsilon_0)^2}\frac{\mu_\mathrm{i}^2\alpha_\mathrm{j}}{d^6} \tag{1.5}$$

instantaneous-induced dipole:
$$U_\mathrm{ij} = -\frac{1}{(4\pi\epsilon_0)^2}\frac{3\alpha_\mathrm{i}\alpha_j}{2d^6}\frac{I_\mathrm{i} I_\mathrm{j}}{I_\mathrm{i} + I_\mathrm{j}} \tag{1.6}$$

Specific interactions consist of hydrogen bonding and electron pair donor (EPD)/ electron pair acceptor (EPA) interactions.[3] These interactions only exist between certain atoms or functional groups and so are not necessarily present in every solution. Hydrogen

bonding is the formation of a bond between a covalently bound hydrogen and another, non-hydrogen atom. For hydrogen bonding to be observed a hydrogen atom must be available for donation *i.e.* acidic. Molecules with functional groups containing H in this form are known as hydrogen bond donors (HBD). Also required is a molecule with an available lone pair to accept the proton, a hydrogen bond acceptor (HBA). In principle hydrogen bonding is possible with any atoms more electronegative than hydrogen, but it is only significant for solvents and solutes containing the most electronegative atoms O, N or F, *e.g.* ethers, carbonyls and amines as HBAs, and alcohol, acid and amino groups as HBDs. H bonds are generally considered a special type of dipole-dipole interaction, however the small size of the H atom permits a close enough approach to the HBA that orbital overlap is possible and a degree of covalent character exists in a H bond. An illustrative example of H bonding is shown in Fig. 1.2a for water.

EPD/EPA complexes, also known as charge transfer interactions, take place between a molecule with an occupied molecular orbital (EPD) and a molecule with a vacant molecular orbital (EPA). Their orbitals can overlap and the EPD donates an electron pair to the EPA and in the limiting case, a bond is formed. The EPD can also be referred to as a Lewis base or nucleophile and the EPA as a Lewis acid or electrophile. The EPD/EPA type interaction is a combination of electrostatic and covalent forces. Electron pair donation can originate from an anion, a lone pair on an atom such as O or N in carbonyls and amines, or the electron pair in an unsaturated bond. Good electron acceptors are vacant valence orbitals such as in a metal cation, a non-bonding σ orbital as in I_2, or from a π bond system with electron withdrawing groups. In principle any combination of donors and acceptors is possible but of particular significance in an electrolyte solution is those between a lone pair on a solvent molecule and a cation, and an anion and a Lewis acid. An illustrative example of of EPA-EPD interactions can be seen in Fig. 1.2b between a carbonyl group and a monoatomic cation.

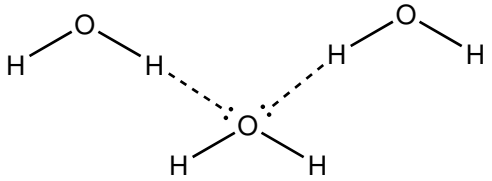

(a) H bonding interaction

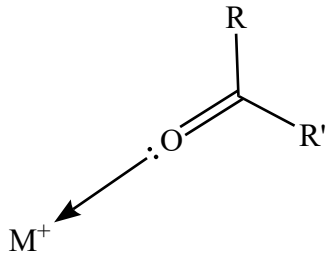

(b) Lewis acid-base interaction

Figure 1.2: Representative schematic of non-specific interactions.

Once the salt is in solution, it is not always possible for the two ions to completely dissociate into individual species, and instead they can exist in solution as a distinct entity

known as an ion pair.

$$(A^+B^-)_{aq} \underset{K_a}{\overset{K_d}{\rightleftharpoons}} A^+_{aq} + B^-_{aq}$$

Ions in solutions therefore exist as an equilibrium mixture of ion pairs and free ions. The position of the equilibrium is described by the dissociation constant, K_d, or by the association constant, K_a. Conventionally, ion pairing is described in terms of K_a. Ion pairs are not simply a transient phenomenon, but exist for a timescale that is experimentally measurable, and their presence results in recognisable chemical behaviours. Meaning they should be recognised as a distinct chemical species. It is possible to estimate K_a with Bjerrum's equation.[4]

$$K_A = 4\pi N_A \left(-\frac{z_i z_j e^2}{4\pi\epsilon_0\epsilon_r k_B T}\right)^3 Q(b) \tag{1.7}$$

$$b = -\frac{z_1 z_2 e^2}{4\pi\epsilon_0\epsilon_r a k_B T} \tag{1.8}$$

Where a is the distance of closest approach of the anion and cation, typically taken as the sum of their radii, and $Q(b)$ is an integral with solutions in the literature for various values of b. The Bjerrum equation predicts an inverse relationship between K_a and ϵ_r, suggesting that the degree of ion pairing increases as the polarity of the solvent decreases. As ϵ_r of the solvent lowers, its ability to solvate the ion and attenuate its charge is lessened, so the ion looks elsewhere for charge stabilisation and forms a pair with an ion of opposite charge. In particularly non polar solvents, or at high concentrations, the formation of triple ions, such as $[ABA]^+$ or $[BAB]^-$ is also possible.

The total energy of interaction between an ion and its solvent can be described in terms of an expression for ΔG_{solv}. This is given in its most basic form by the Born equation which describes the work required to transfer an ion from a vacuum to a particular solvent.[2] The ion is treated as a spherical point charge and the solvent as a dielectric continuum:

$$\Delta G_{solv} = -\frac{N_A z^2 e^2}{8\pi\epsilon_0 r}\left(1 - \frac{1}{\epsilon_r}\right) \tag{1.9}$$

Where N_A is Avogadro's number and r is the radius of the ion.

The Born equation is clearly a highly simplified description of solute- solvent interactions. In fact, quantifying the magnitude of non-specific interactions is difficult when considering the large number of particles involved in a real solution. Furthermore, assessing the degree of specific interactions requires knowledge of the electronic structure of the relevant species and calculations on a quantum mechanical level. A complete picture of ion-solvent and ion-ion interactions requires statistical mechanical calculations of the average relative location and momentum of the particles in a solution and the forces

acting on them. This is a particularly difficult task and is prohibitive to all but those with specialist knowledge and access to significant computing power. However, it is still possible to gain insight into the nature of solute-solvent interactions with recourse to methods which are simpler and more accessible, by use of solvent descriptors.

1.2. Solvent Descriptors

A solvent descriptor is a quantified measure of some property of a solvent which can be used to classify or rank a solvent based upon the magnitude of the descriptor in question. They can be used to understand the role the solvent plays in a particular process, or predict the behaviour of a process in an unknown solvent system. The simplest form of solvent descriptors are the physical constants associated with the solvent molecule. Boiling point, vapour pressure, density, viscosity, dipole moment and refractive index are all examples of solvent descriptors. However, not all of these relate to the way in which a solvent interacts with a dissolved solute.

One descriptor that has become particularly important as an estimate of the polarity of the solvent, *i.e.* the strength of electrostatic interactions between the solvent and a solute, is the dielectric constant, ϵ_r. ϵ_r is particularly popular because of the ready accessibility of values for most common solvents and because it is generally accurate for its desired purpose. Although it is important to understand what exactly is represented by ϵ_r. ϵ_r is obtained by immersing two plates of a capacitor in the solvent and measuring the strength of the electric field between them. The external electric field induces dipoles in the molecules and polarises the permanent dipoles, which causes an attenuation of the applied electric field. A greater degree of polarisation leads to a larger drop in field strength. The magnitude of the decrease, relative to a vacuum, is then ϵ_r. Therefore, ϵ_r describes the ability of the solvent molecules' dipoles to orient themselves in response to an external electric field. It is then implicitly taken that this correlates with the ability of a solvent to electrostatically interact with a solute. However, ϵ_r has been shown to be inadequate in describing, and predicting both homogeneous,[5] and heterogeneous processes (see 1.3). This is because ϵ_r is a macroscopic property describing the average of the bulk solvent, it does not contain information on the solvent molecules in the microscopic environment surrounding the solute. The added disadvantage of solvent descriptors based on physical properties, is that there are none available which accurately describe non-specific interactions.

The failure of the physical properties to understand solute-solvent interactions, with ϵ_r as an example above, has led to work on empirical solvent descriptors. These take a solvent dependent reference process, which probes the solvation shell in the particular solvent, and measures any changes in the process as the solvent is changed. Reference processes can be based on equilibrium, kinetic or spectroscopic measurements.[6] For solvent dipolarity, a good example is Dimroth and Reichardt's $E_T(30)$ parameter.[6] This pa-

rameter uses a solvatochromatic pyridinium betaine based dye, and measures the change in wavelength of the $\pi \longrightarrow \pi*$ absorption band in UV/Vis spectroscopy, with the changing solvent. The position of this absorption peak varies greatly with the solvent, meaning that the $E_T(30)$ is highly sensitive to solvent polarity. One issue with this approach is that the dye is not soluble in non-polar solvents. Meaning that the dye has to be modified, and now the same dye is not used for all measurements. Another notable example of a solvent dipolarity descriptor include Kamlet and Taft's $\pi*$ parameter, which is based on a similar principle to $E_T(30)$, but with different dyes.[7]

Empirical descriptors have also been developed for specific interactions. Gutmann's Donor Number (DN), is used as a measure of the Lewis basicity of a solvent. DN is obtained by the calorimetric measurement of the reaction between $SbCl_5$ and the solvent of interest, both measured in the 'inert' solvent 1,2-dichloroethane.[8] DN is a popular descriptor for estimating Lewis basicity because of its accessibility, however it has also been criticised.[3] For example, the measurement is performed when the solvent molecule is in a dilute solution, and so reflects the Lewis basicity of a single solvent molecule. It is not certain that the solvent will interact with the Lewis acid in the same way when the solvent is in the bulk form. Additionally, the measurement is based on the enthalpy of the process, meaning that values in solvents with a significant entropic contribution will not be measured accurately.[9] Other Lewis basicity descriptors which have been developed include Kamlet and Taft's β parameter based upon solvatochromatic dyes,[7] or Koppel and Palm's B descriptor, developed with IR measurements of alcohols.[10]

Similar to Lewis basicity, descriptors can also be found for the degree of electrophilicity, or Lewis acidity of a solvent. The Acceptor Number (AN) scale was created by Gutmann for this purpose.[3] This parameter is derived from NMR shifts of triethylphosphane oxide in different solvents, relative to a reference. A similar scale was also developed by Kamlet and Taft, called the α descriptor.[7] This is obtained from solvatochromic shifts, measured by UV/Vis spectroscopy, of aniline based dyes. Rather than simply being the inverse of Lewis basicity descriptors, scales of electrophilicity are useful for characterising protic solvents and their capacity for accepting hydrogen bonding.

The use of an empirical solvent descriptor involves some implicit assumptions that must be considered when they are to be interpreted. The first concerns the treatment of the reference process. It is assumed that the solute-solvent interactions between the solvent being measured and the reference probe are the same for every solvent that is studied. But this cannot be known for definite. For example, the dye used in the determination of $E_T(30)$ contains a phenolic oxygen which is protonated in acidic solvents.[6] This prevents the measurement of the absorption peak in such solvents and the descriptor must be obtained by other means. Secondly, it is assumed that the solvent descriptor accurately measures the type of solvent-solute interaction that it has been designed to measure, and does not include information on other types of interactions as well. Kamlet and Taft's $\pi*$ parameter is intended as a measure of the polarity of the solvent, containing information

on electrostatic dipolar and polarisability based interactions.[11] However, it was found that a correction term for more polarisable solvents, such as aromatics, needed to be added to improve the agreement with experiment.[12] Suggesting that the $\pi*$ parameter does not fully account for polarisability based electrostatic interactions. In addition, the ability of a solvent descriptor to accurately represent the solute-solvent interactions that it claims to was considered by Katritsky *et al.*, who used computation to correlate common empirical descriptors with a variety of theoretical and computationally derived descriptors.[13] It was concluded that this is not necessarily true and the usefullness of some descriptors must be questioned. But also that many of the popular descriptors, such as $E_{\mathrm{T}}(30)$, Gutmann's DN and AN, or the Kamlet and Taft parameters are actually successful at measuring their intended interactions.

There are a multitude of descriptors available in the literature and this can make informed choice of descriptor difficult. Marcus,[14] and Abboud and Notario,[10] provided a compilation of the most notable solvent descriptors along with a critical discussion. The authors both also demonstrated that within a particular type of interaction, *i.e.* non-specific or Lewis basicity, the different descriptors generally correlate well with each other. This is reassuring because it suggests that all the descriptors generally measure the same basic interaction. From this it might also mean that, in the absence of a specific conceptual or experimental flaw, there may not be any significant advantage to using one descriptor over another.

From the discussion above, it is clear that a single parameter is not enough to describe the myriad interactions between solvent and solute at the molecular level. As such, solvent descriptors can be combined together in an approach known as Linear Free Energy Relationships (LFERs). LFERs take the general form of:

$$X = X_0 + \mathrm{a}A + \mathrm{b}B + \mathrm{c}C... \tag{1.10}$$

where X is a free energy related solvent dependent property, such as the logarithm of equilibrium constant, or redox potential, X_0 is a statistical quantity that relates the property to a reference such as a solvent which is assumed to have zero or negligible influence on the process, or the gas phase, A, B, C *etc.* are independent solvent descriptors that describe different interactions between solvent and solute, a, b and c are coefficients whose magnitudes reflect the influence of the complementary descriptor on the property in question. The behaviour of a solvent dependent process can then be understood by correlation of X measured in several solvents with the solvent descriptors using multiple linear regressions. A high quality fit indicates that the descriptors are effective at accounting for the solute-solvent interactions that influence the value of the correlated process. LFERs can be used to understand reaction mechanisms, or to predict reaction rates in an unstudied solvent for example. LFERs are based upon principles of additivity and separability,[6] meaning that it is taken to be true that the total solvent-solute interactions in-

volved in process X can be separated into constituent contributions and, conversely that the descriptors used to quantify the interactions account fully for those involved. Therefore it is preferable to use a series of descriptors from the same researcher which have been designed for use in a LFER. This will ensure the descriptors are mutually orthogonal and account fully for the various solvent-solute interactions. Some notable collections of LFERs are those of Kamlet and Taft,[7] Koppel and Palm,[15] and Drago.[16]

1.3. The Role of the Solvent in Electron Transfer

The influence of the solvent on observed electrochemical behaviour is complex and depends not only on the solvent but also the nature of the solute *i.e.* cation/anion, organic compound/metal complex. All will interact with the solvent differently and thus will have its electrochemical response influenced to a greater or lesser extent by the solvent.

Beginning with redox potential, the role of the solvent is manifested in the Gibb's energy of solvation. Different solvents relative to each other will be better able to stabilise either the oxidised or reduced form of the species, and the redox potential will shift accordingly. However, as described above, the solvation energy is composed of different types of interactions and understanding how they each contribute, along with the magnitude of solvent dependent shift in redox potential is more difficult. Most experiments use metal complexes where the oxidised and reduced forms have ligands that are substitutionally inert and involve an outer sphere one electron transfer. This ensures that the inner coordination sphere can be assumed to remain unchanged and any observed relationships are a function of the outer sphere energy of interaction with the solvent only.

According to Lay, the solvent influence on the redox potential can be interpreted as a linear summation, based upon the different types of contribution:[17]

$$E = E^{\circ} + \Delta E_{\mathrm{p}} + \Delta E_{\mathrm{H}} + \Delta E_{\mathrm{s}} \tag{1.11}$$

where E is the observed redox potential, E° is the redox potential in the gas phase (*i.e.* in a noninteracting medium), ΔE_{p} is the shift in redox potential caused by non-specific dipolar interactions, ΔE_{H} describes the strength of interaction between solvent molecules and the extent to which the two species of the couple disrupt the structure of the solvent, ΔE_{s} reflects the change in redox potential as a result of specific solute-solvent interactions. It was then proposed that each term in Eqn. (1.11) can be related to experimentally measurable parameters to understand the influence of each term on the redox potential. The Kamlet-Taft parameters were selected for this task, and thus:

$$\Delta E_{\mathrm{p}} \approx \mathrm{s}(\pi^{*} + \mathrm{d}\delta) \tag{1.12}$$

$$\Delta E_{\mathrm{H}} \approx \mathrm{h}\delta_{\mathrm{H}} \tag{1.13}$$

$$\Delta E_{\mathrm{s}} \approx \mathrm{a}\alpha + \mathrm{b}\beta \tag{1.14}$$

where δ is Kamlet and Taft's polarisability correction factor described above and δ_H is the Hildebrand solubility parameter: the energy needed to create a cavity in the solvent for a solute.[18] Subsequently, Lay *et al.* measured the redox potential of the reduction of various cationic metal complexes in several solvents and correlated them with the above KT parameters.[19] The best correlation was a negative relationship with the β parameter, suggesting EPA/EPD type interactions are the most significant. A negative correlation can be rationalised if the cation is treated as a Lewis acid, it would then be expected that solvents with a larger β (more Lewis basic) more effectively stabilise the positive charge, and so decrease the redox potential. The oxidised form is more highly charged meaning its specific and non-specific interactions with the solvent are stronger, compounding the effect. The correlation was improved when including the π^* term, indicating non-specific interactions play a role, but the magnitude of b was much larger than s. No relationship was observed between E and δ_H.

It must be noted that the effect of the solvent is dependent on the relative changes in charge sign and number between the oxidised and reduced forms of the redox couple. A cation is a Lewis acid, so would be expected to show a solvent dependence with Lewis basic solvents and Lewis acids would have no effect on redox potential. Conversely, an anionic redox couple is Lewis basic, so will interact with a Lewis acidic solvent. Furthermore, for the oxidation of a neutral redox couple to a cation, or a redox couple where both forms are positively charged, the charge of the oxidised form is greater than the charge on the reduced form. Therefore, the strength of interactions between the solvent and the oxidised form will be greater than those between the reduced form of the redox couple and this would shift the redox potential negatively. On the other hand, for the reduction of a neutral species to an anion, or a redox couple where both forms are anionic, the charge is now greater on the reduced rather than the oxidised form of the redox couple. As such, interactions between the solvent and the reduced form are stronger and so this shifts the redox potential in the anodic direction.

The importance of EPA/EPD interactions was also emphasised by Gritzner and Gutmann, in several investigations across multiple non-aqueous solvents. For a metal cation where the product does not interact with the solvent (*e.g.* an amalgam in polarography), the reduction potential was negatively correlated with DN.[20] A positive correlation was observed between anions and AN for the reduction of $[Mn(CN)_6]^{3-}$ and $[Fe(CN)_6]^{3-}$ by Messina and Gritzner.[21] Fe(II) is more electron rich than Fe(III) so is a more effective electron donor and the reduced form is better stabilised. The influence of EPA/D properties of the solvent on anions and cations has been observed elsewhere also.[22–26]

The role of polar interactions have also been considered. Measures of redox potential of various ions across several solvents were correlated with $1/\epsilon_r$ (see Eqn. (1.9)),[20,21] ϵ_r,[22,23,26] and dipole moment (μ).[21–23,26] In all cases, no correlation could be observed. Dipolar interactions clearly make a contribution, as evidenced by Lay, but this exemplifies the inadequacy of bulk solvent descriptors describing solute-solvent interactions.

The contribution of specific interactions to the shift in redox potential is dependent on the ligand complexing the metal however. $[Fe(CN)_6]^{4-}$ for example, has a convenient site of electron donation to the solvent at the N atom. Conversely, complexes with large bulky ligands such as $Cp(CH_3)_5$ (Cp=cyclopentadiene) in decamethylferrocene (DMFc) disrupt the interactions of the complex with the solvent and have been demonstrated to have a redox potential essentially independent of the medium.[27]

Researchers have also attempted to understand the underlying thermodynamic influence of solvent dependence by evaluating the enthalpic and entropic contributions to observed shifts in redox potential. Weaver published two articles where the property $\Delta(\Delta G^0_{rc})^{s-w}$ was measured for multiple metal cations in several non-aqueous solvents.[28,29] $\Delta G^0_{rc} = G^0_{red} - G^0_{ox}$, the free energy for the electron transfer reaction of a redox couple was obtained from measurements of redox potential. $\Delta(\Delta G^0_{rc})^{s-w}$, is then the change in ΔG^0_{rc} between water and a non-aqueous solvent and measures the change in solvation energy between the reduced and oxidised form of the couple upon changing of the solvent. The corresponding $\Delta(\Delta H^0_{rc})^{s-w}$ and $\Delta(\Delta S^0_{rc})^{s-w}$ were also measured. Ligands were selected so that some were expected to exhibit strong specific interactions with the solvent (*e.g.* ethylenediamine) and some that were not expected to display any (*e.g.* 2-2' bipyridine). For the complexes where specific interactions were not expected, the Born equation was used to estimate $\Delta(\Delta G^0_{rc})^{s-w}$. After considering expected variation, reasonable agreement was observed. $\Delta(\Delta G^0_{rc})^{s-w}$ was also correlated with DN and no agreement was observed, indicating dipolar interactions are the primary constituent of the solvation energy for those complexes. On the other hand, for the ions with coordinating ligands, no relationship was found between the measured and predicted values of $\Delta(\Delta G^0_{rc})^{s-w}$, and instead DN proved to be a good predictor. This relationship reflects the enthalpic component of $\Delta(\Delta G^0_{rc})^{s-w}$, increased interaction with the solvent serves to stabilise the ion and so reduce the internal energy.

With regards to the ΔS^0_{rc} term, it was observed to be positive in every solvent and for every redox couple. For a neutral species oxidised to a cation, or a couple where both forms are cations, the solvent dipoles orientate themselves in response to the electric field exerted by the solute ion, the reduced complex exerts a relatively smaller electric field compared to the oxidised form so the extent of solvent polarisation is less and an entropic gain is observed. For redox couples involving anions, the opposite is now true. No relationship was observed between $\Delta(\Delta S^0_{rc})^{s-w}$ and DN indicating the absence of Lewis acid-base interactions on solvent polarisation. Rather, it was observed that generally $\Delta(\Delta S^0_{rc})^{s-w}$ was larger in aprotic than protic solvents. It was concluded that the magnitude of ΔS^0_{rc} is dependent on the ability of the solute to disrupt the solvent's internal ordering. Solvents with hydrogen bonds for example, would be difficult to rearrange and so solvent polarisation is suppressed.

Turning to the role of the solvent in electron transfer kinetics, the Butler-Volmer model is the classical description, however it is not able to account for the role of the

solvent. The theory of Marcus can be used instead because it is capable of explaining how the structure of the reacting species and its environment influence the rate of electron transfer.[30] Marcus theory treats the reactant and product as overlapping free energy curves where the reactant is excited to the transition state, electron transfer occurs and then relaxes to the product. The rate is then a function of the shape of the two parabolas and how they interact.

According to Marcus the expression for the rate constant of heterogeneous electron transfer at the standard potential is:

$$k_s' = K_P \nu_n \kappa_{el} \exp\left(-\Delta G^* / RT\right) \tag{1.15}$$

where k_s' is the heterogeneous rate constant, K_P is the pre-equilibrium constant which represents the ratio of activated reactant (activated reactant meaning it has passed through all the elementary steps prior to electron transfer) to the bulk concentration, ν_n is the nuclear frequency factor describing the frequency with which the precursor reactant reaches the free energy barrier, similar to the collision frequency in classical kinetics,[31] κ_{el} is the electronic transmission coefficient and reflects the probability of electron transfer based on the strength of electronic interaction between the reactant and product, ΔG^* is the Gibbs energy of activation and R is the gas constant. The majority of work has focussed on the influence of the solvent on the values of ΔG^* and ν_n. These studies typically assume that K_P and κ_{el} are independent of the solvent.

ΔG^* is composed of the standard Gibbs energy for the reaction, ΔG^0, plus a reorganisation energy term, which describes the energy required to rearrange the reactant into the form of the product. If the standard electrochemical rate constant, k_s', is measured, then ΔG^* is dependent on the reorganisation energy only. As a result, ΔG^* can be divided into an inner sphere term ΔG_i^*, and an outer sphere term ΔG_o^*, such that $\Delta G^* = \Delta G_i^* + \Delta G_o^*$. ΔG_i^* is associated with reorganisation of the molecule itself such as bond lengths and angles and ΔG_o^* with the product's solvation environment. A value for ΔG_o^* can be estimated by adapting the Born equation:[32]

$$\Delta G_o^* = \frac{N_A e^2}{8\epsilon_0}\left(\frac{1}{r} - \frac{1}{2d}\right)\left(\frac{1}{\epsilon_{op}} - \frac{1}{\epsilon_r}\right) \tag{1.16}$$

where r is the radius of the reacting species, d is the distance between the species and the electrode, ϵ_{op} is the optical dielectric permittivity, often approximated to n^2. Experiments investigating the effect of the solvent on ΔG^* primarily use reagents that display outer sphere electron transfer, and are substitutionally inert such that $\Delta G_i^* \ll \Delta G_o^* \approx \Delta G^*$.

Weaver *et al.* investigated the influence of ΔG_o^* on k_s' in two studies.[33,34] In the first article, using a similar approach to Refs. [28, 29] above, k_s' was measured, and ΔG^0 and ΔG_o^* were obtained for the reduction of $[Co(en)_3]^{3+}$ in various aprotic non-aqueous solvents and standardised with respect to water, giving $\Delta(\Delta G_o^*)^{s-w}$. The pre-exponential

terms were assumed to be solvent independent. $\Delta(\Delta G_o^*)^{s-w}$ was compared with calculated values estimated from eq. (1.16) and large discrepancies were observed. The predicted value being negative, compared with a large positive experimentally obtained value. k_s' was also observed to be smaller in the non-aqueous solvents where DN was larger for the organic solvent than water. These results were attributed to the influence of specific interactions between the solvent and reactant increasing the energy of reorganisation.

Another approach to investigating the influence of electrostatics on ΔG_o^* is to plot $\ln k_s'$ or k_s' as a function of $1/\epsilon_{op} - 1/\epsilon_s$. This method was used for transition metal complexes and organic compounds in aprotic solvents by various researchers, including Fawcett and Jaworski,[35] Kapturkiewicz and Opallo,[36,37] and others.[38,39] In all cases no relationship was observed. This is a somewhat flawed approach though, it is not appropriate to compare k_s' to $1/\epsilon_{op} - 1/\epsilon_s$ since they are exponentially related. It also neglects the $2d$ term in eqn. (1.16). Assuming the reaction takes place at the outer Hemlholtz plane, the distance to the electrode is dependent on the width of the inner Helmholtz plane and so the solvent and supporting electrolyte.[33,40]

Once again, where applicable, the role of specific solvent-solute interactions must not be neglected. In a similar fashion to the redox couple, Lay derived useful modifications for the Marcus expression that accounts for non-specific interaction between the solvent and solute.[17] However no experimental evidence was provided to indicate their efficacy. Weaver derived an additional term to Eqn. (1.16) to account for 'noncontinuum' effects on ΔG_o^*.[41] The value of the term was estimated by plotting the redox potential of $[Co(en)_3]^{3+/2+}$ as a function of DN. This was then extrapolated to 0 where specific interactions would be absent, and the difference taken, to give an estimate of the change in redox potential as a result of the specific interactions. This was then converted to a free energy. The contribution was observed to be small yet significant and displayed improved agreement with experimental values compared to Eqn. (1.16) alone. Fawcett and Jaworski performed a similar investigation on the reduction of organic molecules.[35] A good negative correlation was observed between $\ln k_s'$ and AN. Abbott *et al.* also contributed work towards this question.[42,43] The natural logarithm of theoretical rate constants were plotted as a function of the natural logarithm of experimentally obtained values for solvents of a variety of properties. This was performed for theoretical values obtained using $1/\epsilon_{op} - 1/\epsilon_s$, and also the π^*, β and α parameters of KT. Better agreement was observed for the KT parameters. In a second study, $\ln k_s'$ values of ferrocene were obtained in several solvents and correlated with various parameters including $1/\epsilon_{op} - 1/\epsilon_s$, AN and DN, and the KT parameters. The best correlation was observed with the KT parameters. However, their approach was criticised for not appropriately distinguishing between the pre-exponential factor and ΔG^*, and not fully accounting for iR drop.[44,45]

The solvent has also been observed to influence the ν_n term in the pre-exponential factor. This has been heavily investigated and comprehensive reviews on the subject ex-

ist.[45,46] Under the condition that $\Delta G_{\mathrm{i}}^{*}$ is negligible, ν_{n} can be approximated as:[45]

$$\nu_{\mathrm{n}} = \frac{1}{\tau_{\mathrm{L}}}\left(\frac{\Delta G_{\mathrm{o}}^{*}}{4\pi \mathrm{R}T}\right)^{\frac{1}{2}} \tag{1.17}$$

$$\tau_{\mathrm{L}} = \frac{\tau_{\mathrm{D}}\epsilon_{\mathrm{op}}}{\epsilon_{\mathrm{r}}} \tag{1.18}$$

where τ_{L} is the longitudinal solvent relaxation time, τ_{D} is the Debye relaxation time and ϵ_{op} is the high frequency dielectric constant. τ_{L} measures the delay in the dipole orientation of a dielectric in response to an applied electric field. Slow solvent reorientation reduces the frequency that the reactant arranges itself into the transition state since this requires concurrent movement of the solvent, which is impeded at high values of τ_{L}. τ_{L}^{-1} has been observed to correlate well with k_{s}'.[37] Weaver employed a corrected k_{s}' which accounted for the contribution of the activation barrier.[47,48] Estimates of K_{P} and $\Delta G_{\mathrm{o}}^{*}$ were made and incorporated into a single term with k_{s}'. This was then plotted as a function of τ_{L}^{-1} and reasonable agreement was observed. Fawcett took a similar approach with similar results.[49–51]

τ_{D} can be defined as:[52]

$$\tau_{\mathrm{D}} = \frac{4\pi\eta r^{3}}{\mathrm{R}T} \tag{1.19}$$

where η is viscosity and r is the radius of the reacting particle. Evidence that the viscosity of a solvent can influence k_{s}' was observed in the work of Bard *et al.*, who investigated the rate constants of various metal complexes in water, altering the viscosity by additions of sucrose.[53,54] A good correlation was observed between k_{s}' and $1/\eta$. Murray also observed a relationship between k_{s}' and D where D is diffusion coefficient.[55]

The solvent effect on the kinetics of the mechanistically more complicated process of ion transfer has also been investigated. Galus performed studies on the kinetics of amalgam formation of various metal cations in several aprotic solvents.[52,56,57] Without accounting for any pre-exponential contributions, Galus observed a negative correlation between rate constant and Gutmann's DN and the KT β parameter, in accordance with reports above for outer-sphere electrode reactions. Fawcett observed the same relationship after correcting for τ_{L} by incorporating it into the rate expression .[58]

1.3.1. Electrochemistry in Supercritical Fluids

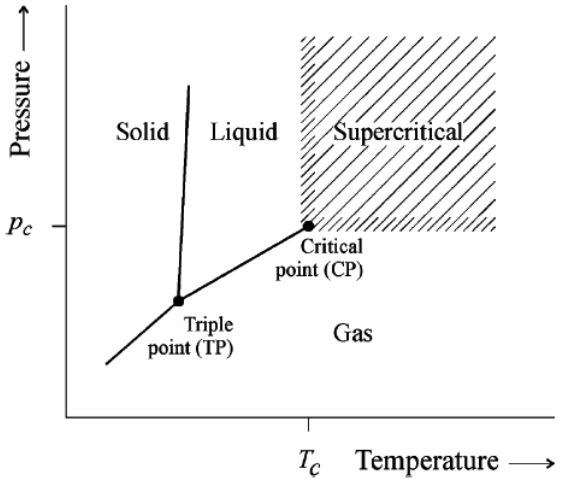

Figure 1.3: p-T phase diagram showing the supercritical region. Reproduced with permission from Ref. [59].

A supercritical fluid (scf) is a state of matter which exists at temperatures and pressures higher than gases and liquids. Specifically they are defined as a species which has a temperature and pressure higher than its critical point, T_c and p_c respectively. Alternatively, Darr and Poliakoff suggested they be defined in terms of a critical density.[60] Fig. 1.3 shows a phase diagram for a single component system.

A clear indicator of a supercritical fluid is its properties, intermediate between liquids and gases. For example its density is comparable to a liquid and its viscosity similar to a gas. They also possess unusual characteristics which make them interesting for research. They are capable of solvating species, the fluid exists as a single phase; meaning an absence of surface tension, and density and viscosity also vary with temperature and pressure, so the solvent properties can be finely tuned. The most widely researched scf is supercritical carbon dioxide ($scCO_2$) however many others such as scH_2O, $scNH_3$ and scXe have also been investigated.[60]

Bard and his group performed pioneering work in the field of supercritical electrochemistry, investigating the electrochemistry of inorganic and organic compounds in $scNH_3$,[61,62] scH_2O,[63–65] and acetonitrile.[66,67] These polar supercritical fluids have the advantage of improved solubility of charged species, but require high operating temperatures and pressure.

As a result of this, $scCO_2$ received some research interest due to its more accessible critical point ($T_c = 304\,K$, $p_c = 7.4\,MPa$).[68] Abbott *et al.* performed some studies but $scCO_2$ has such a low dielectric constant that it is not able to dissolve electrolytes effectively.[69,70] Consequently a co-solvent, typically acetonitrile, can also be added, allowing more effective dissolution of charged species. Much work was performed by Bartlett *et al.* who

investigated the double layer structure,[71] conductivity,[72] mass transport,[73] and also electrodeposition of metals.[74–76] The disadvantage of the two solvent system is that the phase behaviour is made more complicated and the critical point can change. Additionally, the use of MeCN reduces the potential window, making the $scCO_2$/MeCN system less useful for electrodeposition applications.

Around the same time as $scCO_2$/acetonitrile systems were investigated, hydrofluorocarbons were the focus of some attention. They have a similar critical point to CO_2 (CH_2F_2 $T_c = 351\,K$, $p_c = 5.8\,MPa$)[68] but a higher dielectric constant and also the advantages of being a single component system with a wide potential window. Abbott *et al.* reported initial investigations measuring fundamental properties such as dielectric constant in $scCH_2F_2$ (scDFM), $scCF_3CH_2F$ and $scCF_3CHF_2$.[77] Subsequently Bartlett *et al.* presented studies into the electrodeposition of metals from scDFM. Depositing films, and in some cases nanowires, of numerous d- and p-block metals including: Cu,[75] Te,[78,79] Ge,[80] as well as Bi, Sb, Se and others.[78] All metals were cathodically deposited at a fast rate and, excepting Ge, were crystalline. The entirety of the work on electrochemistry in supercritical fluids has recently been reviewed by Bartlett *et al.*[81]

scDFM appears to be the most useful sc solvent for electrodeposition, its properties represent a compromise between relatively low critical point and dielectric constant. Additionally it is the only sc solvent with any significant detail in the literature on metal deposition. To date there is no known literature report on compound deposition from supercritical fluids.

1.4. Electrodeposition of Binary Semiconductors

Binary semiconducting alloys and compounds are commonly grown by techniques such as chemical vapour deposition.[82] These methods are capable of producing device quality materials, however they often require high temperatures and pressures, or vacuum conditions. This often means that equipment and operational costs are high, and slow growth rates can be a problem too. Furthermore, vapour deposition techniques are 'top-down' approaches, meaning that when it comes to the growth of nanostructures, which is currently of research interest, it is often not possible to reliably penetrate the entire depth of high aspect ratio structures due to blocking at the pore mouth, which results in nonuniform and inconsistent nanowire growth. Electrodeposition is an attractive alternative technique for a number of reasons. Deposition only occurs in areas with electrical contact, allowing precise control over the size and shape of the deposit, and deposition occurs under the control of the potential or current, providing a tuneable composition. It also occurs outwards from the electrode surface, in other words 'bottom up', permitting growth of large aspect ratio nanostructures. Additionally, there is a low cost to entry for electrodeposition and fast growth rates are also possible.

The promise of electrodeposition as a method to grow binary semiconductors first

began to emerge with the first reports of the electrodeposition of II-VI semiconductors, as in CdSe or CdTe, for photovoltaic applications.[83] The first successful report of CdTe electrodeposition was by Panicker, Knaster and Kröger in 1978 for example.[84] The initial interest then expanded to cover attempts at the deposition of other II-VI semiconductors such as Zn based chalcogenides and interest has remained strong, with the electrodeposition of III-V based semiconductors (GaAs, InSb), those from groups four and six such as Sn or Pb chalcogenides, and also V-VI semiconductors such as Bi_2S_3 or Sb_2Te_3 are now possible. Clearly, much of the work involves chalcogenide based semiconductors. The electrodeposition of metal oxides is also an active area. Semiconductor electrodeposition has been reviewed at different points in time.[83,85–87] There are however, no reports available which cover the most recent work of the last twenty years. For example, much of the earlier work was performed in aqueous electrolytes, but semiconductor electrodeposition from non-aqueous solvents or ionic liquids is now a well established alternative.

Kröger developed a model to describe the effect of the applied potential and metal precursor concentration on deposition composition,[88] which was subsequently developed further by Engelken.[89–91] Considering a system with an electrolyte containing two electroactive species, A and B, which can be deposited onto an electrode, a typical codeposition process has the following scheme:

$$\begin{aligned} aA^{m+} + me^- &\longrightarrow aA_{(s)} \\ bB^{n+} + ne^- &\longrightarrow bB_{(s)} \\ aA_{(s)} + bB_{(s)} &\rightleftharpoons A_aB_{b\,(s)} \end{aligned}$$

The ability of the two metals to form a compound is then because of the gain in free energy as a result of compound formation, *i.e.* a negative value for ΔG_f, the free energy of formation.

Typically in the electrodeposition of alloys, codeposition begins at potentials more negative than the onset of deposition of both metals. However for compound electrodeposition, codeposition can also occur at potentials more positive of the less noble (most difficult to reduce) species, in between the deposition potentials of the two components. The initial deposition of the more easily deposited species onto the surface induces the deposition of the more noble metal driven by the gain in free energy associated with the formation of the compound. The positive shift is given by $\Delta E = \Delta G_f/nF$, assuming $E^0(B^+) < E^0(A^+)$. The induced deposition mechanism means that the deposition process is regulated by the thermodynamics of the solid state reaction above, and the rate of deposition of the less noble metal only. As a result, good control of the deposit composition can be achieved in the potential region where codeposition is possible.

Assuming the standard electrochemical rate constant of each species is similar, Kröger then identified two classes of the deposition process, based upon whether the difference in deposition potential of the individual components, is larger (Class 1) or smaller

(Class 2) than the positive shift in deposition potential as a result of compound formation. Engelken subsequently simplified this to a rule of thumb: species with significantly different deposition potentials ($\Delta E > 250\,\mathrm{mV}$) are Class 1 and species with similar potentials are Class 2.[91]

In the Class 1 system the rate of deposition of component A is so much faster than the induced deposition of component B, that stoichiometric deposition of A and B can only be achieved by lowering the activity of component A in the electrolyte. This is done by having a much larger concentration of component B than of species A in the plating bath. Under these conditions, the cathodic portion of a voltammogram has three sections. Firstly, the deposition of the more easily reduced species A begins, as this becomes diffusion limited the current then plateaus. During this plateau codeposition of stoichiometric A_aB_b is possible, with the composition of B gradually increasing with decreasing potential. The composition can then be optimised with tuning of the precursor concentration, stirring rate or temperature, for example. With continuation of the cathodic sweep, eventually the onset potential of the deposition of B is reached and begins to deposit as a separate phase, so control of the codeposit composition is lost.

For a Class 2 system, the voltammogram should take a similar appearance to that described above, but the conditions required to achieve codeposits of the desired composition are more system dependent. If the fraction of A is greater than B in the compound, then the concentration of A should be higher than B in the electrolyte, and *vice versa*. When the proportion of the two components is similar, the concentrations in the electrolyte should also be similar. In these compounds, codeposition is also possible at potentials more positive than the deposition potential of either pure species, and indeed has been experimentally observed.[88] This was considered in more detail by Engelken who termed the phenomenon Pure Underpotential Deposition (PUD).[91] The free energy of formation of the compound reduces the current of the anodic term of the corresponding Butler-Volmer equation (the anodic term referring to the dissolution of the compound) to a value less than the cathodic, resulting in deposition. At an applied potential in the PUD region, neither metal can electrodeposit individually and as a result, a 'feedback loop' exists. An increase in activity of either species above the equilibrium value would dissolve the excess and so deposits of almost exactly equal stoichometry can be achieved. The above description of PUD appears to indicate a cyclic argument where each species is dependent on the deposition of the other for deposition to take place. In fact, the models predict very low rates of deposition and significant issues with nucleation, deposition only beginning after spontaneous formation of nuclei on the electrode surface.[88,91] Kröger has since used the model of compound deposition to successfully electrodeposit CdTe from acidic aqueous electrolytes for the first time.[84]

An alternative model was also developed by Plieth, based upon the concept of residence times in kink sites.[92] During the electrodeposition of an alloy, the reduced metal atoms pass through an intermediate stage where they reside at a kink site. Once at the kink

site, the atom can become incorporated into the metal lattice by arrival of more reduced atoms or it can separate from the kink site and return to the electrolyte.[93] For atoms A* or B*, where the asterisk denotes its location in a kink site, there are four possibilities upon the arrival of a newly reduced atom. The arriving atom can be the same or different than the atom presiding in the kink site such that: AA*, AB*, BB*, BA*.[94] The residence time is then defined as the average time that the new atom spends in each of the possible kink sites. If the residence time for the formation of the AB* or BA* kink sites is greater than for AA* or BB*, then alloy or compound formation is favoured. If the opposite is true then a solid solution forms. Plieth then went on to derive an expression which related the ratio of the concentration of the metal precursors in the electrolyte, to the composition in the deposit. The differences between the two are mediated by so called selectivity constants which are obtained from the ratio of the residence times of the same, or the other metal, for A and B. Therefore representing the preference of A and B for association with itself, or the other metal in the alloy. With knowledge of the selectivity constants it would then be possible to estimate the composition of a codeposit simply from the concentration of the metal ions in the electrolyte. Plieth presented a method for calculating the selectivity constants from experimental data,[95] however currently it does not appear possible to estimate the selectivity constants from first principles.

1.5. The Properties of Weakly Coordinating Solvents

A Weakly Coordinating Solvent (WCS) can be defined as a solvent that is not a Lewis base, and does not interact strongly with electrophilic atoms. In the context of metal complexes, a WCS is a solvent that is a poor ligand, and does not strongly coordinate to a metal cation to form a complex.

In quantitative terms, a WCS has a low value for a solvent descriptor measuring Lewis basicity, such as Gutmann's DN or Kamlet and Taft's β parameter. A WCS can then be identified by inspection of databases of solvent descriptors. Table 1.2 shows a selection of solvents with varying values of β and DN. The most coordinating solvents are evidently those which contain O atoms; such as water and dimethylsulphoxide, or N atoms as in pyridine or N,N-dimethylformamide. These are electronegative atoms, with a lone pair of electrons which are available to interact with electrophiles. Conversely, those solvents which are weakly coordinating have no such functionalities. These include hydrocarbon solvents such as benzene or hexane, or chlorinated aliphatics and aromatics as with dichloromethane (DCM) or chlorobenzene. It is also apparent that a disadvantage of WCS is that they are commonly of intermediate or low polarity.

Another interesting approach to quantifying the coordinating nature of a solvent was presented by Alvarez.[97,98] This method used crystal structure entries of d-block complexes and, for a given anion or solvent, took the logarithm of the ratio of the number of submissions where the solvent was found to be coordinated, to the number of sub-

missions where the species was employed *i.e.* as a solvent or reagent, but was not found coordinated to the metal centre, resulting in a coordination ability index, a^{TM}. The greater the index is above 0 indicates a greater likelihood that the species was found coordinated to a metal cation, whereas the further the index is below zero indicates a greater likelihood that the species was present but did not coordinate. Values can be found in
Table 1.2. As can be seen, the same general trend is observed for the coordination ability index, as is predicted by the solvent descriptors. There are some interesting exceptions however, for example pyridine which was found coordinated in 96% of the structures where it was used.

WCS have found applications across the breadth of chemistry. They are frequently used, in conjunction with weakly coordinating anions, in coordination chemistry where a coordinating solvent could interfere with the speciation of the metal complex which is being synthesised. More exotic complexes can be electrophilic or unstable, and it is important that the medium does not interfere. For example, s-block elements are of synthetic interest to produce complexes for catalysis as alternatives to other more common metals.[99] However, the resulting compounds are highly Lewis acidic, which makes the ligands vulnerable to displacement by a more coordinating solvent. As such, WCS with some degree of polarity such as benzene, chlorobenzene and o-difluorobenzene have been used as reaction media. These are weakly coordinating but also sufficiently polar to solubilise the metals and ligands. In some cases, even halogenated solvents are too strongly coordinating, and hexane was used instead. WCS are similarly exploited in p-block chemistry for the synthesis of highly reactive p-block metal cations, where the metal centre is coordinated to various ligands.[100] As above, these compounds are particularly electrophilic or the ligands are weakly bound, meaning that it is important the solvent remains uninvolved. Here the solvents typically need to be somewhat polar, meaning that dichloromethane, 1,2-dichloroethane and chlorobenzene, as well as fluorinated solvents

Solvent	β	DN	a^{TM}
c-hexane	0	0	−1.0
chloroform	0.10	4.0	−2.2
dichloromethane	0.10	1.0	−1.7
toluene	0.11	0.1	−1.2
acetonitrile	0.40	14.1	−0.2
diethylether	0.47	19.2	−1.4
water	0.47	18.0	−0.1
pyridine	0.64	33.1	1.4
N,N-dimethylformamide	0.69	26.6	−0.2
dimethylsulphoxide	0.76	29.8	0.3
hexamethylphosphoramide	1.00	38.8	0.2

Table 1.2: Solvent descriptors of Lewis basicity and coordination ability index for some common solvents. β and DN from Ref. [96]. a^{TM} from Ref. [97].

such as fluorobenzene or 1,2-difluorobenzene are commonly used.

WCS have also found themselves to be useful in the colloidal synthesis of high quality semiconductor nanocrystals. These are of interest for optoelectronic applications. Peng *et al.* reported the use of octadecene as a WCS for the growth of various materials including CdS, ZnSe and InP.[101,102] In the solvent it was possible to grow nanocrystals with a narrow size distribution, with a tunable size controlled by the concentration of surfactant. Prior to the use of octadecene, more coordinating solvents were used and it was not possible to synthesise nanocrystals of certain semiconductors, such as ZnSe,[101] or as in the case of InP, crystals were grown but were of poor quality with a broad size distribution.[102] Similar successes have been reported for the growth of $CuInS_2$ and $CuInSe_2$ in dioctyl phthalate.[103]

1.6. Electrochemistry in Weakly Coordinating Solvents

The applications of WCS in electrochemistry thus far have been limited. Since they are typically of low polarity, this complicates their use in electrochemistry where a highly conducting electrolyte is preferred. However WCS, particularly DCM, have been extensively exploited by Bond throughout his career for the synthesis, and electrochemical characterisation of unusual transition metal organometallic complexes. The list is long so some selected, illustrative examples are given here. Bond electrochemically oxidised metal amalgams in DCM and benzene to form, *in situ*, cations of various metals such as Cd(II), Bi(III), Sn(II) and Pb(II).[104–107] The generated cations were highly reactive and in more coordinating solvents such as water or DMSO, the solvated complexes would rapidly form, preventing any further study.[104,106] However in DCM and benzene, the cations remained uncoordinated and so were used to form complexes with anions typically considered to be weakly coordinating, such as $[BF_4]^-$ or $[PF_6]^-$. Thermodynamic information on the formation of such complexes was also measurable, and this presents a route to the synthesis and study of relatively inaccessible complexes.

In other work, Bond *et al.* used DCM as a weakly coordinating solvent to electrochemically synthesise Co(IV) complexes.[108] Ethyl or cyclohexyl substituted tris(dithiocarbamate)cobalt(III) was electrochemically oxidised to successfully form a tris(dithiocarbamate)cobalt(IV) complex in DCM, the nature of which was contentious in the literature at the time. It was found that use of acetonitrile as a solvent caused the partial displacement of the ligands by molecules of acetonitrile, and the complexes were similarly unstable when acetone was used. Instead in DCM, the complexes were stable over sufficient timescales to allow detailed characterisation. Bond also studied the electrochemistry of the binuclear $Pt(II)_2(\mu-pop)_4]^{4-}$ anion, where pop = pyrophosphite, $[P_2O_5H_2]^{2-}$.[109] Such complexes are of interest because of the possibility of its oxidation to form mixed valent Pt(II)-Pt(III) complexes, which had also shown solvent dependent reaction pathways. Previous attempts at oxidation in water and acetonitrile showed that the

complex disproportionated upon oxidation in water, and in aceonitrile coordination of a solvent molecule was observed. In DCM, no disproportionation was observed, since the solvent was inert towards the complex. Instead the oxidised species appeared to react further to form an oligomer, the structure of which could not be resolved. Therefore demonstrating that it was possible to access new chemistry of Pd complexes when the solvent is not involved. In further studies of the electrochemistry of Pt(II) complexes, Bond *et al.* reported a study on the electrooxidation of $Pt[(p-BrC_6F_4)NCH_2CH_2NEt_2]Cl(py)$, where py is pyridine, an anticancer compound in DCM, acetone and acetonitrile.[110] Evidence for oxidation to a monomeric Pt(III) species, which was rare since the complex often dimerises, was found in all three solvents, but was most stable in DCM the least coordinating solvent.

Other researchers have also used weakly coordinating solvents to study the electrochemistry of organometallic complexes. For example O'Toole *et al.* used o-difluorobenzene to generate and characterise reactive intermediates which decomposed in more coordinating solvents such as acetonitrile, and also investigate the electropolymerisation of some porphyrin complexes.[111] Schreiber and Vicic electrochemically characterised bridged Co(III) fluorocarbon dimers in acetonitrile and DCM.[112] The electrochemistry was simpler in DCM which permitted easier characterisation, suggesting that the complex had been solvated by acetonitrile molecules when it was used as a solvent.

DCM has been used as a WCS in the work of Deronzier on the synthesis of polypyrrole electrodes modified with $[Ru(trpy)(bpy)(OH_2)]^{2+}$ complexes, where trpy is 2,2':6',2"-terpyridine and bpy is 2,2'-bipyridine.[113–117] Such complexes were connected to the pyrrole group by a carbon chain and were of interest for applications to the electrocatalytic oxidation of alcohols, water or chloride. The pyridine ligands can also be modified in various ways to improve their properties.[115–117] Previous attempts at growth and immobilisation in water were unsuccessful, necessitating the use of an organic solvent.[113] Experiments in acetonitrile also failed because the acetonitrile molecules coordinated to the Ru centre and displaced the H_2O ligands.[113] Instead, DCM was used as a weakly coordinating solvent which was inert towards the complex and polymer. The resulting films were successfully applied to the selective catalysis of benzyl alcohol to benzaldehyde.[117] In similar work, a relationship between the Lewis basicity of a solvent, and the conductivity of electropolymerised polypyrrole films was demonstrated.[118,119] It was reported that polypyrrole films grown from solvents with a lower DN, such as nitromethane, were more conducting than those when more coordinating solvents, including dimethylsulphoxide and N,N-dimethylformamide, were used as the medium for the monomer. The polymer typically grows *via* a radical cation intermediate, meaning that a Lewis basic solvent can interact more strongly with the intermediate and shortens its lifetime. This then results in shorter polymer chains and so a lower conductivity.

Geiger has also used WCS, typically DCM, to investigate the effect of solvent Lewis basicity on the electrochemistry of metallocenes. Moraczewski and Geiger studied the voltammetry of CoCp(COT) where Cp is the cyclopentadienyl anion and COT = cyclooc-

tatetraene, in acetonitrile a coordinating solvent, and also in DCM, a WCS.[120] It was found that in the coordinating solvent, the voltammetry appeared irreversible and with a significant dependence on scan rate. There was also evidence of the oxidation of free COT. The evidence appeared to suggest that upon formation of $[CoCp(COT)]^+$, the solvent rapidly displaced the COT ligand, and coordinated with the metal centre before slowly decomposing to generate $[Cp_2Co]^+$ and Co^{2+}. When the same experiments were performed in DCM, the CoCp(COT) still decomposed but at a significantly slower rate since it was not driven by the coordination of solvent molecules. A similar experiment was performed in α,α,α-trifluorotoluene, another solvent which has been proposed as a weakly coordinating solvent for electrochemistry.[121] The oxidation of CoCp(COD) where COD = cyclooctadiene, was investigated, and the cation decomposed on a similar timescale to that in DCM. Suggesting that trifluorotoluene is similarly weakly coordinating. Geiger has also used the electrochemistry of nickelocene in solvents of varying donor strength, such as DCM, PhCl, MeCN and tetrahydrofuran, to investigate similar effects.[122] Nickelocene, $Ni(II)Cp_2$ can undergo two subsequent oxidations forming the cation, $[Ni(III)Cp_2]^+$, and the dication $[Ni(IV)Cp_2]^{2+}$. No relationship between the Lewis basicity of the solvent and the peak shape of the first oxidation was observed. However for the second oxidation, the cathodic peak was significantly smaller than the anodic peak in coordinating solvents, suggesting the presence of an EC process. In the weakly coordinating solvents, the second redox couple appeared Nernstian with no evidence of complicating behaviour. It was proposed that in the Lewis basic solvents, the solvent molecules were coordinated to the metal cation, driven by the electrophilicity of the dication, and consuming the Ni(IV) species.

1.6.1. Electrodeposition from Weakly Coordinating Solvents

There have been few reports of electrodeposition from WCS. The majority of the work has been performed by Abbott and Schiffrin, or by Bartlett. Abbott and Schiffrin used mixtures of aromatic and polyaromatic solvents to electrodeposit various metals such as Zn, Cd, Sn and Pb.[123–125] Pd was deposited from a solvent mixture of 15 mol% phenanthrene in anisole.[123] It was possible to achieve reasonable conductivities with electrolytes such as $[N^nBu_4][BF_4]$ and reasonable solubility of the Pd precursor, up to 10 mM, was achieved with the use of hydrophobic long chain amine ligands. The resulting deposit was thick and adherent to the Au substrate. A significant advantage of aromatic solvents is with the electrodeposition of more noble metals, such as Ti, W or Al. It is difficult to deposit such metals from aqueous electrolytes because of the narrow potential window of water. Deposition from polar aprotic solvents also proved complicated because the more coordinating solvent tended to act as a ligand towards the metal cation and stabilise the metal such that its deposition potential lay outside the available potential window. Abbott *et al.* achieved Ti deposition from 15 mol% phenanthrene in anisole with $[N^nBu_4][BF_4]$ at a bath temperature of 100 °C.[124] Ti(IV) based precursors were used with various nitrile or amine based

ligands, such as $TiCl_2(PhCN)_2$, which was soluble at concentrations of 91 mM and gave nodular deposits. Interestingly adherent deposits were only possible with small amounts of Ag^+ as an additive, which appeared to assist with nucleation. Since there is little interaction between the aromatic solvent and the Ti complex, deposition was possible within the solvent window. Thick, bright Al deposits have also been reported from toluene.[125]

The remainder of the work on electrodeposition from WCS has been performed by Bartlett, who used DCM to deposit p-block metals or compounds. Complexes of p-block elements are characterised by having particularly labile ligands and undergo facile ligand exchange. For all p-block elements that form aquo complexes, the mean lifetime of a water molecule in the primary coordination shell is less than 1 s,[126] and they lie on the labile side of Taube's inert/labile boundary.[127] This is because of the low lying valence p-orbitals. In solution the solvent molecules can compete with the ligands present in the initial complex for coordination to the metal cation. As such, a complex with labile ligands in a Lewis basic solvent is vulnerable to displacement by the solvent molecule. Different metal cations differ in their interaction with the solvent, and therefore in a donor solvent differences in speciation across different metal precursors and oxidation states will occur. For electrodeposition of alloys and compounds this is a problem because more than one metal complex must be present and because speciation affects all aspects of an electron transfer reaction. Unpredictable changes in metal speciation greatly complicates the process of metal codeposition.

To overcome this, a generalised plating bath was developed composed of a tetrabutylammonium chlorometallate metal precursor, $[N^nBu_4]_{y-x}[M^{x+}Cl_y]$, with tetrabutylammonium chloride, $[N^nBu_4]Cl$, as the supporting electrolyte. With common ligands in the electrolyte and the metal precursor, and a weakly coordinating solvent, this ensures there can be no interference with the structure of the metal complex. This was used to successfully electrodeposit thin films of In, Sb, Bi, Se and Te from DCM onto glassy carbon and TiN substrates.[128] Adhesion was found to be good for all metals on a TiN electrode with homogeneous morphology, but poor with glassy carbon for In, Sb and Se. X-ray analysis showed that all films were crystalline. The electrochemistry of the precursors was also studied at a glassy carbon electrode. Sb^{3+} and Bi^{3+} showed simple deposition and stripping, but In^{3+} and, Se^{4+} and Te^{4+} did not. This was attributed to the possible formation of intermediate species or cathodic stripping. The electrodeposition of crystalline Pb using a similar approach has also been reported.[129] In a more advanced study, the templated electrodeposition of Sn nanowires was attempted.[130] Sn was deposited in nanoporous templates with diameters of 13 and 55 nm. It was found that material could be grown through pores of both diameters but that nanowire growth was discontinuous, with Sn not nucleating in every pore and also not always growing along its entire length. The wires also showed a strong degree of preferential orientation along the (200) direction.

Of greater interest is the electrodeposition of semiconducting alloys and compounds. Thin films of InSb, an infra-red detector, were electrodeposited from DCM onto

TiN with an electrolyte composed of 10 mM $[N^nBu_4][InCl_4]$ and 2 mM $[N^nBu_4][SbCl_4]$, with 100 mM $[N^nBu_4]Cl$.[128] The correct composition of 50% In for stoichiometric InSb was achieved and X-ray diffraction (XRD) analysis indicated the films were crystalline. Similarly, stoichiometric HgTe was electrodeposited onto TiN from a bath of 5 mM $[N^nBu_4]_2[HgCl_4]$ and 5 mM $[N^nBu_4]_2[TeCl_6]$ in DCM.[131] Stoichiometric HgTe was readily achieved with the composition being essentially independent of potential. The deposits were crystalline and relatively smooth.

More detailed work has been performed on the electrodeposition of the thermoelectric material bismuth telluride, with Meng reporting a study on its deposition from DCM.[132] Stoichiometric Bi_2Te_3 could be deposited onto TiN from an electrolyte containing 2.5 mM $[N^nBu_4][BiCl_4]$ and 3 mM $[N^nBu_4]_2[TeCl_6]$, with the composition broadly independent of potential. Scanning Electron Microscopy (SEM) showed that the grown material was composed of a compact layer ontop of the electrode surface, followed by porous spongy material. According to XRD analysis, the deposits appeared to be nanocrystalline. This was progressed by Cicvarić, who developed a pulsed deposition routine to grow dense and compact Bi_2Te_3 films with larger crystallites; the preferred morphology for a thermoelectric material.[133] The concentration of $[N^nBu_4][BiCl_4]$ was lowered to 2.25 mM and the smoothest films with the largest crystallite sizes was achieved when a nucleation pulse of −1 V *vs.* Ag/AgCl for 5 s was used, followed by pulsed deposition at −0.6 V with an on time of 5 s and an off time of 10 s. The theromelectric properties of the films were characterised and found to be comparable to previous work in the literature.

The largest body of work exists on the electrodeposition of germanium antimony telluride (GST) from DCM. In its atom ratio 2:2:5, GST (GST-225) is interesting as a phase change material for computer memory applications. The material can readily transition between an amorphous and crystalline form by the application of an external potential which causes a significant change in electrical conductivity. The interplay between precursor ratio and applied potential on the composition makes optimisation of the plating recipe complicated. Kissling *et al.* performed a detailed study on the effect of the concentration of each metal precursor and deposition potential on the deposit composition.[134] It was found that the composition of the deposit could be readily tuned by varying the concentration of $[N^nBu_4][GeCl_5]$, $[N^nBu_4][SbCl_4]$ and $[N^nBu_4]_2[TeCl_6]$ in the electrolyte. For a constant $[N^nBu_4][GeCl_5]$ and $[N^nBu_4][SbCl_4]$ concentration, increasing the concentration of $[N^nBu_4]_2[TeCl_6]$ resulting in an approximately linear increase in Te content, with the ratio of Ge/Sb essentially unchanged. Upon varying the $[N^nBu_4][GeCl_5]$ concentration, Ge initially appears in the deposit at the expense of Te, until a certain concentration when it then begins to replace Sb. Increasing the concentration of the Sb precursor causes a decrease in the presence of Ge and Te by an approximately constant ratio. The effect of deposition potential was also studied, decreasing the potential significantly increased the Ge content in the deposit due to its lower deposition potential. Much more detailed characterisation was also performed, including the effect of the total precursor concentration,

and the effect of the variation of the individual precursors on voltammetry, deposit morphology and crystal structure. Nevertheless, it was established that the optimum conditions for GST-225 deposition were at −1.75 V *vs.* Ag/AgCl with 1 mM $[N^nBu_4][GeCl_5]$ and $[N^nBu_4][SbCl_4]$, and 2 mM $[N^nBu_4]_2[TeCl_6]$.[135] The deposited thin films of GST-225 have displayed switching behaviour with good changes in resistance upon switching, and reasonable durability.[135,136]

The electrodeposition of GST-225 was also exploited to manufacture more advanced devices. GST-225 was deposited from DCM, into arrays of recessed TiN microdiscs with a diameter of 50 nm.[135] Each GST-225 filled recess counts as one device, equivalent to a single thin film, and the substrate was filled with many. Representing a significant increase in the capabilities of the device. Phase change switching was observed in the devices with reasonable longevity. Further to this, GST was also deposited onto a different substrate called a 'crossbar array' and switching behaviour demonstrated.[137] Such substrates are similar to the microarrays described above, in that that they are composed of recessed microdiscs 1 µm in diameter, except the substrate is manufactured in such a way so that during the electrodeposition process each disc is connected to a global electrode which provides the contact to the potentiostat. Meaning that GST grows uniformly in each recess. Then after deposition, the material in the recesses can be contacted so that they are individually addressable, which is representative of a computer memory device. Under different conditions, GST electrodeposited in the crossbar arrays can also be induced to display resistive switching properties, instead of phase change.[138] Resistive switching arises from changes in the resistivity of the GST, caused by the formation of localised filaments of crystalline conducting material.

Finally, Bartlett has used DCM to electrodeposit Transition Metal Dichalocgenides (TMDCs). These are classed as 2D layered materials, similar to graphite/graphene, where the bonds between layers are van der Waals in form and so the layers are readily separated. TMDCs are of interest for electronic and optical applications. The first report was on the deposition of MoS_2 by Thomas *et al.* onto TiN.[139] Electrodeposition was performed using a single source precursor of $[N^nBu_4]_2[MoS_4]$. The major advantage of such precursors is that all the elements of the desired material are contained in one precursor, meaning that achieving deposits of the desired composition was far simpler. A proton source, $[Me_3NH]Cl$, was also included in the electrolyte to clean up the excess sulphur in the precursor, by formation of H_2S, and drive the reaction towards the formation of MoS_2. The resulting deposits were smooth and uniform, but amorphous, with crystalline material achieved by annealing *post hoc*. A few layers of MoS_2 were also successfully deposited onto graphene.[140] Such 2D heterostructures with graphene are interesting because of their expected unusual optoelectronic properties. The graphene/MoS_2 structure displayed a photocurrent, where an incident laser beam generates a measurable current.

In another interesting application; MoS_2 was grown on an insulator by lateral electrodeposition.[141] A substrate was designed where the area of interest took the form of a

trench. The 200 nm high walls were composed of TiN on the bottom, followed by insulating SiO_2 on top. The bed of the trench was then also SiO_2 approximately 6.5 µm in width, such that the only conducting area was the TiN on the walls of the trench. Thus when immersed in the electrolyte, MoS_2 grows laterally, from each wall of the trench, across the insulator. Furthermore, vertical growth was minimal and so the deposited material did not exceed the height of the walls of the trench. The deposited MoS_2 displayed conductivity similar to previous literature reports, and an induced photocurrent was also observed.

WS_2 was also deposited in a similar fashion to Ref. [139] above.[142] A single source precursor, $[N^nEt_4]_2[WS_2Cl_4]$, was also used here except that the W/S ratio was the same in the precursor as in the desired material, removing the need for a proton source. The deposited films were homogeneous and crystallised after annealing.

As shown by the foregoing discussion, electrodeposition from WCS remains an active and fruitful area of research. Significant scope remains for further work into the electrodeposition of alloys or compounds for electronic devices, particularly where the constituent elements are unstable in the liquid phase.

1.7. Thesis Aims and Outline

This Chapter has provided an introduction into the nature of the interactions between a solute and its solvent, how these complicated interactions can be quantified with solvent descriptors, and then the consequences of this for heterogeneous electron transfer reactions. In addition, weakly coordinating solvents were defined and some of their interesting applications to electrochemistry and electrodeposition were reviewed. As was clear from the foregoing discussion, dichloromethane has been the weakly coordinating solvent of choice for the majority of work on electrodeposition. However, dichloromethane is volatile with a relatively low boiling point of 40 °C,[143] which can make its use experimentally challenging. For example, the solvent can evaporate over the course of an experiment, changing the concentration of the dissolved reagents. Further to this, there has been relatively little investigation into electrochemistry, and in particular into semiconductor electrodeposition, in weakly coordinating solvents and they remain poorly understood. Therefore, the aims of this thesis are twofold: firstly, solvent descriptors will be used to identify alternative weakly coordinating solvents to dichloromethane with a higher boiling point. The identified solvents will be characterised with a variety of electrochemical methods in an attempt to improve the knowledge of electrochemistry in weakly coordinating solvents. Secondly, the higher boiling points will be exploited to attempt semiconductor electrodeposition at elevated temperatures. Which is expected to provide an enhancement in the material properties of the deposit.

To this end, in Chapter three alternative solvents are identified with solvent descriptors and then characterised electrochemically. The solvents are subjected to a portfolio of measurements; including conductivity, potential window, and the electrochemistry of

some model redox couples. The most promising solvents for further application to high temperature electrodeposition are then identified.

In Chapter four, the candidate solvents are characterised further and their suitability as solvents for metal electrodeposition assessed. This is achieved by studying the voltammetry, and attempting electrodeposition of, antimony, bismuth and tellurium, three well known metal deposition systems which are also interesting as components of binary semiconductors. Dichloromethane is also included as a comparison, since this is the most investigated weakly coordinating solvent.

In Chapter five, the ability of the identified solvents to electrodeposit semiconductors is studied by attempting the electroplating of antimony telluride and bismuth telluride. Electrodeposition of bismuth telluride from a supercritical fluid is also attempted, as work towards the electrodeposition of bismuth telluride nanowires.

In Chapter six, the last results Chapter, electrochemistry at elevated temperatures is investigated. Initially the effect of temperature on the solvent is probed with electrochemical measurements of model redox couples. Subsequently, the possibility of electrodepositing metals and semiconductors is explored. The material properties of the resulting deposits are then characterised in order to study the effect of the increased temperature.

Finally in Chapter seven, the final Chapter, conclusions are drawn on the knowledge gained from this work on the nature of electrochemistry in weakly coordinating solvents, and the suitability of weakly coordinating solvents for electrodeposition at elevated temperatures. Possible experiments for further work are also suggested.

1.8. References

(1) J. M. G. Barthel, H. Krienke and W. Kunz, *Physical Chemistry of Electrolyte Solutions*, Springer, New York, 1998.

(2) P. Atkins and J. de Paula, *Physical Chemistry*, Oxford University Press, Oxford, 10th edn., 2014.

(3) C. Reichardt and T. Welton, *Solvents and Solvent Effects in Organic Chemistry*, Wiley-VCH Verlag GmbH, Weinheim, 4th edn., 2011.

(4) Y. Marcus and G. Hefter, *Chem. Rev.*, 2006, **106**, 4585–4621.

(5) C. Reichardt and T. Welton, in *Solvents and Solvent Effects in Organic Chemistry*, Wiley-VCH, Weinheim, 4th edn., 2011, ch. 5.

(6) C. Reichardt and T. Welton, in *Solvents and Solvent Effects in Organic Chemistry*, Wiley-VCH, Weinheim, 4th edn., 2011, ch. 7.

(7) M. J. Kamlet, J. L. M. Abboud, M. H. Abraham and R. W. Taft, *J. Org. Chem.*, 1983, **48**, 2877–2887.

(8) V. Gutmann, *The Donor Acceptor Approach to Molecular Interactions*, Plenum Press, New York, 1978.

(9) R. W. Taft, N. J. Pienta, M. J. Hamlet and E. M. Arnett, *J. Org. Chem.*, 1981, **46**, 661–667.

(10) J. L. Abboud and R. Notario, *Pure Appl. Chem.*, 1999, **71**, 645–718.

(11) M. J. Kamlet, J. L. Abboud and R. W. Taft, *J. Am. Chem. Soc.*, 1977, **99**, 6027–6038.

(12) R. W. Taft, M. J. Kamlet and J. L. M. Abboud, *J. Am. Chem. Soc.*, 1981, **103**, 1080–1086.

(13) A. R. Katritzky, T. Tamm, Y. Wang, S. Sild and M. Karelson, *J. Chem. Inf. Comput. Sci.*, 1999, **39**, 684–691.

(14) Y. Marcus, *Chem. Soc. Rev.*, 1993, **22**, 409–416.

(15) I. A. Koppel and V. A. Palm, in *Advances in Linear Free Relationships*, ed. N. B. Chapman and J. Shorter, Plenum Press, London, 1972, ch. 5.

(16) R. S. Drago, *Coord. Chem. Rev.*, 1980, **33**, 251–277.

(17) P. A. Lay, *J. Phys. Chem.*, 1986, **90**, 878–885.

(18) A. F. M. Barton, *Chem. Rev.*, 1975, **75**, 731–753.

(19) P. A. Lay, N. S. McAlpine, J. T. Hupp, M. J. Weaver and A. M. Sargeson, *Inorg. Chem.*, 1990, **29**, 4322–4328.

(20) G. Gritzner, *J. Phys. Chem.*, 1986, **90**, 5478–5485.

(21) A. Messina and G. Gritzner, *J. Electroanal. Chem.*, 1979, **101**, 201–209.

(22) G. Gritzner, K. Danksagmuller and V. Gutmann, *J. Electroanal. Chem.*, 1978, **90**, 203–210.

(23) G. Gritzner, H. Murauer and V. Gutmann, *J. Eletroanal. Chem.*, 1979, **101**, 185–200.

(24) G. Gritzner, *J. Electroanal. Chem.*, 1983, **144**, 259–277.

(25) V. Gutmann, G. Gritzner and K. Danksagmuller, *Inorganica Chim. Acta*, 1976, **17**, 81–86.

(26) G. Gritzner, K. Danksagmüller and V. Gutmann, *J. Electroanal. Chem.*, 1976, **72**, 177–185.

(27) I. Noviandri, K. N. Brown, D. S. Fleming, P. T. Gulyas, P. A. Lay, A. F. Masters and L. Phillips, *J. Phys. Chem. B*, 1999, **103**, 6713–6722.

(28) S. Sahami and M. J. Weaver, *J. Electroanal. Chem.*, 1981, **122**, 155–170.

(29) S. Sahami and M. J. Weaver, *J. Electroanal. Chem.*, 1981, **122**, 171–181.

(30) A. J. Bard and L. R. Faulkner, *Electrochemical Methods: Fundamentals and Applications*, Wiley-VCH, Hoboken, NJ, 2nd edn., 2001.

(31) M. Weaver and J. Hupp, *J. Electroanal. Chem.*, 1983, **152**, 1–14.

(32) R. A. Marcus, *J. Chem. Phys.*, 1965, **43**, 679–701.

(33) S. Sahami and M. J. Weaver, *J. Electroanal. Chem.*, 1981, **124**, 35–51.

(34) J. K. Farmer, T. Gennett and M. J. Weaver, *J. Electroanal. Chem.*, 1985, **191**, 357–366.

(35) W. R. Fawcett and J. S. Jaworski, *J. Phys. Chem.*, 1983, **87**, 2972–2976.

(36) A. Kapturkiewicz and M. Opallo, *J. Electroanal. Chem.*, 1985, **185**, 15–28.

(37) M. Opallo and A. Kapturkiewicz, *Electrochim. Acta*, 1985, **30**, 1301–1306.

(38) H. Elzanowska, Z. Galus and Z. Borkowska, *J. Electroanal. Chem.*, 1983, **157**, 251–268.

(39) E. S. Yang, M. S. Chan and A. C. Wahl, *J. Phys. Chem.*, 1980, **84**, 3094–3099.

(40) M. J. Weaver and T. L. Satterberg, *J. Phys. Chem.*, 1977, **81**, 1772–1783.

(41) J. T. Hupp and M. J. Weaver, *J. Phys. Chem.*, 1985, **89**, 1601–1608.

(42) A. P. Abbott and D. J. Schiffrin, *J. Chem. Soc. Faraday Trans.*, 1990, **86**, 1453–1459.

(43) A. P. Abbott, C. L. Miaw and J. F. Rusling, *J. Electroanal. Chem.*, 1992, **327**, 31–46.

(44) W. R. Fawcett and M. Opallo, *Angew. Chem., Int. Ed.*, 1994, **33**, 2131–2143.

(45) M. J. Weaver, *Chem. Rev.*, 1992, **92**, 463–480.

(46) M. J. Weaver and G. E. McManis, *Acc. Chem. Res.*, 1990, **23**, 294–300.

(47) D. K. Phelps, M. T. Ramm, Y. Wang, S. F. Nelsen and M. J. Weaver, *J. Phys. Chem.*, 1993, **97**, 181–188.

(48) R. M. Nielson and M. J. Weaver, *J. Electroanal. Chem.*, 1989, **260**, 15–24.

(49) W. R. Fawcett and C. A. Foss, *J. Electroanal. Chem.*, 1989, **270**, 103–118.

(50) W. R. Fawcett and C. A. Foss, *J. Electroanal. Chem.*, 1988, **252**, 221–229.

(51) W. R. Fawcett and C. A. Foss, *Electrochim. Acta*, 1991, **36**, 1764–1774.

(52) Z. Galus, in *Advances in Electrochemical Science and Engineering*, ed. H. Gerischer and C. W. Tobias, VCH, Weinheim, 1996, ch. 4.

(53) X. Zhang, J. Leddy and A. J. Bard, *J. Am. Chem. Soc.*, 1985, **107**, 3719–3721.

(54) X. Zhang, H. Yang and A. J. Bard, *J. Am. Chem. Soc.*, 1987, **109**, 1916–1920.

(55) R. Pyati and R. W. Murray, *J. Am. Chem. Soc.*, 1996, **118**, 1743–1749.

(56) J. Broda and Z. Galus, *J. Electroanal. Chem.*, 1986, **198**, 233–244.

(57) K. Maksymiuk and Z. Galus, *J. Electroanal. Chem.*, 1987, **234**, 361–368.

(58) W. R. Fawcett, *Langmuir*, 1989, **5**, 661–671.

(59) G. Brunner, *J. Food Eng.*, 2005, **67**, 21–33.

(60) J. A. Darr and M. Poliakoff, *Chem. Rev.*, 1999, **99**, 495–542.

(61) R. M. Crooks, F. R. F. Fan and A. J. Bard, *J. Am. Chem. Soc.*, 1984, **106**, 6851–6852.

(62) R. M. Crooks and A. J. Bard, *J. Electroanal. Chem.*, 1988, **240**, 253–279.

(63) A. C. McDonald, F. R. F. Fan and A. J. Bard, *J. Phys. Chem.*, 1986, **90**, 196–202.

(64) W. Flarsheim and Y. Tsou, *J. Phys. Chem.*, 1986, **90**, 3857–3862.

(65) W. M. Flarsheim, A. J. Bard and K. P. Johnston, *J. Phys. Chem.*, 1989, **93**, 4234–4242.

(66) R. M. Crooks and A. J. Bard, *J. Electroanal. Chem.*, 1988, **243**, 117–131.

(67) C. R. Cabrera and A. J. Bard, *J. Electroanal. Chem.*, 1989, **273**, 147–160.

(68) E. W. Lemmon, M. O. McLinden and D. G. Friend, in *NIST Chem. WebBook, NIST Stand. Ref. Databse No. 69*, ed. P. J. Lindstrom and W. G. Mallard, National Institute of Standards and Technology, Gaithersburg MD.

(69) A. P. Abbott and J. C. Harper, *J. Chem. Soc. Trans.*, 1996, **92**, 3895–3898.

(70) A. P. Abbott and J. C. Harper, *Phys. Chem. Chem. Phys.*, 1999, **1**, 839–841.

(71) P. N. Bartlett and D. A. Cook, *J. Electroanal. Chem.*, 2015, **746**, 18–24.

(72) P. N. Bartlett, D. C. Cook, M. W. George, J. Ke, W. Levason, G. Reid, W. Su and W. Zhang, *Phys. Chem. Chem. Phys.*, 2010, **12**, 492–501.

(73) J. A. Branch, Ph.D. Thesis, University of Southampton, 2015.

(74) D. Cook, P. N. Bartlett, W. J. Zhang, W. Levason, G. Reid, J. Ke, W. T. Su, M. W. George, J. Wilson, D. Smith, K. Mallik, E. Barrett and P. Sazio, *Phys. Chem. Chem. Phys.*, 2010, **12**, 11744–11752.

(75) J. Ke, W. Su, S. M. Howdle, M. W. George, D. Cook, M. Perdjon-Abel, P. N. Bartlett, W. Zhang, F. Cheng, W. Levason, G. Reid, J. Hyde, J. Wilson, D. C. Smith, K. Mallik and P. Sazio, *Proc. Natl. Acad. Sci. U. S. A.*, 2009, **106**, 14768–14772.

(76) P. N. Bartlett, D. A. Cook, M. W. George, A. L. Hector, J. Ke, W. Levason, G. Reid, D. C. Smith and W. Zhang, *Phys. Chem. Chem. Phys.*, 2014, **16**, 9202–9219.

(77) A. P. Abbott, C. A. Eardley and R. Tooth, *J. Chem. Eng. Data*, 1999, **44**, 112–115.

(78) P. N. Bartlett, J. Burt, D. A. Cook, C. Y. Cummings, M. W. George, A. L. Hector, M. M. Hasan, J. Ke, W. Levason, D. Pugh, G. Reid, P. W. Richardson, D. C. Smith, J. Spencer, N. Suleiman and W. Zhang, *Chem. - A Eur. J.*, 2016, **22**, 302–309.

(79) P. N. Bartlett, D. A. Cook, M. M. Hasan, A. L. Hector, S. Marks, J. Naik, G. Reid, J. Sloan, D. C. Smith, J. Spencer and Z. Webber, *RSC Adv.*, 2017, **7**, 40720–40726.

(80) J. Ke, P. N. Bartlett, D. Cook, T. L. Easun, M. W. George, W. Levason, G. Reid, D. Smith, W. Su and W. Zhang, *Phys. Chem. Chem. Phys.*, 2012, **14**, 1517–1528.

(81) P. N. Bartlett, D. Smith and M. Alibouri, in *Supercritical and Other High-pressure Solvent Systems*, The Royal Society of Chemistry, London, 2018, ch. 9.

(82) *Nanoelectronics and Information Technology: Advanced Electronic Materials and Novel Devices*, ed. R. Waser, Wiley-VCH, Weinheim, 3rd edn., 2012.

(83) D. Lincot, *Thin Solid Films*, 2005, **487**, 40–48.

(84) M. P. R. Panicker, M. Knaster and F. A. Kroger, *J. Electrochem. Soc.*, 1978, **125**, 566–572.

(85) G. . F. Fulop and R. M. Taylor, *Ann. Rev. Mater. Sci.*, 1985, **15**, 197–210.

(86) C. D. Lokhande and S. H. Pawar, *Phys. Status Solidi*, 1989, **111**, 17–40.

(87) R. K. Pandey, S. N. Sahu and S. Chandra, *Handbook of semiconductor electrodeposition*, Taylor & Francis, New York, 1996.

(88) F. A. Kroger, *J. Electrochem. Soc.*, 1978, **125**, 2028–2034.

(89) R. D. Engelken, *J. Electrochem. Soc.*, 1985, **132**, 2910–2919.

(90) R. D. Engelken, *J. Electrochem. Soc.*, 1987, **134**, 832–837.

(91) R. D. Engelken, *J. Electrochem. Soc.*, 1988, **135**, 834–839.

(92) W. Plieth, in *Electrochem. Mater. Sci.* Elsevier, Amsterdam, 2008, ch. 8, pp. 231–262.

(93) G. S. Georgiev, V. T. Georgieva and W. Plieth, *Electrochim. Acta*, 2005, **51**, 870–876.

(94) W. Plieth, *Electrochim. Acta*, 2007, **53**, 245–249.

(95) W. Plieth and G. S. Georgiev, *Russ. J. Electrochem.*, 2006, **42**, 1093–1100.

(96) Y. Marcus, *The Properties of Solvents*, Wiley, Chichester, 1998.

(97) R. Diaz-Torres and S. Alvarez, *Dalt. Trans.*, 2011, **40**, 10742–10750.

(98) S. Alvarez, *Chem. - A Eur. J.*, 2020, **26**, 4350–4377.

(99) M. R. Buchner and L. R. Thomas-Hargreaves, *Dalt. Trans.*, 2021, **50**, 16916–16922.

(100) T. A. Engesser, M. R. Lichtenthaler, M. Schleep and I. Krossing, *Chem. Soc. Rev.*, 2016, **45**, 789–799.

(101) W. W. Yu and X. Peng, *Angew. Chemie Int. Ed.*, 2002, **41**, 2368–2371.

(102) D. Battaglia and X. Peng, *Nano Lett.*, 2002, **2**, 1027–1030.

(103) S. L. Castro, S. G. Bailey, R. P. Raffaelle, K. K. Banger and A. F. Hepp, *Chem. Mater.*, 2003, **15**, 3142–3147.

(104) A. M. Bond, *Pure Appl. Chem.*, 1990, **62**, 1043–1046.

(105) A. M. Bond, S. R. Ellis and A. F. Hollenkamp, *J. Am. Chem. Soc.*, 1988, **110**, 5293–5297.

(106) A. M. Bond and S. R. Ellis, *J. Chem. Soc. Dalt. Trans.*, 1988, **9**, 2379–2383.

(107) A. M. Bond, A. Bobrowski and F. Scholz, *J. Chem. Soc. Dalt. Trans.*, 1991, 411–416.

(108) R. D. Webster, G. A. Heath and A. M. Bond, *J. Chem. Soc. Dalt. Trans.*, 2001, 3189–3195.

(109) M. A. Bennett, S. K. Bhargava, A. M. Bond, V. Bansal, C. M. Forsyth, S. X. Guo and S. H. Privér, *Inorg. Chem.*, 2009, **48**, 2593–2604.

(110) R. Ojha, A. Nafady, M. J. Shiddiky, D. Mason, J. F. Boas, A. A. Torriero, A. M. Bond, G. B. Deacon and P. C. Junk, *ChemElectroChem*, 2015, **2**, 1048–1061.

(111) T. R. O'Toole, J. N. Younathan, B. P. Sullivan and T. J. Meyer, *Inorg. Chem.*, 1989, **28**, 3923–3926.

(112) S. T. Shreiber and D. A. Vicic, *J. Organomet. Chem.*, 2021, **949**, 121974.

(113) W. F. De Giovani and A. Deronzier, *J. Electroanal. Chem.*, 1992, **337**, 285–298.

(114) M. N. Collomb Dunand-Sauthier, A. Deronzier and M. Navarro, *Chem. Commun.*, 1996, **2**, 2165–2166.

(115) M. N. Collomb-Dunand-Sauthier, A. Deronzier, H. Le Bozec and M. Navarro, *J. Electroanal. Chem.*, 1996, **410**, 21–29.

(116) M. Navarro, M. N. Collomb and A. Deronzier, *J. Electroanal. Chem.*, 2002, **520**, 150–156.

(117) M. Rodríguez, I. Romero, C. Sens, A. Llobet and A. Deronzier, *Electrochim. Acta*, 2003, **48**, 1047–1054.

(118) J. Ouyang and Y. Li, *Polymer*, 1997, **38**, 1971–1976.

(119) Q. Yan, W. Pan, S. Zhong, R. Zhu and G. Li, *Prog. Org. Coatings*, 2019, **132**, 298–304.

(120) J. Moraczewski and W. E. Geiger, *Organometallics*, 1982, **1**, 1385–1389.

(121) C. Ohrenberg and W. E. Geiger, *Inorg. Chem.*, 2000, **39**, 2948–2950.

(122) D. Chong, J. Slote and W. E. Geiger, *J. Electroanal. Chem.*, 2009, **630**, 28–34.

(123) A. P. Abbott, E. E. Long, A. Bettley and D. J. Schiffrin, *J. Electroanal. Chem.*, 1989, **261**, 449–453.

(124) A. P. Abbott, A. Bettley and D. J. Schiffrin, *J. Electroanal. Chem.*, 1993, **347**, 153–164.

(125) A. P. Abbott, *Chem. Soc. Rev.*, 1993, **22**, 435–440.

(126) D. T. Richens, *Chem. Rev.*, 2005, **105**, 1961–2002.

(127) H. Taube, *Chem. Rev.*, 1952, **50**, 69–126.

(128) P. N. Bartlett, D. Cook, C. H. de Groot, A. L. Hector, R. Huang, A. Jolleys, G. P. Kissling, W. Levason, S. J. Pearce and G. Reid, *RSC Adv.*, 2013, **3**, 15645–15654.

(129) P. N. Bartlett, J. Burt, M. M. Hasan, A. L. Hector, W. Levason, G. Reid and P. W. Richardson, *RSC Adv.*, 2016, **6**, 73323–73330.

(130) A. W. Lodge, M. M. Hasan, P. N. Bartlett, R. Beanland, A. L. Hector, R. J. Kashtiban, W. Levason, G. Reid, J. Sloan, D. C. Smith and W. Zhang, *RSC Adv.*, 2018, **8**, 24013–24020.

(131) G. P. Kissling, M. Aziz, A. W. Lodge, W. Zhang, M. Alibouri, R. Huang, A. L. Hector, G. Reid, C. H. de Groot, R. Beanland, P. N. Bartlett and D. C. Smith, *J. Electrochem. Soc.*, 2018, **165**, D802–D807.

(132) L. Meng, K. Cicvarić, A. L. Hector, C. de Groot and P. N. Bartlett, *J. Electroanal. Chem.*, 2019, **839**, 134–140.

(133) K. Cicvarić, L. Meng, D. W. Newbrook, R. Huang, S. Ye, W. Zhang, A. L. Hector, G. Reid, P. N. Bartlett and C. H. De Groot, *ACS Omega*, 2020, **5**, 14679–14688.

(134) G. P. Kissling, R. Huang, A. Jolleys, S. L. Benjamin, A. L. Hector, G. Reid, W. Levason, C. Groot, de Groot and P. N. Bartlett, *J. Electrochem. Soc.*, 2018, **165**, D557–D567.

(135) P. N. Bartlett, S. L. Benjamin, C. H. De Groot, A. L. Hector, R. Huang, A. Jolleys, G. P. Kissling, W. Levason, S. J. Pearce, G. Reid and Y. Wang, *Mater. Horiz.*, 2015, **2**, 420–426.

(136) R. Huang, G. P. Kissling, A. Jolleys, P. N. Bartlett, A. L. Hector, W. Levason, G. Reid and C. H. De Groot, *Nanoscale Res. Lett.*, 2015, **10**, 4–10.

(137) Y. J. Noori, L. Meng, A. H. Jaafar, W. Zhang, G. P. Kissling, Y. Han, N. Abdelazim, M. Alibouri, K. Leblanc, N. Zhelev, R. Huang, R. Beanland, D. C. Smith, G. Reid, K. De Groot and P. N. Bartlett, *ACS Appl. Electron. Mater.*, 2021, **3**, 3610–3618.

(138) A. H. Jaafar, L. Meng, Y. J. Noori, W. Zhang, Y. Han, R. Beanland, D. C. Smith, G. Reid, K. De Groot, R. Huang and P. N. Bartlett, *J. Phys. Chem. C*, 2021, **125**, 26247–26255.

(139) S. Thomas, D. E. Smith, V. K. Greenacre, Y. J. Noori, A. L. Hector, C. H. de Groot, G. Reid and P. N. Bartlett, *J. Electrochem. Soc.*, 2020, **167**, 106511.

(140) Y. J. Noori, S. Thomas, S. Ramadan, D. E. Smith, V. K. Greenacre, N. Abdelazim, Y. Han, R. Beanland, A. L. Hector, N. Klein, G. Reid, P. N. Bartlett and C. H. De Groot, *ACS Appl. Mater. Interfaces*, 2020, **12**, 49786–49794.

(141) N. M. Abdelazim, Y. J. Noori, S. Thomas, V. K. Greenacre, Y. Han, D. E. Smith, G. Piana, N. Zhelev, A. L. Hector, R. Beanland, G. Reid, P. N. Bartlett and C. H. de Groot, *Adv. Electron. Mater.*, 2021, **7**, 2100419.

(142) S. Thomas, V. K. Greenacre, D. E. Smith, Y. J. Noori, N. M. Abdelazim, A. L. Hector, C. H. de Groot, W. Levason, P. N. Bartlett and G. Reid, *Chem. Commun.*, 2021, **57**, 10194–10197.

(143) W. M. Haynes, D. R. Lide and T. J. Bruno, *CRC Handbook of Chemistry and Physics*, CRC Press, New York, 96th edn., 2016.

2

Experimental

2.1. Chemicals

The solvents dichloromethane CH_2Cl_2 (95% Sigma-Aldrich), α,α,α-trifluorotoluene $C_7H_5F_3$ (>99%, Sigma-Aldrich), 1,2-dichlorobenzene $C_6H_4Cl_2$ (>99%, Sigma-Aldrich), 4-fluoro-toluene C_7H_7F (>97%, Sigma-Aldrich), chlorobenzene C_6H_5Cl (>99%, Sigma-Aldrich) and 1,2-dichloroethane $C_2H_4Cl_2$ (>99%, Sigma-Aldrich) were dried and purified by refluxing and subsequent distillation from CaH_2 and were stored in an inert atmosphere of N_2. Difluoromethane, CH_2F_2 (Apollo Scientific Ltd., 99.9%) was used without alteration.

The supporting electrolytes tetrabutylammonium chloride, $[N^nBu_4]Cl$ ($\geqslant$ 99%, Sigma-Aldrich) and tetrabutylammonium tetrafluoroborate, $[N^nBu_4][BF_4]$ (>99%, Sigma-Aldrich) were dried by heating at 100°C under vacuum for several hours. Decamethyl-ferrocene, $(C_5(CH_3)_5)_2Fe$ (97%, Sigma-Aldrich) was purified by sublimation. Decamethylferrocenium hexafluorophosphate, $[(C_5(CH_3)_5)_2Fe][PF_6]$ was synthesised according to a procedure in the literature by Duggan and Hendrickson.[1] Cobaltocenium hexafluorophosphate, $[(C_5H_5)_2Co][PF_6]$ (98%, Sigma-Aldrich) was used without alteration. Tetrabutylammonium antimony(III)tetrachloride, $[N^nBu_4][SbCl_4]$, tetrabutylammonium bismuth(III) tetrachloride, $[N^nBu_4][BiCl_4]$, and ditetrabutylammonium tellurium(IV) hexachloride, $[N^nBu_4]_2TeCl_6$, were synthesised by collaborators in the Department of Chemistry at the University of Southampton using a method described in the literature.[2] $[Ru(NH_3)_6]Cl_3$ (98%, Sigma-Aldrich) was used without further purification. All chemicals were stored in a glovebox under an inert atmosphere of N_2.

2.2. Electrodes

For a typical electrochemical experiment, a three electrode system was used. Macroelectrodes used were Pt r = 0.25, 0.375 and 1 mm, Au r = 0.25 mm and glassy carbon r =1.5 mm. Microelectrodes used were Pt discs of radii 5, 12.5 and 25 µm. Microelectrodes were calibrated using SEM (Philips XL30 ESEM). The counter electrode (CE) was a Pt mesh and the reference electrode (RE) was a home-made Ag/AgCl, immersed in a solution of 100 mM $[N^nBu_4]Cl$ for dichloromethane, o-dichlorobenzene and 1,2-dichloroethane separated from the electrolyte by a porous glass frit. For trifluorotoluene, p-fluorotoluene and chlorobenzene a Pt wire pseudo reference was used. For high pressure experiments, a 0.5 mm Ø Pt disc pseudo reference electrode was used. Working electrodes were polished using a 5 µm alumina (Buehler, USA) paste, followed by 1 µm and 0.3 µm, on a microcloth polishing pad (Buehler, USA)

Substrates for electrodeposition were 20x10 mm thin film TiN on Si chips with a 4 mm diameter exposed area as substrates. The Pt and TiN substrates were manufactured using typical microfabrication methods in a manner that has been described previously.[3] Briefly, 200 nm thick layer TiN was plasma sputtered onto Si/SiO_2 wafers followed by the sputtering of a 200 nm SiO_2 layer. The top SiO_2 layer was patterned by photolithography and half etched by plasma dry etching and removed completely using a buffered oxide etchant. A Cr/Au 10/190 nm layer was deposited via thermal evaporation onto the contact area to minimise contact resistance. A 10 mm diameter Pt:Ir (90%:10%) disc was used as the CE.

2.3. High-Pressure Electrodes

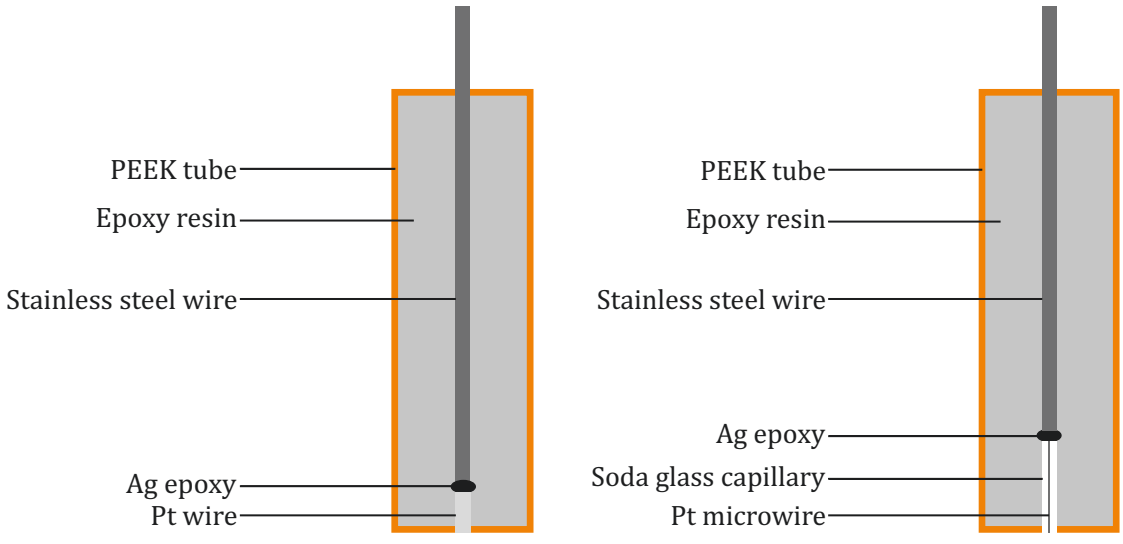

(a) Macrodisc (b) Microdisc

Figure 2.1: Schematic diagrams of electrodes used at high pressures.

Fig. 2.1a shows a diagram of a macrodisc electrode used in experiments. The electrodes were prepared by contacting 0.5 mm Ø Pt wire (Goodfellow, Advent Research Materials Ltd.) with 0.5 mm Ø stainless steel wire using a two part silver loaded epoxy adhesive (RS components) which was sealed in PEEK tubing (1.6 mm OD, 0.5 - 1 mm ID, Supelco.) with bisphenol A epoxy resin (EpoFix, Struers).

Fig. 2.1b shows a diagram of a microdisc electrode used in high pressure experiments. Microdisc electrodes were prepared by sealing the Pt microwire in a soda glass capillary which is contacted to 0.5 mm Ø stainless steel wire and sealed in PEEK tubing as described above.

Due to the low viscosity of sfc's, natural convection can be significant and cause noise. Fitting a baffle around the electrode has been demonstrated to solve the problem.[4] A baffle of length ~ 1 cm PEEK tubing (1.5 mm OD, 1.4 mm ID, Supelco.) was used for all electrodes.

The counter electrode was prepared by spot welding the Pt mesh to a length of 0.5 mm Ø Pt wire which was contacted to 0.5 mm Ø stainless steel wire and sealed in PEEK using the method described for macrodisc electrodes.

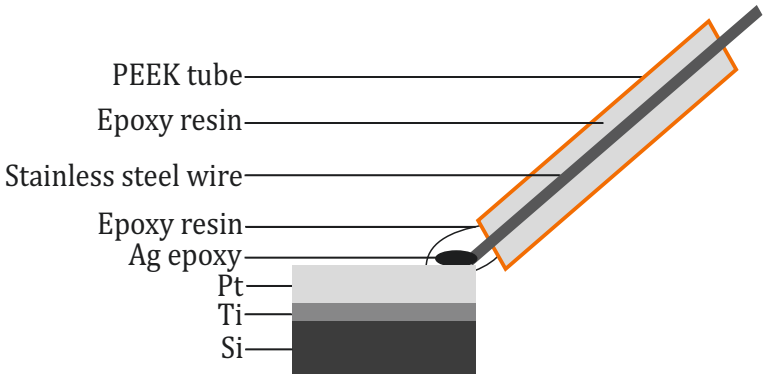

Figure 2.2: Schematic diagram of deposition substrates.

Fig. 2.2 shows a diagram of the substrate used for electrodeposition. The substrates comprised of a foundation of intrinsic Si upon which a 10 nm layer of Ti was sputtered followed by a layer of 180 - 200 nm Pt. The substrates, prepared by colleagues in the Department of Electronics and Computer Science, were 2 cm x 1 cm in size. The rectangles were shaped to the desired dimensions by scoring the Si face with a tungsten carbide scribe and manually fracturing. Afterwards, the flag was contacted to a steel wire sealed in PEEK using a two part silver loaded epoxy adhesive (RS, UK). The adhesive and exposed wire then insulated using bisphenol A epoxy resin (EpoFix kit, Struers UK).

2.4. Equipment

All ambient pressure experiments were performed in a recirculating glovebox (Belle Technology, UK) under a N_2 atmosphere. The oxygen and water levels in the glove box were

controlled via recirculation of the N_2 atmosphere through O_2 reducing catalyst and molecular sieve cartridges, keeping O_2 and H_2O levels below 10 ppm.

Electrochemical experiments were performed used a Metrohm Autolab PGSTAT302, PGSTAT30 with a BIPOT module, PGSTAT μIII or PGSTAT 302N potentiostats with data recorded using GPES or NOVA 1.11 (Metrohm, UK) software.

Electrochemical Quartz Crystal Microbalance (EQCM) experiments were performed using a QCM 200 (Standford Research Systems, USA) connected to a PGSTAT302N with a 5 MHz AT-cut quartz crystal coated with a layer of $r = 0.65$ mm Pt. A custom glass cell in a three electrode set up was used with CE and RE as above.

A Philips XL30 ESEM scanning electron microscope (SEM) was used to image the deposits. Elemental composition was determined by energy dispersive X-ray spectroscopy (EDX) using a Thermo Scientific NORAN System 7 X-ray Microanalysis System at a working distance of 10 mm and an accelerating voltage of 10 or 15 kV. Grazing incidence X-ray diffraction (XRD) patterns were collected using a Rigaku SmartLab thin film (9 kW) diffractometer (Cu-Kα, $\lambda = 1.5418$ Å) with a parallel incident beam at an angle of 1° and Hypix-3000 detector. Phase identification was performed with the Rigaku PDXL-2 package and diffraction patterns from the Inorganic Crystal Structure Database (ICSD). Instrumental line broadening was corrected using a LaB_6 external standard. Raman spectroscopy was performed using a Renishaw InVia microscope coupled to a 785 nm laser at a power of 0.1 mW. An exposure time of 15 s was used with 10 accumulations. Data was collected with WiRE 4.1 software. All data was analysed with Origin 2020 (Origin Lab, USA).

2.5. High-Temperature Equipment

Fig. 2.3 shows a schematic of the cell used for high temperature experiments. A non-isothermal cell design was used, where the cell consists of two compartments, the main compartment which holds the WE and CE where the temperature is varied, and an unheated section containing the RE connected to the main compartment by a Luggin capillary. This is to avoid errors in measured potential caused by variations in the reference potential with temperature. The glass cell was custom built at the University of Southampton with a volume of 50 ml. Gas taps allow the sealing of the cell and also the flow of gas to maintain an inert atmosphere. The cell and the lid were held together with clamps. The electrode ports were a GL14 type, the electrodes then held in place with screw caps and a PTFE coated Si gasket (DWK, Germany), ensuring the cell remained sealed. An oil filled gas bubbler was used for the inert gas exhaust. Heat was provided by a RCT digital stirrer hotplate (IKA, Germany). The temperature inside the cell was monitored with a PT 1000 coated temperature sensor (IKA, Germany).

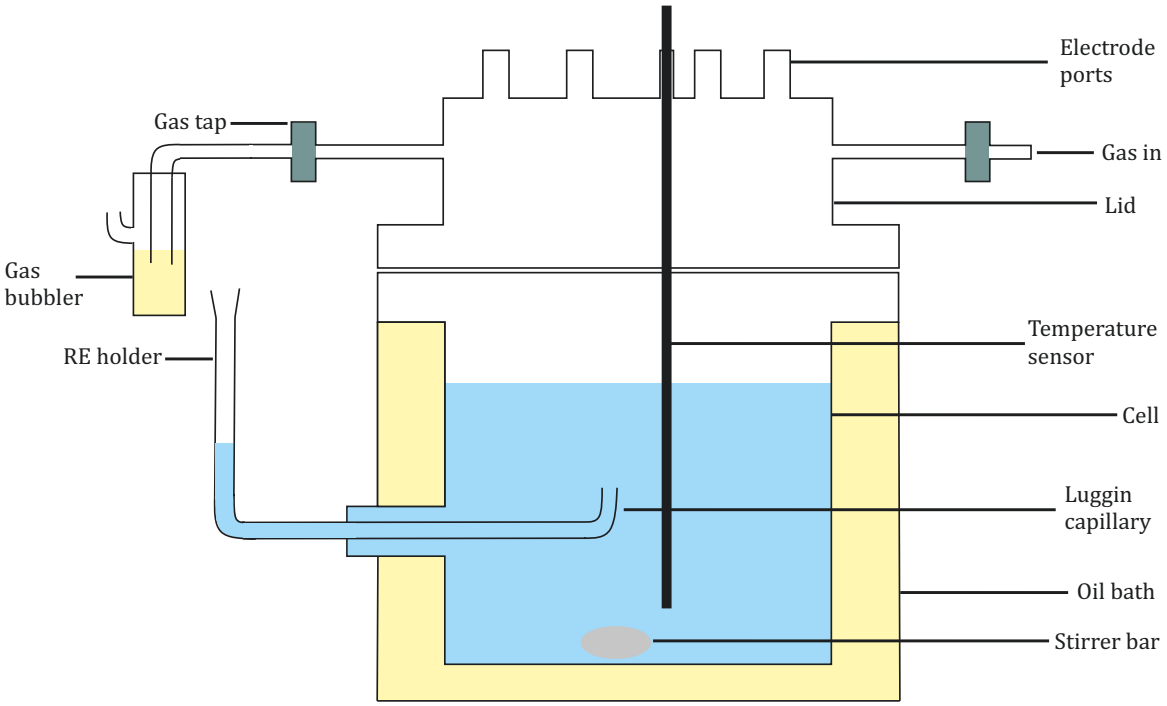

Figure 2.3: Schematic diagram of the cell used for electrochemistry at elevated temperatures.

2.6. High-Pressure Equipment

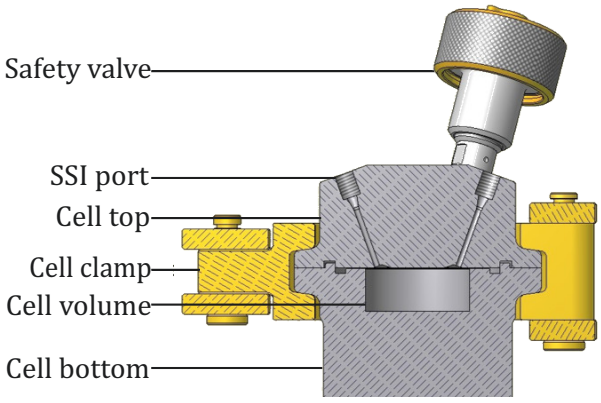

Figure 2.4: Cross-sectional diagram of the high pressure cell.

Fig. 2.4 shows a diagram of the high pressure cell used in experiments, and Fig. 2.5 a photograph of the assembled cell. The reaction vessel used was made of 316 stainless steel and manufactured in the Department of Physics workshop as described in the literature.[5] The cell is composed of two parts; top and bottom. The top contains seven 1/16" female SSI type fittings and a safety valve. The bottom contains the 10 mL working volume of the cell. The two are sealed using an EPDM O-ring (42 mm ID, Engineering Services Fasteners Ltd.) and a 316 stainless steel clamp. The safety valve contained a key which is necessary to unlock the clamp, meaning the clamp cannot be removed whilst the cell is under pres-

sure, improving the operational safety of the cell. Fittings were secured using 1/16" PEEK 'finger tight' nut and ferrule (Supelco).

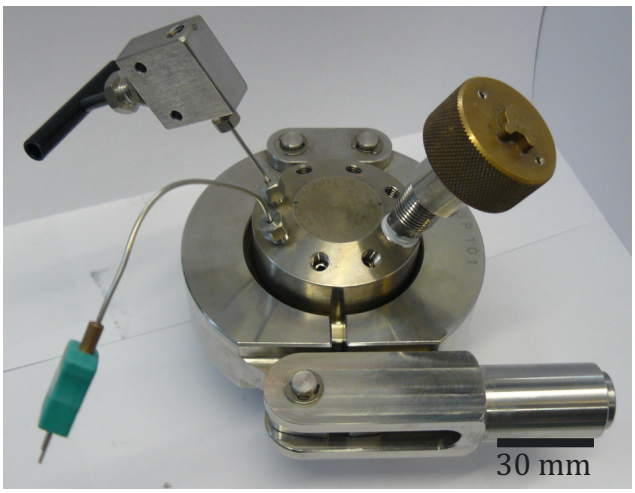

Figure 2.5: Photograph of the high pressure cell.

Of the 7 ports available in the top section, one contained tubing fitted to a needle valve which was contained to the gas line. Another was used for a thermocouple (XF-341-FAR, sensor type K, Farnell). The remaining five ports are available for electrodes and therefore a capacity of three working electrodes.

Flow of gas from the cylinder was controlled by a JASCO PU-1580 pump. Exhaust gas was controlled with a JASCO BP-2080 back pressure regulator. Pressure in the line was measured using a pressure transducer (TJE model and E725 display, Honeywell). The temperature of the cell was controlled using an Omega band heater and a thermocouple inserted vertically, from the bottom, into the wall of the lower part of the cell. These were connected to a temperature controller manufactured in the workshop in the Department of Physics at the University of Southampton. The temperature inside the cell was monitored with the thermocouple connected to a Standard ST-9612 portable digital thermometer.

2.7. Methodology

All glassware was cleaned by soaking in Decon 90 (Decon Laboratories Ltd., UK), a basic surfactant decontaminant, for a minimum of 24 hours followed by rinsing several times with 0.055 µS cm^{-1} water. The glassware was then dried in an oven at 40 °C for another 24 hours. All solutions were prepared volumetrically.

2.7.1. Conductivity

Measurements were performed using Electrochemical Impedance Spectroscopy (EIS) in a two electrode configuration with a Pt disc as the WE and a Pt gauze electrode as the CE and RE. An Autolab PGSTAT 302N potentiostat (Metrohm, UK) with a FRA32M module

was used. Data was collected using NOVA 1.11 software (Metrohm, UK) for 50 frequencies logarithmically in the range 40 kHz to 10 Hz at an amplitude of 5 mV RMS. Analysis was performed in the linear portion of the Nyquist plots with ZView 3.5 (Scribner, USA) by fitting to an equivalent circuit composed of a resistor in series with a constant phase element (CPE). The CPE exponent, α, was greater than 0.90 for all experiments. Measurements were performed at Pt discs of radii 0.25, 0.375 and 1 mm. The resistance was converted to conductivity by plotting R_u *vs.* $1/a$ using Newman's equation shown below,[6] assuming the solution resistance is the primary source of resistance and a CE at infinity.

$$R_u = \frac{1}{4a\kappa} \tag{2.1}$$

where R_u: solution resistance, a: radius of the electrode and κ: specific conductivity. According to Myland and Oldham, Eqn. (2.1) is valid if the CE is located at a distance greater than $5a$ from the WE.[7] For the 1 mm radius electrode, this corresponds to a separation of 5 mm which was more than satisfied. Fig. 2.6 shows a Nyquist plot, and a plot of R_u *vs.* $1/a$ for 100 mM $[N^nBu_4][BF_4]$ in DCM, which is representative of the collected data.

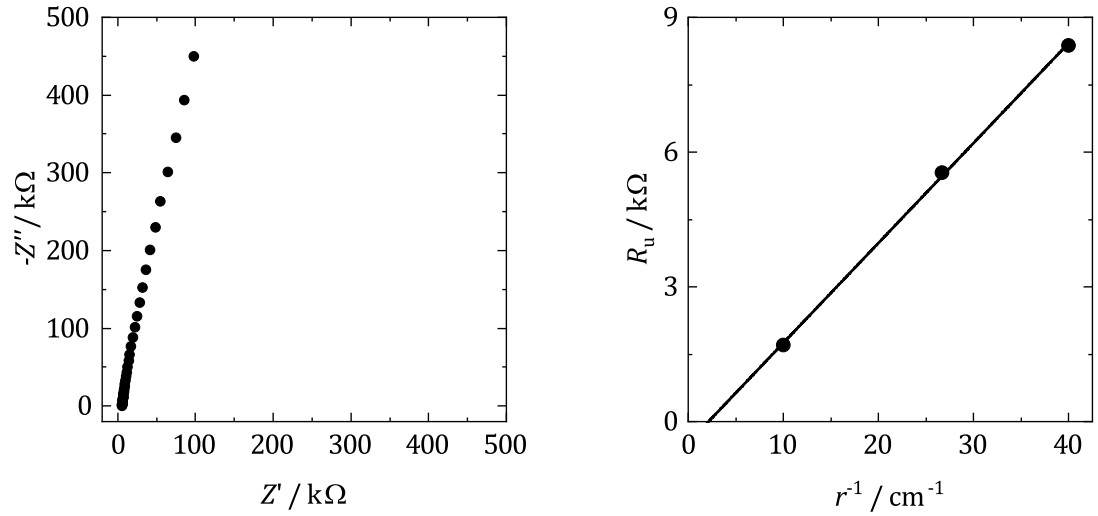

(a) (b)

Figure 2.6: Plots typical of those used to calculate conductivity, for 100 mM $[N^nBu_4][BF_4]$ in DCM. a) Nyquist plot at a r =0.375 mm Pt disc, measured for 50 frequencies logarithmically between 40 kHz and 10 Hz at an amplitude of 5 mV, b) plot of R_u *vs.* $1/a$ for Pt discs of radii 0.25, 0.375 and 1 mm.

2.7.2. Double-Layer Capacitance

EIS was used as described in 2.7.1 for 20 frequencies logarithmically. However a three electrode cell was used with an Ag/AgCl RE with 100 mM $[N^nBu_4]Cl$ for dichloromethane, 1,2-dichlorobenzene, 1,2-dichoroethane and sat. $[N^nBu_4]Cl$ for trifluorotoluene, p-fluorotoluene and chlorobenzene. A 10 nF capacitor and 0.25 mm radius Pt wire was used

in series with the RE to act as a low impedance bypass at high frequencies.[8] The high impedance of the RE has been demonstrated to cause artefacts in EIS.[9] Measurements were collected as a function of potential at 200 mV intervals within the solvent potential window.

2.7.3. Electrochemistry

Electrochemical experiments were performed using a standard five necked pear shaped cell. The solution was allowed to equilibrate for at least ten minutes before measurements began. Decamethylferrocene was used as an internal reference and 1 mM was added at an appropriate point in the experiment.

2.7.4. Electrodeposition

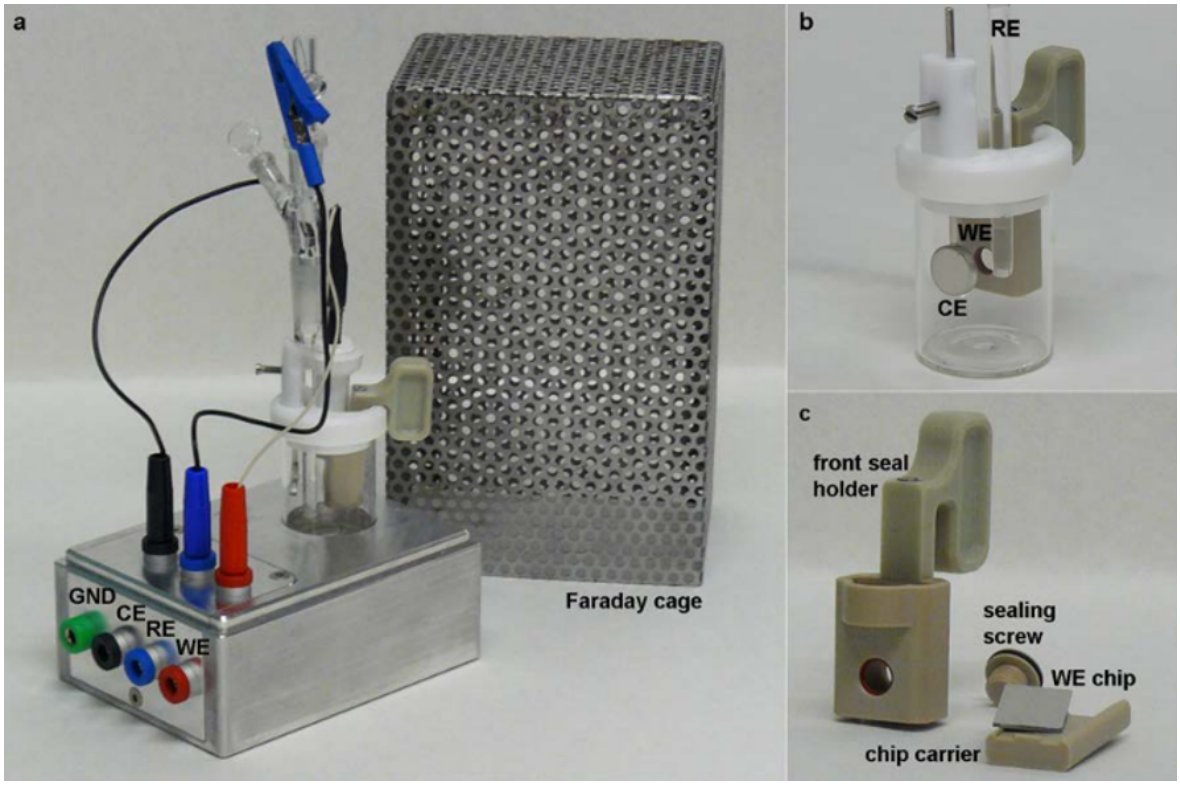

Figure 2.7: Photographs of electrodeposition set up. a) fully assembled cell and holder showing electrode connections and Faraday cage, b) electrochemical cell with WE holder, CE and RE, c) front-seal holder with substrate, substrate holder and holding screw. Reproduced from Ref. [10] under Creative Commons 4.0 license (CC BY 4.0).

For electrodeposition a custom-built small volume electrochemical cell, named the front-seal holder, was used to ensure correct placement of the working, reference and counter electrode, shown in Fig. 2.7. Details of the cell have been given elsewhere.[10] The cell was assembled with the substrate inside the glovebox. The contact resistance between the contact pad on the substrate and the connector was measured with a digital voltmeter before use. Substrates with a resistance greater than 1 Ω were discarded. The potential was stepped to a potential of zero current for 10 s, followed by a step to the

applied potential. Post electrodeposition the substrate was rinsed by dipping in DCM. Decamethylferrocene was used as an internal reference and 1 mM was added at an appropriate point in the experiment.

2.7.5. High Temperature Electrochemistry

The high temperature cell was assembled and transported into the glovebox where the electrolyte was prepared and added to the cell. The cell was then sealed, removed from the glovebox and transported to a fumehood, where an Ar gas line and gas bubbler were connected. The gas taps were opened and Ar slowly bubbled through. The cell was wrapped in cotton wool for insulation and heating began. The cell was heated with stirring with a jacketed Si oil bath, once the desired temperature in the cell had been reached, stirring and gas flow was stopped and the cell was allowed to equilibrate for *ca.* 5 minutes before beginning experiments.

2.7.6. Supercritical Fluid Electrochemistry

The cell was stored in a drying oven between experiments. The electrodes were fitted into the ports, the o-ring and a PTFE magnetic stirrer bar inserted. The cell was assembled and placed into a glove-box. The reagents and supporting electrolyte were weighed out and the cell reassembled. The safety valve was inserted and the solvent line valve closed, sealing the cell.

The cell was connected to the rigging and heated. The tubing was flushed with liquid R32 several times before filling the cell to remove oxygen and moisture. The cell was filled, with stirring, until the desired pressure reached. Stirring was stopped and the solution left for a minimum of five minutes before experiments were performed to allow it to settle and equilibrate.

All experiments were performed in the temperature range 357-359 K and pressure range 16.89-17.58 MPa. This corresponds to a variation in density of 0.822-0.820 g cm^{-3},[11] in dynamic viscosity of 0.079-0.078 mPa s,[11] and a dielectric constant of ~ 8.46.[12] At the end of the experiment the cell was emptied and allowed to cool. The cell was disassembled and cleaned.

2.8. References

(1) D. M. Duggan and D. N. Hendrickson, *Inorg. Chem.*, 1975, **14**, 955–970.

(2) P. N. Bartlett, D. Cook, C. H. de Groot, A. L. Hector, R. Huang, A. Jolleys, G. P. Kissling, W. Levason, S. J. Pearce and G. Reid, *RSC Adv.*, 2013, **3**, 15645–15654.

(3) S. J. Reeves, Y. J. Noori, W. Zhang, G. Reid and P. N. Bartlett, *Electrochim. Acta*, 2020, **354**, 136692.

(4) J. A. Branch, Ph.D. Thesis, University of Southampton, 2015.

(5) J. Ke, W. Su, S. M. Howdle, M. W. George, D. Cook, M. Perdjon-Abel, P. N. Bartlett, W. Zhang, F. Cheng, W. Levason, G. Reid, J. Hyde, J. Wilson, D. C. Smith, K. Mallik and P. Sazio, *Proc. Natl. Acad. Sci. U. S. A.*, 2009, **106**, 14768–14772.

(6) J. Newman, *J. Electrochem. Soc.*, 1966, **113**, 501–502.

(7) J. C. Myland and K. B. Oldham, *Anal. Chem.*, 2000, **72**, 3972–3980.

(8) C. C. Herrmann, G. G. Perrault and A. A. Pilla, *Anal. Chem.*, 1968, **40**, 1173–1174.

(9) A. Tran, F. Huet, K. Ngo and P. Rousseau, *Electrochim. Acta*, 2011, **56**, 8034–8039.

(10) G. P. Kissling, M. Aziz, A. W. Lodge, W. Zhang, M. Alibouri, R. Huang, A. L. Hector, G. Reid, C. H. de Groot, R. Beanland, P. N. Bartlett and D. C. Smith, *J. Electrochem. Soc.*, 2018, **165**, D802–D807.

(11) E. W. Lemmon, M. O. McLinden and D. G. Friend, in *NIST Chem. WebBook, NIST Stand. Ref. Databse No. 69*, ed. P. J. Lindstrom and W. G. Mallard, National Institute of Standards and Technology, Gaithersburg MD.

(12) A. P. Abbott, C. A. Eardley and R. Tooth, *J. Chem. Eng. Data*, 1999, **44**, 112–115.

3

Identification and Characterisation of Weakly Coordinating Solvents

3.1. Overview

This Chapter firstly details the selection of Weakly Coordinating Solvents. Based upon specified requirements, five candidate solvents are identified using Kamlet and Taft's solvent descriptors. The selected solvents are then subjected to a suite of measurements in order to characterise them and they are compared to a control solvent, dichloromethane. Measurements of the potential window, conductivity and double-layer capacitance are detailed. Additionally, decamethylferrocene and cobaltocenium hexafluorophosphate are employed as model redox couples to investigate the influence of the solvents on electrochemical reactions. Finally, the most promising solvents for electrodeposition are identified.

3.2. Kamlet-Taft Parameters

The Kamlet-Taft (KT) parameters are a set of solvent descriptors designed to collectively describe all aspects of solute/solvent interactions.[1,2] The three major parameters are: $\pi*$ the polarity descriptor, α the hydrogen-bond donor acidity and β the hydrogen-bond acceptor basicity. Together, they are used in Linear Solvation Energy Relationships (LSER), a type of linear free energy relationship as discussed in Section 1.2, the general form of which is shown below

$$A = A_0 + s\pi* + a\alpha + b\beta \tag{3.1}$$

where A is some solvent dependent property and A_0 is a reference quantity which corresponds to a medium in which the effects of solute/solvent interactions on the process are negligible, s, a and b are then the independent coefficients that indicate the contribution of the descriptor to the solvent dependent property. These are equivalent to X and X_0 in Eqn. (1.10). The KT descriptors are obtained by UV/Vis spectroscopy of several solvatochromic dyes in the appropriate solvent and measuring the peak shift in the spectrum relative to a reference solvent, in this case cyclohexane. The shift is then averaged over the different dyes and normalised to bring the values between 0 and 1. Full details of the method to obtain each descriptor can be found elsewhere.[1,2]

What is displayed in Eqn. (3.1) is not the complete set but only those relevant for the discussion here. The terms to be used can be included or removed based upon their applicability to the correlated property. Those that are omitted here are used only for specific situations, for example a molecular volume term is included when the process involves solvent/solvent transfer of a non-electrolyte. The complete list of descriptors can be found in Ref. [2]. $\pi*$ describes electrostatic, non-specific interactions between the solvent and solute,[3] and contains information on the dipolarity and polarisability of the solvent. For α, the hydrogen-bond donor acidity refers to the capacity of the solvent to donate a proton for hydrogen bonding and so is equivalent to Lewis acidity.[4] Conversely, β is a measure of a solvent's ability to donate a lone pair for hydrogen bonding and is analogous to Lewis basicity.[5]

Clearly the key consideration for the KT descriptors is the choice of solvatochromic dye for each descriptor. It is important that the chosen dye accurately samples the information on the type of interaction that it is intended to. This has been identified as a failure of the $\pi*$ parameter for example. It has been found that the descriptor does not fully include polarisability based interactions, and that a correction term to properly account for this must be included.[6] Indeed, statistical analysis has indicated that dipolar and polarisability interactions are two separate categories of interaction with distinct descriptors,[7] suggesting that these two types of interaction are best described by two different indicators, optimised for the particular interaction. It is also important that the chosen dyes do

not describe more than one type of interaction. The use of multiple dyes and the averaging of the response alleviates some of this uncertainty since it can 'smooth' out any issues with particular dyes. However, this has also been criticised on the grounds of losing its relation to a direct chemical process and instead becoming an optimised number based upon approximations; masking flaws in the dyes used.[8] Whether the KT descriptors successfully measure the solute/solvent interactions that they claim to has been considered by Katritzky *et al.*[9] Using computing power and a swathe of theoretical molecular descriptors, $\pi*$ was found to be best described by dipolar and non-specific based descriptors, but not polarisability, and also agrees well with the authors' stated intentions. α and β were also found to agree with the original idea for which they were constructed. Further discussion of the flaws of KT descriptors, and how they compare to others in the literature can be found in Ref. [10]. Despite their criticism, the KT parameters have proven to be one of the most widely applied set of solvent descriptors. One major reason for this is that descriptors are available for a great number of solvents.[11] Or, if descriptors have not been directly measured, then there are methods to readily predict them from their relationship with other solvent descriptors, such as dielectric constant. Meaning that it is possible to obtain KT parameters even for unusual solvents.

The objective of this Chapter is to use solvent descriptors to identify interesting weakly coordinating solvents as alternatives to DCM for the electrodeposition of semiconductors. Once the alternative solvents have been identified they will be electrochemically characterised in order to determine their suitability for application to electrodeposition, the most promising solvents will be chosen for further characterisation in subsequent Chapters.

3.3. Selection of Candidate Solvents

As has been previously described, a WCS is one that is not strongly Lewis basic and consequently does not coordinate with dissolved metal cations. There are however other requirements for a solvent to be useful for electrochemistry. The solvent must be reasonably polar such that charged species can be dissociated to ensure the electrolyte is conducting and metal precursors are soluble. The solvent must also be aprotic so that hydrogen evolution does not limit the accessible potential window of the solvent and electrodeposition of more noble metals is possible. Also desirable is a solvent of high boiling point to permit electrodeposition at elevated temperatures, a useful practical capability which can improve the material properties of the deposit. It is upon the aforementioned criteria that the suitability of solvents will be judged.

The KT solvent descriptors: π^*, β and α can be used for the solvent screening process since each parameter describes the underlying solvent properties associated with the stated solvent requirements above. In the context of the KT parameters, a suitable solvent will have a high value for π^*, associated with dissolution and dissociation of charged

species, a low value of β so is a poor Lewis base, and a low α denoting aproticity. This should approximately correspond to solvents with $\pi^* \geqslant 0.55$, $\beta \leqslant 0.2$ and $\alpha \leqslant 0.2$.

From this filtering process five candidate solvents emerge: trifluorotoluene (TFT), o-dichlorobenzene (oDCB), p-fluorotoluene (pFT), chlorobenzene (CB) and 1,2-dichloroethane (DCE). Fig. 3.1 shows the KT parameters of the candidate WCS to be studied plus DCM as a control solvent and their values can be found in Table 3.1. A compilation of relevant physical properties of these solvents is given in Table 3.2. In Fig. 3.1, the solvents occupy a specific volume of the 3D solvent descriptor space. The solvents in this region are primarily halogenated aromatics or short chain aliphatics. Also shown are some commonly used solvents in electrochemistry and some typical ionic liquids. Their identities are given in Table 3.1. Clearly, none of the solvents most frequently encountered in electrochemistry are suitable for use here, they do not lie in the suitable region of descriptor space and cannot be considered WCS. This emphasises the need for a more general method of solvent selection, which can identify the solvent(s) most suitable for the required application.

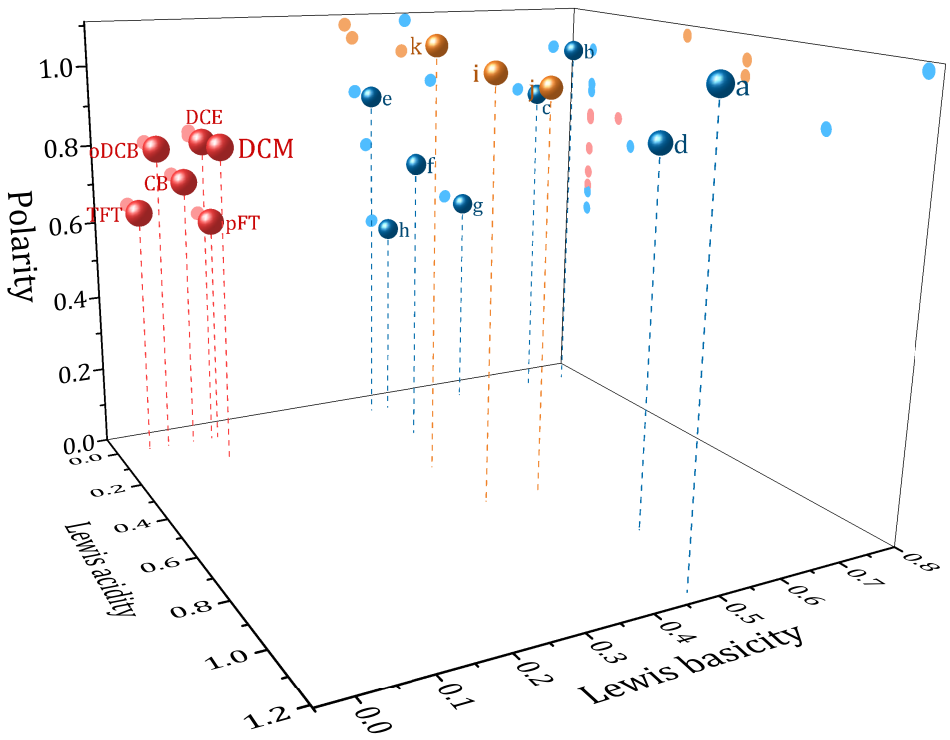

Figure 3.1: Kamlet and Taft solvent descriptors of various solvents. Red: candidate weakly coordinating solvents, blue: common electrochemical solvents, yellow: example ionic liquids. The identity of the solvents and their KT parameters can be found in Table 3.1.

The solvents have a range of π^* values, meaning it might be expected that the solvents behave in a similar way except for properties determined by their polarity. The sol-

Solvent	Code	π^*	β	α	Ref.
DCM		0.82	0.10	0.13	[12]
TFT		0.64	0	0	[13]
oDCB		0.80	0.03	0	[12]
pFT		0.60	0.11	0	π^* estimated from eqn. 25 in [1]. β, α from [14]
CB		0.71	0.07	0	[12]
DCE		0.81	0.10	0	[12]
Water	a	1.09	0.47	1.17	[12]
DMSO	b	1.00	0.76	0	[12]
DMF	c	0.88	0.69	0	[12]
EG	d	0.92	0.52	0.90	[12]
PC	e	0.90	0.38	0	[12]
ACN	f	0.75	0.40	0.19	[12]
THF	g	0.58	0.55	0	[12]
DME	h	0.53	0.41	0	[12]
[bmim][BF_4]	i	1.05	0.38	0.63	[15]
[bmim][TfO]	j	1.01	0.46	0.63	[15]
[bm_2im][BF_4]	k	1.08	0.36	0.40	[15]

Table 3.1: Literature compilation of Kamlet and Taft parameters of candidate weakly coordinating solvents, common electrochemical solvents and typical ionic liquids from Fig. 3.1. DCM: dichloromethane, TFT: trifluorotoluene, oDCB: o-dichlorobenzene, pFT: p-fluorotoluene, CB: chlorobenzene, DCE: 1,2-dichloroethane, DMSO: dimethyl sulphoxide, DMF: dimethylformamide, EG: ethylene glycol, PC: propylene carbonate, ACN: acetonitrile, THF: tetrahydrofuran, DME: dimethyoxyethane, [bmim][BF_4]: 1-butyl-3-methylimidazolium tetrafluoroborate, [bmim][TfO]: 1-butyl-3-methylimidazolium triflate, [bm_2im][BF_4]: 1-butyl-2,3-dimethylimidazolium tetrafluoroborate.

Solvent	T_b / °C	p_v / kPa	η / mPa s	ρ / g cm^{-3}	ϵ_r	n	μ / D
DCM[a]	40	58.3	0.41	1.39	8.9	1.42	1.1
TFT	102[b]	5.3[b]	0.47[c]	1.18[b]	9.2[d]	1.48[d]	2.9[b]
oDCB[a]	181	0.2	1.32	1.30	9.9	1.55	2.5
pFT	117[d]	3.0[e]	0.62[f]	1.00[d]	5.9[d]	1.47[d]	2.0[d]
CB[a]	132	1.6	0.76	1.10	5.6	1.52	1.7
DCE[a]	83	10.6	0.78	1.25	10.4	1.44	1.8

Table 3.2: Literature compilation of selected physical properties of candidate weakly coordinating solvents. T_b: boiling point, p_v: vapour pressure, η: viscosity, ρ: density, ϵ_r: dielectric constant, n: refractive index, μ: dipole moment in the gas phase. All measurements at 25 °C. [a]: ref. [11] , [b]: ref. [16], [c]: ref. [17], [d]: ref. [18], [e]: ref. [19], [f]: ref. [20].

vents also possess similar dielectric constants, presenting an interesting test of the use of the two descriptors in describing solvent polarity. The candidate solvents have seen little use in electrochemistry. As result of this it is important to characterise the solvents in order to improve understanding of electrochemistry in weakly coordinating solvents and to assess their suitability as solvents for electrodeposition.

3.4. Potential Window

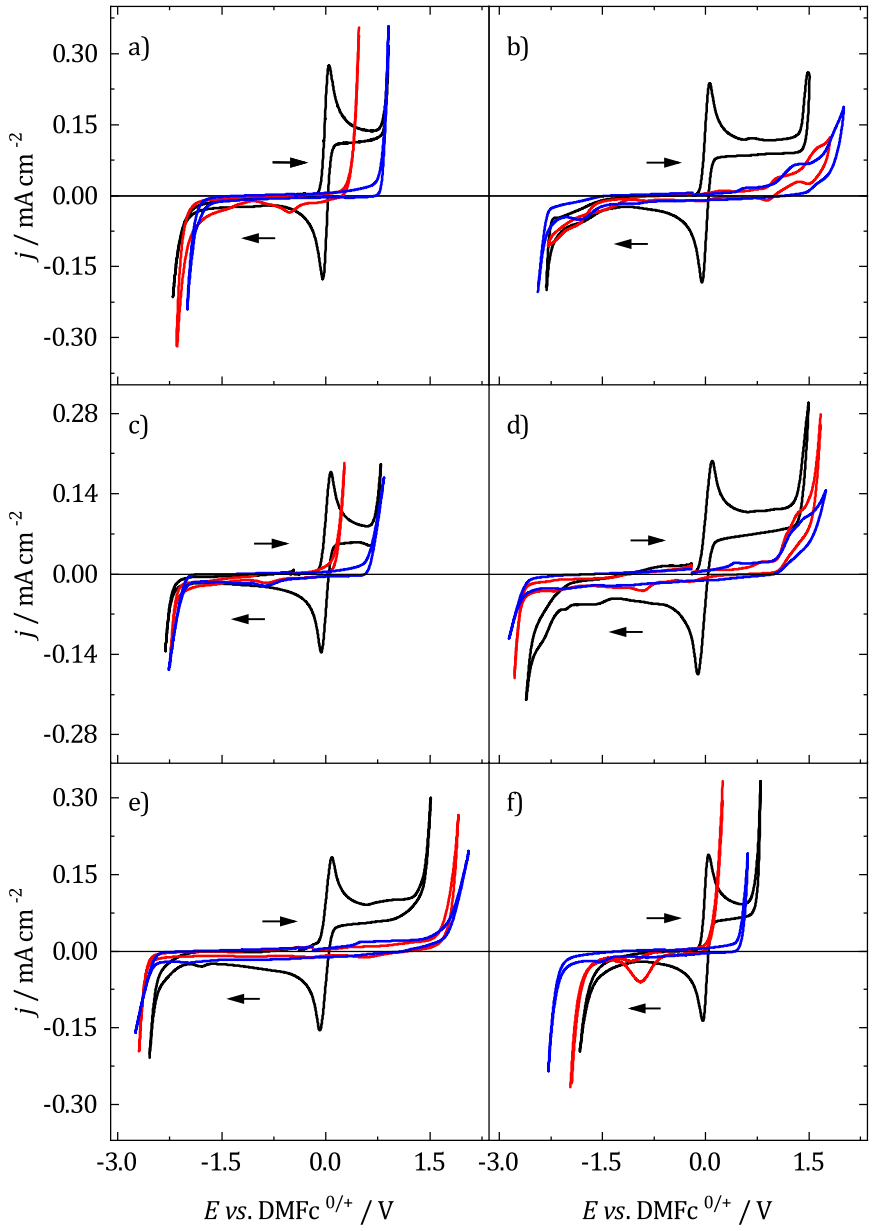

Figure 3.2: Solvent windows at Pt, Au and GC electrodes with 100 mM a), c), f) $[N^nBu_4]Cl$ and b), d), e) $[N^nBu_4][BF_4]$. Working electrode was swept from −0.4 V *vs.* DMFc (added only when using Pt) at 50 mV s^{-1} in the direction indicated by the arrows. CE: Pt grid, RE: Ag/AgCl. Black: Pt, red: Au, blue: GC. a) DCM, b) TFT, c) oDCB, d) pFT, e) CB, f) DCE.

Fig. 3.2 shows voltammograms of the available potential window of the studied solvents at Pt, Au and glassy carbon (GC) electrodes. For the Pt CV, 1 mM DMFc was added to act as a current reference, giving an indication of the current density associated with a 1 mM, one electron process. The electrolyte was considered to have reached its solvent limit, anodic or cathodic, when the current was equal to the anodic or cathodic peak current for 1 mM DMFc. The potential window was calculated using a 0.25 mm radius Pt disc but was also recorded at Au and GC to give an indication of the effect of the electrode material on the limits. The results are shown in Table 3.3. In those cases where 100 mM $[N^nBu_4]Cl$ was insoluble in the solvent (TFT, pFT and CB) 100 mM $[N^nBu_4][BF_4]$ was used instead.

For the majority of solvents, the available potential window, E_{window}, is similar for the solvents with the same electrolyte. Additionally, those solutions that share a common anion have a similar anodic limit, E_a. E_a is greater when $[BF_4]^-$ is used, indicating that Cl^- is more easily oxidised. It has been shown that the addition of strongly withdrawing groups in the anion can increase its resistance to oxidation.[21] The electrochemistry of the chloride/chlorine system at a Pt surface was studied by Sereno *et al.* in the aprotic solvent acetonitrile.[22] The overall redox reaction appears to be

$$2\,Cl^- \longrightarrow Cl_{2\,(g)} + 2\,e^-$$

which proceeded *via* a Volmer-Heyrovsky mechanism. Xiao and Johnson performed bulk electrolysis of the ionic liquid [bmim][BF_4] at Pt electrodes.[23] The anodic product was found to be primarily BF_3. With $[N^nBu_4][BF_4]$ it might therefore be expected that the anodic decomposition reaction is

$$[BF_4]^- \longrightarrow BF_{3\,(g)} + F^-$$

The similarity of the cathodic limits, E_c, suggest that the available window is limited by decomposition of the supporting electrolyte rather than the solvent itself. Dahm and Peters investigated the electroreduction of the tetrabutylammonium cation in dimethylformamide at carbon electrodes.[24] It was found that the cation is reduced to form butane and 1-butene. It was also found to be possible for intermediates to react with trace water to form alkanes and tributylamine. The exception to this rule is DCE which has a much lower cathodic limit, suggesting the solvent itself is decomposing, instead of the electrolyte. The electrochemical reduction of DCE has been studied at GC and Ag electrodes in acetonitrile and dimethylformamide.[25,26] The proposed mechanism is one of stepwise dechlorination forming a carbon radical followed by a carbanion, with the reaction terminated by the formation of ethylene.[26] Protonation of the anion by trace water to give chloroethane or ethane is also possible. Although due to the trace amounts of water present, this is expected to only be a minor product.

Slight variations of the limits can still be observed between solvents, this could be associated with the effect of water impurities, which have been observed to narrow the potential window of ionic liquids.[27] The same study also reported that ionic liquids containing the $[BF_4]^-$ anion were significantly more hygroscopic than those with Cl^-. Potentially explaining the small amounts of current activity observed in the solvents where $[N^nBu_4][BF_4]$ was used. Traces of water can remain in the solvent even after drying.

The negative limit is similar for the different electrode materials GC and Au. DCE is once again an exception showing some variability with electrode material, presumably due to varying favourability of the solvent decomposition at the different electrodes. A similar effect is observed for the anodic limit in the di-chlorinated solvents. Gold appears to be a superior catalyst for the reaction. A reduction peak can also be observed in some solvents on the reverse sweep at the Au electrode. This was associated with the reduction of the anodic decomposition product and was only observed upon extended excursions past the anodic limit.

Solvent	E_a *vs.* DMFc / V	E_c *vs.* DMFc / V	E_{window} / V
DCM	0.89	−2.18	3.07
TFT	1.45	−2.30	3.76
oDCB	0.78	−2.31	3.09
pFT	1.40	−2.56	3.97
CB	1.45	−2.51	3.95
DCE	0.75	−1.77	2.52

Table 3.3: Experimental anodic and cathodic limits, and available potential window at a Pt electrode. Electrolyte composed of 100 mM $[N^nBu_4]Cl$ in DCM, oDCB and DCE, and 100 mM $[N^nBu_4][BF_4]$ in TFT, pFT and CB.

3.5. Conductivity

Table 3.4 shows normalised uncompensated resistance values, $R_u a$ where a is the radius of the electrode and molar conductivities, Λ_m, of 100 mM $[N^nBu_4]Cl$ and $[N^nBu_4][BF_4]$, excepting TFT, pFT and CB where 100 mM $[N^nBu_4]Cl$ was insoluble. Insolubility is presumably caused by their lower polarity. R_u was measured at three electrode sizes and the specific conductivity, κ, was determined from the slope of a plot of R_u *vs.* $1/a$ with use of Newman's equation,[28] assuming the solution resistance is the primary source of resistance and that the counter electrode was at infinity. Λ_m was then obtained from κ since $\Lambda_m = \kappa/c$ where c is the concentration of electrolyte. Also given in Table 3.4 is $\Lambda_m\eta$, the conductivity viscosity product, an attempt to account for the effect of solvent viscosity on conductivity. Now that conductivity has been normalised for viscosity, $\Lambda_m\eta$ should be approximately proportional to the degree of ion pairing in the solvent, assuming that the viscosity of the electrolyte is not significantly different from the pure solvent. The values

Electrolyte	Solvent	$R_u a$ / kΩ cm	Λ_m / S cm^2 mol^{-1}	$\Lambda_m \eta$ / S cm^2 mPa s mol^{-1}
$[N^nBu_4]Cl$	DCM	0.28(1)	9.04(20)	3.71(8)
	TFT	-	-	-
	oDCB	2.35(4)	1.07(2)	1.42(2)
	pFT	-	-	-
	CB	-	-	-
	DCE	0.34(1)	7.42(11)	5.78(8)
$[N^nBu_4][BF_4]$	DCM	0.22(1)	11.61(38)	4.76(16)
	TFT	1.09(1)	2.30(5)	1.17(2)
	oDCB	1.45(1)	1.74(2)	2.29(3)
	pFT	3.53(10)	0.71(3)	0.44(2)
	CB	3.24(6)	0.78(2)	0.59(1)
	DCE	0.24(1)	10.69(12)	8.33(10)

Table 3.4: Experimentally obtained resistances and conductivities of 100 mM $[N^nBu_4]Cl$ and $[N^nBu_4][BF_4]$ in weakly coordinating solvents from EIS with electrode radii of 0.025 cm, 0.0375 cm and 0.1 cm Pt disc electrodes. $R_u a$ values given for the $r = 0.025$ cm electrode. Obtained using EIS with 50 frequencies logarithmically between 40 kHz and 10 Hz at an amplitude of 5 mV. A blank cell indicates insolubility. Values are the average of three repeats and the error the standard deviation.

observed here are comparable to those previously reported in the literature for the same or similar electrolyte conditions in DCM,[29–32] TFT,[29,33] oDCB,[32] and DCE.[30,32]

As might be expected, conductivity is observed to be greater for $[N^nBu_4][BF_4]$ based electrolytes than for $[N^nBu_4]Cl$ in the solvents where both are soluble. The $[BF_4]^-$ anion is larger than Cl^-. Meaning it has a lower charge density which permits a superior stabilisation of the negative charge and reduces the degree of ion association.[34] Such trends have been observed previously in the WCS. Geiger *et al.* measured the conductance of tetrabutylammonium electrolytes in DCM and TFT.[29] For a common cation, changing to a larger anion with a lower charge density resulted in a decrease in the association constant, K_A, and increase in conductivity. Such an effect has been observed elsewhere in DCM by Svorstol and Songstad,[31] in TFT by Boitsov *et al.*,[33] and in oDCB.[35] Additionally, the ratio $\Lambda_m\eta([N^nBu_4][BF_4])/\Lambda_m\eta([N^nBu_4]Cl)$ is similar for DCM, oDCB and DCE with values of 1.3, 1.6 and 1.4 respectively. This indicates that the relative strengths of the electrolytes remain the same in the solvents and that both interact in a similar manner with the solvent. Typically, a larger ion has a lower mobility and this can lower electrolyte conductivity. However in less polar solvents such as those studied here, where ion pairing is significant, this becomes an advantage since the lowering of ion pairing more than compensates for any losses in mobility.

It is also interesting to note that many solvents have similar dielectric constants but display significantly different values for $\Lambda_m\eta$. The experimental order of $\Lambda_m\eta$ is pFT < CB < TFT < oDCB < DCM < DCE, however that predicted by ϵ_r is CB < pFT < DCM ≈ TFT < oDCB < DCE. Additionally DCM, TFT, oDCB and DCE all have similar dielectric constants

but TFT and oDCB display significantly lower conductivities. Since $\pi*$ of TFT is lower than DCM, oDCB and DCE's this could be rationalised as a consequence of the inaccuracies of ϵ_r and a lower solvent polarity. Nevertheless, this suggests that ion pairing is greater in TFT and oDCB than DCM and DCE. This would appear to represent a break down of the so called 'isodielectric rule' which, based upon simple models of ion pairing, predicts that solvents with similar dielectric constants should possess similar degrees of ion pairing,[36] the breakdown being caused by short-range specific interactions in the aromatic solvents.[37]

Fundamentally, ion pair formation is the result of competition between solvent molecules and the counter ion for interaction with the ion. One possible reason for differences in the levels of ion pairing is the presence of favourable interactions between solvent molecules, which gives a degree of structure to the solvent. This could make ion solvation less favoured and lead to an increase in the degree of ion pairing. Such an effect has previously been observed in water where the degree of ion pairing increased with ion size because larger ions disrupted the H bonding network of water and so ions were forced into pairs in order to preserve it.[34] This has been termed 'structure enforced ion pairing'. One measure of the structuredness of a solvent is the Kirkwood correlation parameter, g_K, which gives information on the orientation of a solvent molecules' dipoles.[38] g_K can be estimated from the Onsager-Kirkwood-Frölich equation for the dielectric dispersion of a dipolar liquid.[38] For a solvent with no alignment of dipoles, $0.7 \leqslant g_K \leqslant 1.3$ and is considered unstructured, $g_K > 1.3$ corresponds to dipoles oriented parallel to each other such as H bonded solvents, and $g_K < 0.7$ corresponds to neighbouring dipoles oriented in an antiparallel fashion, for example nitriles which has been attributed to the formation of dimers.[39] Values for the present solvents can be taken from the literature or calculated,[38] giving values for DCM, TFT, oDCB and DCE of 1.04, 0.56, 0.68 and 1.17 respectively. This would suggest that DCM and DCE can be considered unstructured, and that the solvent molecules of TFT and oDCB are oriented in an antiparallel manner and this arrangement is preferred to ion solvation to a certain extent, causing a greater degree of ion pairing. There is no direct evidence of such structures in TFT or oDCB but dielectric measurements of bromobenzene and benzonitrile, two solvents with $g_K < 0.7$, have shown them to form stable antiparallel dimers, similar to nitriles.[40] Furthermore, crystal structures of TFT and oDCB showed TFT molecules arranged in a head to tail fashion, and favourable Cl-Cl interactions leading to a 'zig-zag' structure in oDCB,[41,42] suggesting that associations of this type are energetically favourable in solution for the two solvents.

3.6. Double-Layer Structure

Fig. 3.3 shows differential capacitance curves of 100 mM $[N^nBu_4][BF_4]$ at a Pt disc electrode in the studied solvents. Generally, the double-layer capacitance, C_{DL}, decreases with potential before plateauing at the most negative potentials. The exception to this

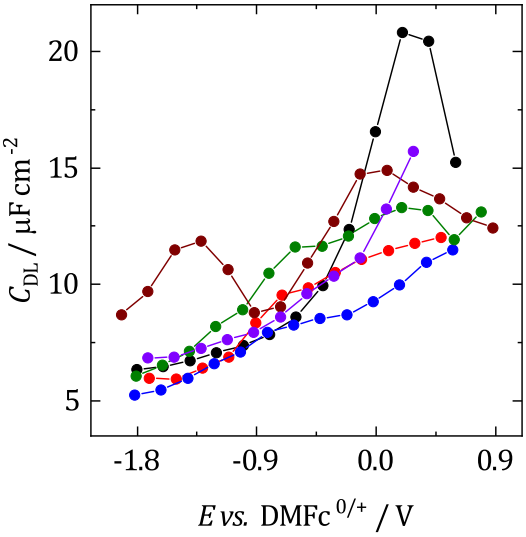

Figure 3.3: Differential capacitance curves for 100 mM $[N^nBu_4][BF_4]$ at a $r = 0.25$ mm Pt electrode, scanning in the anodic direction. Obtained from EIS for 20 frequencies logarithmically between 40 kHz and 10 Hz at an amplitude of 5 mV fitted to a RCPE equivalent circuit, at 200 mV intervals within the solvent window. Black: DCM, red: TFT, blue: oDCB, green: pFT, brown: CB, purple: DCE.

rule appears to be CB where instead two capacitance humps are observed, with a minimum at *ca.* −0.8 V *vs.* DMFc. Scans performed in the opposite direction, positive to negative, showed no major differences.

A simple model of the electrical double-layer (EDL) describes the total capacitance, C_{DL}, as the sum of two capacitors in series

$$\frac{1}{C_{DL}} = \frac{1}{C_H} + \frac{1}{C_D} \tag{3.2}$$

where C_H is the capacitance of the Helmholtz layer and C_D is the capacitance of the diffuse layer.[43] At high electrolyte concentrations such as those used here, C_D becomes large enough that it no longer contributes significantly to C_{DL}, meaning it can be ignored. C_{DL} is then primarily determined by C_H.[44] C_H can be simply described as a parallel plate capacitor

$$\frac{C_H}{A} = \frac{\epsilon_i \epsilon_0}{d} \tag{3.3}$$

where A is the area of the electrode, ϵ_i is the dielectric constant of the inner layer and d the distance between the two plates. This model predicts that C_{DL} is independent of potential, which is clearly only the case here at the most negative potentials.

The results in Fig. 3.3 appear to be in agreement with the work of Fawcett at the Hg/propylene carbonate interface with 100 mM $[N^nBu_4][ClO_4]$.[45] Abbott observed a similar plateau at negative potentials in DCE with 300 mM $[N^nBu_4][BF_4]$.[46] According to Fawcett, at the most positive potentials the inner layer is occupied by solvent molecules, then

as the potential decreases these are replaced by $[N^nBu_4]^+$ and ϵ_i decreases until eventually the double-layer is wholly populated by $[N^nBu_4]^+$ cations and C_{DL} plateaus. Taking a value of 6.5 µF cm^{-2} for the plateau and assuming $\epsilon_i = 3.2$, as given by Fawcett,[45] gives a thickness of 0.44 nm. This is comparable to 0.41 nm, the crystallographic radius of the $[N^nBu_4]^+$ cation.[47] Suggesting that the inner layer is indeed populated by $[N^nBu_4]^+$ at negative potentials. Although, since d calculated here is greater than the radius of $[N^nBu_4]^+$, this might suggest that the dielectric constant of the inner layer is less than 3.2. Abbott reported a value of 2.6 for the ϵ_i of $[N^nBu_4]^+$, for example.[46] Taking ϵ_i as 2.6 gives d as 0.35 nm. This might be a more reasonable value when considering that it is possible for the $[N^nBu_4]^+$ cation to electrostrict, where the negatively charged electrode pulls the charge centre on the ion closer to the electrode surface.[45]

As described above, the exception to the trend appears to be CB where two capacitance humps were observed. This was also reported by Abbott for 300 mM $[N^nBu_4][BF_4]$ in DCE at a Pt electrode.[46] The humps were attributed to the adsorption/desorption of electrolyte ions and ion aggregates onto the electrode surface. Although it is not clear why this is only observed in CB.

Based upon the discussion above (Section 3.5) ion pairs are undoubtedly present in the electrolytes studied here and it might be expected that double-layer capacitance studies give some indication of this. Drogowska and Fawcett studied the EDL with a dropping mercury electrode (DME) in tetrahydrofuran, a solvent of similar polarity to those studied here.[48] Evidence of the diffuse layer at high electrolyte concentrations was observed, in the form of a capacitance minimum, caused by a decrease in ionic strength as a result of ion pair formation. This does not appear to have manifested itself in the solvents studied here, and could point to the benefits of using a DME for EDL studies where the history of the electrode surface is not an issue.

3.7. Electrochemistry of Decamethylferrocene and Cobaltocenium Hexafluorophosphate

Decamethylferrocene (DMFc) and cobaltocenium hexafluorophosphate ($CcPF_6$) were used as model redox probes to investigate the nature of electrochemistry in DCM, TFT, oDCB, pFT, CB and DCE. Metallocene electron transfer is an outer sphere, mechanistically simple electron transfer process with a low inner and outer sphere reorganisation energy. They are characterised by fast, stable electrochemistry and as such are regularly used for the characterisation of unknown solvents. For example, metallocenes have been used to understand electrochemistry in novel media such as supercritical fluids,[49] and ionic liquids.[50]

DMFc is specifically selected because of its intended use as an internal reference, this assumes that the redox potential of DMFc is independent of the solvent. The most recent IUPAC advice on internal references recommends the use of ferrocene or

bis(biphenyl)chromium.[51] But this must be considered obsolete since there is evidence of both redox couples being solvent dependent.[52–56] On the other hand, the superiority of DMFc has been demonstrated.[52,53] The methyl groups on the cyclopentadienyl (Cp) rings sterically shield the metal atom centre and the Cp rings from interactions with the solvent. The electron transfer process also has a minimal effect on the Fe-Cp bonding, with the bond lengths remaining essentially unchanged between the oxidised and reduced forms. It is wrong to assume that DMFc has a totally solvent independent redox potential. But based upon the available information, DMFc is the most suitable couple and in a practical sense minimal variation can be expected. $CcPF_6$ is then complementary to DMFc, it has a different size and is positively charged with an initial reduction step.

A mixed electrolyte of 1 mM of DMFc and 0.5 mM $CcPF_6$ were used. 1 mM $CcPF_6$ was found to be insoluble in some of the solvents and so 0.5 mM was used instead. To determine the effective concentration in solution, a potential step to a mass transport limiting potential at a microelectrode was used. The data was fitted to the Shoup-Szabo equation shown in Eqn. (3.4).

$$\frac{i}{i_{\mathrm{L}}} = 0.7854 + 0.8862\tau^{-1/2} + 0.2146e^{-0.7823\tau^{-1/2}} \tag{3.4}$$

Where $\tau = Dt/a^2$, D is the diffusion coefficient, t is time and a is the radius of the microelectrode.[57] This expression accurately describes the current response for all times. A non-linear least squares fit allows the determination of two of n, a, D and c, where n is the number of electrons transferred and c is the concentration of electroactive species, provided knowledge of at least two of the remaining variables. c was extracted from chronoamperograms recorded at microelectrodes of radii 5 µm, 12.5 µm and 25 µm. The average was then taken and used in all subsequent calculations.

Fig. 3.4 shows CVs in the studied solvents at Pt, Au and (GC) macroelectrodes. Scanning in the anodic direction from the region of zero current a redox couple at *ca.* 0 V can be observed, corresponding to the oxidation of DMFc to $DMFc^+$:

$$[(Me_5Cp)_2Fe(II)] \longrightarrow [(Me_5Cp)_2Fe(III)]^+ + e^-$$

Then, on the reverse sweep a second redox process takes place, associated with the reduction of Cc^+ to Cc:

$$[Cp_2Co(III)]^+ + e^- \longrightarrow [Cp_2Co(II)]$$

At a macrodisc electrode the effect of iR drop was significant and so the CVs were compensated *post hoc* for 95% of the solvents' R_{u} value, taken from Table 3.4. Voltammograms were recorded at the different electrode materials and the resulting redox potential is given in Table 3.5. As can be seen, the redox potentials of both couples are essentially independent of electrode material, demonstrating the expected behaviour of an outer-sphere redox couple.

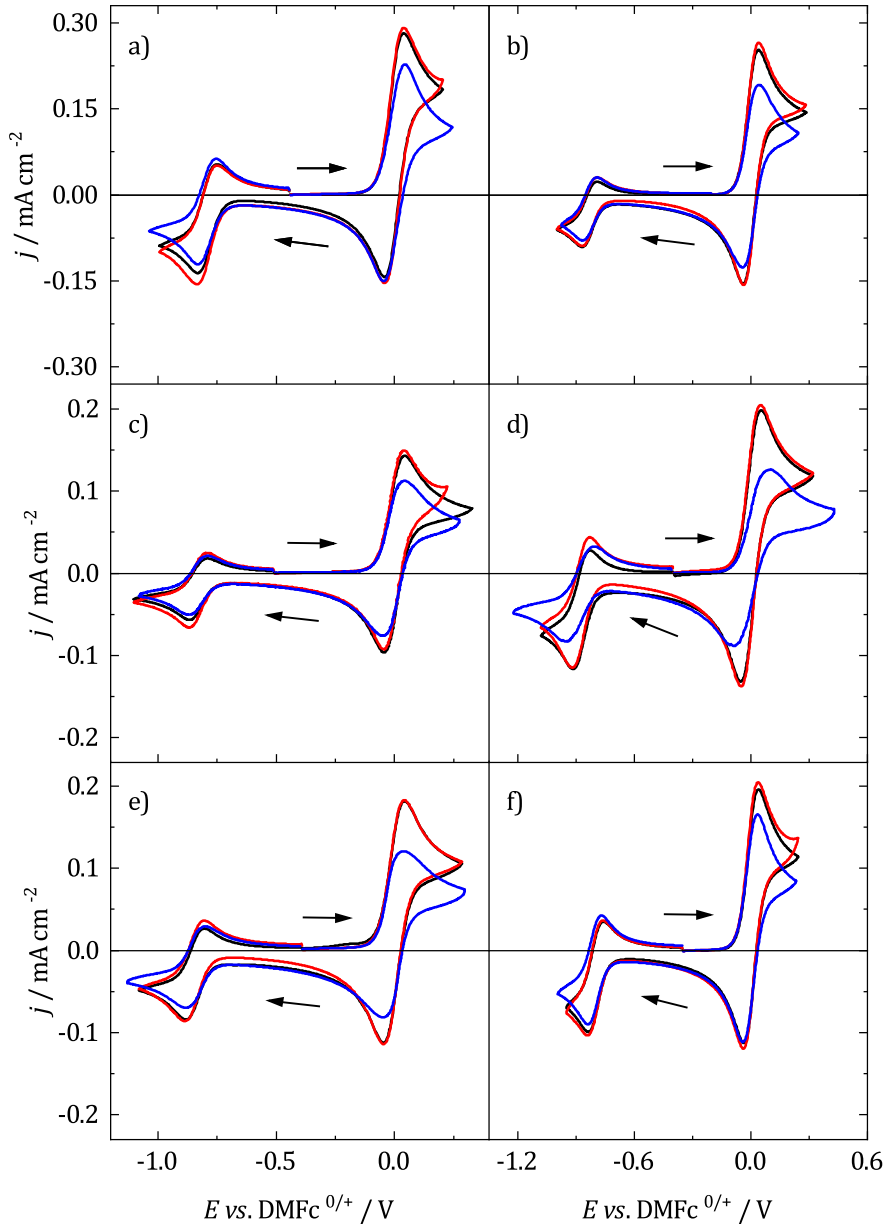

Figure 3.4: Voltammograms of 1 mM DMFc and 0.5 mM $CcPF_6$ with 100 mM a, c, f: $[N^nBu_4]Cl$ b,d, e: $[N^nBu_4][BF_4]$ at macroelectrodes of varying electrode material. Working electrode was swept from −0.4 V *vs.* DMFc at 50 mV s^{-1} in the direction indicated by the arrows. CE: Pt grid, RE: Ag/AgCl, referenced to DMFc at Pt. CVs corrected for 95 % of the solvents' R_u value. Black: r = 0.25 mm Pt, red: r = 0.25 mm Au and blue: r = 1.5 mm GC. a) DCM, b) TFT, c) oDCB, d) pFT, e) CB, f) DCE.

	$E_{1/2}$(DMFc) *vs.* DMFc(Pt) / mV		$E_{1/2}$($CcPF_6$) *vs.* $CcPF_6$ (Pt) / mV	
Solvent	Au	GC	Au	GC
DCM	0	−1	−2	−2
TFT	2	−1	−1	−1
oDCB	−2	−5	0	−1
pFT	−2	6	−4	−8
CB	−1	−5	−3	3
DCE	−1	−1	−4	−7

Table 3.5: $E_{1/2}$ values for DMFc and $CcPF_6$ obtained from macrodisc voltammograms at varying electrode materials. Referenced to $E_{1/2}$ at Pt of each redox couple.

The Randles-Sevčik equation for a planar disc electrode is given by:

$$i_p = 0.4463\,Ac\,(nF)^{\frac{3}{2}}\left(\frac{\nu D}{RT}\right)^{\frac{1}{2}} \tag{3.5}$$

Where i_p is the peak current, A is the area of the electrode and ν is the scan rate. Plots of i_p *vs.* $\nu^{\frac{1}{2}}$ are linear for a diffusion limited process. Fig. 3.5 shows Randles-Sevčik plots for DMFc and $CcPF_6$. As can be seen, both are linear with intercepts close to the origin, demonstrating that both redox couples are diffusion limited.

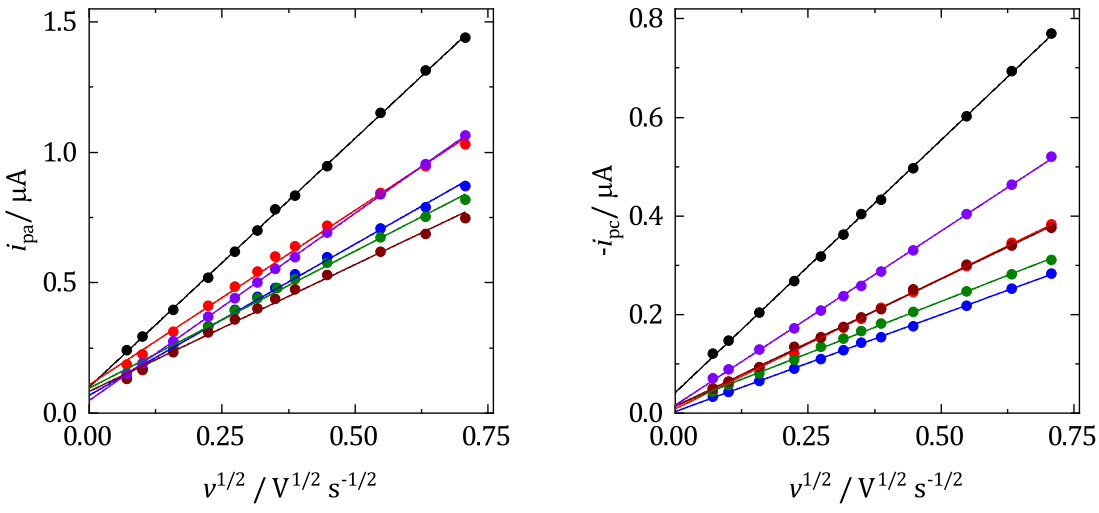

(a) DMFc (b) $CcPF_6$

Figure 3.5: Randles-Sevčik plots for a) 1 mM DMFc and b) 0.5 mM $CcPF_6$ collected at a r = 0.25 mm Pt WE for scan rates between 5-500 mV s^{-1}. Black: DCM, red: TFT, blue: oDCB, green: pFT, brown: CB, purple: DCE.

Fig. 3.6 shows voltammograms at varying sizes of microelectrode in the investigated solvents. For resistive solvents such as those studied here, microelectrodes are especially useful because their smaller sizes minimise the effect of iR drop. This then allows artefact free, quantitative analysis of voltammograms. A plateau in current is observed for both

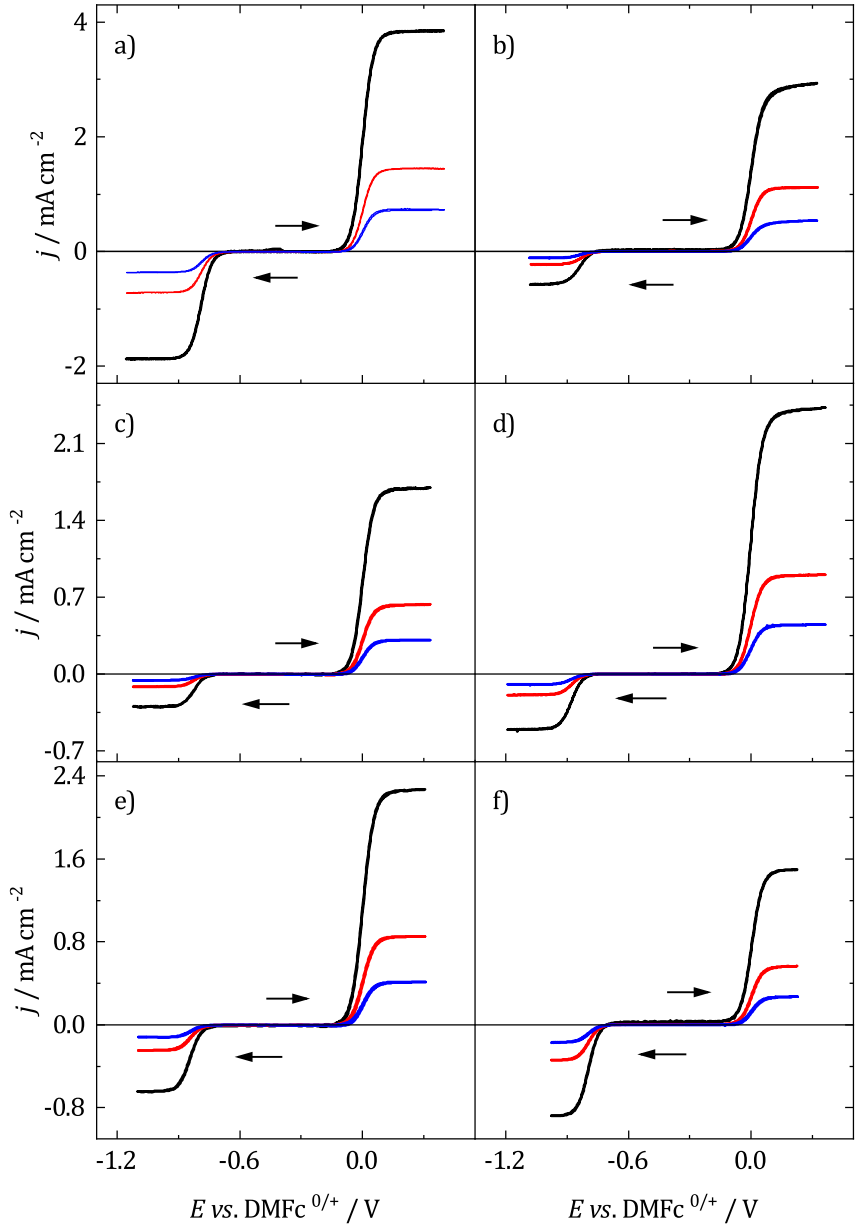

Figure 3.6: Voltammograms of 1 mM DMFc and 0.5 mM $CcPF_6$ with 100 mM a, c, f: $[N^nBu_4]Cl$, b, d, e: $[N^nBu_4][BF_4]$ at Pt microelectrodes of radius 5, 12.5 and 25 µm. Working electrode was swept from −0.4 V *vs.* DMFc at 5 mV s^{-1} in the direction indicated by the arrows. CE: Pt grid, RE: Ag/AgCl. Black: 10 µm, red: 25 µm and blue: 50 µm. a) DCM, b) TFT, c) oDCB, d) pFT, e) CB, f) DCE.

redox couples in every solvent, indicating the formation of a steady state. The limiting current varies with the solvent because of differences in the viscosity of the solvents which then affects the diffusion coefficient.

3.7.1. Thermodynamics

The thermodynamically informative half wave potential, $E_{1/2}$, of a microelectrode CV, where $E_{1/2}$ is the potential at $i_L/2$, can be extracted by use of the mass transport corrected Tafel equation for a reversible redox couple, Eqn. (3.6):

$$E = E_{1/2} + \frac{RT}{nF} \ln\left(\frac{i_L}{i} - 1\right) \tag{3.6}$$

where R is the gas constant, n is the number of electrons transferred and i_L is the limiting current. For a reversible redox couple, a plot of E *vs.* $\ln(i_L/i - 1)$ (see 3.7.2) is linear with an intercept of $E_{1/2}$. This approach assumes the diffusion coefficients of the oxidised and reduced species are equal. The possible effect of iR drop on $E_{1/2}$ was also considered. The true half-wave potential, $E_{1/2,true}$, is related to the uncorrected, apparent half-wave potential, $E_{1/2,app}$, by $E_{1/2,true} = E_{1/2,app} - 1/2 i_L R_u$ for any size of microelectrode.[58,59] For almost all electrode size and electrolyte combinations, to an accuracy of 1 mV, no correction was required. For those that were corrected, it was by no more than 1 mV; indicating the negligible influence of Ohmic drop on the recorded voltammograms. Furthermore, no relationship between electrode size and $E_{1/2}$ was observed, which would be another indicator of iR effects. Table 3.6 shows $E_{1/2}$ values for DMFc and $CcPF_6$.

$E_{1/2}$(DMFc) can be seen to be solvent dependent, this is due to the solvent dependence of the Ag/AgCl reference electrode. Since $E_{1/2}(CcPF_6)$ has been referenced against the solvent independent redox couple DMFc, all changes in its redox potential can be attributed to the effect of the solvent. The $Cc^{0/+}$ couple has previously displayed solvent dependent redox behaviour,[60–62] and inspection of Table 3.6 indicates that this is also the case in the present solvents. Based upon the above discussion and the solvents' descriptors, it is expected that specific interactions between solvent and Cc^+ would be minimal, and therefore that the solvent dependence of $E_{1/2}(CcPF_6)$ is primarily described by the polarity of the solvents. As noted previously, the Born equation is a simple model for electrostatic interactions between solute and solvent. Fig. 3.7a shows a plot of $E_{1/2}(CcPF_6)$ *vs.* $1/\epsilon_r$, which should be linear if the Born equation was valid. A weakly linear relationship is observed: $E_{1/2}(CcPF_6)$ decreases as solvent polarity does, with $R^2 = 0.65$. It would appear that ϵ_r is failing to fully describe the effects of the solvent on redox potential. Previous attempts at such a correlation have also been unsuccessful.[63] Shown in Fig. 3.7b is the relation between $E_{1/2}(CcPF_6)$ and $\pi*$, the KT solvent polarity descriptor. With an R^2 of 0.77 the correlation is improved, suggesting $\pi*$ is the superior descriptor of solvent polarity. Attempts in the literature to correlate redox potential with $\pi*$ have previously been successful.[64]

Solvent	DMFc				$CcPF_6$				
	$E_{1/2}$ *vs.* Ag/AgCl / V	$\lvert E_{3/4} - E_{1/4} \rvert$ / mV	b / mV	D / 10^{-5} cm^2 s^{-1}	$E_{1/2}$ *vs.* Ag/AgCl / V	$E_{1/2}$ *vs.* DMFc	$\lvert E_{3/4} - E_{1/4} \rvert$ / mV	b / mV	D / 10^{-5} cm^2 s^{-1}
DCM	0.438(10)	58(1)	26.6(3)	1.68(2)	−0.350(10)	−0.788(1)	56(1)	25.4(3)	1.35(1)
TFT	0.192(4)	63(2)	28.6(6)	1.18(3)	−0.637(2)	−0.830(1)	57(1)	26.0(1)	0.38(2)
oDCB	0.499(20)	59(1)	26.8(1)	0.52(1)	−0.323(20)	−0.822(1)	55(2)	24.8(8)	0.24(1)
pFT	0.198(7)	62(1)	28.9(8)	1.10(11)	−0.678(7)	−0.875(2)	57(1)	26.2(1)	0.31(3)
CB	0.145(1)	62(2)	28.2(8)	0.87(3)	−0.692(1)	−0.840(4)	58(1)	26.3(9)	0.32(2)
DCE	0.376(1)	57(1)	26.1(2)	0.88(3)	−0.418(1)	−0.795(2)	55(1)	25.0(1)	0.61(3)

Table 3.6: Thermodynamic, kinetic and mass transport parameters of 1 mM DMFc and 0.5 mM $CcPF_6$ in various solvents at 25 °C using microelectrodes. Obtained with 100 mM $[N^nBu_4]Cl$ in DCM, oDCB and DCE and 100 mM $[N^nBu_4][BF_4]$ in TFT, pFT and CB. Values are the average of three repeats with the error the standard deviation.

Interestingly, the direction of the correlation is opposite to what would be expected. A solvent with a higher dielectric constant will solvate a species more strongly, lowering its redox potential. Although for the $Cc^{+/0}$ redox couple, the magnitude of this effect would be somewhat compensated because the charged form is also more strongly solvated. Which would have the effect of making the redox couple easier to reduce. Here, the redox potential is lowest in the least polar solvents instead. One possible explanation for this is ion pairing. If the Cc^+ was paired with Cl^- or $[BF_4]^-$ then this could stabilise the cation and decrease its redox potential. In the less polar solvents the degree of ion pairing is greater, and therefore so is the stabilisation. The presence of ion pairing effects on voltammetry in DCM has been reported for ferrocene (Fc) and DMFc.[65,66] Hupp estimated such a shift for an electrolyte of $FcPF_6$ with 100 mM $[N^nBu_4][PF_6]$ in DCM to be −229 mV.[55] Indicating that the effect can potentially be significant.

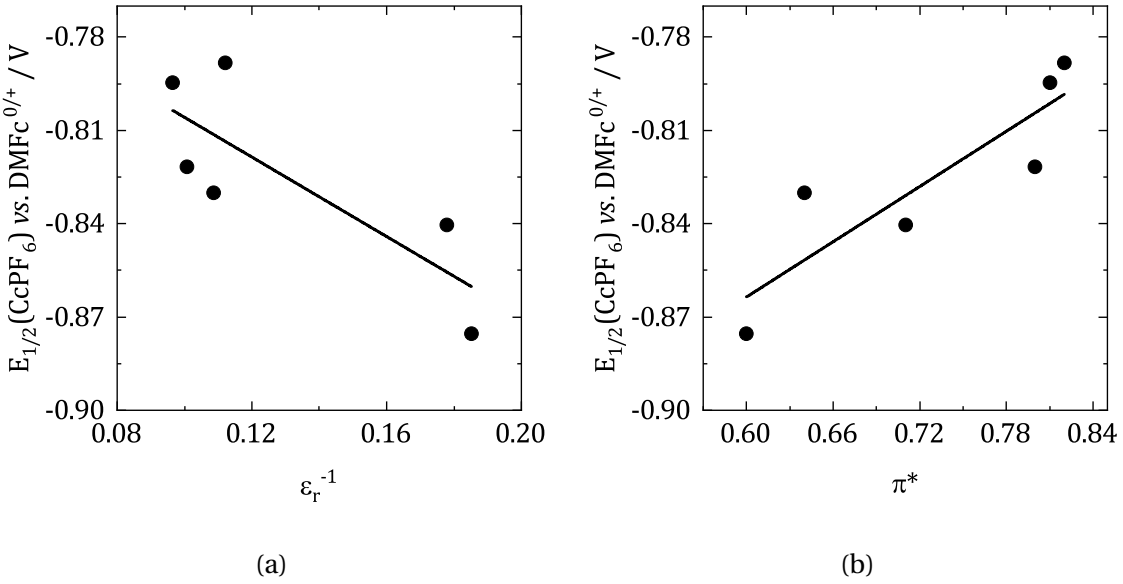

(a) (b)

Figure 3.7: Dependence of $E_{1/2}(CcPF_6)$ on the solvent polarity descriptors ϵ_r and $\pi*$. Obtained from microelectrode voltammograms of 0.5 mM $CcPF_6$ with 100 mM $[N^nBu_4]Cl$ in DCM, oDCB and DCE, 100 mM $[N^nBu_4][BF_4]$ in TFT, pFT and CB.

3.7.2. Kinetics

Eqn. (3.6) can be used to test the electrochemical reversibility of a redox couple. For a reversible couple, a plot of E *vs.* $\ln(i_L/i-1)$ is linear with a slope, b, of RT/nF. Slopes greater than RT/nF indicate a decreasing degree of reversibility. For a one electron process at 25 °C b = 25.7 mV. Fig. 3.8 shows such plots for DMFc and $CcPF_6$ in the WCS. Values of b are given in Table 3.6. As can be seen, in all solvents both DMFc and $CcPF_6$ are reversible or near reversible. The original derivation of Eqn. (3.6) assumed reversibility, a uniformly accessible working electrode and $D_R = D_O$.[67] A planar microdisc electrode is not uniformly accessible, and it has not been verified that the diffusion coefficients of the oxidised and reduced species are equal. Streeter and Compton simulated the case of a

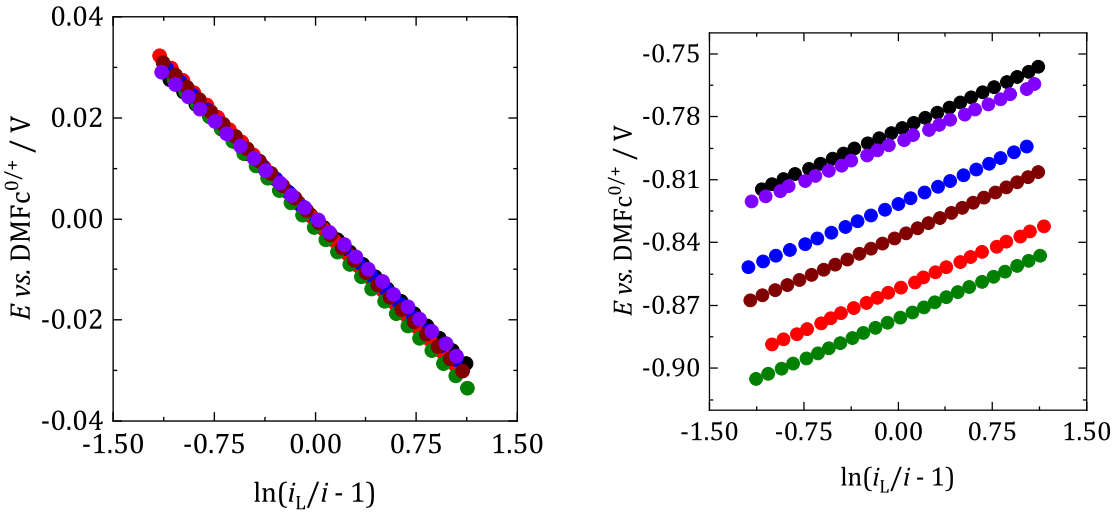

(a) DMFc

(b) $CcPF_6$

Figure 3.8: Representative mass transport correct Tafel plots for 1 mM DMFc and 0.5 mM $CcPF_6$ at a $r = 12.5\,\mu m$ microelectrode in various solvents with 100 mM $[N^nBu_4]Cl$ in DCM, oDCB and DCE, 100 mM $[N^nBu_4][BF_4]$ in TFT, pFT and CB, and 50 mM $[N^nBu_4]Cl$ in lR32. Black: DCM, red: TFT, blue: oDCB, green: pFT, brown: CB, purple: DCE.

Nernstian couple, a non-uniformly accessible electrode and equal diffusion coefficients of the oxidised and reduced couple, it was found that Eqn. (3.6) remained valid.[67]

Another indicator of reversibility is the difference in quartile potentials $E_{1/4}$ and $E_{3/4}$, where $E_{1/4}$ and $E_{3/4}$ are the potentials at $i_L/4$ and $3i_L/4$ respectively. For a steady state voltammogram $|E_{3/4} - E_{1/4}|$ is given by:

$$|E_{3/4} - E_{1/4}| = \frac{2.196RT}{nF} \tag{3.7}$$

which corresponds to 56 mV at 25 °C. The values for DMFc and $CcPF_6$ can be found in Table 3.6. These also demonstrate the reversibility of DMFc and $CcPF_6$ in the studied solvents.

3.7.3. Mass Transport

The mass transport limiting current at a microelectrode, i_L, is given by:

$$i_L = 4nFDca \tag{3.8}$$

where D is the diffusion coefficient and a is the radius of microelectrode. Therefore, with use of multiple microelectrodes of differing a, D can be obtained from the slope of a plot of i_L *vs.* a. It is important to determine precise values for the effective (not measured) concentration of electroactive species in solution and the radius of the electrode also. Errors in these can create inaccuracies in calculated value of D. The effective concentration

of electroactive species in solution was determined using a potential step at a microelectrode and the Shoup-Szabo equation (see Section 3.7). The calculated concentration was averaged over all three electrode sizes and the resulting value was used as c to calculate D. The effective radii of the microelectrodes were measured using SEM. Using multiple sizes of microelectrode is additionally useful because it helps to smooth out any errors in i_L, c or a.

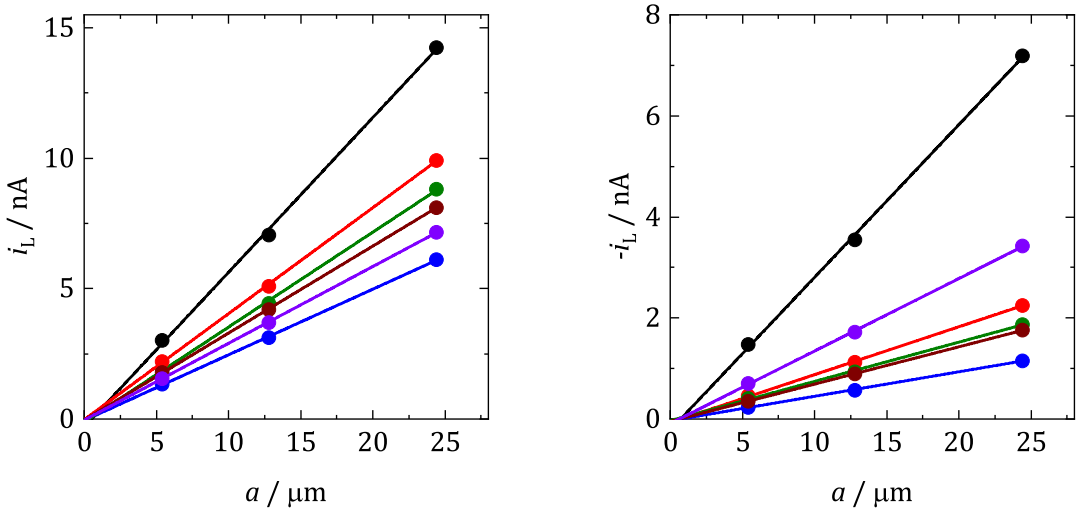

(a) DMFC (b) $CcPF_6$

Figure 3.9: Representative limiting currents of 1 mM DMFc and 0.5 mM $CcPF_6$ with 100 mM $[N^nBu_4]Cl$ or $[N^nBu_4][BF_4]$ at Pt microelectrodes of radii 5 µm, 12.5 µm and 25 µm at 25 °C. Black: DCM, red: TFT, blue: oDCB, green: pFT, brown: CB, purple: DCE.

Fig. 3.9 shows plots of i_L of DMFc and $CcPF_6$ at electrodes of radii 5 µm, 12.5 µm and 25 µm. Calculated diffusion coefficients are shown in Table 3.6. D was also calculated using a potential step at a microelectrode and Eqn. (3.4). The results corroborate those from the voltammograms and are given in the Appendix. The values in DCM show agreement with those given in the literature. Weaver obtained a value of 1.30×10^{-5} cm^2 s^{-1} for DMFc using DC polarography at 23 °C.[68] Matsumoto and Swaddle reported a mean value of 1.07×10^{-5} cm^2 s^{-1} using peak currents of CVs at 25 °C.[69] Branch obtained a value for DMFc of 1.48×10^{-5} cm^2 s^{-1} from a microelectrode CV and a mean value of 7.95×10^{-6} cm^2 s^{-1} from macrodisc CV's at 25 °C.[49] Ohrenberg and Geiger reported D to be 1.2×10^{-5} cm^2 s^{-1} in TFT from a potential step at a macroelectrode at 23 °C.[70] Peljo *et al.* gave a value of 4.51×10^{-6} cm^2 s^{-1} for DMFc in oDCB using microelectrode CVs at 20 °C.[71] Tsierkezos reported a value of 1.35×10^{-5} cm^2 s^{-1} for the neutral Cc species in DCM, similar to the value obtained here.[72] There appears to be no record of measurements in other solvents.

An accessible approach to interpreting diffusion coefficients is with hydrodynamic theory and the Stokes-Einstein (SE) equation.[73]

$$D = \frac{k_B T}{f_{tot}} \tag{3.9}$$

Where k_B is Boltzmann's constant, The product $k_B T$ represents the thermal driving force for particle motion. f_{tot} is then the friction factor, describing the total force impeding movement of the particle. f_{tot} is given by

$$f_{tot} = 6\pi\eta r_S \tag{3.10}$$

where η is the viscosity of the solvent and r_S the Stokes radius, the radius of the diffusing species. Typically, D would be plotted against $1/\eta$ in a Stokes-Einstein plot with the slope then used to estimate r_S. However what is poorly recognised in the literature, and particularly in electrochemistry, is that the SE equation in the form presented above carries several assumptions with it. If these are not properly accounted for it can potentially lead to errors in the interpretation of diffusion coefficients. The SE has proven to be remarkably effective for large particles such as colloids, but as the size of the particle decreases its flaws start to become apparent. When the SE equation is applied to small molecules, of a similar size to solvent molecules, which is typical in electrochemistry then theory and experiment begin to significantly diverge.[74]

The SE equation firstly assumes infinite dilution of the diffusing particle *i.e.* particle-particle interactions are negligible. It is also assumed that the solvent is a continuum described only by its viscosity. Finally, the diffusing particle is assumed to be a sphere. Clearly, the solvent is not a continuum, but composed of discrete molecules that can interact specifically with the particle. Rarely are molecules spheres either, but globular with a variable size and shape and it is these assumptions that cause the SE equation to fail for small molecules.

This has resulted in the development of corrections to the SE equation to improve its description of small particles. Infinite dilution can readily be approximated by use of low concentrations of analyte. Molecularity of the solvent can be accounted for by replacing the number 6 in Eqn. (3.10) with a variable c.[75] Where $4 \leqslant c \leqslant 6$ and is dependent on the relative sizes of the solvent and solute. The upper limit when $c = 6$ is found when the particle is significantly larger than the solvent and is described as 'slipping' motion. When $c = 4$, the lower bound, the movement is described as 'sticking' and is observed if solute and solvent are of similar size. In reality, and particularly for ions, c is rarely 4 or 6 but some value in between. With knowledge of the radius of the solvent molecule and of the diffusing species, it is possible to obtain an exact estimate of c using expressions developed by Gierer and Wirtz,[75] and by Chen and Chen.[75] Non-sphericity of the diffusing particle can be accounted for using a correction factor. Perrin developed correction fac-

tors for ellipsoids of revolution, a more realistic shape of a molecule.[76] f_{tot} then becomes

$$f_{tot} = f_{HS} f_P \tag{3.11}$$

Where f_{HS} is the hard sphere friction factor equal to $c\pi\eta r_S$, and f_P is the friction factor associated with the Perrin correction.

Estimating electrolyte viscosity

The first step to constructing a Stokes-Einstein plot for the interpretation of the diffusion coefficients of DMFc and $CcPF_6$ is to determine the viscosity of the electrolyte solution. Addition of an electrolyte can increase the viscosity of solvent in a manner described by the empirical Jones-Dole equation.[77]

$$\eta_{rel} = \frac{\eta}{\eta_0} = 1 + Ac^{1/2} + Bc \tag{3.12}$$

Where η_{rel} is the relative viscosity, the ratio of the solution viscosity, η, to the viscosity of the pure solvent, η_0. c is the concentration of the solute and A and B are constants which reflect the influence of the salt on the electrolyte viscosity. A describes the effect of ion-ion interactions and B ion-solvent. For a 1:1 electrolyte, A can be estimated with the Falkenhagen-Vernon equation.[78]

$$A = \frac{0.2577\Lambda_m^0}{\eta_0(\epsilon_r T)^{1/2}\lambda_+^0\lambda_-^0}\left[1 - 0.6863\left(\frac{\lambda_+^0 - \lambda_-^0}{\Lambda_m^0}\right)^2\right] \tag{3.13}$$

Where Λ_m^0 is the limiting molar conductivity of the electrolyte, and λ_+^0 and λ_-^0 the limiting ionic conductivities of the individual ions. For the electrolytes used in the present work, data was only available for $[N^nBu_4]Cl$ in DCM and $[N^nBu_4][BF_4]$ in TFT.[29,79] The literature values and resulting A are summarised in Table 3.7.

Solvent	Electrolyte	Λ_m^0 / S cm^2 mol^{-1}	λ_+^0 / S cm^2 mol^{-1}	λ_-^0 / S cm^2 mol^{-1}	A / dm$^{3/2}$ mol$^{-1/2}$
DCM[a]	$[N^nBu_4]Cl$	104	38	64	0.0050
TFT[b]	$[N^nBu_4][BF_4]$	83	36	47	0.0060

Table 3.7: Predicted values of the Jones-Dole A coefficient using Eqn. (3.13) and relevant literature values. [a]: Ref. [79]. [b]: Ref. [29].

It is common for values of A to be small and have a small contribution to η_{rel}.[77] Experimental measurements of different electrolytes by Svorstol *et al.* in DCM found A to be negligible also.[80] This appears to be the case here too, and A can be ignored.

B cannot be predicted and instead it must be determined experimentally.[77] It has been established that B coefficients are additive and so can be divided into individual ionic contributions, *i.e.* $B = \Sigma z_i B_i$.[77] Svorstol *et al.* determined $B(N^nBu_4^+)$ and $B(Cl^-)$ to be

0.69 and 0.33 $dm^3\ mol^{-1}$ respectively in DCM at 25 °C. Giving η_{rel}(DCM) as 1.1 for 100 mM $[N^nBu_4]Cl$

For similarly unstructured solvents, B is approximately the same. $B(N^nBu_4^+)$ in acetonitrile is reported to be $0.6-0.7\,dm^3\ mol^{-1}$, $0.63\,dm^3\ mol^{-1}$ in nitrobenzene, and $B(Cl^-)$ was found to be $0.37\,dm^3\ mol^{-1}$ in acetonitrile also.[77] No data is available for the $[BF_4]^-$ anion. Therefore, it is assumed that $\eta_{rel} = 1.1$ for all solvents. Ion pairs can also contribute to electrolyte viscosity, and it is possible to incorporate their effect into the Jones-Dole equation.[77] However, studies of B coefficients in DCM concluded that the influence of ion pairs on viscosity was indistinguishable from those of free ions or that they made no contribution to η.[80]

Accounting for non-sphericity

As described previously, Perrin developed correction factors for oblate and prolate spheroids. Determination of f_P for DMFc and Cc^+ requires knowledge of which type of spheroid each is, and also values for the lengths of axes of the molecule. Ellipsoids of revolution can be described by two semi-axes: a and b. Where a is the axial semiaxis and b is the equatorial semiaxis. Characterisation was achieved by measurement of the crystal structures for DMFc and Cc^+ using the .cif files of DMFc (DMFERR08) Cc^+ (RAQVEK07) obtained from the Cambridge Structural Database. Measurements were performed with the software package CrystalMaker v. 9.0.3 (CrystalMaker Software Ltd., UK) using the 'distance tool'. The distance between the centre of the spheroid, taken as the the centre of the metal atom, to the perimeter was measured for both semi-axes. Representative screen captures of their measurement for DMFc are shown in Fig. 3.10. Dimensions can be found in Table 3.8.

	a / nm	b / nm	b/a	f_P
DMFc	0.286	0.336	1.175	1.002
Cc^+	0.186	0.228	1.226	1.004

Table 3.8: Measured solid state dimensions and corresponding Perrin friction factor of DMFc and Cc^+.

Since $b > a$ for both DMFc and Cc^+ they can be categorised as oblate spheroids. The Perrin correction for an oblate spheroid is given by Eqn. (3.14).[81] The calculated values of f_P can also be found in Table 3.8.

$$f_P = \frac{\left[\left(\frac{b}{a}\right)^2 - 1\right]^{1/2}}{\left(\frac{b}{a}\right)^{2/3} \arctan\left[\left(\frac{b}{a}\right)^2 - 1\right]^{1/2}} \tag{3.14}$$

As can be seen, f_P is close to 1 for both DMFc and Cc^+ and they can be considered spherical.

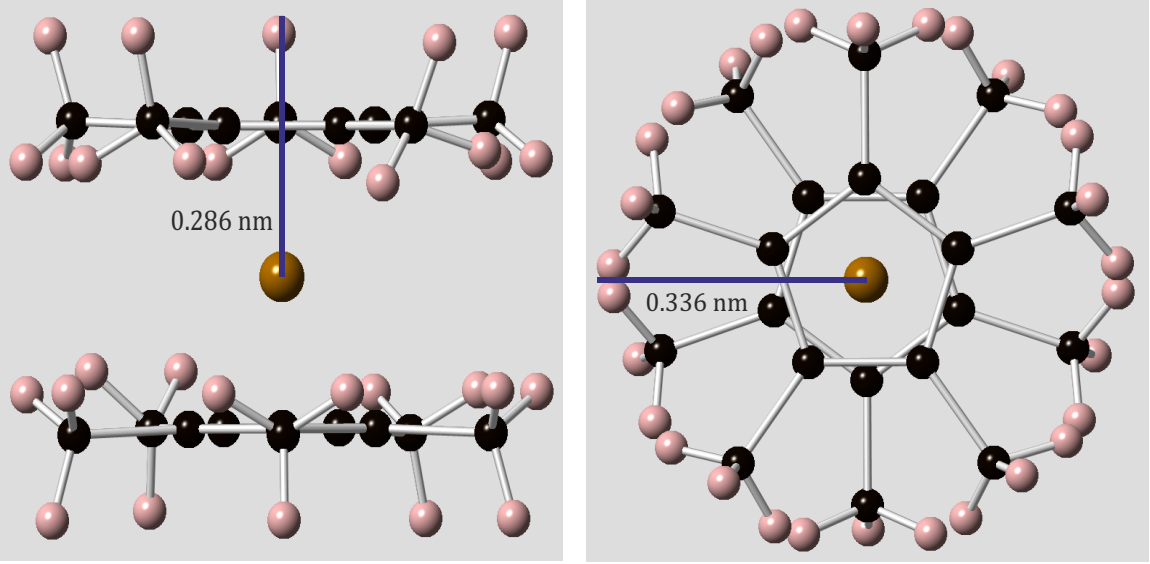

(a) Axial view (b) Equatorial view

Figure 3.10: Screen captures of the CrystalMaker software demonstrating the measurement of the semi-axes of an ellipsoid of revolution for DMFc. Distance bar and label added manually.

Another pertinent question when interpreting diffusion coefficients is the significance of the Stokes radius, and how it relates to other measures of molecular size. This is particularly important when attempting to predict diffusion coefficients. There is a multitude of different approaches to estimating the size of a molecule and it is not clear which best describes the size of the molecule in solution. Furthermore, molecules are not smooth spheres, but contain bumps and inlets which add texture to the surface of the molecule resulting in spatial variation of a measured radius. Molecules can possess cavities which solvent molecules cannot access, nor can solvent molecules approach the solute so closely that they are in contact with each other because of repulsion forces.[74] It is not clear to what extent these void spaces contribute to a particular measurement of molecule size.[82] This can make the choice of which measure of molecular size to use when predicting diffusion coefficients a confusing one, and there is no definite answer. The upper and lower bounds of r_S are known however, the lower limit is said to be the van der Waals radius, r_{vdW}, and the upper limit the crystallographic radius, r_{crs}.[81,82] The van der Waals radius is taken from computational calculations of the van der Waals volume (assuming sphericity), V_{vdW}, which itself is taken from the sum of the volumes of individual atoms, taking into account bonding.[82] V_{vdW} describes only the absolute volume occupied by the molecule, so does not include information on depressions in the molecules' surface which would be inaccessible to a solvent, or that the solvent molecule cannot directly contact the particle. r_{crs} is obtained from X-ray crystal structure measurements, again assuming a sphere, using the crystallographic volume, V_{crs}, provided by refining the diffraction pattern of the crystal. r_{crs} represents the distance between molecules in the solid state so contains information on the size of the species, plus void spaces caused by

repulsive interactions.

As described above, $4 \leqslant c \leqslant 6$ and $r_{vdW} \leqslant r_S \leqslant r_{crs}$. Therefore, the minimum possible diffusion coefficient, D_{min}, would be when $c = 6$ and $r = r_{crs}$, and the maximum diffusion coefficient, D_{max}, when $c = 4$ and $r = r_{vdW}$. The experimental diffusion coefficient, D_{exp}, might then be expected to fall between D_{min} and D_{max}: $D_{min} \leqslant D_{exp} \leqslant D_{max}$. The diffusion behaviour can then be analysed by comparison of D_{exp} with D_{min} and D_{max}. Analysis using this approach avoids calculating a definite value of c or r_S and so removes any uncertainties associated with values of molecular size.

V_{vdW}(DMFc) was calculated by Tran *et al.* and this was used to determine r_{vdW}, values are given in Table 3.9.[83] $V_{vdW}(Cc^+)$ was not available, but V_{vdW} has been shown to correlate well with the readily accessible intrinsic McGowan volume, V_{McG}.[11] Shown in the below relationship

$$V_{McG}(\mathrm{cm^3\,mol^{-1}}) = 1.47 V_{vdW}(\mathrm{cm^3\,mol^{-1}}) - 4.96 \tag{3.15}$$

$V_{McG}(Cc^+)$ was taken as $120.2\,\mathrm{cm^3\,mol^{-1}}$ and the results are given in Table 3.9. The crystallographic radius is taken from the volume of the unit cell, V_{cell} from crystal structure information. The crystallographic volume, V_{crs}, is obtained from V_{cell} since $V_{crs} = V_{cell}/Z$ where Z is the number of molecules in the unit cell. Values for DMFc are give in Table 3.9. For a salt such as $CcPF_6$ the situation is made complicated because the cell volume contains contributions from both the anion and the cation. However, according to Glasser and Jenkins, V_{crs} is an additive sum of the constituent ions,[84,85] such that

$$V_{crs}\left(M_pX_q\right) = pV_{crs}\left(M^{p+}\right) + qV_{crs}\left(X^{q-}\right) \tag{3.16}$$

Therefore

$$V_{crs}\left(Cc^+\right) = V_{crs}\left(CcPF_6\right) - V_{crs}\left([PF_6]^-\right) \tag{3.17}$$

Glasser and Jenkins also provided a database of optimised volumes for common ions.[84] $V_{crs}\left([PF_6]^-\right)$ was not available, but instead was obtained, using the same additivity principle, from KPF_6 (ICSD entry 56255). Giving $V_{crs}\left([PF_6]^-\right)$ as $78\,\text{Å}^3$. It is now possible to simulate D_{min} and D_{max} for DMFc and $CcPF_6$, with values given in the appendix.

	V_{vdW} / $\mathrm{cm^3\,mol^{-1}}$	r_{vdW} / nm	V_{crs} / Å^3	r_{crs} / nm
DMFc	187[a]	0.42	453[c]	0.48
Cc^+	85[b]	0.32	219[d]	0.37

Table 3.9: Molecular volumes and radii of DMFc and Cc^+. [a]: from Ref. [83], [b]: from V_{McG} using the correlation of Marcus in Ref. [11], [c] from CSD entry DMFERR, [d]: from CSD entry RAQVEK01.

Fig. 3.11a shows a Stokes-Einstein plot for DMFc. As can be seen, the plot is linear ($R^2 > 0.99$) with a small but finite intercept, suggesting that r_S is constant. Fig. 3.11a also

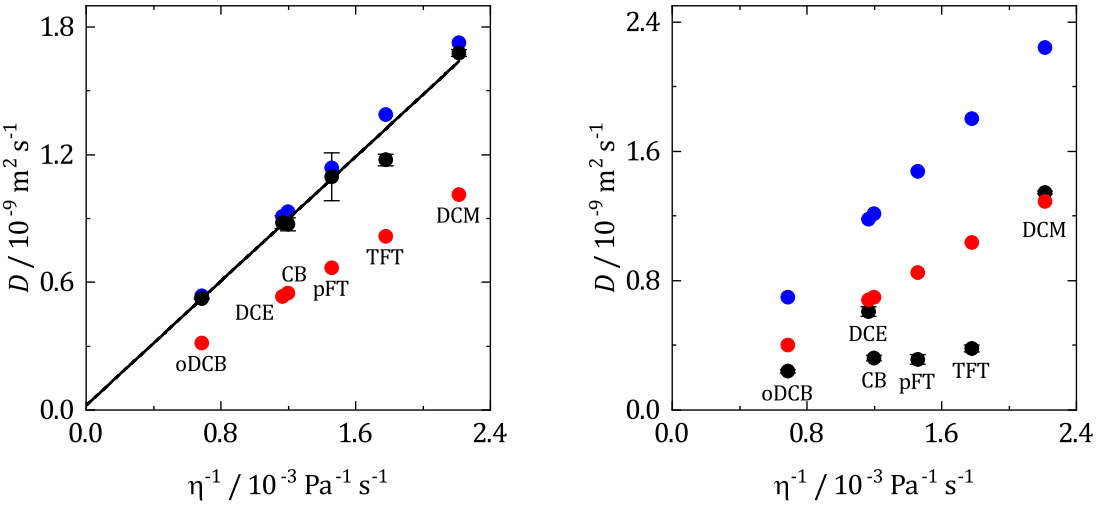

(a) DMFC (b) $CcPF_6$

Figure 3.11: Stokes-Einstein plot of experimental diffusion coefficients of DMFc and $CcPF_6$ in black with line of best fit. Along with simulated D_{min} in red and D_{max} in blue at 25 °C. Values are the average of three repeats and the error bars the standard deviation.

shows plots of D_{min} and D_{max}. Clearly D_{exp}(DMFc) agrees closely with D_{max}, indicating that the SE equation is obeyed in the studied solvents, and also that $c \approx 4$ and $r_S \approx r_{vdW}$. This can readily be rationalised since c typically approaches 4 for molecules of a similar size to the solvent.[81] Additionally, r_S tends towards r_{vdW} for small, compact molecules such as DMFc.[81] This also emphasises the importance of considering the modifications to the SE equation when analysing diffusion coefficients in electrochemistry. If r_S was calculated from the slope using c as 6, as is common, then this would give a misleading value for the Stokes radius of DMFc.

To prove that the approach outlined above is a useful method of analysis rather than fortuitous agreement for the solvents studied here; diffusion coefficients of DMFc in different solvents were compiled from the literature and plotted along with D_{min} and D_{max}, in Fig. 3.12. The values are tabulated in the Appendix. As can be seen, excepting a few outliers, all known values for the diffusion coefficient of DMFc lie within D_{min} and D_{max}. The three data points with the largest discrepancy, one for THF and two from DCM, are all from the same source, Ref. [86], suggesting there were systematic issues with the method for calculating D.

It is also interesting to note that where there are multiple values for the same solvent, large variations are observed in the reported value. This might point to previously unrecognised errors arising from the method of acquisition or the supporting electrolyte. It also reiterates the importance of accounting for the electrode size and concentration.

Turning to $CcPF_6$, a SE plot can be seen in Fig. 3.11b. Unlike DMFc it is not linear, indicating that the SE equation is not obeyed and f_{tot} is varying with the solvent. Unlike DMFc, $D_{exp}(Cc^+)$ is close to or less than D_{min}, the minimum expected diffusion co-

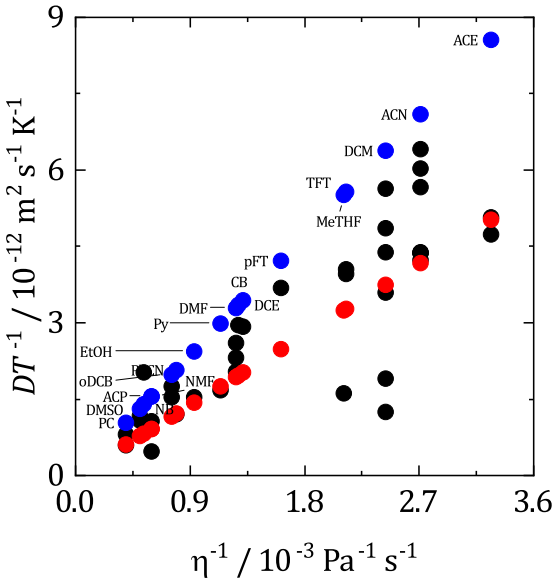

Figure 3.12: Stokes-Einstein plot of experimental diffusion coefficients of DMFc, normalised by temperature, compiled from the literature, along with simulated D_{min} and D_{max}. Black: D_{exp}, red: D_{min}, blue: D_{max}.

efficient. A dramatic increase in viscosity caused by electrolyte addition is unreasonable, meaning it would appear that r_S is changing. One plausible explanation for this is that Cc^+ is ion paired with Cl^- or $[BF_4]^-$ creating a larger diffusing particle. This would be reasonable when considering the low polarity of the solvents where the degree of ion pairing is expected to be high. Evidence of metallocene ion pairing,[65,66] has been reported in DCM and other solvents of a similar polarity. When studying the electrochemistry of $DMFc^+$ in DCM; Goldfarb and Corti reported a lower diffusion coefficient for the charged than the neutral species and, based upon the calculated Stokes radius, concluded that solvent separated ion pairs were forming.[66] Although modifications of the SE equation were not considered so the obtained radii are likely to be inaccurate. The formation of triple ions is also likely in the studied solvents. Fuoss provided a rule of thumb for the maximum concentration, c_{max}, at which only ion pairs are expected for a symmetrical electrolyte, and above which triple ions could be expected to be observed: $c_{max} = 1.2 \times 10^{-14} (\epsilon_r T)^3$.[34] For DCE, the solvent with the highest dielectric constant, at 298 K, c_{max} is 0.4 mM. Indicating that triple ions of Cc^+ are likely in the solvents studied here. This also means that the measured diffusion coefficients are an average of Cc^+ in its different forms.

The fraction of ions that are paired, β_{IP}, with Cc^+ in a solvent can be estimated with Bjerrum's equation.[87]

$$\beta_{IP} = \frac{4\pi N_A c}{1000} \left(\frac{|z_1 z_2| e^2}{4\pi\epsilon_0 \epsilon_r k_B T} \right)^3 Q(b) \tag{3.18}$$

Where $Q(b)$ is an integral of b, solutions of which are given in the literature,[87] and b is:

$$b = \frac{|z_1 z_2| e^2}{4\pi\epsilon_0\epsilon_r k_B T a} \tag{3.19}$$

where a is the distance of closest approach of the two interacting ions. Assuming 0.5 mM Cc^+ is paired with Cl^- in DCM, oDCB and DCE, and with $[BF_4]^-$ in TFT, pFT and CB at 25 °C gives β_{IP} as 1.3, 0.4, 0.3, 30.2, 42.0 and 0.3% for DCM, TFT, oDCB, pFT, CB and DCE respectively. These values must be considered a lower bound only. The equation presumes the isodielectric rule, which as has been established is not valid in the studied solvents. Nevertheless, it is apparent that a reasonable fraction of Cc^+ ions are paired in the studied solvents.

3.8. Electrochemistry of Decamethylferrocenium Hexafluorophosphate

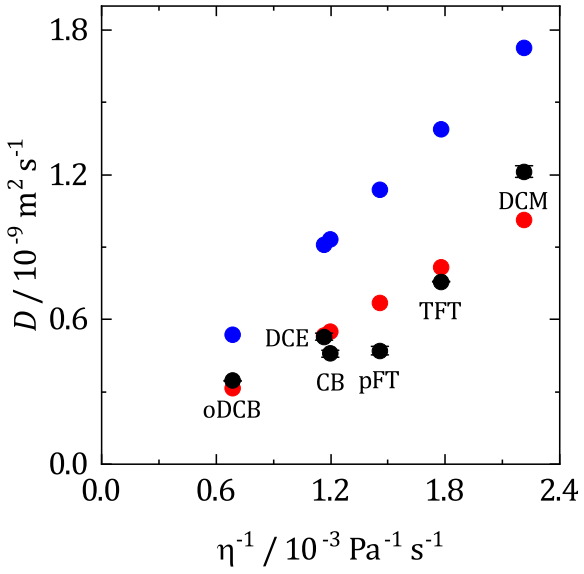

Figure 3.13: Stokes-Einstein plot of experimental diffusion coefficients of $DMFcPF_6$, along with simulated D_{min} and D_{max} of DMFc at 25 °C. Black: D_{exp}, red: D_{min}, blue: D_{max}.

To investigate the effect of ion pairing on diffusion coefficients further, the electrochemistry of decamethylferrocenium hexafluorophosphate was studied. The structure of DMFc does not change significantly upon oxidation to $DMFc^+$ except from gaining a positive charge. Therefore, any changes in the measured diffusion coefficient can be attributed to the presence of ion pairing. $DMFcPF_6$ was characterised with the same method as above and the measured diffusion coefficients can be found in Table 3.10. Goldfarb and Corti also measured the diffusion coefficient of $DMFc^+$ in DCM,[66] reporting a value of 1.07×10^{-5} cm^2 s^{-1}, similar to that measured here. Also shown in Table 3.10 is

the ratio $D(\mathrm{DMFcPF_6})/D(\mathrm{DMFc})$. As can be seen, the diffusion coefficient of the charged $\mathrm{DMFc^+}$ is less than the reduced, neutral form in all solvents, indicating the influence of ion pairing on the $\mathrm{DMFc}^{0/+}$ redox couple. Fig. 3.13 shows a Stokes-Einstein plot of D_{exp} , along with the simulated values of D_{min} and D_{max} for DMFc. $D_{\mathrm{exp}}(\mathrm{DMFcPF_6})$ now lies close to, or below, $D_{\mathrm{min}}(\mathrm{DMFc})$; indicating an increase in c and r_{S}.

Solvent	D / 10^{-5} cm^2 s^{-1}	$D_{\mathrm{O}}/D_{\mathrm{R}}$
DCM	1.21(3)	0.72
TFT	7.57(1)	0.64
oDCB	3.46(1)	0.66
pFT	4.71 (2)	0.43
CB	4.59(1)	0.53
DCE	5.23(1)	0.60

Table 3.10: Diffusion coefficients of [DMFc][$\mathrm{PF_6}$] calculated using microelectrodes at 25 °C with 100 mM [$\mathrm{N^nBu_4}$][$\mathrm{PF_6}$] in DCM and DCE and 100 mM [$\mathrm{N^nBu_4}$][$\mathrm{BF_4}$] in TFT, oDCB, pFT and CB. Values are the average of three repeats with the error the standard deviation.

3.9. Conclusions

This Chapter aimed to further the understanding of electrochemistry in weakly coordinating solvents and to identify alternative solvents to dichloromethane that might be more useful for electrodeposition. To this end, Kamlet and Taft's $\pi*$, α and β parameters were employed to identify other weakly coordinating solvents similar to DCM. A suitable solvent would be polar, aprotic and weakly coordinating, corresponding to a high value for $\pi*$ and low values of α and β. Inspection of the solvent descriptors also revealed that the solvents commonly used in electrochemistry would not be suitable for application in the present work because they were protic and/or coordinating. Five potential solvents were identified: trifluorotoluene, o-dichlorobenzene, p-fluorotoluene, chlorobenzene and 1,2-dichloroethane. The added advantage of the above solvents was that they all possessed a higher boiling point than DCM, creating the possibility of electrodeposition at elevated temperatures.

The five solvents, along with DCM as a reference, were subjected to a thorough electrochemical characterisation. This consisted of potential window measurements where it was found that the cathodic limit of the candidate solvents were comparable to DCM, and sufficiently wide enough for electrodeposition. The exception to this rule was DCE, which had a shorter negative limit, attributed to the decomposition of the solvent, rather than the supporting electrolyte as for the other solvents. The conductivity of 100 mM [$\mathrm{N^nBu_4}$]Cl and [$\mathrm{N^nBu_4}$][$\mathrm{BF_4}$] was also measured. [$\mathrm{N^nBu_4}$]Cl was found to be insoluble in TFT, pFT and CB. The conductivity of [$\mathrm{N^nBu_4}$][$\mathrm{BF_4}$] was found to be greater than [$\mathrm{N^nBu_4}$]Cl, as expected. The dielectric constant also proved to be a poor predictor of conductivity because

multiple solvents with similar dielectric constants displayed widely different levels of ion pairing. It was suggested that this was because a degree of structure was present in the aromatic solvents which was preferential to ion solvation. The structure of the double-layer structure was studied with capacitance measurements, all solvents showed a similar relationship with potential which was well described by a Helmholtz model. Finally, the electrochemistry of the model redox couples decamethylferrocene and cobaltocenium hexafluorophosphate was investigated. Both redox couples behaved reversibly, in agreement with results in other solvents. The importance of incorporating the modifications of the Stokes-Einstein equation was also emphasised and this was then used to interpret the diffusion coefficients of DMFc and $CcPF_6$. DMFc obeyed the SE equation but $CcPF_6$ did not, this was attributed to the effect of ion pairing.

It was previously predicted that the solvents would behave similarly, except for those properties determined by polarity and this appears partially true. Despite the demonstration of the advantages of using the KT descriptors to choose a solvent, it also became clear that they cannot account for all of the behaviours reported here. Increasing the number of descriptors considered could be a solution but this would greatly increase the complexity of the selection process. It is also unlikely that all necessary descriptors can be identified *a priori*. The most profitable approach would seem to be to choose 2-4 key descriptors and use those to identify the candidate solvents for investigation, and then based upon experimental evidence, choose the optimum solvent(s). This would most likely be more resource intensive but it does allow for the possibility of unforeseen behaviours.

In a general sense, all the candidate solvents would appear to be useful as weakly coordinating solvents for electrochemistry. However, because of the low polarity of some, they are unlikely to be useful for application to electrodeposition. The ability of a solvent to dissolve and dissociate charged species in reasonable quantities is a key requirement of a useful plating bath. The most polar solvents oDCB and DCE are therefore the most promising and most likely to be useful for electrodeposition. Application of these solvents to electrodeposition will be the focus of subsequent Chapters.

3.9.1. The Effect of Ion Pairing

What has also become clear as a result of this work is that, because of the low polarity of the solvents, ion pairing is an important factor in determining the electrochemical response. The effects of ion pairing were observed in the measurements of conductivity, redox potential and diffusion coefficient and must be considered when interpreting electrochemical data in solvents of low polarity. It is also expected that the ions will exist in multiple forms, including free ions, ion pairs and triple ions. Meaning that the experimental response is an average of the species' response in all its arrangements.

Fig. 3.14 shows a plot of $E_{1/2}(CcPF_6)$ *vs.* theoretical potential shifts calculated from the Born equation. In black, r_{vdW} was used as the radius and this gave a poor relationship with $R^2 = 0.65$. The experimental variation in potential shift is greater than predicted by

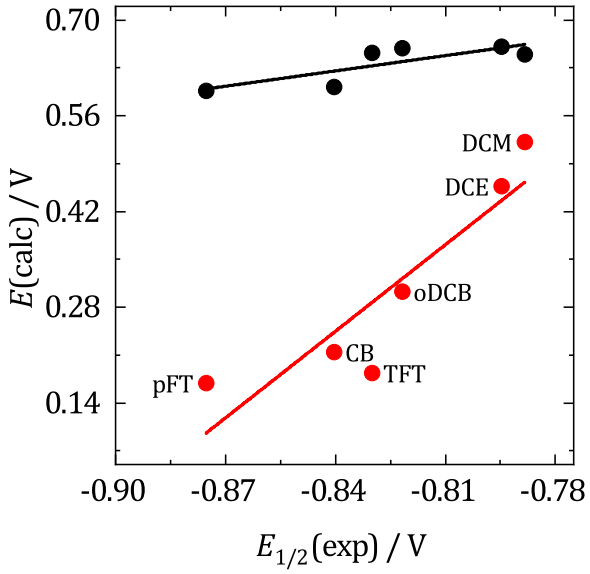

Figure 3.14: Relationship between the experimentally determined redox potential for $CcPF_6$ and the theoretical potential shift from the Born equation for the van der Waals radius of Cc^+ (black), and the Stokes radius (red).

variation in dielectric constant alone. Also shown is the expected potential shift when taking the radius as the Stokes radius, calculated from experimental diffusion coefficients of $CcPF_6$ with c as 4. Agreement with the experimental redox potential is improved, $R^2 = 0.81$, suggesting that the species radius is varying as a function of the solvent, as well as dielectric constant. This would be the case if the Cc^+ ion was ion paired.

It was assumed in the use of Eqn. (3.6) to describe the redox potential that $D_O = D_R$, but as evidenced from this work this is clearly is not the case. Instead, it is possible to account for the effect of unequal diffusion coefficients with Eqn. (3.20) below.

$$E = E^{0\prime} + \frac{RT}{nF}\ln\left(\frac{i_L}{i} - 1\right) + \frac{RT}{nF}\ln\left(\frac{D_O}{D_R}\right) \tag{3.20}$$

When using an internal reference it is implicitly assumed that $D_O = D_R$ and therefore that $E_{1/2} = E^{0\prime}$. However, as evidenced above, this is no longer the case in the solvents studied here because $DMFc^+$ is partially ion paired, and so DMFc is now solvent and electrolyte dependent. This reduces confidence in the ability of DMFc to act as a solvent independent internal reference redox species and adds a degree of uncertainty to redox potentials measured against DMFc, particularly in low polarity solvents where ion pairing is significant. The consequences of ion pairing for an internal reference has been discussed previously.[88,89] Activity coefficient measurements by Redepenning *et al.* in acetonitrile revealed the presence of ion pairing of ferrocenium and decamethylferrocenium, and its significant effects on redox potential. Table 3.11 shows a correction for $E_{1/2}$, accounting for the differences in the diffusion coefficients of the oxidised and reduced forms. The

variation in diffusion coefficient ratio leads to a small error of 10-20 mV in $E_{1/2}$. When using an internal reference in a solvent of intermediate or low polarity, it would certainly seem to be sensible to measure the diffusion coefficient of the oxidised and reduced forms to verify that there are not major differences in the diffusion coefficient. One solution to remove any uncertainties associated with ion pairing on the internal reference might be to measure the potential at varying electrolyte concentrations and extrapolate to infinite dilution, where the potential will be free from such effects.[90] Alternatively the potential could be measured with both forms of the redox couple in solution.

Solvent	$\frac{RT}{nF} \ln \frac{D_O}{D_R}$ / mV
DCM	−8
TFT	−11
oDCB	−11
pFT	−22
CB	−17
DCE	−13

Table 3.11: Correction factor for $E_{1/2}$ for DMFc caused by inequality of oxidised and reduced diffusion coefficients at 25 °C.

3.10. References

(1) M. J. Kamlet, J. L. M. Abboud, M. H. Abraham and R. W. Taft, *J. Org. Chem.*, 1983, **48**, 2877–2887.

(2) C. Reichardt and T. Welton, *Solvents and Solvent Effects in Organic Chemistry*, Wiley-VCH Verlag GmbH, Weinheim, 4th edn., 2011.

(3) M. J. Kamlet, J. L. Abboud and R. W. Taft, *J. Am. Chem. Soc.*, 1977, **99**, 6027–6038.

(4) R. W. Taft and M. J. Kamlet, *J. Am. Chem. Soc.*, 1976, **98**, 2886–2894.

(5) M. J. Kamlet and R. W. Taft, *J. Am. Chem. Soc.*, 1976, **98**, 377–383.

(6) R. W. Taft, M. J. Kamlet and J. L. M. Abboud, *J. Am. Chem. Soc.*, 1981, **103**, 1080–1086.

(7) A. R. Katritzky, D. C. Fara, M. Kuanar, E. Hur and M. Karelson, *J. Phys. Chem. A*, 2005, **109**, 10323–10341.

(8) T. W. Bentley and G. E. Carter, *J. Am. Chem. Soc.*, 1982, **2**, 5741–5747.

(9) A. R. Katritzky, T. Tamm, Y. Wang, S. Sild and M. Karelson, *J. Chem. Inf. Comput. Sci.*, 1999, **39**, 684–691.

(10) C. Reichardt and T. Welton, in *Solvents and Solvent Effects in Organic Chemistry*, Wiley-VCH, Weinheim, 4th edn., 2011, ch. 7.

(11) Y. Marcus, *The Properties of Solvents*, Wiley, Chichester, 1998.

(12) Y. Marcus, *Chem. Soc. Rev.*, 1993, **22**, 409–416.

(13) W. K. Stephenson and R. Fuchs, *Can. J. Chem.*, 1985, **63**, 2535–2539.

(14) J. P. Hickey and D. R. Passino-Reader, *Environ. Sci. Technol.*, 1991, **25**, 1753–1760.

(15) L. Crowhurst, P. R. Mawdsley, J. M. Perez-Arlandis, P. A. Salter and T. Welton, *Phys. Chem. Chem. Phys.*, 2003, **5**, 2790–2794.

(16) J. J. Maul, P. J. Ostrowski, G. A. Ublacker, B. Linclau and D. P. Curran, in *Modern Solvents in Organic Synthesis*, ed. P. Knochel, Springer-Verlag, Berlin, 1999.

(17) L. De Lorenzi, M. Fermeglia and G. Torriano, *J. Chem. Eng. Data*, 1996, **41**, 1121–1125.

(18) W. M. Haynes, D. R. Lide and T. J. Bruno, *CRC Handbook of Chemistry and Physics*, CRC Press, New York, 96th edn., 2016.

(19) D. R. Lide, *Basic Laboratory and Industrial Chemicals: A CRC Quick Reference Handbook*, CRC Press, Boca Raton, 1993.

(20) O. Ivanciuc, T. Ivanciuc, P. A. Filip and D. Cabrol-Bass, *J. Chem. Inf. Comput. Sci.*, 1999, **39**, 515–524.

(21) J. Barthel and H. J. Gores, in *Handbook of Battery Materials*, ed. C. Daniel and J. O. Besenhard, Wiley-VCH Verlag GmbH, Weinheim, 2nd edn., 2011, ch. 17.

(22) L. Sereno, V. A. Macagno and M. C. Giordano, *Electrochim. Acta*, 1972, **17**, 561–575.

(23) L. Xiao and K. E. Johnson, *J. Electrochem. Soc.*, 2003, **150**, E307–E311.

(24) C. E. Dahm and D. G. Peters, *J. Electroanal. Chem.*, 1996, **402**, 91–96.

(25) O. Scialdone, C. Guarisco, A. Galia and R. Herbois, *J. Electroanal. Chem.*, 2010, **641**, 14–22.

(26) G. Fiori, S. Rondinini, G. Sello, A. Vertova, M. Cirja and L. Conti, *J. Appl. Electrochem.*, 2005, **35**, 363–368.

(27) A. M. O'Mahony, D. S. Silvester, L. Aldous, C. Hardacre and R. G. Compton, *J. Chem. Eng. Data*, 2008, **53**, 2884–2891.

(28) J. Newman, *J. Electrochem. Soc.*, 1966, **113**, 501–502.

(29) R. J. LeSuer, C. Buttolph and W. E. Geiger, *Anal. Chem.*, 2004, **76**, 6395–6401.

(30) K. M. Kadish, J. Q. Ding and T. Malinski, *Anal. Chem.*, 1984, **56**, 1741–1744.

(31) I. Svorstol and J. Songstad, *Acta Chem. Scand. B*, 1985, **39**, 639–655.

(32) T. Sigvartsen, B. Gestblom, E. Noreland and J. Songstad, *Acta Chem. Scand. B*, 1989, **43**, 103–115.

(33) S. Boitsov, K. J. Borve, S. Rayyan, K. W. Tornroos and J. Songstad, *J. Mol. Liq.*, 2003, **103-104**, 221–233.

(34) Y. Marcus and G. Hefter, *Chem. Rev.*, 2006, **106**, 4585–4621.

(35) F. Accascina, E. Lowell Swarts, P. L. Mercier and C. A. Kraus, *Proc. Natl. Acad. Sci.*, 1953, **39**, 917–924.

(36) R. M. Fuoss, *Proc. Natl. Acad. Sci.*, 1978, **75**, 16–20.

(37) R. M. Fuoss, *J. Solution Chem.*, 1986, **15**, 231–235.

(38) Y. Marcus, *J. Solution Chem.*, 1992, **21**, 1217–1230.

(39) W. Dannhauser and A. F. Flueckinger, *J. Phys. Chem.*, 1964, **68**, 1814–1819.

(40) T. Shikata, N. Sugimoto, Y. Sakai and J. Watanabe, *J. Phys. Chem. B*, 2012, **116**, 12605–12613.

(41) K. Merz, M. V. Evers, F. Uhl, R. I. Zubatyuk and O. V. Shishkin, *Cryst. Growth Des.*, 2014, **14**, 3124–3130.

(42) M. Bujak, K. Dziubek and A. Katrusiak, *Acta Crystallogr. Sect. B Struct. Sci.*, 2007, **63**, 124–131.

(43) B. B. Damaskin and O. A. Petrii, *J. Solid State Electrochem.*, 2011, **15**, 1317–1334.

(44) A. J. Bard and L. R. Faulkner, *Electrochemical Methods: Fundamentals and Applications*, Wiley-VCH, Hoboken, NJ, 2nd edn., 2001.

(45) W. R. Fawcett, M. Fedurco and M. Opallo, *J. Phys. Chem.*, 1992, **96**, 9959–9964.

(46) A. P. Abbott and J. C. Harper, *J. Chem. Soc. Trans.*, 1997, **93**, 3981–3984.

(47) Y. Marcus, *Ions in Solution and Their Solvation*, Wiley, Hoboken, NJ, 2015.

(48) M. A. Drogowska and W. R. Fawcett, *J. Electroanal. Chem.*, 1987, **222**, 293–303.

(49) J. A. Branch, Ph.D. Thesis, University of Southampton, 2015.

(50) E. I. Rogers, D. S. Silvester, D. L. Poole, L. Aldous, C. Hardacre and R. G. Compton, *J. Phys. Chem. C*, 2008, **112**, 2729–2735.

(51) G. Gritzner and J. Kuta, *Pure Appl. Chem.*, 1984, **56**, 461–466.

(52) I. Noviandri, K. N. Brown, D. S. Fleming, P. T. Gulyas, P. A. Lay, A. F. Masters and L. Phillips, *J. Phys. Chem. B*, 1999, **103**, 6713–6722.

(53) J. R. Aranzaes, M.-C. Daniel and D. Astruc, *Can. J. Chem.*, 2006, **84**, 288–299.

(54) S. Sahami and M. J. Weaver, *J. Electroanal. Chem.*, 1981, **122**, 171–181.

(55) J. T. Hupp, *Inorg. Chem.*, 1990, **29**, 5010–5012.

(56) J. S. Jaworski, *Polyhedron*, 1987, **6**, 2151–2153.

(57) D. Shoup and A. Szabo, *J. Electroanal. Chem.*, 1982, **140**, 237–245.

(58) C. Amatore and F. Pflüger, *Organometallics*, 1990, **9**, 2276–2282.

(59) A. Bond, K. Oldham and C. Zoski, *Anal. Chim. Acta*, 1989, **216**, 177–230.

(60) W. R. Fawcett and M. Opallo, *Angew. Chem., Int. Ed.*, 1994, **33**, 2131–2143.

(61) M. J. Weaver, *Chem. Rev.*, 1992, **92**, 463–480.

(62) G. Gritzner, *Pure Appl. Chem.*, 1988, **60**, 1743–1756.

(63) G. Gritzner, *Rev. Inorg. Chem.*, 1990, **11**, 81–122.

(64) P. A. Lay, N. S. McAlpine, J. T. Hupp, M. J. Weaver and A. M. Sargeson, *Inorg. Chem.*, 1990, **29**, 4322–4328.

(65) T. Kondo, M. Okamura and K. Uosaki, *J. Organomet. Chem.*, 2001, **637-639**, 841–844.

(66) D. L. Goldfarb and H. R. Corti, *J. Electroanal. Chem.*, 2001, **509**, 155–162.

(67) I. Streeter and R. G. Compton, *Phys. Chem. Chem. Phys.*, 2007, **9**, 862–870.

(68) T. Gennett, D. F. Milner and M. J. Weaver, *J. Phys. Chem.*, 1985, **89**, 2787–2794.

(69) M. Matsumoto and T. W. Swaddle, *Inorg. Chem.*, 2004, **43**, 2724–2735.

(70) C. Ohrenberg and W. E. Geiger, *Inorg. Chem.*, 2000, **39**, 2948–2950.

(71) P. Peljo, T. Rauhala, L. Murtomäki, T. Kallio and K. Kontturi, *Int. J. Hydrogen Energy*, 2011, **36**, 10033–10043.

(72) N. G. Tsierkezos, *J. Mol. Liq.*, 2008, **138**, 1–8.

(73) H. J. V. Tyrell and K. R. Harris, in *Diffus in Liquids*, Butterworths, London, 1984, ch. 6.

(74) J. T. Edward, *J. Chem. Educ.*, 1970, **47**, 261–270.

(75) R. Evans, G. Dal Poggetto, M. Nilsson and G. A. Morris, *Anal. Chem.*, 2018, **90**, 3987–3994.

(76) P. F. Perrin, *J Phys. Rad. Srer. VII*, 1936, **5**, 497–511.

(77) B. D. H. Jenkins and Y. Marcus, *Chem. Rev.*, 1995, **95**, 2695–2724.

(78) H. S. Harned and B. B. Owen, *The Physical Chemistry of Electrolytic Solutions*, Reinhold, New York, USA, 1943.

(79) I. Svorstøl, H. Høiland and J. Songstad, *Acta Chem. Scand. B*, 1984, **38**, 885–893.

(80) I. Svorstøl, T. Sigvartsen and J. Songstad, *Acta Chem. Scand. B*, 1988, **42**, 133–144.

(81) A. Macchioni, G. Ciancaleoni, C. Zuccaccia and D. Zuccaccia, *Chem. Soc. Rev.*, 2008, **37**, 479–489.

(82) Y. Marcus, *J. Phys. Org. Chem.*, 2003, **16**, 398–408.

(83) D. Tran, J. P. Hunt and S. Wherland, *Inorg. Chem.*, 1992, **31**, 2460–2464.

(84) L. Glasser and H. D. B. Jenkins, *Inorg. Chem.*, 2008, **47**, 6195–6202.

(85) H. D. B. Jenkins and J. F. Liebman, *Inorg. Chem.*, 2005, **44**, 6359–6372.

(86) F. S. T. Khan, A. L. Waldbusser, M. C. Carrasco, H. Pourhadi and S. Hematian, *Dalt. Trans.*, 2021, **50**, 7433–7455.

(87) R. A. Robinson and R. H. Stokes, *Electrolyte Solutions*, Butterworths, London, 2nd edn. Revised, 1965.

(88) J. Redepenning and E. Mechalke, *Anal. Chem.*, 1997, **69**, 5094–5102.

(89) J. Redepenning, E. Castro-Narro, G. Venkataraman and E. Mechalke, *J. Electroanal. Chem.*, 2001, **498**, 192–200.

(90) M. W. Lehmann and D. H. Evans, *J. Phys. Chem. B*, 1998, **102**, 9928–9933.

4

Electrodeposition of Antimony, Bismuth and Tellurium

4.1. Overview

In Chapter 3, oDCB and DCE were identified as the most promising solvents for further application to electrodeposition. This Chapter therefore presents further characterisation of oDCB and DCE, along with DCM as a comparative solvent. The simple metal precursors $[N^nBu_4][SbCl_4]$ and $[N^nBu_4][BiCl_4]$ are used to test the suitability of the two solvents for electrodeposition. The behaviour of the precursors are investigated using voltammetry at macro- and microdisc electrodes and the Electrochemical Quartz Crystal Microbalance. The resulting deposits are then characterised using SEM, XRD and Raman spectroscopy. The electrochemistry of $[N^nBu_4]_2[TeCl_6]$ is also investigated in preparation for compound deposition in later Chapters.

4.2. Introduction

One conclusion of the previous Chapter was that, out of the candidate weakly coordinating solvents, oDCB and DCE were the most promising for further investigation into electrodeposition. This Chapter therefore intends to explore the possibility of electrodeposition from the two solvents. The two metals Sb and Bi are employed as model electrodeposition systems since it has previously been shown that both are readily deposited from DCM. It is also necessary to properly understand the behaviour of the two redox couples in oDCB and DCE to prepare for the more complicated task of semiconductor electrodeposition in subsequent Chapters. For this reason, Te electrodeposition is investigated also.

The main focus of Sb in electrochemistry has been on achieving its electrodeposition. Sb has a high corrosion resistance and does not tarnish, making it useful as a coating material in a variety of applications.[1] Sb has been successfully deposited from a variety of aqueous electrolytes, which gave deposits of differing properties. The earlier work on Sb electrodeposition has been reviewed by Sadana *et al.*[1] More recently, bulk Sb has been electrochemically exfoliated to form the 2D layered material antimonene, which is of interest for optoelectronic applications.[2] In terms of non-aqueous electrochemistry, its electrodeposition has been reported from ionic liquids,[3] and Deep Eutectic Solvents.[4]

Additionally, Sb has been electrodeposited from DCM, by Bartlett *et al.*,[5] and also by Reeves *et al.*[6] In the work of Reeves, the electrochemistry of the Sb precursor $[N^nBu_4][SbCl_4]$, was investigated in detail using various methods, including microelectrodes, the rotating disc electrode, and the electrochemical quartz crystal microbalance. The electrochemistry was found to be well behaved, with simple deposition and stripping the only redox processes observed. Sb was then successfully electrodeposited onto Pt and TiN substrates, with an amorphous deposit being collected. Bartlett *et al.* then reported comparable electrochemistry with the same precursor with glassy carbon electrodes.[5] Sb was also deposited onto TiN in this work, but interestingly the deposit was crystalline.

The primary use of Sb is as an alloy, and is commonly electrodeposited alongside other metals in the bath to form binary or ternary alloys and compounds. Sb readily forms alloys with several other metals, such as Cu, Zn, Pb and Sn. Multiple reports detail the electrodeposition of Sb alloys with these metals.[7] Sb is also of interest as it forms semiconducting compounds with other p-block metals, which can be electrodeposited for electronic applications. For example, GeSbTe in the atom ratio 2:2:5 is a promising phase change memory material which has recently been electrodeposited.[8] Additionally there have recently been reports of the electrodeposition of Sb_2Te_3, a thermoelectric material,[9] and InSb an infra-red detector.[10]

The successful electrodeposition of bismuth from acidic aqueous electrolytes has been reported by Yang and Hu,[11] and also by Sandnes *et al.*[12] Voltammetry demonstrated that, similar to Sb, Bi is in the Bi^{3+} oxidation state in aqueous electrolytes, and crystalline

material is readily deposited. Bi electrodeposition is of particular interest for application to electrochromic devices,[13] and also as a safer alternative to Hg for adsorptive stripping voltammetric measurements for metal ion sensing.[14]

The electrochemistry of $[N^nBu_4][BiCl_4]$ was investigated in DCM by Bartlett *et al.* where, as in aqueous electrolytes, simple deposition and stripping was observed.[5] Crystalline Bi was also successfully deposited onto a TiN substrate. Interest in codeposition of Bi is mainly restricted to chalcogenide elements. Bi_2Te_3 is a thermoelectric material, for example.[15]

Elemental tellurium possesses an unusual crystal structure, which is highly anisotropic and also chiral, which gives rise to interesting properties.[16] Te is readily electrodeposited from aqueous electrolytes,[17] and also from DCM.[5] Despite this, Te in fact displays complicated electrochemistry. Te possesses multiple oxidation states and readily moves between them. Liftman *et al.* investigated the electrochemistry of $TeCl_4$ in DCM in detail, publishing two articles.[18,19] Two cathodic regions were reported, one was attributed to the deposition of Te and the second, more cathodic peak to the formation of Te^{2-}. Two anodic peaks, corresponding to the stripping of deposited Te were also observed. The first peak was attributed to formation of Te^{2+} and the second to the formation of Te^{4+}. Oxidation of Te^{2-} was not observed because Te^{2-} underwent a subsequent reaction with Te^{4+} forming a transient precipitate $TeCl_2$, which reacted further to form $TeCl_4^{2-}$:

$$Te^{2-} + 2\,TeCl_4 \longrightarrow 3\,TeCl_2 + 2\,Cl^-$$
$$TeCl_2 + 2\,Cl^- \longrightarrow TeCl_4^{2-}$$

The authors also investigated the effect of chloride ions on the electrochemistry. In a system with excess chloride, the number of cathodic and anodic peaks remained unchanged, but both stripping peaks corresponded to the formation of Te^{2+}. The presence of two peaks was explained by the presence of two activity states of deposited Te. It was also found that chloride ions supplied by the deposition of Te^{4+} were adsorbed onto the Te surface and activated Te^0 atoms towards oxidation. The deposited Te could be stripped to form $[TeCl_4]^{2-}$, where the rate of dissolution was proportional to the concentration of Cl^-, as might be expected.

Another possibility for the reactions of Te^{2-} is the formation of polytellurides (Te_x^{2-}, $x \geqslant 2$). Polytellurides have been reported to form complexes with metals and organic compounds,[20–22] including with the $[N^nBu_4]^+$ cation. Kalisman investigated the electrochemistry of Te^{4+} in DMSO with $[N^nBu_4]Cl$ as a supporting electrolyte.[23] Using a Te^0 working electrode, it was found that Te^{2-} formed a precipitate with the supporting electrolyte.

The aim of this Chapter is to further characterise the solvents oDCB and DCE, and assess their suitability for the electrodeposition of metals and semiconductors. The voltammetry of some model redox couples will be studied, in order to investigate the behaviour of redox processes involving metal deposition. The deposition of the same metals will be

attempted on larger electrodes to characterise their physical properties.

4.3. Electrochemistry of $[SbCl_4]^-$ and $[BiCl_4]^-$

Fig. 4.1 shows voltammograms of 1 mM $[N^nBu_4][SbCl_4]$ and 1 mM $[N^nBu_4][BiCl_4]$ in DCM, oDCB and DCE at a Pt macrodisc electrode. Turning first to Sb^{3+}, scanning in the negative direction a decrease in current is observed at *ca.* −0.7 V *vs.* DMFc. This can be attributed to the three electron reduction of Sb^{3+} to Sb^0, resulting in the electrodeposition of elemental Sb.

$$Sb^{3+} + 3\,e^- \longrightarrow Sb_{(s)}$$

No further reduction processes are then observed within the solvent potential window. On the reverse sweep, scanning anodically, the current reaches zero at approximately −0.6 V, before an increase in current occurs and two oxidation peaks can be seen, associated with the stripping of the deposited Sb to Sb^{3+} in solution. It is possible that two peaks are observed because two different forms of deposited Sb are being stripped, or alternatively the deposited material is oxidised to two different species in solution. There appeared to be no evidence of the possible formation of Sb^{5+}, as was the case in previous work in DCM by Reeves *et al.*[6] Suggesting it takes place outside of the available potential window. On subsequent scans, no significant changes to the voltammetry take place, but the onset of deposition shifts slightly anodically since Sb is already nucleated on the electrode surface. With oDCB, the broad features of the electrochemistry appear to be similar. Only peaks associated with the deposition and stripping of Sb appear to be present. A small hump is present anodic to the stripping peak which is possibly due to the removal of amorphous material. The current density is slightly lower because of the greater viscosity of oDCB. No major differences can be found for the voltammetry in DCE.

Voltammograms of $[SbCl_4]^-$ with a glassy carbon WE are shown in Fig. 4.2. Glassy carbon was used as an alternative electrode material to investigate the effect of the electrode surface on the voltammetry. In fact however, the nature of the electrode material does not appear to significantly change the features of $[SbCl_4]^-$ voltammograms. Fig. 4.3 also shows voltammograms of $[SbCl_4]^-$ at increasing concentration of precursor. The cathodic peak current naturally increases because of the increase in the rate of deposition. The size of the stripping peaks also grow since there is more material on the electrode to oxidise. The onset of deposition shifts slightly in the anodic direction with increasing concentration also, but otherwise there are no major changes in $[SbCl_4]^-$ as concentration increases.

With regards to Bi, in DCM a single reduction peak begins at *ca.* −0.5 V, a positive shift of approximately 100 mV from Sb. The cathodic process is presumably the electrodeposition of elemental Bi

$$Bi^{3+} + 3\,e^- \longrightarrow Bi_{(s)}$$

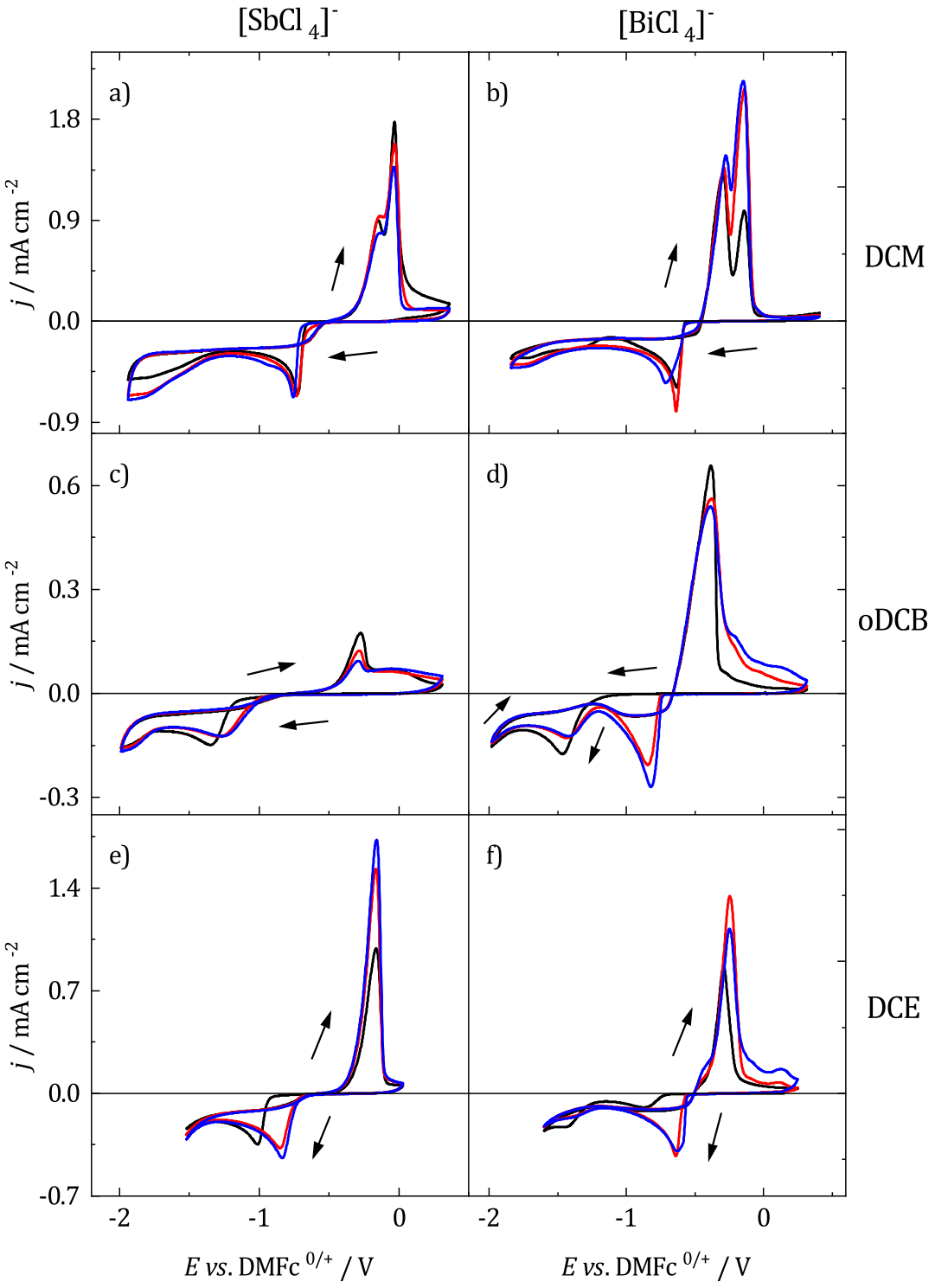

Figure 4.1: Voltammograms of 1 mM $[N^nBu_4][SbCl_4]$ and 1 mM $[N^nBu_4][BiCl_4]$ with 100 mM $[N^nBu_4]Cl$ in DCM, oDCB and DCE at a Pt macroelectrode. Working electrode was swept from 0 V at 50 mV s^{-1} in the direction indicated by the arrows. CE: Pt grid, RE: Ag/AgCl, WE: r = 0.25 mm Pt disc. Black: scan 1, red: scan 2, blue: scan 3. a) Sb^{3+} in DCM, b) Bi^{3+} in DCM, c) Sb^{3+} in oDCB, d) Bi^{3+} in oDCB, e) Sb^{3+} in DCE, f) Bi^{3+} in DCE.

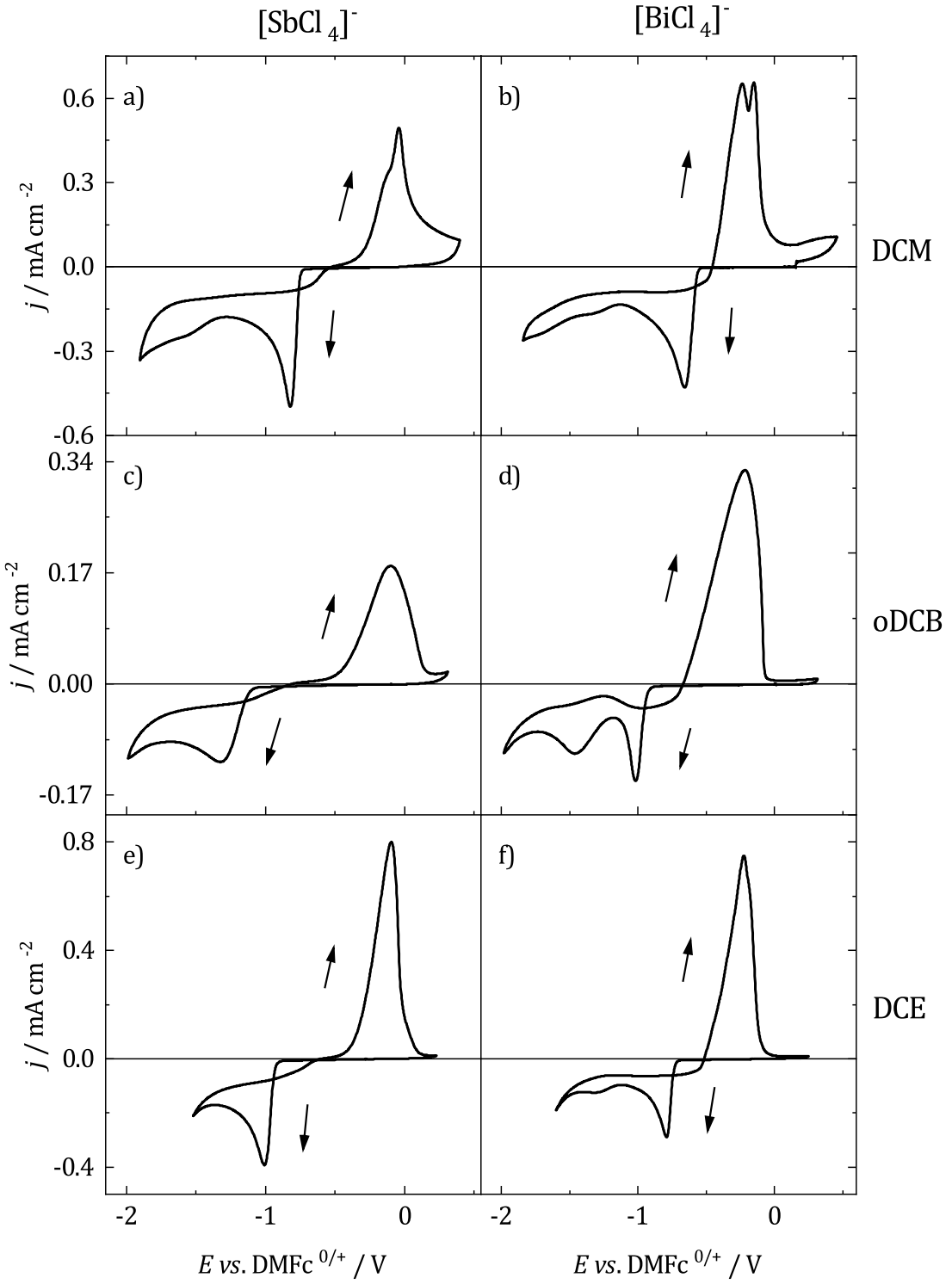

Figure 4.2: Voltammograms of 1 mM $[N^nBu_4][SbCl_4]$ and 1 mM $[N^nBu_4][BiCl_4]$ with 100 mM $[N^nBu_4]Cl$ in DCM, oDCB and DCE at a glassy carbon macroelectrode. Working electrode was swept from 0 V at 50 mV s^{-1} in the direction indicated by the arrows. CE: Pt grid, RE: Ag/AgCl, WE: r = 1.5 mm GC disc. a) Sb^{3+} in DCM, b) Bi^{3+} in DCM, c) Sb^{3+} in oDCB, d) Bi^{3+} in oDCB, e) Sb^{3+} in DCE, f) Bi^{3+} in DCE.

There is no evidence of any further reduction processes up to the cathodic limit. On the reverse scan, two oxidation peaks occur, corresponding to the stripping of deposited Bi. As with Sb, the formation of Bi^{5+} was not observed within the solvent limits. The voltammograms do not change significantly on subsequent scans. Interestingly in oDCB, the voltammogram is somewhat different to that observed in DCM. The first cathodic event begins at *ca.* −1.3 V which is expected to be the onset of Bi deposition but is significantly more negative than the onset of deposition in DCM. On the reverse sweep an increase in current is observed followed by a single stripping peak. On subsequent scans a third reduction peak can be seen. On a fresh electrode surface, the voltammetry displays a high nucleation overpotential. However on the second and third scans this is no longer the case and the onset of deposition increases by approx. 0.7 V to −0.7 V. This suggests that the kinetics of nuclei formation are slow, possibly caused by the electrolyte, until the later scans when nuclei are already formed on the surface. The initial stages of deposition are also unusual with DCE as a solvent, where a fully formed deposition peak is not present on the first scan. On subsequent scans, the onset of deposition shifts by ~ 150 mV in the anodic direction, with an increase in the peak current.

When changing the electrode material to glassy carbon, the votammogram in DCM does not change significantly. However in oDCB, the voltammogram now appears as that at a Pt WE when Bi is already nucleated on the surface, as in the second or third scans in Fig. 4.1d. This suggests that there is a process specific to the Pt surface which is inhibiting the nucleation of Bi, such as a blocking layer of adsorbed electrolyte perhaps. A similar situation is observed in DCE. Increasing the concentration of precursor in oDCB and DCE causes the first reduction peak to emerge also.

Fig. 4.4 shows a voltammograms of 1 mM $[N^nBu_4][SbCl_4]$ and $[N^nBu_4][BiCl_4]$ at a $r = 25\,\mu m$ Pt disc in DCM, oDCB and DCE. The electrochemistry appears to be simplified at a microelectrode, a single reduction process takes place, followed by a single stripping peak. A limiting current plateau can be observed for both redox couples in all three solvents, showing that electrodeposition is diffusion limited for both metals. The nucleation overpotential is much smaller than those observed at macrodisc electrodes above. This is because of the slow scan rate required to reach a steady state, emphasising the stochastic nature of nucleation. In some voltammograms the current can be seen to increase slightly as the scan progresses, this is most likely as a result of the increasing electrode size caused by metal deposition.

Taking the potential where the current passes through zero on the anodic sweep, the crossover potential, as the redox potential, $E^{0\prime}$, gives thermodynamic information on the redox couples in each solvent. Values are given in Table 4.1. There is a notable difference in the shape of the voltammograms at the crossing point for the two metals. The current is close to vertical for Bi, indicating fast electron transfer kinetics and allowing accurate determination of $E^{0\prime}$. Conversely, the current is much flatter for Sb, suggesting slow electron transfer kinetics. It also makes accurate estimation of the crossover potential more

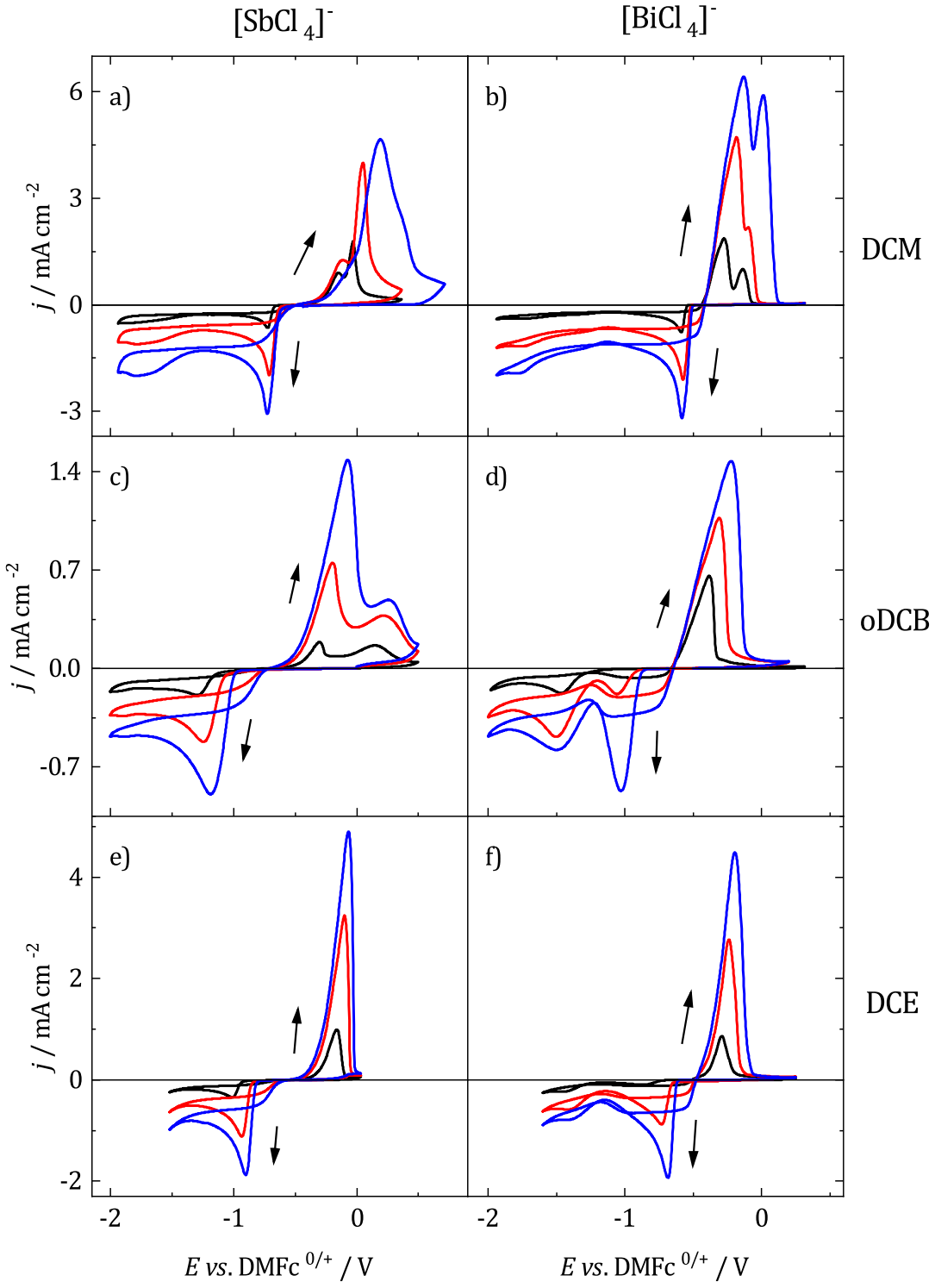

Figure 4.3: Voltammograms of $[N^nBu_4][SbCl_4]$ and $[N^nBu_4][BiCl_4]$ at varying concentrations with 100 mM $[N^nBu_4]Cl$ in DCM, oDCB and DCE. Working electrode was swept from 0 V at 50 mV s^{-1} in the direction indicated by the arrows. CE: Pt grid, RE: Ag/AgCl, WE: r = 0.25 mm Pt disc. Black: 1 mM, red: 3 mM, blue: 5 mM a) Sb^{3+} in DCM, b) Bi^{3+} in DCM, c) Sb^{3+} in oDCB, d) Bi^{3+} in oDCB, e) Sb^{3+} in DCE, f) Bi^{3+} in DCE.

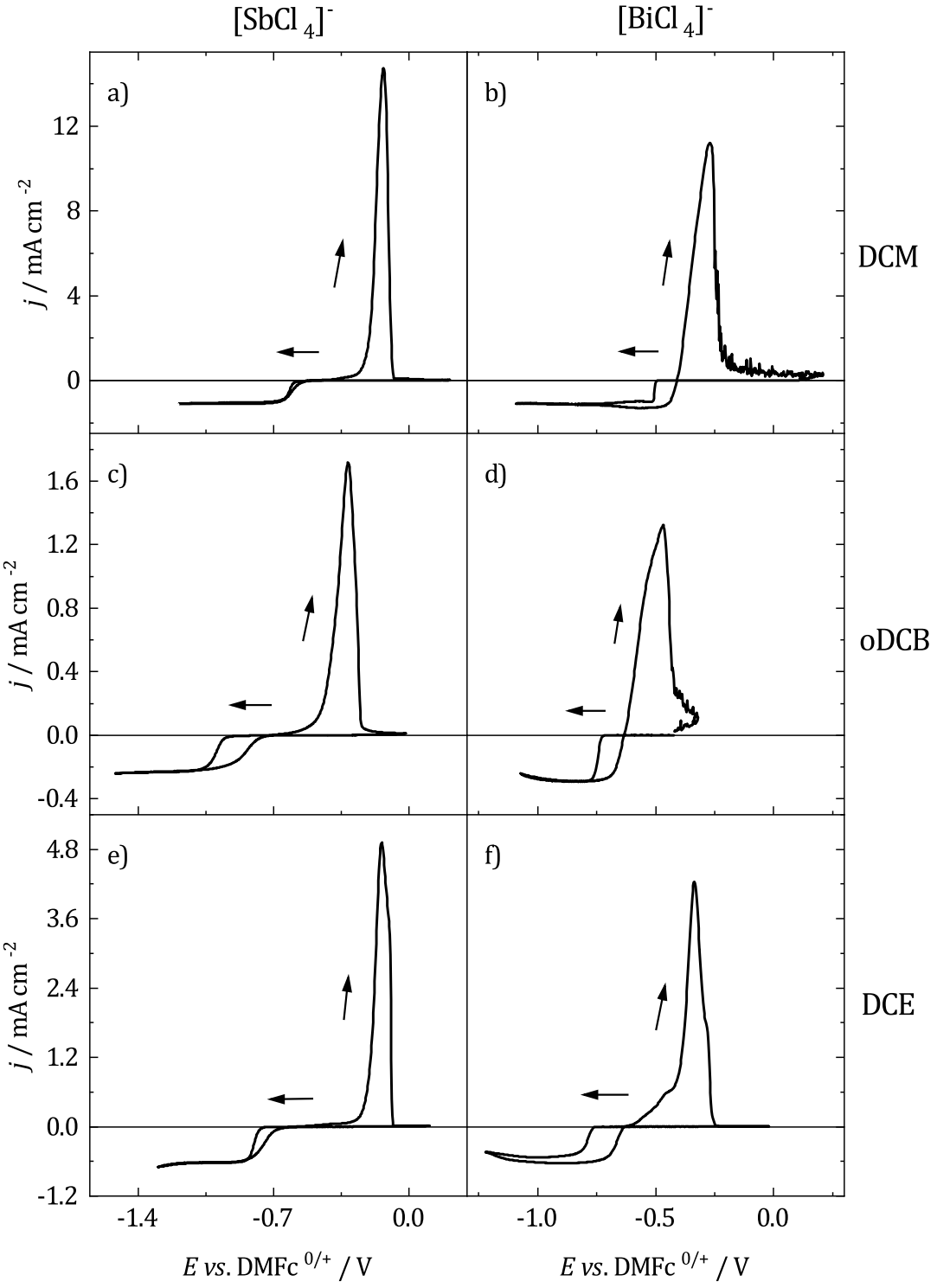

Figure 4.4: Voltammograms of 1 mM $[N^nBu_4][SbCl_4]$ and 1 mM $[N^nBu_4][BiCl_4]$ with 100 mM $[N^nBu_4]Cl$ in DCM, oDCB and DCE at a $r = 25\,\mu m$ Pt microelectrode. Working electrode was swept from $-0.3\,V$ *vs.* DMFc at $5\,mV\,s^{-1}$ in the direction indicated by the arrows. CE: Pt grid, RE: Ag/AgCl. a) Sb^{3+} in DCM, b) Bi^{3+} in DCM, c) Sb^{3+} in oDCB, d) Bi^{3+} in oDCB, e) Sb^{3+} in DCE, f) Bi^{3+} in DCE.

difficult, and so is likely to be less reliable for Sb.

In a given solvent the redox potential of $Sb^{3+/0}$ is generally more negative than $Bi^{3+/0}$. This is also the case in aqueous electrolytes.[24] The redox potential also varies with the solvent, decreasing in the order: DCM, DCE, oDCB for both redox couples. The ratio $E^{0\prime}\left(Sb^{3+}\right)/D\left(Bi^{3+}\right)$ is 1.2, 1.1 and 1.1 for DCM, oDCB and DCE respectively. Suggesting that the solvent influences both of the redox couples equally. Despite the solvents being ostensibly the same, there are quite significant differences in redox potential for both species between solvents. One possible reason for this is the influence of ion pairing. As described in previous Chapters; the pairing of the electroactive species, in this case with the $[N^nBu_4]^+$ cation, appeared to stabilise the ion and decrease its redox potential.

	$[SbCl_4]^-$		$[BiCl_4]^-$	
	$E^{0\prime}$ *vs.* $DMFc^{0/+}$ / V	D / 10^{-6} cm^2 s^{-1}	$E^{0\prime}$ *vs.* $DMFc^{0/+}$ / V	D / 10^{-6} cm^2 s^{-1}
DCM	−0.478(6)	8.35(68)	−0.408(1)	7.26(28)
oDCB	−0.735(7)	1.75(5)	−0.642(2)	1.87(8)
DCE	−0.614(9)	4.25(7)	−0.537(3)	3.67(19)

Table 4.1: Experimental redox potentials and diffusion coefficients of $[SbCl_4]^-$ and $[BiCl_4]^-$ in DCM, oDCB and DCE. $E^{0\prime}$ was taken as the crossover potential and D using Eqn. (3.8), from voltammograms at Pt microdisc electrodes of radii 5, 12.5 and 25 µm at 25 °C. Values are the average of three repeats with the error the standard deviation.

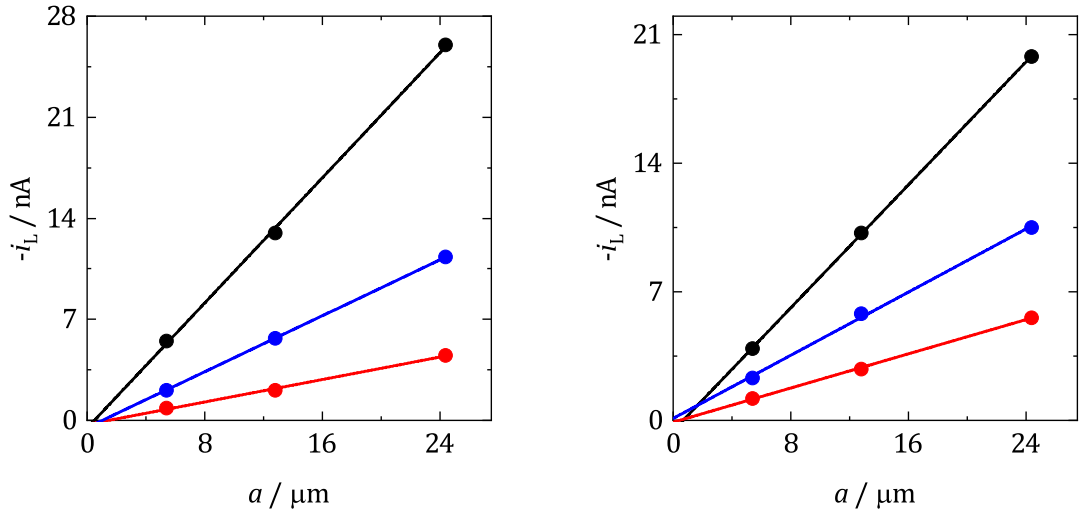

(a) $[SbCl_4]^-$ (b) $[BiCl_4]^-$

Figure 4.5: Representative limiting currents of 1 mM $[N^nBu_4][SbCl_4]$ and $[N^nBu_4][BiCl_4]$ with 100 mM $[N^nBu_4]Cl$ at Pt microelectrodes of radii 5, 12.5 and 25 µm at 25 °C. Black: DCM, red: oDCB, blue: DCE.

As demonstrated in previous Chapters, plots of i_L at different sizes of microelectrode can be used to accurately determine diffusion coefficients of electroactive species.

Such plots are shown in Fig. 4.5 for 1 mM $[SbCl_4]^-$ and $[BiCl_4]^-$ in DCM, oDCB and DCE, at microelectrodes of radii 5, 12.5 and 25 µm. The plots are linear, with intercepts close to the origin, demonstrating the suitability of this approach for the calculation diffusion coefficients of heterogeneous reactions.

Diffusion coefficients are then calculated without concentration correction, assuming three electrons transferred, and values are given in Table 4.1. The value for $[SbCl_4]^-$ in DCM the result is in agreement with that found by Reeves *et al.* using microelectrodes, 9.20×10^{-6} cm^2 s^{-1}.[6] Diffusion coefficients of $[SbCl_4]^-$ are generally larger than $[BiCl_4]^-$, presumably on account of the smaller Sb^{3+} ion. The ratio $D\left(Sb^{3+}\right)/D\left(Bi^{3+}\right)$ is 1.2, 0.9 and 1.2, for DCM, oDCB and DCE respectively, suggesting that the solvent affects the two redox couples similarly in DCM and DCE, but not oDCB. The effect of the solvent on the diffusion of the two species can be examined using the Stokes-Einstein equation in a similar manner to that which was described in an earlier Chapter. On the basis of bond lengths and the geometry of the $[SbCl_4]^-$ anion, Reeves *et al.* determined that the complex was an oblate spheroid.[6] However the resulting Perrin correction was close enough to one that it was be assumed the ion was essentially spherical and that the correction could be ignored. This is taken to be true in the present work also. Spectroscopic measurements also indicate that the $[BiCl_4]^-$ anion has a similar geometry to $[SbCl_4]^-$.[25] So it is assumed that $[BiCl_4]^-$ is spherical also, and therefore that no correction is required.

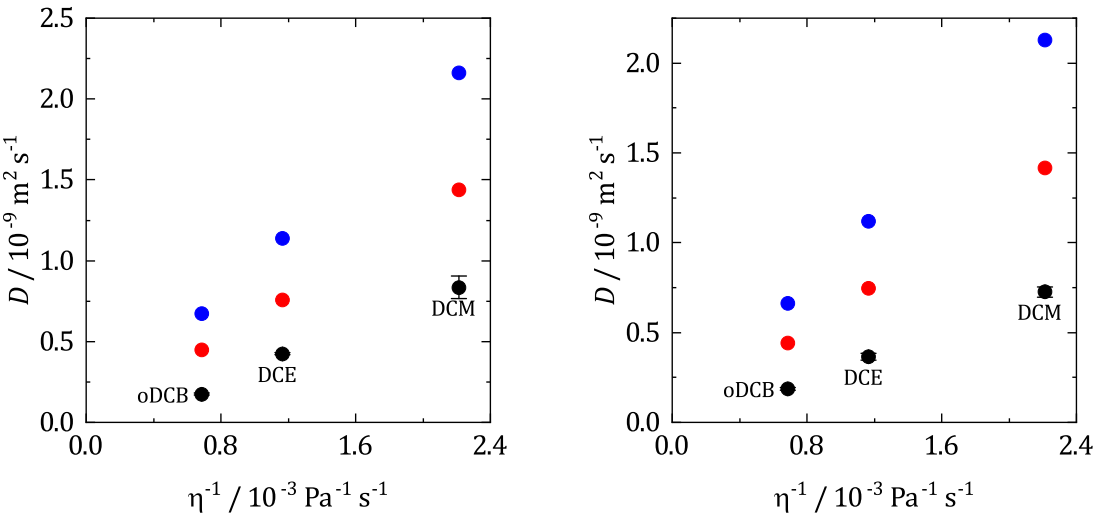

(a) $[SbCl_4]^-$ (b) $[BiCl_4]^-$

Figure 4.6: Stokes-Einstein plot of experimental diffusion coefficients of $[N^nBu_4][SbCl_4]$ and $[N^nBu_4][BiCl_4]$ in black at 25 °C using the Stokes-Einstein equation, Eqn (3.9). Diffusion coefficients calculated using the limiting current at a microelectrode. Also shown with simulated D_{min} in red and D_{max} in blue, using the McGowan radius.

Fig. 4.6 shows Stokes-Einstein plots for $[SbCl_4]^-$ and $[BiCl_4]^-$ in DCM, oDCB and DCE. Upon inspection of the plots it is clear that the equation is not obeyed. The plots are apparently linear, but a fit does not pass through the origin for either metal complex.

Also shown in Fig. 4.6 is D_{min} and D_{max} for both species. The van der Waals radius, r_{vdW}, and crystallographic radius, r_{crs}, are not available for either complex so the readily accessible McGowan radius, r_{McG}, is used instead.[26] The McGowan radius is taken from the McGowan volume, V_{McG}, which is typically intermediate between V_{crs} and V_{vdW}. V_{McG} of ions have been obtained by correlations with ionic radii, and then the volume of the molecule taken from the sum of the constituent atoms taken as was done in Chapter 3.[26] D_{min} is therefore when $c = 6$ and D_{max} when $c = 4$. Evidently, the experimental diffusion coefficients are lower than those predicted by theory for both redox couples in all three solvents. It would seem that the Stokes radii of the diffusing particles are larger than r_{McG} and this is lowering the measured diffusion coefficients. Since $[SbCl_4]^-$ and $[BiCl_4]^-$ are both charged, this would appear to represent further evidence of the ion pairing of the two species in DCM, oDCB and DCE.

4.3.1. The Effect of Chloride

Previous work on $[SbCl_4]^-$ in DCM showed that the nature of the anion in the supporting electrolyte can have a significant influence on the resulting electrochemistry.[6] Here, this is extended to include $[BiCl_4]^-$, and oDCB and DCE, to investigate this effect further in weakly coordinating solvents. Figs. 4.7 and 4.8 show voltammograms of $[SbCl_4]^-$ and $[BiCl_4]^-$ in DCM, oDCB and DCE with 100 mM $[N^nBu_4][BF_4]$, in place of Cl^-, at macro- and microdisc electrodes.

As with the work of Reeves *et al.*,[6] it is clear that changing the supporting electrolyte anion has marked consequences for the voltammetry of the two redox couples. The voltammograms of $[SbCl_4]^-$ appear similar in all three solvents. One reduction process takes place; interestingly, at the macroelectrodes a nucleation loop is no longer present. On the anodic scan three stripping peaks are observed. Reeves *et al.* speculated that the peaks corresponded to the oxidation of Sb which formed complexes with varying numbers of Cl^- ligands, still present in the diffusion layer after being discharged in the deposition process. $[BF_4]^-$ could then fill the remaining coordination sites. The largest stripping peak at *ca.* 0.75 V could then correspond to the formation of a $[Sb^{3+}(BF_4)_x]^{x-3}$ complex, since $[BF_4]^-$ is in excess. At microelectrodes, the limiting current densities are similar to those recorded with $[N^nBu_4]Cl$, suggesting that the diffusion coefficient remains the same. A single stripping peak is now observed, in a similar position to the major peak at macroelectrodes. None of the minor oxidation peaks are present because the faster mass transport at a microelectrode means that the free Cl^- generated from Sb deposition has diffused away in the time taken for the potential to be scanned into the anodic region.

The situation is similar for $[BiCl_4]^-$ electrochemistry. A single reduction peak can be found within the solvent window. The broad features of the anodic region are also comparable. However, some additional smaller peaks are also present, for reasons unknown. Interestingly, the limiting current densities are lower than those for $[SbCl_4]^-$ in Fig. 4.8, and also lower than when measured with $[N^nBu_4]Cl$, by approximately a factor of 2 in

all three solvents. Without accurate diffusion coefficient calculations it is not possible to draw any conclusions but it is possible the speciation of the Bi^{3+} ion changes now that $[BF_4]^-$ is in excess, resulting in a larger particle size and lower diffusion coefficient.

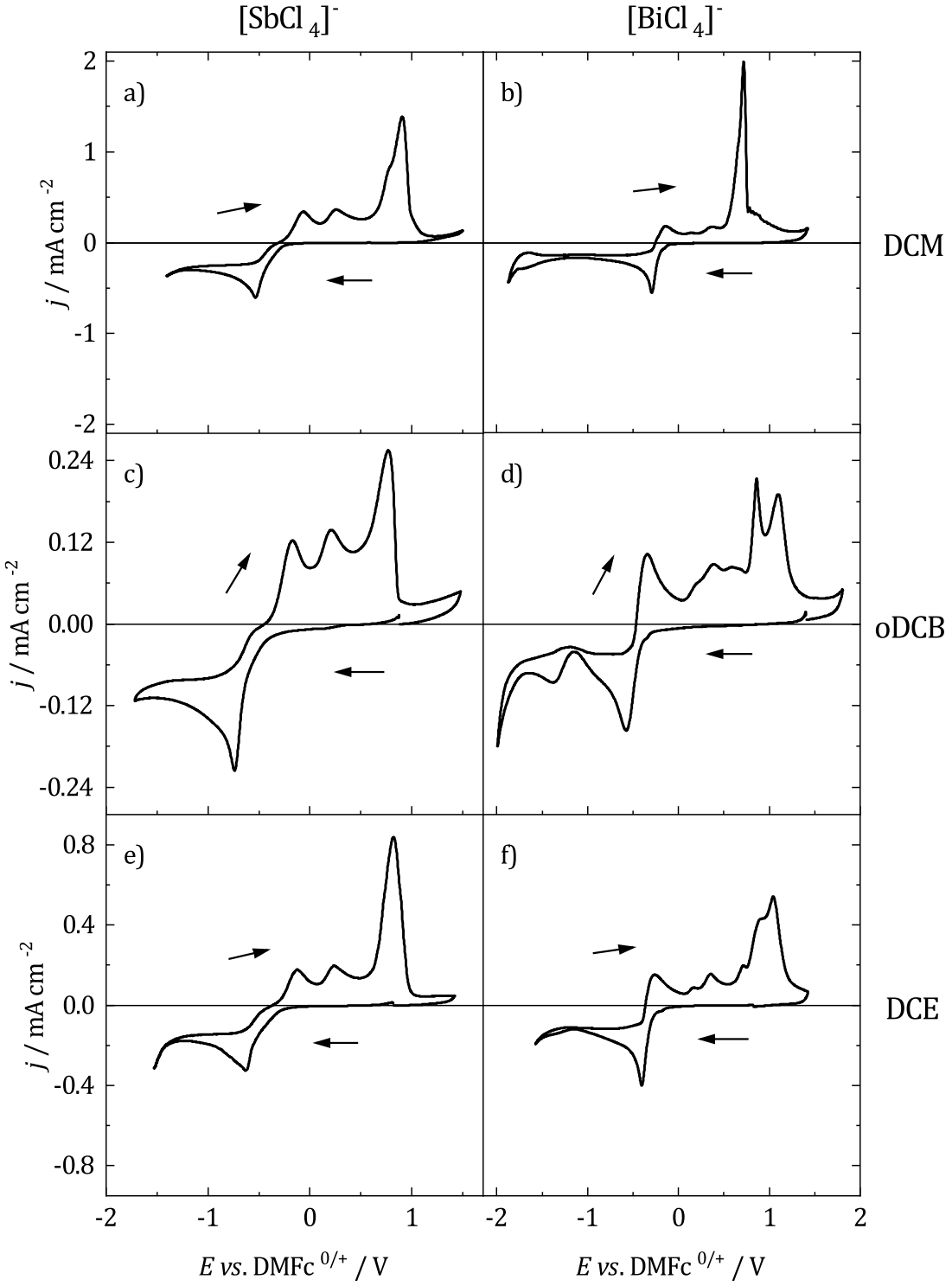

Figure 4.7: Voltammograms of 1 mM $[N^nBu_4][SbCl_4]$ and $[N^nBu_4][BiCl_4]$ with 100 mM $[N^nBu_4][BF_4]$ in DCM, oDCB and DCE at a $r = 0.5$ mm Pt WE. Working electrode was swept from 0 V at 50 mV s^{-1} in the direction indicated by the arrows. CE: Pt grid, RE: Ag/AgCl. a) Sb^{3+} in DCM, b) Bi^{3+} in DCM, c) Sb^{3+} in oDCB, d) Bi^{3+} in oDCB, e) Sb^{3+} in DCE, f) Bi^{3+} in DCE.

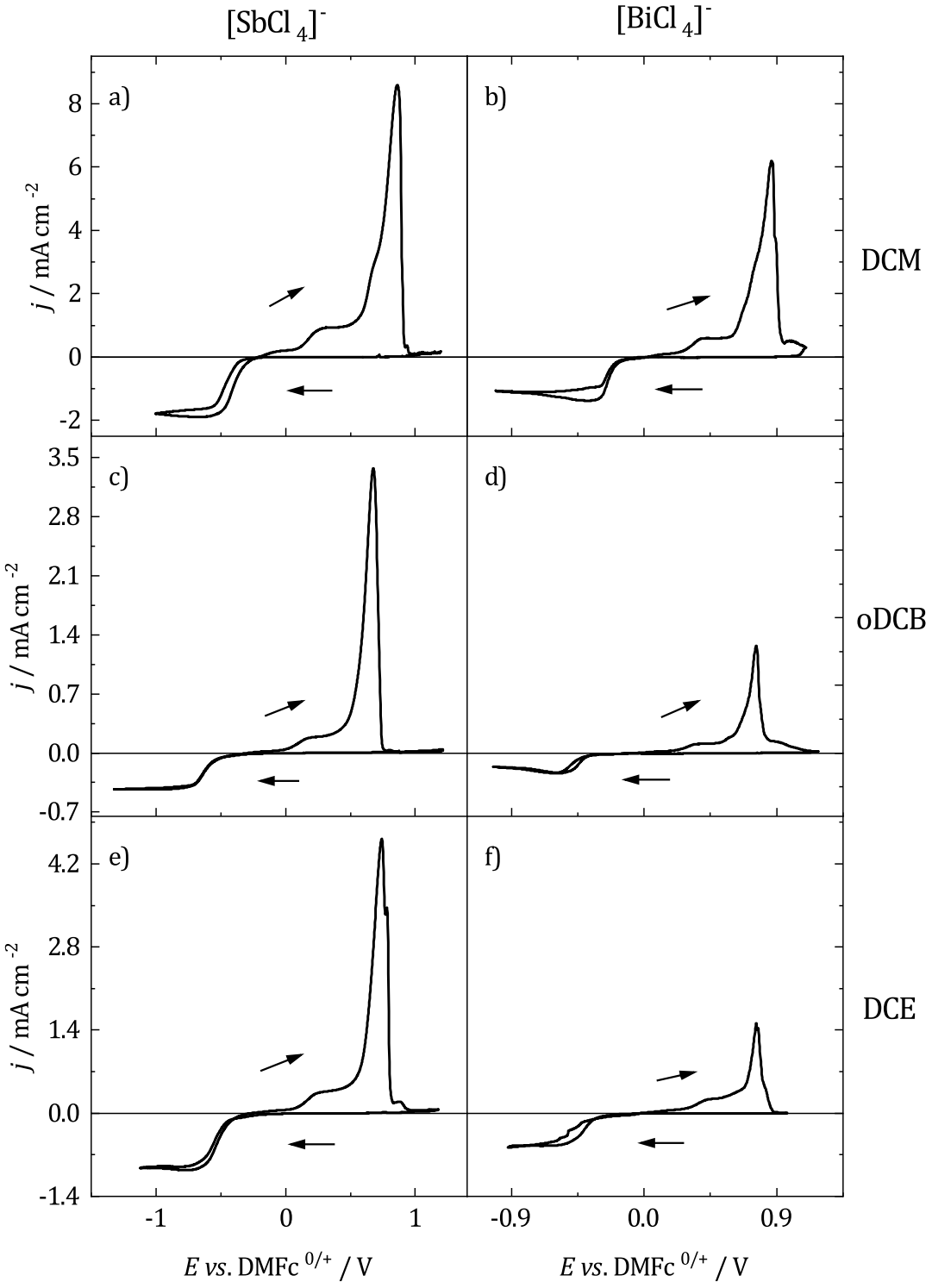

Figure 4.8: Voltammograms of 1 mM $[N^nBu_4][SbCl_4]$ and $[N^nBu_4][BiCl_4]$ with 100 mM $[N^nBu_4][BF_4]$ in DCM, oDCB and DCE at a $r = 25\,\mu m$ Pt WE. Working electrode was swept from 0 V at 50 mV s^{-1} in the direction indicated by the arrows. CE: Pt grid, RE: Ag/AgCl. a) Sb^{3+} in DCM, b) Bi^{3+} in DCM, c) Sb^{3+} in oDCB, d) Bi^{3+} in oDCB, e) Sb^{3+} in DCE, f) Bi^{3+} in DCE.

4.4. Electrochemistry of Tellurium

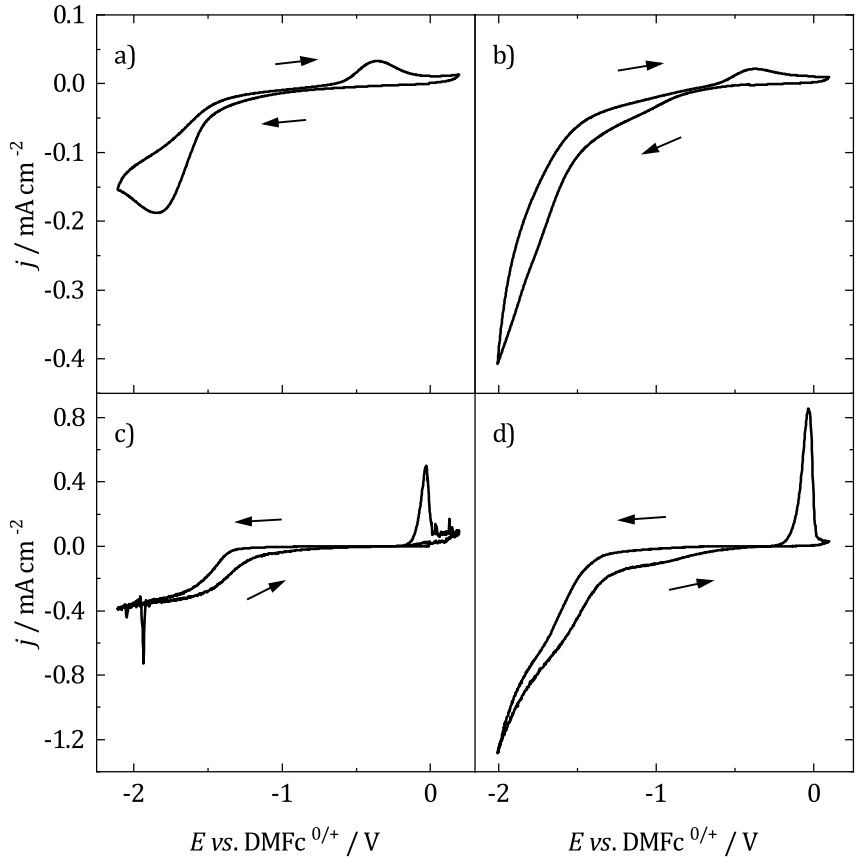

Figure 4.9: Voltammograms of 1 mM $[N^nBu_4]_2[TeCl_6]$ with 100 mM $[N^nBu_4]Cl$ in oDCB and DCE at macro- and microdisc electrodes. Working electrode was swept from −0.5 V at a), b) 50 mV s^{-1}, c), d) 5 mV s^{-1} in the direction indicated by the arrows. CE: Pt grid, RE: Ag/AgCl, WE: a), b) r = 0.5 mm c), d) r = 25 µm Pt disc. a) macrodisc in oDCB, b) macrodisc in DCE, c) microdisc in oDCB, d) microdisc in DCE.

$[TeCl_6]^{2-}$ was found to display quite different electrochemistry to $[SbCl_4]^-$ and $[BiCl_4]^-$, and this warrants a separate treatment. Fig. 4.9 shows voltammograms of 1 mM $[N^nBu_4]_2[TeCl_6]$ at macro- and microdisc electrodes in oDCB and DCE. In oDCB, a single peak at *ca.* −1.75 V can be seen at a macroelectrode, which is followed by a small oxidation peak on the reverse sweep. With the microelectrode, a limiting current forms. On the anodic scan hysteresis can be observed, and a stripping peak at 0 V. No peaks can be resolved from the macrodisc voltammogram in DCE, with the solvent limit indistinguishable from any electrochemistry of the redox active species. The same is also true at the microelectrode, where a limiting current does not form. The reduction currents in both solvents are presumably due to the electrodeposition of Te:

$$Te^{4+} + 4\,e^- \longrightarrow Te$$

However, the voltammograms do not appear to display the typical features of metal deposition and stripping, such as a nucleation loop for example. The low current densities, poor resolution of voltammetric features, and the absence of a limiting current at a microelectrode all suggest poor electron transfer kinetics for the reduction of Te^{4+}, resulting in slow growth rates of Te. In Fig. 4.9c), a current spike is observed at −2 V, this is possibly associated with the formation of Te^{2-} from deposited Te. Although it is not clear why the current returns to the same levels after the spike. Similar behaviour has been observed in detailed experiments into Te electrochemistry in unpublished works in DCM.[27]

4.5. Electrochemical Quartz Crystal Microbalance

The electrochemical quartz crystal microbalance (EQCM) can be used to monitor changes in mass on the electrode as a function of potential, and this can then be correlated with voltammetric data to gain insight into the nature of deposit growth on the electrode surface. The relation between the change in frequency, Δf, of a resonating quartz crystal as a result of mass added to the surface, Δm, is given by the Sauerbrey equation.[28]

$$\Delta f = -\frac{2f_0^2 \Delta m}{A\left(\rho_q \mu_q\right)^{1/2}} = -C_f \Delta m \tag{4.1}$$

where f_0 is the resonant frequency of the crystal, A is the area of the electrode, ρ_q the density of the quartz crystal and μ_q the shear modulus of the quartz crystal. For a 5 MHz quartz crystal of area 1.33 cm^2 this simplifies to a sensitivity factor, C_f, with a value of 56.6 Hz cm^2 μg^{-1}. This was then used, alongside voltammetry and chronoamperometry, to study the electrodeposition behaviour of Sb, Bi and Te in oDCB and DCE.

4.5.1. $[SbCl_4]^-$

Fig. 4.10 shows a combined voltammogram in black, and massogram in red for an electrolyte of 3 mM $[N^nBu_4][SbCl_4]$ at a Pt electrode in oDCB and DCE. The large electrode size required for the EQCM crystal causes severe distortion in the voltammetry due to the low conductivity of the solvents, this limits the usefulness of the EQCM but features can still be resolved. The potential scale is also the same in both solvents to emphasise this and allow comparison. On the cathodic sweep the mass increases in a linear fashion in both solvents, corresponding to the electrodeposition of Sb, before stripping with a high oxidation efficiency on the reverse sweep. The oxidation efficiency (o.e.), defined as the mass lost in the anodic sweep to the mass gained in the cathodic sweep, was close to 100% in both solvents with values shown in Table 4.2.

Also shown in Fig. 4.10 is the expected mass change, assuming n = 3, calculated from the charge passed. Interestingly in oDCB, on the reverse sweep the observed mass change is greater than the theoretical mass change. This was also reported by Reeves *et al.* for Sb deposition in DCM.[6] Such a phenomenon was investigated further by Bund *et*

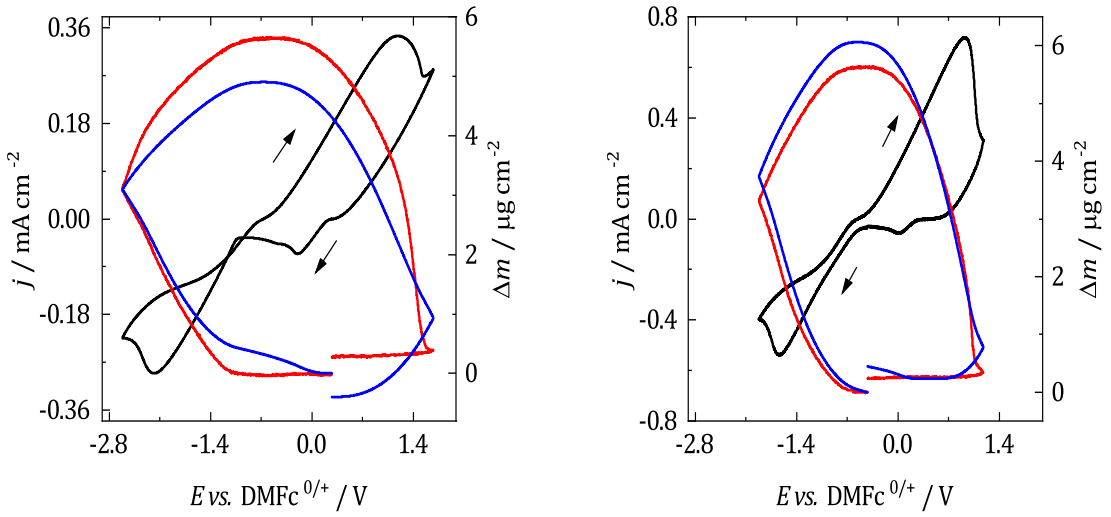

(a) oDCB (b) DCE

Figure 4.10: Combined voltammogram and massogram of 3 mM $[N^nBu_4][SbCl_4]$ with 100 mM $[N^nBu_4]Cl$ at a 5 MHz Pt coated, $r = 0.65$ mm quartz crystal in oDCB and DCE. The potential was scanned beginning at 0.2 V *vs.* DMFc in the direction indicated by the arrows at a scan rate of 50 mV s^{-1}. CE: Pt mesh, RE: Ag/AgCl. Current density shown in black on the left hand y-axis, and on the right hand axis the mass change from the frequency is given in red, and from the charge in blue.

al., using a combined EQCM and AFM study for the electrodeposition of Cu on Au.[29] It was found that this was caused by surface roughness in the electrodeposit. The uneven surface of the deposit trapped solvent molecules in the cavities, causing an apparent increase in the mass loading of the quartz crystal. Therefore it is possible that the Sb deposit from oDCB is rough, and this is the cause of the observed mass being greater than the expected mass. For DCE the observed mass was instead less than the expected mass, which could be due to the electrolysis of impurities or an electrochemical step preceding mass growth. Mechanical stress in the deposit can also influence the frequency change.[28]

The rate of mass growth of Sb from oDCB and DCE was also calculated from chronoamperograms, with values given in Table 4.2. Sb appears to deposit faster in DCE than in oDCB, which can be attributed to the lower viscosity of DCE and larger diffusion coefficient. However, differences in the overpotential of deposition, caused by a greater iR drop in oDCB could also be affecting this, making comparison difficult.

Metal	Solvent	o.e. / %	Growth rate / $ng\,cm^{-2}\,min^{-1}$
Sb	oDCB	95	0.55
	DCE	96	1.11
Bi	oDCB	99	1.08
	DCE	97	2.04
Te	oDCB	-	0.02
	DCE	16	0.17

Table 4.2: Parameters calculated from EQCM voltammograms and chronoamperograms of 3 mM $[N^nBu_4]_{y-x}[M^xCl_y]$, where M=Sb, Bi, Te, in oDCB and DCE containing 100 mM $[N^nBu_4]Cl$ at a $r = 0.65$ mm Pt 5 MHz quartz crystal.

4.5.2. $[BiCl_4]^-$

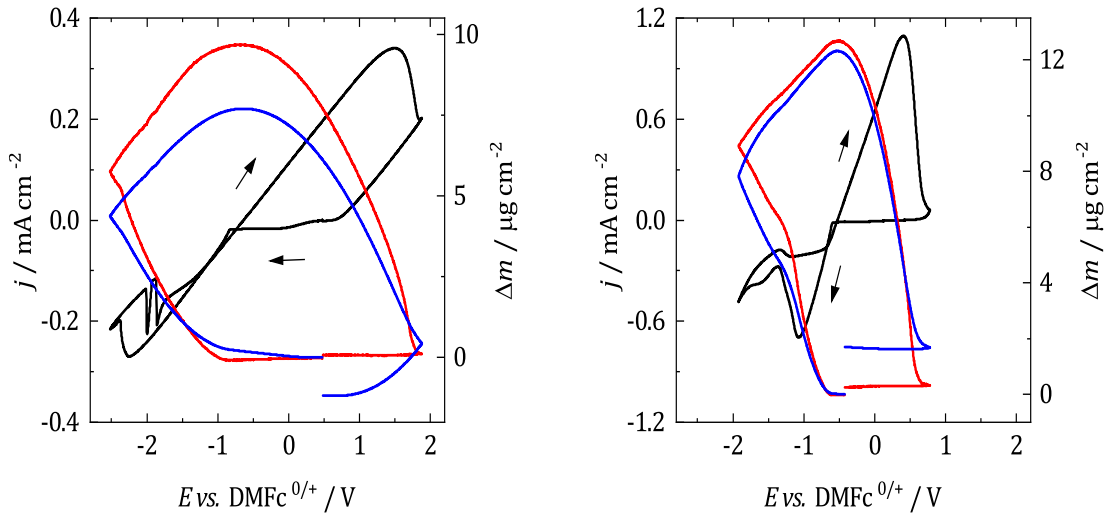

(a) oDCB (b) DCE

Figure 4.11: Combined voltammogram and massogram of 3 mM $[N^nBu_4][BiCl_4]$ with 100 mM $[N^nBu_4]Cl$ at a 5 MHz Pt coated, $r = 0.65$ mm quartz crystal in oDCB and DCE. The potential was scanned beginning at 0.5 V *vs.* DMFc in the direction indicated by the arrows at a scan rate of 50 mV s^{-1}. CE: Pt mesh, RE: Ag/AgCl. Current density shown in black on the left hand y-axis, and on the right hand axis the mass change from the frequency is given in red, and from the charge in blue.

The massograms for Bi deposition, shown in Fig. 4.11 appear similar in form to those for Sb, with simple linear growth and stripping taking place. In oDCB the observed mass is once again greater than the theoretical mass from the charge, which is also attributed to roughness of the deposit surface. In DCE on the other hand, agreement between the actual and expected mass change is reasonable. Bi also appears to grow faster than Sb, in both oDCB and DCE, as evidenced by faster growth rates. Since the diffusion coefficients of the two precursors are similar (see above), this might be indicative of faster electron transfer kinetics for Bi than Sb. However, this may also be an artefact of iR drop, as described above.

None of the unusual features of Bi voltammetry described previously could be observed in Fig. 4.11a, and so understanding of them could not be improved. This is in part because a fresh electrode was not used in the EQCM experiments, and a higher concentration of precursor was also present. Both of which, as shown above, improved the nucleation of Bi on a Pt electrode.

4.5.3. $[TeCl_6]^{2-}$

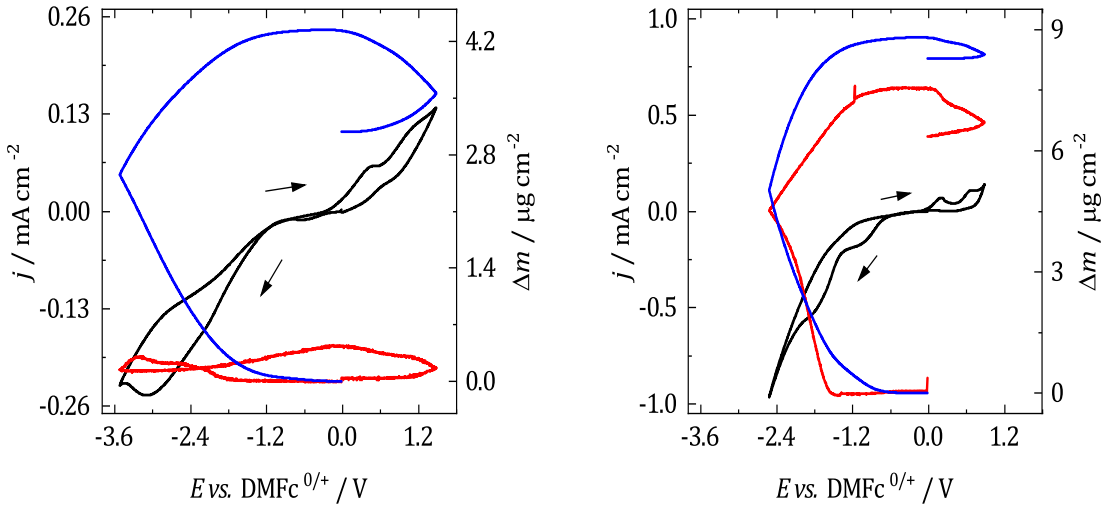

(a) oDCB (b) DCE

Figure 4.12: Combined voltammogram and massogram of 3 mM $[N^nBu_4]_2[TeCl_6]$ with 100 mM $[N^nBu_4]Cl$ at a 5 MHz Pt coated, r = 0.65 mm quartz crystal in oDCB and DCE. The potential was scanned beginning at 0 V *vs.* DMFc in the direction indicated by the arrows at a scan rate of 50 mV s^{-1}. CE: Pt mesh, RE: Ag/AgCl. Current density shown in black on the left hand y-axis, and on the right hand axis the mass change from the frequency is given in red, and from the charge in blue.

Te appears to have quite a different relationship between mass and potential in oDCB and DCE. When depositing from oDCB, a small mass increase is observed, this is then followed by a slight decrease in mass at the most negative potentials. This is possibly evidence for the formation of Te^{2-}. Mass growth then continues on the reverse sweep despite the passage of small amounts of current, before oxidation takes place. A value for o.e. is not given because of the apparent formation of Te^{2-}. The disagreement between observed and expected mass is striking. One potential reason for this is that other electron transfer processes are taking place simultaneously, which do not contribute to mass gain on the electrode. Another possibility is that deposited Te adheres poorly to the Pt substrate. Small black particulates were observed to be suspended in solution at the end of the solution, which could be Te lost from the electrode surface.

From DCE, no mass loss could be observed when the potential was swept across the entire solvent window, suggesting that Te^{2-} forms at potentials more negative than those

available in oDCB. The agreement between actual and theoretical mass change is once again poor, but less so than that observed from oDCB. The same processes are potentially also taking place in DCE, therefore. The growth of Te is quite slow when deposited from both oDCB and DCE. Suggesting slow electron transfer kinetics for Te electrodeposition.

4.6. Electrodeposition

Sb, Bi and Te were successfully deposited onto a TiN substrate from oDCB and DCE. The potential for deposition was determined using a voltammogram with a TiN substrate WE. This was necessary because the deposition substrate was larger than the previously used Pt electrodes, and also more resistive, meaning that the curve was distorted by iR drop effects. The electrode was held at a potential where no reaction occurred before stepping to the appropriate potential for deposition. Deposits were collected with a cutoff of charge passed corresponding to 500 nm material, or 1800 s, whichever came first. This was to ensure that all deposits were of a similar thickness and that there was enough material for characterisation. Table 4.3 shows representative experimental parameters used to collect the deposits. Also shown in Table 4.3 is CR, the 'Charge Rate', which is defined here as:

$$CR = -\frac{Q}{ntA} \tag{4.2}$$

where t is the deposition time. This is an attempt to give an indication of the rate of material growth on the electrode during the electrodeposition process. Typical thickness calculations were avoided because they carry assumptions, such as 100% Faradaic efficiency and formation of a compact film, that could not be verified as valid in the experiments here. It is not possible to fully account for differences in overpotential and iR between the electrolytes, which limits the use of comparison. But generally, deposition appears faster from DCE than oDCB because of its lower viscosity. Bi also appears to deposit the fastest, and Te the slowest.

Metal	Solvent	E_{dep} *vs.* DMFc / V	t / s	$-Q$ / mC	CR / mC cm^{-2} min^{-1}
Sb	oDCB	−2.3	1800	29	2.6
	DCE	−1.7	965	100	16.5
Bi	oDCB	−2.6	1800	67	5.9
	DCE	−1.8	1219	100	13.1
Te	oDCB	−2.4	3600	54	1.8
	DCE	−1.6	1800	7	0.5

Table 4.3: Experimental parameters for the electrodeposition of Sb, Bi and Te onto a TiN substrate from oDCB and DCE containing 3 mM $[N^nBu_4]_{y-x}[M^xCl_y]$ where M = Sb, Bi, Te, and 100 mM $[N^nBu_4]Cl$.

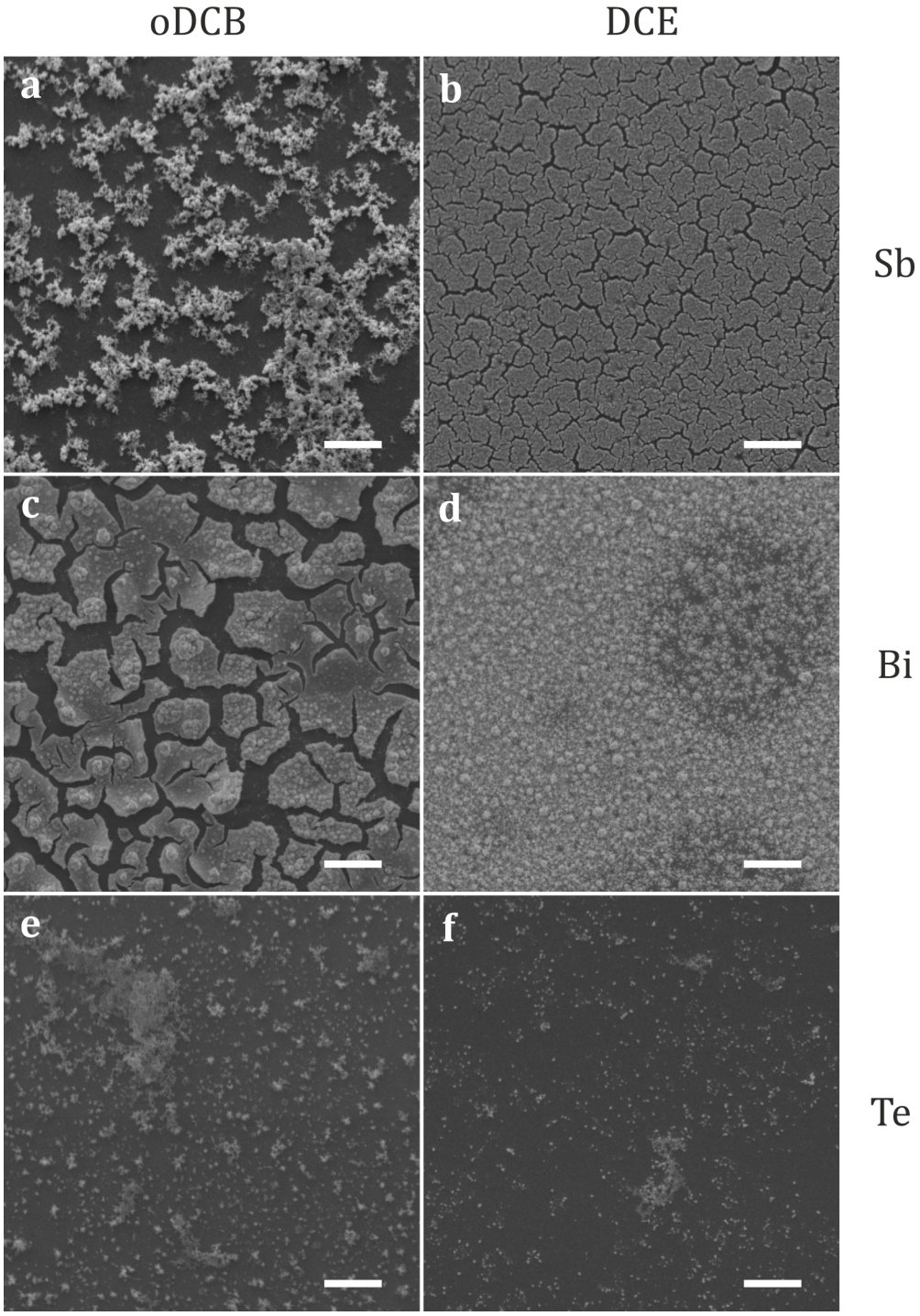

Figure 4.13: SEM images of Sb, Bi and Te electrodeposited onto a r = 2 mm TiN WE from oDCB and DCE containing 3 mM $[N^nBu_4]_{y-x}[M^xCl_y]$ where M = Sb, Bi, Te, with 100 mM $[N^nBu_4]Cl$. a) Sb from oDCB, b) Sb from DCE, c) Bi from oDCB, d) Bi from DCE, e) Te from oDCB, f) Te from DCE. Scale bar represents 10 µm.

Fig. 4.13 shows SEM images of the electrodeposited Sb, Bi and Te onto a TiN substrate. The presence of the desired metal was confirmed by EDX measurements. Clearly the different metals and solvents give rise to a variety of deposit morphologies. Although once again, comparison between metals and solvents is quite difficult because it is not possible to fully correct for differences in overpotential and iR drop. There are uncertainties with the redox potential, as discussed above, meaning that it is not simple to perform depositions at the same overpotential for the different metals. Additionally, differences in solution resistance mean that a given deposition potential corresponds to a different overpotential in oDCB and DCE. It is not obvious how to properly account for both of these issues. For Sb deposited from oDCB, the deposit appears discontinuous, forming clumps of Sb on top of a thin layer of Sb. The Sb deposit from DCE grows more uniformly and forms a continuous, cracked film. For Bi, the film grown from oDCB is cracked giving the appearance of platelets. From DCE, a homogeneous layer of Bi can be seen; interspersed with clumps. Te appears to grow quite poorly from both oDCB and DCE. Small, isolated islands of Te form from both solvents. Interestingly, when Te was deposited from DCM onto a TiN substrate with the same electrolyte composition, a uniform film was reported.[5] It is possible the deposited Te does not adhere well to the substrate surface.

The deposited films were characterised using grazing incidence XRD. Patterns for Sb, Bi and Te can be found in Fig. 4.14. For Sb, a single diffraction peak is observed at *ca.* 28° for the deposits collected from both oDCB and DCE. This corresponds to the primary diffraction peak for elemental Sb and the calculated lattice parameters agree with the literature values, shown in Table 4.4. The peak shape indicates that Sb is amorphous or partially crystalline when deposited from oDCB and DCE at room temperature, and this is reflected in the small crystallite sizes calculated from the peak widths also given in Table 4.4. Since only one peak can be directly attributed to Sb, the Scherrer equation was used to calculate the crystallite sizes. Reeves *et al.* also reported the electrodeposition of amorphous Sb from DCM with a similar electrolyte composition, in agreement with the results here.[6] However interestingly, Bartlett *et al.* observed that Sb electrodeposits in a crystalline form using the same electrolyte.[5] The reason for such discrepancies is not clear, but one possibility is the occurrence of explosive Sb.[30,31]

Far more intense diffraction peaks are observed for the spectra collected from the deposited Bi, in the same positions as the literature record. The pattern was successfully indexed as elemental Bi, and the large crystallite sizes indicates the presence of crystalline Bi. The same is observed for Te and crystalline Te appears to form also.

Raman spectroscopy is a complementary technique to XRD. Raman active materials give characteristic spectra, and information can be gained on the crystallinity of the material also. Fig. 4.15 shows representative Raman spectra for Sb, Bi and Te electrodeposited from oDCB and DCE. For Sb, a single broad peak occurs at 142 cm^{-1} and 152 cm^{-1} for oDCB and DCE respectively. Literature results report two peaks at 115 cm^{-1} and 150 cm^{-1} for crystalline Sb,[32] suggesting that the spectra shown here correspond to amorphous Sb.

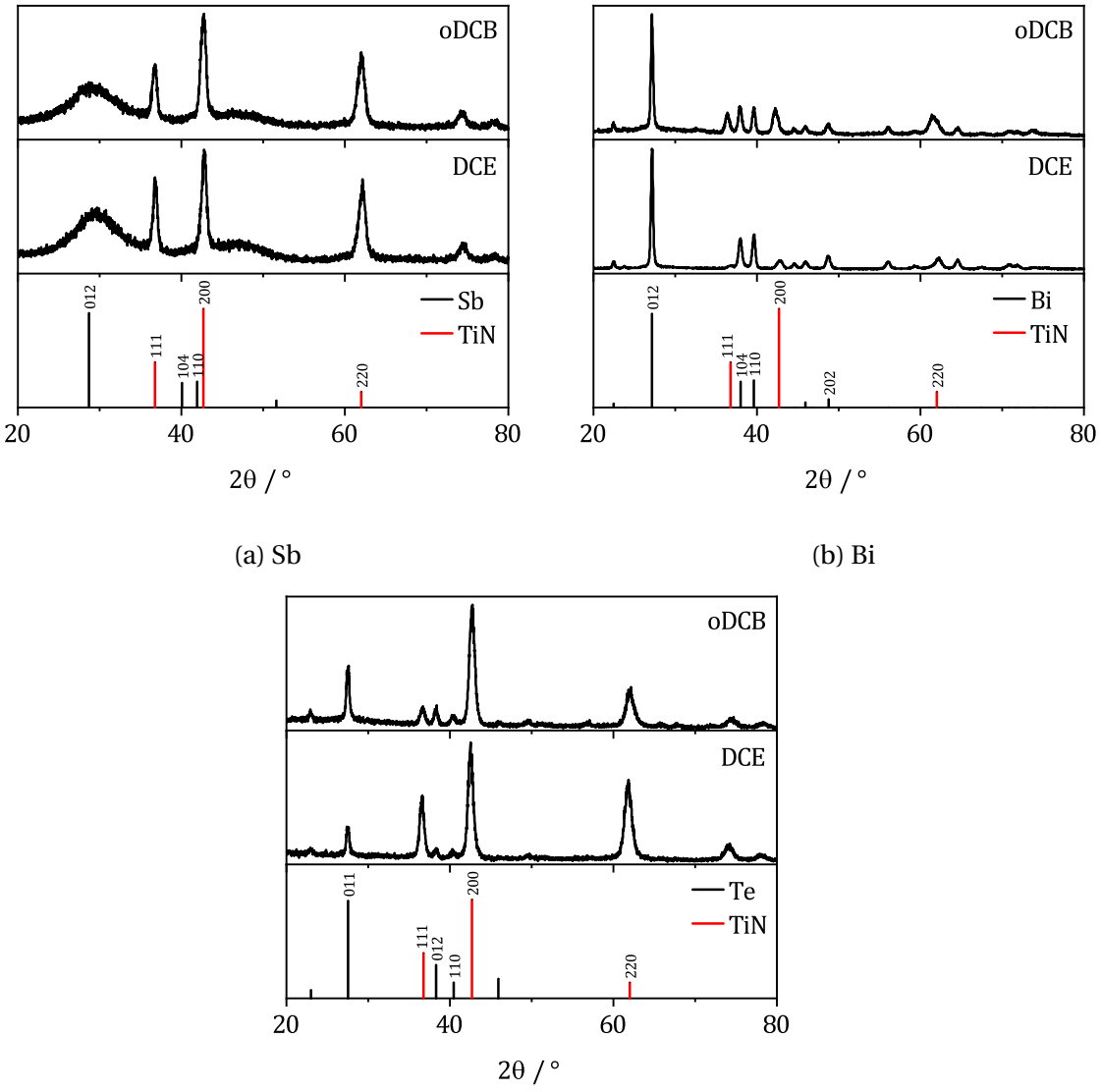

(a) Sb

(b) Bi

(c) Te

Figure 4.14: Grazing incidence XRD patterns of a) Sb, b) Bi, c) Te electrodeposited from oDCB and DCE onto a TiN substrate. Deposits were collected at room temperature from an electrolyte containing 3 mM $[N^nBu_4]_{y-x}[M^xCl_y]$ where M = Sb, Bi, Te, and 100 mM $[N^nBu_4]Cl$. The bottom panel shows in black: the metal's literature XRD pattern and in red: the same for the substrate. Sb: ICSD 64695, Bi: ICSD 64703, Te: ICSD 96502, TiN: ICSD 152807.

The spectra collected of deposited Bi display two peaks with maxima at 75 and 99 cm^{-1} from oDCB and 71 and 96 cm^{-1} from DCE. These are in agreement with previous measurements in the literature,[32,33] and the peaks correspond to the E_g and A_{1g} Raman bands of crystalline Bi. For Te, two peaks are also observed at 122 and 140 cm^{-1} for the deposits collected from both oDCB and DCE. Peaks at similar locations were also reported by Pine and Dresselhaus, and by Bartlett *et al.*[32,34] The peaks are associated with the A_1 and E_2 Raman modes of crystalline Te. Bartlett *et al.* also recorded a minor peak at 92 cm^{-1} associated with the E_1 Raman band and this can be weakly observed in Fig. 4.15c also.[32]

Metal	Solvent	$a = b$ / Å	c / Å	Crystallite size / Å
Sb	oDCB	4.24(7)	11.4(2)	13.4(3)[a]
	DCE	4.23(1)	10.3(1)	8.8(11)[a]
	lit.[b]	4.31	11.3	
Bi	oDCB	4.55(1)	11.9(1)	180(49)[c]
	DCE	4.55(1)	11.8(1)	208(48)[c]
	lit.[d]	4.55	11.9	
Te	oDCB	4.44(2)	6.0(1)	230(73)[c]
	DCE	4.45(3)	5.9(1)	226(17)[c]
	lit.[e]	4.46	5.9	

Table 4.4: Lattice parameters and average crystallite sizes for electrodeposited Sb, Bi and Te refined from XRD patterns, along with literature values. [a]: Obtained using the Scherrer method, [b]: ICSD 64695, [c]: Obtained using the Halder-Wagner method, [d]: ICSD 64703, [e]: ICSD 96502.

Although it must be noted that the features at lower wavenumbers are close to the cutoff for the spectrometer and must be interpreted with care.

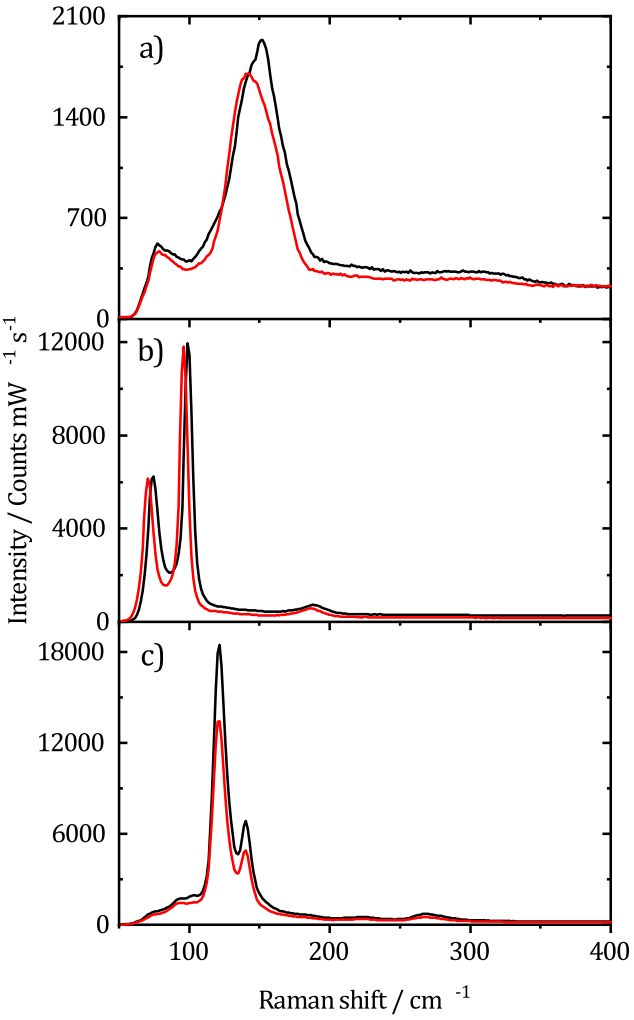

Figure 4.15: Representative Raman spectra of a) Sb, b) Bi, c) Te electrodeposited from oDCB and DCE. Collected using a 785 nm excitation laser and presented without background correction. Intensity normalised by collection time and laser power. Black: oDCB, red: DCE.

4.7. Conclusions

This Chapter intended to further characterise the candidate solvents to assess their suitability as solvents for electrodeposition. To this end, the electrochemistry of $[SbCl_4]^-$, $[BiCl_4]^-$ and $[TeCl_6]^{2-}$ was studied using voltammetry at macro- and microelectrodes. $[SbCl_4]^-$ was found to broadly display simple deposition and stripping behaviour. As was $[BiCl_4]^-$, although with some unexplained features in the voltammetry. Microelectrodes were used to calculate the redox potential and diffusion coefficient of two species in DCM, oDCB and DCE. The redox potentials and Stokes-Einstein plots indicated that the precursors were ion paired in solution. On the other hand, $[TeCl_6]^{2-}$ electrochemistry appeared more complicated, there was an indication of irreversibility and a limiting current did not form at a microelectrode. There was also evidence to suggest the formation of Te^{2-}. EQCM was used to monitor the mass changes as a function of potential, the results appeared to

support the conclusions drawn from the voltammetry.

This Chapter also demonstrated the successful electrodeposition of Sb, Bi and Te from oDCB and DCE. The first report of metal electrodeposition from the two solvents. Sb and Bi were found to deposit with good coverage, with the deposit morphology appearing rougher in oDCB than in DCE. However, Te grew patchily, with poor electron transfer kinetics. Although comparison is difficult due to the effects of iR drop. XRD and Raman spectroscopy showed that Sb deposited in an amorphous or partially crystalline form at room temperature, with small grain sizes. Whereas Bi and Te appeared crystalline. oDCB and DCE were chosen because they were expected to behave similarly to DCM and this Chapter demonstrates that this is true for the electrodeposition of metals. The solvents are now ready for attempts at semiconductor electrodeposition, which will be the focus of subsequent Chapters. Additionally, the added advantage of the two studied solvents is that they have a higher boiling point, creating the possibility of electrodepositing the metals at higher temperatures in the future.

4.8. References

(1) Y. N. Sadana, J. P. Singh and R. Kumar, *Surf. Technol.*, 1985, **24**, 319–353.

(2) A. M. Marzo, R. Gusmão, Z. Sofer and M. Pumera, *Chem. - A Eur. J.*, 2020, **26**, 6583–6590.

(3) M. H. Yang and I. W. Sun, *J. Appl. Electrochem.*, 2003, **33**, 1077–1084.

(4) J. Bu, J. Ru, Z. Wang, Y. Hua, C. Xu, Y. Zhang and Y. Wang, *Adv. Powder Technol.*, 2019, **30**, 2859–2867.

(5) P. N. Bartlett, D. Cook, C. H. de Groot, A. L. Hector, R. Huang, A. Jolleys, G. P. Kissling, W. Levason, S. J. Pearce and G. Reid, *RSC Adv.*, 2013, **3**, 15645–15654.

(6) S. J. Reeves, Y. J. Noori, W. Zhang, G. Reid and P. N. Bartlett, *Electrochim. Acta*, 2020, **354**, 136692.

(7) A. Brenner, *Electrodeposition of Alloys II*, Academic Press, London, 1963.

(8) A. H. Jaafar, L. Meng, Y. J. Noori, W. Zhang, Y. Han, R. Beanland, D. C. Smith, G. Reid, K. De Groot, R. Huang and P. N. Bartlett, *J. Phys. Chem. C*, 2021, **125**, 26247–26255.

(9) K. Tittes and W. Plieth, *J. Solid State Electrochem.*, 2007, **11**, 155–164.

(10) E. Fahrenkrug, J. Rafson, M. Lancaster and S. Maldonado, *Langmuir*, 2017, **33**, 9280–9287.

(11) M. Yang and Z. Hu, *J. Electroanal. Chem.*, 2005, **583**, 46–55.

(12) E. Sandnes, M. E. Williams, U. Bertocci, M. D. Vaudin and G. R. Stafford, *Electrochim. Acta*, 2007, **52**, 6221–6228.

(13) S. I. Córdoba De Torresi and I. A. Carlos, *J. Electroanal. Chem.*, 1996, **414**, 11–16.

(14) A. Królicka and A. Bobrowski, *Electrochem. commun.*, 2004, **6**, 99–104.

(15) P. Magri, C. Boulanger and J.-M. Lecuire, *J. Mater. Chem.*, 1996, **6**, 773–779.

(16) Y. Du, G. Qiu, Y. Wang, M. Si, X. Xu, W. Wu and P. D. Ye, *Nano Lett.*, 2017, **17**, 3965–3973.

(17) T. Wu, J. Kim and N. V. Myung, *Front. Chem.*, 2020, **8**, 1–10.

(18) Y. Liftman, M. Albeck, J. M. E. Goldschmidt and C. Yarnitsky, *Electrochim. Acta*, 1984, **29**, 1673–1678.

(19) Y. Liftman and M. Albeck, *Electrochim. Acta*, 1985, **30**, 381–385.

(20) C. Graf, A. Assoud, O. Mayasree and H. Kleinke, *Molecules*, 2009, **14**, 3115–3131.

(21) Norman A. D., *Inorganic Reactions and Methods, Volume 6: Formation of Bonds to O, S, Se, Te, Po, Part 2*, Wiley-VCH, Weinheim, 2009.

(22) M. A. Ansari and J. A. Ibers, *Coord. Chem. Rev.*, 1990, **100**, 223–266.

(23) P. T. Kalisman, Ph.D. Thesis, University of California, Berkeley, 2012.

(24) W. M. Haynes, D. R. Lide and T. J. Bruno, *CRC Handbook of Chemistry and Physics*, CRC Press, New York, 96th edn., 2016.

(25) G. Y. Ahlijah and M. Goldstein, *J. Chem. Soc. A*, 1970, 326.

(26) Y. H. Zhao, M. H. Abraham and A. M. Zissimos, *J. Chem. Inf. Comput. Sci.*, 2003, **43**, 1848–1854.

(27) D. A. Cook and P. N. Bartlett, *Personal communication*, 2022.

(28) A. R. Hillman, *J. Solid State Electrochem.*, 2011, **15**, 1647–1660.

(29) A. Bund, O. Schneider and V. Dehnke, *Phys. Chem. Chem. Phys.*, 2002, **4**, 3552–3554.

(30) C. C. Coffin, *Proc. R. Soc. Lond. A*, 1935, **152**, 47–63.

(31) S. G. Vadchenko, D. Y. Kovalev, A. S. Shchukin and A. S. Rogachev, *Int. J. Self-Propagating High-Temperature Synth.*, 2018, **27**, 180–183.

(32) P. N. Bartlett, J. Burt, D. A. Cook, C. Y. Cummings, M. W. George, A. L. Hector, M. M. Hasan, J. Ke, W. Levason, D. Pugh, G. Reid, P. W. Richardson, D. C. Smith, J. Spencer, N. Suleiman and W. Zhang, *Chem. - A Eur. J.*, 2016, **22**, 302–309.

(33) K. Trentelman, *J. Raman Spectrosc.*, 2009, **40**, 585–589.

(34) A. S. Pine and G. Dresselhaus, *Phys. Rev. B*, 1971, **4**, 356–371.

5

Electrodeposition of Antimony Telluride and Bismuth Telluride

5.1. Overview

This Chapter describes further investigations into electrodeposition from oDCB and DCE. The electrodeposition of Sb_2Te_3 and Bi_2Te_3 is attempted in order to assess the possibility of semiconductor electrodeposition from the studied solvents. The resulting deposits are characterised using SEM, EDX and XRD and the mechanism of codeposition from both solvents is discussed.

5.2. Introduction

Previous Chapters demonstrated the feasibility of electrochemistry in oDCB and DCE by use of model redox couples. Firstly the outer-sphere, solution based DMFc and $CcPF_6$ in Chapter 3, then the more complex deposition and stripping processes of Sb^{3+} and Bi^{3+} in Chapter 4. In this Chapter, further characterisation of the solvents is performed, using the most complex system which will be required of the solvents: the codeposition of two elements to form a compound. For this purpose, the electrodeposition of antimony telluride and bismuth telluride are chosen as model systems. The preparation of both by electrodeposition has been reported extensively in the literature in both aqueous and non-aqueous systems, and their stoichiometric deposition is readily achieved. The successful deposition of antimony telluride and bismuth telluride would therefore prove the suitability of oDCB and DCE as WCS for semiconductor electrodeposition.

Bismuth telluride deposition presents a process which is well understood but possesses some desirable properties which have yet to be achieved, primarily in its application as a thermoelectric material and in the realm of nanowires. Fabrication of wires of a sufficiently small diameter is predicted to significantly improve the thermoelectric properties of Bi_2Te_3.[1] A common problem in nanowire fabrication by electrodeposition is pore wetting and consequent inconsistent filling of the pores. Supercritical fluids (scf's) have a low viscosity and are a single phase, therefore removing any surface tension at interfaces. As such, nanowire growth should be significantly improved from a scf. Supercritical difluoromethane (scDFM) is also employed in this Chapter as a solvent for the attempted electrodeposition of Bi_2Te_3.

5.2.1. Electrodeposition of Antimony Telluride

The first report of Sb_2Te_3 thin film electrodeposition was from aqueous electrolytes in 2003 by Leimkühler *et al.*[2] Since then, several other reports of aqueous electrodeposition have emerged.[3–8] Depositions are typically performed under acidic conditions, in order to improve the solubility of the Sb and Te precursor.[2] Tartaric acid is also almost always employed as a chelating agent to increase the solubility of the Sb precursor even further.[8] In an acidic aqueous electrolyte, Sb_2Te_3 deposits according to

$$2\,SbO^+ + 3\,HTeO_2^+ + 13\,H^+ + 18\,e^- \longrightarrow Sb_2Te_3 + 8\,H_2O$$

Work in aqueous electrolytes has generally focussed on the effect of deposition potential and precursor concentration. The standard reduction potentials of Sb and Te are given below.[2]

$$SbO^+ + 2\,H^+ + 3\,e^- \longrightarrow Sb + H_2O,\ E^0 = 0.212\ \text{V}\ \textit{vs.}\ \text{SHE}$$
$$HTeO_2^+ + 3\,H^+ + 4\,e^- \longrightarrow Te + 2\,H_2O,\ E^0 = 0.551\ \text{V}\ \textit{vs.}\ \text{SHE}$$

Codeposition of stoichiometric Sb_2Te_3 is generally possible at potentials shortly after the onset of Te deposition, but more anodic than the onset of Sb deposition,[2,6] and continues until the potential at which Sb deposition begins is reached.[4,6] The compositions of codeposits collected close to the Te onset potential therefore have a Te content > 60%, before decreasing with potential until deposits with 60% Te are achieved. The composition of the deposits then becomes approximately independent of potential,[3] up to the onset of Sb deposition, at which point the films become Sb rich.[6]

There is less available information on the effect of the precursor concentration. The scope for varying the precursor concentrations in the electrolyte is limited because of the poor solubility of both precursors. Typically, an excess of Sb^{3+} over Te^{4+} has been reported to be necessary for the stoichiometric deposition of Sb_2Te_3, with a Sb^{3+}/Te^{4+} ratio of at least 2.[8] However, Sb_2Te_3 has also been successfully deposited from an equimolar electrolyte.[3] This variation is likely caused by the interdependence of the factors affecting deposition composition, and differences in tartaric acid concentration or pH, for example.

The resulting deposited film of Sb_2Te_3 is amorphous when deposited at room temperature, and annealing is necessary to produce crystalline material.[3,4] However, it has been found to be possible to deposit crystalline Sb_2Te_3 at room temperature, with use of a rotating disc electrode and high rates of agitation,[6] or with a pulsed deposition routine.[7] Alternatively, crystalline Sb_2Te_3 has also been achieved by performing the deposition at 100 °C, rather than room temperature.[2]

There are even fewer reported studies of antimony telluride deposition in non-aqueous solvents. Nguyen *et al.* reported the deposition of non-stoichiometric antimony telluride alloys from an acetamide eutectic.[9] Wu *et al.* also reported the deposition of Sb_2Te_3 from ethylene glycol,[10] and Catrangiu *el al.* deposited antimony telluride alloys from an oxalic acid-choline chloride deep eutectic solvent.[11] The deposition reaction from aprotic solvents is now

$$2\,Sb^{3+} + 3\,Te^{4+} + 18\,e^- \longrightarrow Sb_2Te_3$$

In acetamide, depositions were performed galvanostatically. The Te content decreased with increasing current density, and it was found that lower current densities and an equimolar electrolyte were necessary to achieve the appropriate Te content in the deposit. Close to stoichiometric antimony telluride could be deposited from ethylene glycol with equal concentrations of reagent at the most negative potentials of the range studied. Deposits with the correct composition for Sb_2Te_3 were not obtained from the deep eutetic solvent. However, deposits with a nearly stoichiometric composition were achieved from an electrolyte with an excess of the Te reagent, at a Sb-Te precursor ratio of 0.63, with an applied potential slightly anodic of the onset of Sb deposition. Finally, Cicvaric recently presented work on the electrodeposition of Sb_2Te_3 from DCM.[12] Depositions were performed from a chloride based electrolyte containing 2 mM $[N^nBu_4][SbCl_4]$ and 3 mM $[N^nBu_4]_2[TeCl_6]$. The deposit composition displayed little variation with potential over

the range studied, even at potentials more negative than the onset of Sb deposition. The resulting films were smooth with cracks throughout the surface, and a pulsed potential waveform was used to produce dense and compact deposits. The as deposited films were amorphous at room temperature, and crystalline material was achieved by annealing.

Little dedicated work has been performed on the mechanism of Sb_2Te_3 electrodeposition, however it is possible to gain insight from the more general reports. Codeposition of Sb and Te can be observed at potentials more positive than the onset of Sb deposition. This is indicative of the presence of deposited Te inducing the deposition of Sb, an anodic potential shift driven by the gain in free energy as a result of alloy formation. Taking ΔG_f^0 as $-57.5\,\mathrm{kJ\,mol^{-1}}$,[2] gives an expected positive shift in the onset of Sb deposition of $|-57500/3\mathrm{F}| = 200\,\mathrm{mV}$. Inspection of the standard potentials for the deposition of Sb and Te gives $\Delta E = 350\,\mathrm{mV}$. This is greater than the $\Delta G_f^0/am\mathrm{F}$ limit, which has a value of 99 mV. Where a is 2, the number of Sb atoms in Sb_2Te_3, and m is 3, the number of electrons required to deposit Sb.[13] Suggesting that Sb-Te is a Kröger Class 1 system.[13] According to Kröger, a Class 1 system requires the species which is more difficult to deposit to be in excess in the electrolyte. Which in aqueous conditions corresponds to Sb. Compound deposition is then possible in the potential range positive of the onset of Sb deposition. In the theory of Kröger it is important to have an excess of Sb^{3+} in the electrolyte, otherwise the deposition of Te would dominate in the codeposition region. This would appear to be in agreement with the experimental results described above, where Sb^{3+} is typically present in larger concentrations than Te^{4+} in the electrolyte. The deposition composition is also approximately independent of potential in the codeposition region, except for potentials close to the onset of Te deposition where Te is favoured, and potentials negative of the onset of Sb deposition where Sb is favoured. Which is also in agreement with expectations. Conversely, in non-aqueous electrolytes the concentration of the Te reagent is required to be present in larger concentrations than the Sb precursor to achieve Sb_2Te_3. The redox potentials of Sb^{3+} and Te^{4+} are less well studied in non-aqueous solvents, but the experimental results would suggest that Sb-Te remains a Class 1 system where Te is now more difficult to deposit.

5.2.2. Electrodeposition of Bismuth Telluride

The electrodeposition of bismuth telluride (Bi_2Te_3) films in aqueous conditions was first achieved by Takahashi in 1993.[14] Since then there has been significant research into various features of the plating process, including: the influence of reagent concentrations and applied potential on the deposit composition,[14–19] the mechanism of deposition,[17,19–22] the influence of pulsing the potential[23–25] and the effect of surfactant on morphology and crystal orientation.[26–29]

Typically in aqueous electrodeposition experiments, compounds of Bi and Te are dissolved in concentrated nitric acid, such that the electroactive species in solution are Bi^{3+} and $HTeO_2^+$. The overall reaction for the electrodeposition of bismuth telluride from

acidic aqueous conditions is therefore:

$$2\,Bi^{3+} + 3\,HTeO_2^+ + 9\,H^+ + 18\,e^- \longrightarrow Bi_2Te_3 + 6\,H_2O$$

To achieve stoichiometric deposition of Bi_2Te_3, it has been reported that an excess of $HTeO_2^+$ over Bi^{3+} in the electrolyte is required. Takahashi observed that at pH 1 onto a Ti electrode, a concentration ratio of Bi/Te 1/1.4 was necessary for a deposit of stoichiometric compostion.[14] Additionally, Liu deposited Bi_2Te_3 at pH 0.1 onto a Pt substrate using Bi/Te concentrations in the ratio 1/1.3.[18] Conversely Magri reported that at pH 0 with a stainless steel working electrode, increasing the Bi/Te ratio to 1/0.75 was required to deposit Bi_2Te_3.[15] Michel *et al.* observed similar results to Magri under the same conditions.[30]

The required concentration of Bi and Te species to deposit Bi_2Te_3 is variable and it appears necessary to consider the nature of the substrate when designing an electrolyte. But typically a small excess of $HTeO_2^+$ over Bi^{3+} in the electrolyte appears to be best for stoichiometric Bi_2Te_3 deposition (Bi/Te 1/1.2-1.4), and the results reported by Magri and Michel seem to be unique to the stainless steel substrate. One reason for the difference might be the lattice structure of steel, or perhaps a galvanic reaction between Te(IV) and steel.

The relationship between applied potential and deposit composition appears to be simpler. The Bi content of the deposit generally increases with decreasing potential. This can be expected since the deposition potential of Bi is lower than Te:[31,32]

$$Bi^{3+} + 3\,e^- \longrightarrow Bi,\ E^0 = 0.308\ V\ \textit{vs.}\ SHE$$
$$HTeO_2^+ + 3\,H^+ + 4\,e^- \longrightarrow Te + 2\,H_2O,\ E^0 = 0.551\ V\ \textit{vs.}\ SHE$$

As the applied potential increases, so does the overpotential for Bi deposition and therefore an increase in the rate of Bi deposition is observed. This relationship has numerous reports in the literature.[17,30,33] However the actual increase in Bi content is quite low, for example Martín-González *et al.* reported 5% over 400 mV,[17] so there does not appear to be a strong relationship between composition and potential.

Whilst the overall reaction above appears simple, the mechanism, and theoretical explanation is more complex. Martín-González *et al.* reported that initially $[HTeO_2]^+$ was adsorbed on the surface of the Pt electrode and electrochemically reduced to Te^0. Bi^{3+} in solution then reacts with the deposited Te to form Bi_2Te_3, the driving force being the gain in free energy as a result of compound formation ($\Delta G_f^0(Bi_2Te_3) = -16.56\,kJ\,mol^{-1}$):[34]

$$3\,Te_{(s)} + 2\,Bi^{3+}_{(aq)} + 6\,e^- \longrightarrow Bi_2Te_{3(s)}$$

in a similar fashion to Sb_2Te_3 deposition above. Since the deposition potentials of the two precursors are reasonably close together, Bi-Te is expected to be a Kröger Class 2 type sys-

tem. When the activities (concentrations) of the two metal ions in solution are similar, the relationship between current and potential is similar to that for a Class 1 system.[13] Since Te is depositing as a consequence of a chemical reaction, this additionally helps to explain the observed relationship between composition and potential. It was also observed that compound deposition began at potentials more anodic than that at which either of the species deposit individually.[17] This is a feature of Engelken's 'Pure Underpotential Deposition' (PUD) model, as described in Chapter 1, and of Kröger Class 2 systems too. Indications of the Kröger mechanism and a positive shift in codeposition potential can be observed in other publications, even if the works of Kröger and Engelken are not addressed directly.[18,19,21,35,36]

Non-aqueous electrodeposition of Bi_2Te_3 films has received comparatively less research, but deposition has been achieved from dimethylsulphoxide (DMSO),[37,38] ethylene glycol (EG),[39] choline chloride-oxalic acid Deep Eutectic Solvent,[40] and DCM.[41] The solvents are aprotic so the deposition reaction changes:

$$2\,Bi^{3+} + 3\,Te^{4+} + 18\,e^- \longrightarrow Bi_2Te_3$$

As in aqueous conditions, a slight excess of Te over Bi in the electrolyte appears to be most appropriate for stoichiometric deposition of Bi_2Te_3. From a solution of Bi/Te 1/1.3, Abellan deposited Bi_2Te_3 of almost perfect stoichiometry onto FTO from DMSO.[38] Meng observed similar results in DCM, depositing Bi_2Te_3 onto TiN using an electrolyte composition Bi/Te 1/1.2.[41] Bi content in the deposit was found to increase with decreasing Bi/Te electrolyte ratio, as reported in aqueous solutions. This trend is also supported by the work of Nguyen in EG.[39]

The influence of deposition potential on deposit composition appears to be the same as in aqueous conditions. Meng found little variation in composition with applied potential over a wide deposition range (1.4 V). Li in DMSO and Nguyen in EG both reported a general increase in Bi content with increasing cathodic deposition potential.

The mechanism of deposition seems less clear in non-aqueous solvents, deposition potentials can shift depending on the speciation in solution and are not always close to each other. For example in DCM, voltammograms indicate the deposition potentials are similar and a positive shift in the onset of codeposition can be observed, suggesting that the PUD and induced codeposition mechanism is taking place. However in DMSO, from the work of Li, the difference in deposition potential is less than 250 mV and no positive shift in deposition potential can be observed. On the other hand, Abellan's investigation into DMSO showed $\Delta E \approx 300$ mV, but a slight anodic shift in deposition potential can be observed. Factors such as the substrate might be having an influence in this situation. It is likely that deposition in all the non-aqueous solvents occurs *via* some form of the induced codeposition mechanism.

The objective in this Chapter is to attempt the electrodeposition of semiconductors

from the candidate solvents oDCB and DCE to assess their capabilities for this application. Antimony telluride and bismuth telluride are to be used as model systems. The voltammetry of their precursors will be studied and the effect of potential on the composition and material properties of the deposit will be investigated.

5.3. Antimony telluride

5.3.1. Electrochemistry

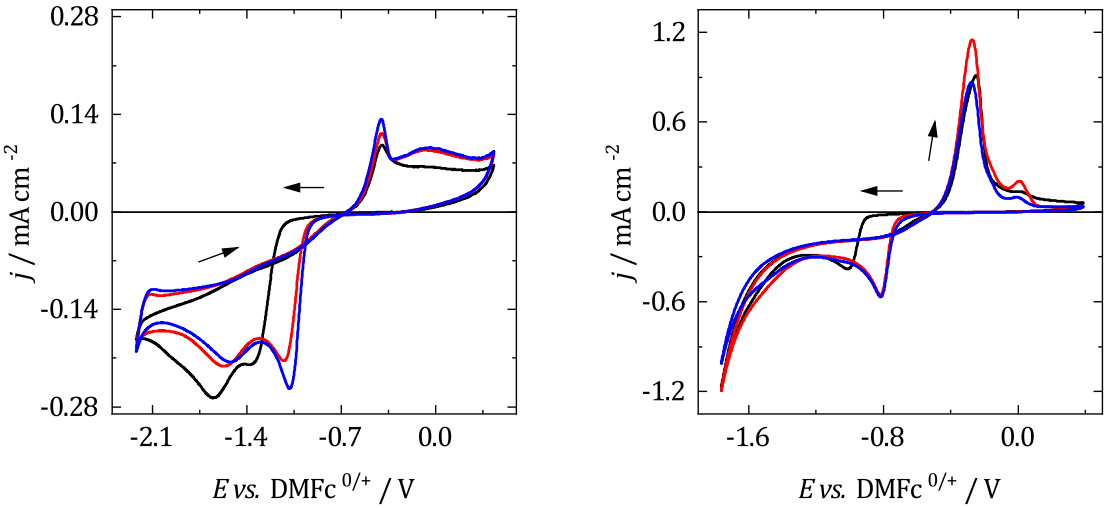

(a) oDCB (b) DCE

Figure 5.1: Voltammograms of a mixed 1 mM $[N^nBu_4][SbCl_4]$ and 1 mM $[N^nBu_4]_2[TeCl_6]$ electrolyte with 100 mM $[N^nBu_4]Cl$ in oDCB and DCE. WE was swept from 0.2 V *vs.* DMFc at 50 mV s^{-1} in the direction indicated by the arrows. CE: Pt grid, RE: Ag/AgCl, WE: r = 0.25 mm Pt disc. Black: scan 1, red: scan 2, blue: scan 3.

Fig. 5.1 shows voltammograms of a mixed $[SbCl_4]^-$ and $[TeCl_6]^{2-}$ precursor electrolyte at a Pt macrodisc in oDCB and DCE. Scanning negatively in oDCB, reduction begins at *ca.* −1.2 V *vs.* DMFc with a peak emerging at approximately −1.3 V. As the scan continues, a second peak emerges at −1.7 V. On the reverse sweep a nucleation loop is present, suggesting that the cathodic current is the electrodeposition of a Sb and Te codeposit. A single stripping peak is then observed, along with a broad shoulder, suggesting the stripping of crystalline and amorphous material. The first scan has relatively poor oxidation efficiency (o.e.) of 20%. On the second and third scans, the onset potential shifts anodically to *ca.* −1 V, further evidence of deposition taking place since reduction is easier when material is already nucleated on the electrode surface. The two reduction peaks are also shifted slightly anodically, and more easily resolved.

For DCE, deposition begins at a slightly more positive potential of −0.9 V. Only one reduction peak is observed on the cathodic sweep; scanning further in the negative direction results in an increase in current, but it is indistinguishable from the eventual onset

of electrolyte decomposition. The reduction is presumably associated with the codeposition of Sb and Te, as in oDCB. On the forward scan, a single sharp stripping peak occurs with an o.e. of 28%, similar to but slightly higher than oDCB.

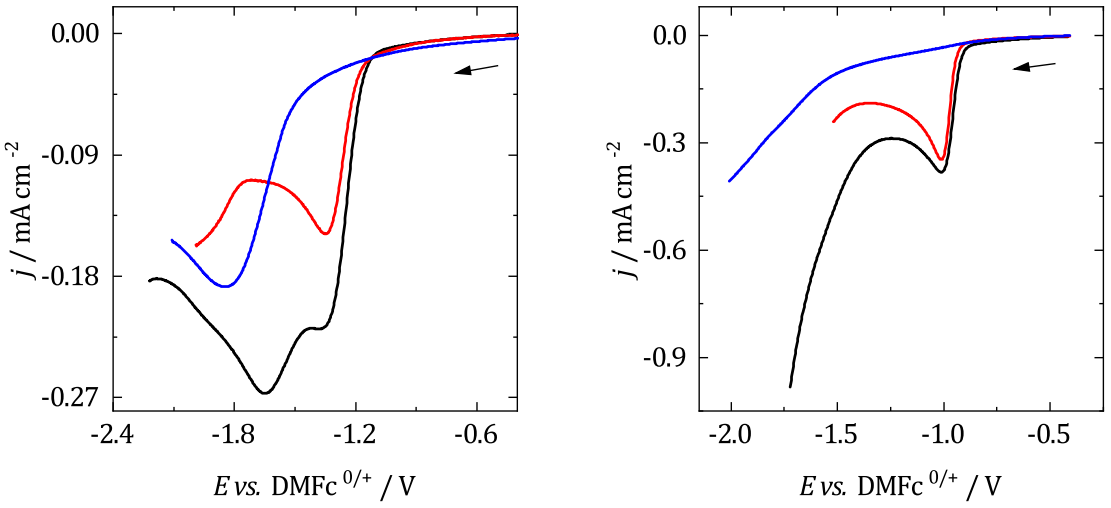

(a) oDCB (b) DCE

Figure 5.2: Voltammograms of a mixed 1 mM $[N^nBu_4][SbCl_4]$ and $[N^nBu_4]_2[TeCl_6]$ electrolyte overlaid with voltammograms of 1 mM of the individual precursors, along with 100 mM $[N^nBu_4]Cl$ in oDCB and DCE. WE was swept from 0.2 V *vs.* DMFc at 50 mV s^{-1} in the direction indicated by the arrows. CE: Pt grid, RE: Ag/AgCl, WE: $r = 0.25$ mm Pt disc. Black: 1 mM $[N^nBu_4][SbCl_4]$ and 1 mM $[N^nBu_4]_2[TeCl_6]$, red: 1 mM $[N^nBu_4][SbCl_4]$, blue: 1 mM $[N^nBu_4]_2[TeCl_6]$.

Understanding of the electrochemical processes taking place in the mixed electrolyte system, and the nature of the voltammetric peaks can be improved by overlaying the voltammogram of the mixed electrolyte with those of the individual precursors, and also by changing the concentration of the metal precursors in the mixed electrolyte. Fig. 5.2 shows a sweep in the cathodic direction for each metal precursor and also the combined electrolyte, Fig. 5.3 shows the effect of varying concentration. In oDCB, the first reduction peak in the mixed electrolyte has similar onset and peak potentials to that for $[SbCl_4]^-$ only. Furthermore, the height of the same peak increases significantly when the concentration of $[SbCl_4]^-$ is increased in Fig. 5.3a, suggesting that this peak is associated with the electrodeposition of Sb. The second peak in the mixed electrolyte approximately coincides with the onset of Te deposition, indicating those peaks are associated with each other. It therefore appears possible to conclude that as the potential is decreased in the mixed electrolyte, Sb deposition begins which is then followed by Te deposition. However the current density in the mixed electrolyte is greater than for either of the individual precursors, Sb^{3+} and Te^{4+} depositing individually suggesting that the additional current is a result of the formation of a mixed Sb/Te phase.

Upon inspection of the overlays in DCE, it can be seen that the first reduction peak agrees well with that for the deposition of Sb. No peak is observed for Te reduction and this is reflected in the voltammetry of the mixed electrolyte. The current density is greater however, suggesting the presence of co-deposition. The voltammetry does not appear to change significantly when increasing the concentration of either precursor, the peak current of the first reduction peak is slightly increased, as is the current at more negative potentials.

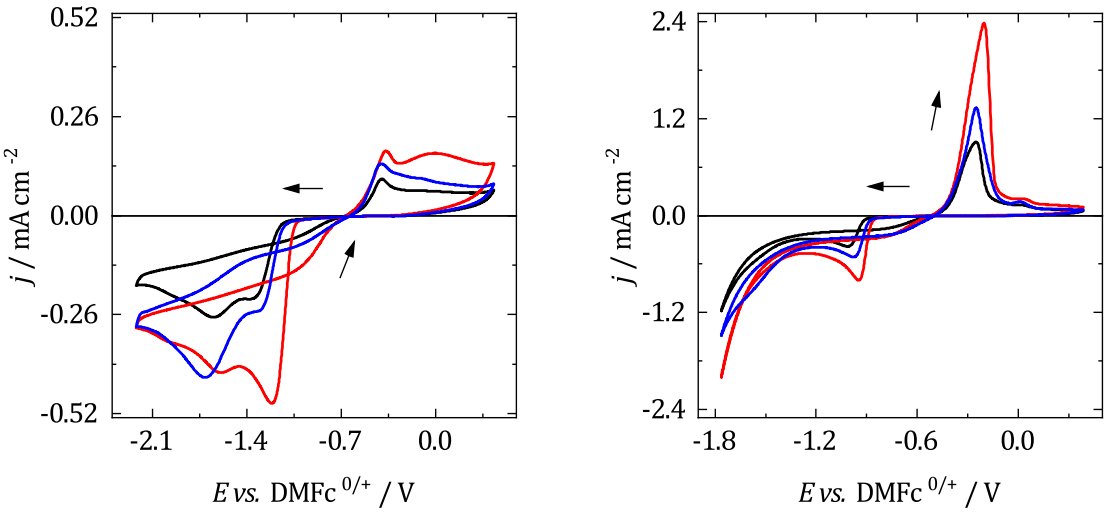

(a) oDCB (b) DCE

Figure 5.3: Voltammograms of a mixed $[N^nBu_4][SbCl_4]$ and $[N^nBu_4]_2[TeCl_6]$ electrolyte at varying concentrations, along with 100 mM $[N^nBu_4]Cl$ in oDCB and DCE. WE was swept from 0.2 V *vs.* DMFc at 50 mV s^{-1} in the direction indicated by the arrows. CE: Pt grid, RE: Ag/AgCl, WE: $r = 0.25$ mm Pt disc. Black: 1 mM $[N^nBu_4][SbCl_4]$ and 1 mM $[N^nBu_4]_2[TeCl_6]$, red: 2 mM $[N^nBu_4][SbCl_4]$ and 1 mM $[N^nBu_4]_2[TeCl_6]$, blue: 1 mM $[N^nBu_4][SbCl_4]$ and 2 mM $[N^nBu_4]_2[TeCl_6]$.

5.3.2. Electrodeposition

Initial scoping experiments found that precursor concentrations of 1.5 mM $[N^nBu_4][SbCl_4]$ and 3 mM $[N^nBu_4]_2[TeCl_6]$ in oDCB, and 1.75 mM $[N^nBu_4][SbCl_4]$ and 3 mM $[N^nBu_4]_2[TeCl_6]$ in DCE appeared to be the most promising for electrodeposition of stoichiometric Sb_2Te_3. A Sb/Te ratio of 0.5 and 0.6 for oDCB and DCE respectively. As in previous Chapters, it is necessary to perform voltammograms using the chosen substrate to determine suitable potentials for depositions. Fig. 5.4 shows voltammograms at a $r =$ 2 mm TiN substrate, clearly the appearance changes significantly from those collected at a Pt WE. Deposits were collected potentiostatically at five potentials at 250 mV intervals between −1.5 and −2.5 V *vs.* DMFc from both oDCB and DCE, covering the majority of the available deposition range. The WE was held at a potential where no reaction occurred, before stepping to the relevant potential. Deposits were collected until a cutoff charge

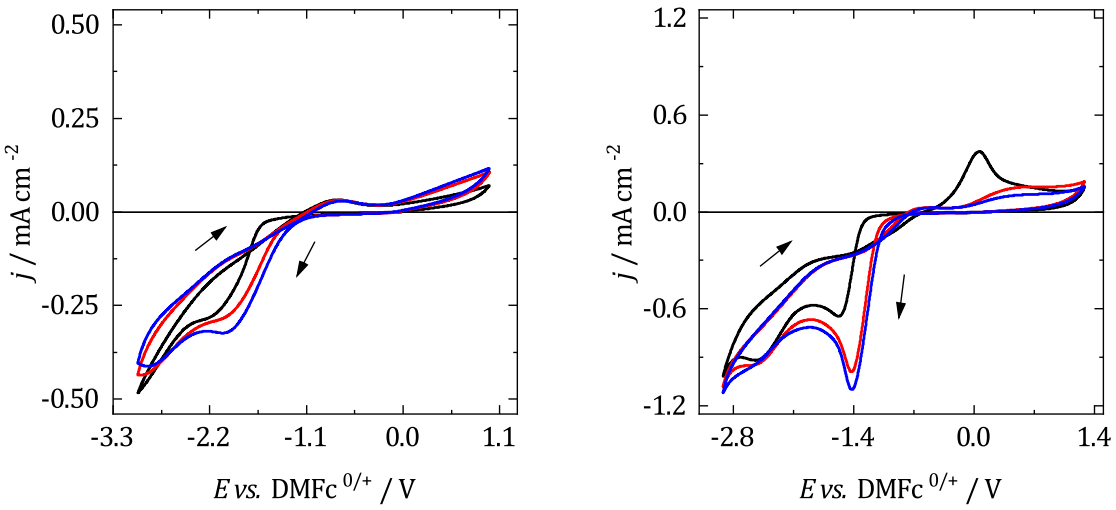

(a) oDCB (b) DCE

Figure 5.4: Voltammograms of a) 1.5 mM $[N^nBu_4][SbCl_4]$ and 3 mM $[N^nBu_4]_2[TeCl_6]$, b) 1.75 mM $[N^nBu_4][SbCl_4]$ and 3 mM $[N^nBu_4]_2[TeCl_6]$ with 100 mM $[N^nBu_4]Cl$ in oDCB and DCE at a r = 2 mm TiN WE. WE was swept from 0.2 V *vs.* DMFc at 50 mV s^{-1} in the direction indicated by the arrows. CE: Pt grid, RE: Ag/AgCl. Black: scan 1, red: scan 2, blue: scan 3.

corresponding to a 500 nm thick film was reached, or 1800 s passed, whichever came first. This was to ensure enough material was grown for further analysis and also to ensure the deposits were of approximately the same thickness. The deposition at each potential was repeated three times to ensure reproducibility. Table 5.1 shows representative parameters of the deposits collected. CR (as defined in Chapter 4), assuming the formation of Sb_2Te_3, indicates the rate of material growth generally increases with decreasing potential, and was also faster in DCE than oDCB, on account of its lower viscosity.

Solvent	E_{dep} *vs.* DMFc / V	t / s	$-Q$ / mC	CR / mC cm^{-2} min^{-1}
oDCB	−1.5	1800	21	0.3
	−1.75	1800	23	0.3
	−2	1800	32	0.5
	−2.25	1800	44	0.6
	−2.5	1800	47	0.7
DCE	−1.5	1800	63	0.9
	−1.75	1800	87	1.3
	−2	1800	94	1.4
	−2.25	1679	113	1.8
	−2.5	1645	113	1.8

Table 5.1: Representative deposition parameters of deposits collected from oDCB containing 1.5 mM $[N^nBu_4][SbCl_4]$ and 3 mM $[N^nBu_4]_2[TeCl_6]$, and from DCE containing 1.75 mM $[N^nBu_4][SbCl_4]$ and 3 mM $[N^nBu_4]_2[TeCl_6]$ with 100 mM $[N^nBu_4]Cl$ onto a r = 2 mm TiN substrate at 25 °C.

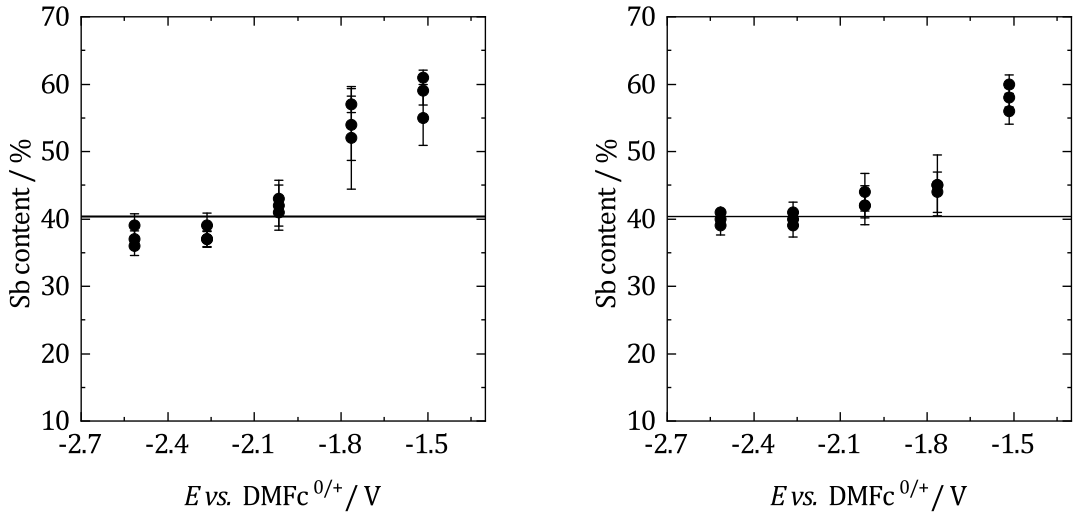

(a) oDCB

(b) DCE

Figure 5.5: Sb content by EDX of electrodeposited antimony and tellurium at various potentials on a TiN working electrode from oDCB and DCE with a bath composed of a) 1.5 mM $[N^nBu_4][BiCl_4]$ and 3 mM $[N^nBu_4]_2[TeCl_6]$, b) 1.75 mM $[N^nBu_4][BiCl_4]$ and 3 mM $[N^nBu_4]_2[TeCl_6]$. The horizontal line is the composition of a commercial Sb_2Te_3 sample. The composition was determined at three locations on the deposit and averaged and the error corresponds to the standard deviation.

Fig. 5.5 shows the composition by EDX of antimony telluride codeposits collected from oDCB and DCE. The composition was measured at three different locations on the deposits and averaged, and the standard deviation taken as the error. The error bars are small for all deposits collected from both solvents, demonstrating minimal spatial variation of the composition. The deposition at each potential was repeated three times, and as can be seen there is little variation between repeats, showing that it is possible to reproducibly deposit the composition measured at each potential. The Sb/Te ratio in a commercial Sb_2Te_3 sample was measured and used as a reference which is represented by a horizontal line in the plots. The Sb/Te ratio generally decreases with potential. In both solvents, at the most positive potentials, around 50-60% Sb is present in the deposit, greater than the required 40% for Sb_2Te_3. As the potential is lowered, so does the Sb content. At −2 V in oDCB the composition is close to stoichiometric $SbTe_3$ and as the potential is decreased further, the composition becomes essentially independent of potential. The same relationship is observed in DCE and the necessary ratio for Sb_2Te_3 can then be achieved at −2.25 V and −2.5 V. The averaged ratio of Sb and Te in the deposits at each potential is given in Table 5.2.

Representative SEM images of deposits collected at each potential are shown in Fig. 5.6 for oDCB and 5.7 for DCE. At −1.5 V from oDCB, the deposit appears homogeneous, with pinholes. For the deposition at −1.75 V the film also appears dense and uniform, with cracks and pinholes. There are also some larger areas where no material is grown. As the potential was decreased further to −2 V, the morphology of the deposits changes.

A thin compact layer of Sb and Te forms on the substrate and on top of that the deposit clusters into spongy, porous islands. The morphology of the deposits at −2.25 and −2.5 V appears similar, with the clumps growing larger at the lower potential.

The appearance of the films deposited from DCE is similar to those obtained from oDCB. At −1.5 V, the material is compact and uniform, with regular cracks propagating through the film. The deposits at −1.75 V and beyond adopt a morphology similar to that observed for the deposited collected at the most negative potentials from oDCB. A thin layer of Sb and Te grows, above which loose clumps of material form. As the potential decreases the clumps increase in size and eventually join to form a continuous porous film.

The crystal structure of the deposits were investigated with XRD. Spectra for the deposits collected at each potential are shown in Figs. 5.8 and 5.9 for oDCB and DCE respectively, along with literature patterns for Sb_2Te_3 and TiN. One peak associated with Sb-Te diffraction can be observed at *ca.* 28°. According to the phase diagram of the Sb-Te system, the stoichiometric Sb_2Te_3 phase only exists in a narrow composition range around 40% Sb.[42] The deposits collected at −2 to −2.5 V from both oDCB and DCE were successfully indexed as Sb_2Te_3, with lattice parameters similar to those in the literature. Values can be found in Table 5.2.

The phase diagram for Sb content > 40% is less well established.[43] It has been found experimentally that in the composition range 52 − 59% Sb, an intermediate γSb-Te phase forms.[42] Then, between 41 − 52% Sb no defined phase is observed, but the Sb-Te structure in the composition range 41 − 59% Sb arranges itself into units of Sb bilayers, and Sb_2Te_3 according to the general formula $(Sb_2)_n(Sb_2Te_3)_m$ ($n, m = 1, 2, 3...$), with n decreasing with Sb content.[44] Based upon the composition information of the deposits collected here, those at −1.5 and −1.75 V from oDCB, and −1.5 V from DCE would appear to adopt the γ phase where $n = m = 2$,[44] and −1.75 V from DCE, a phase of the form $(Sb_2)_n(Sb_2Te_3)_m$ where n and m are not known. Since no definite phase is formed, there was no literature crystallographic data that the patterns could be indexed against, and so quantitative analysis is not attempted for the deposits at these potentials.

When the Sb content is lowered below 40%, the additional Te forms a separate phase of elemental Te. Although, the differences in phase do not appear to be manifested in recorded XRD patterns. The peaks are in approximately the same position for all potentials, and there are no significant differences in the resulting lattice parameters. This may be because the low intensity peaks reduce the accuracy of the lattice parameter calculations and so any changes are not detectable. Additionally, the limitations in accuracy of the elemental composition when determined by EDX means that those deposits where Sb_2Te_3 is apparently formed most likely include a small amount of elemental Te or $(Sb_2)_n(Sb_2Te_3)_m$ as impurities.

Solvent	E_{dep} *vs.* DMFc / V	Composition[a]	Phase	$a = b$ / Å	c / Å	Crystallite size / Å
oDCB	−1.5	$Sb_{0.58}Te_{0.42}$	γSb-Te			16.2(3)
	−1.75	$Sb_{0.54}Te_{0.46}$	γSb-Te			20.2(11)
	−2	$Sb_{0.42}Te_{0.58}$	Sb_2Te_3	4.23(6)	31.0(7)	16.3(3)
	−2.25	$Sb_{0.38}Te_{0.62}$	Sb_2Te_3	4.28(4)	31.1(3)	21.5(4)
	−2.5	$Sb_{0.38}Te_{0.62}$	Sb_2Te_3	4.23(6)	31.0(7)	21.3(6)
DCE	−1.5	$Sb_{0.58}Te_{0.42}$	γSb-Te			16.4(8)
	−1.75	$Sb_{0.46}Te_{0.54}$				17.1(3)
	−2	$Sb_{0.42}Te_{0.58}$	Sb_2Te_3	4.24(6)	31.1(7)	17.8(2)
	−2.25	$Sb_{0.40}Te_{0.60}$	Sb_2Te_3	4.30(17)	30.5(15)	18.0(3)
	−2.5	$Sb_{0.40}Te_{0.60}$	Sb_2Te_3	4.33(4)	30.0(9)	60(3)
Lit.			Sb_2Te_3[b]	4.26	30.5	

Table 5.2: Phase identification and quantitative analysis of bismuth and tellurium electrodeposited from oDCB and DCE indexed using grazing incidence XRD. Crystallite sizes obtained using the Scherrer equation. [a]average of three repeats using EDX data. [b]ICSD 2084.

The average crystallite size in the deposits, calculated using the peak at 28° and the Scherrer equation, are shown in Table 5.2. The sizes are small, but similar to those reported for Bi_2Te_3 deposited from DCM.[41] The size of the crystallite generally increases slightly with decreasing deposition potential, possibly as a result of changes in the rate of deposition. Based upon the shape of the peaks and the calculated crystallite sizes, the deposits are likely amorphous or nanocrystalline.

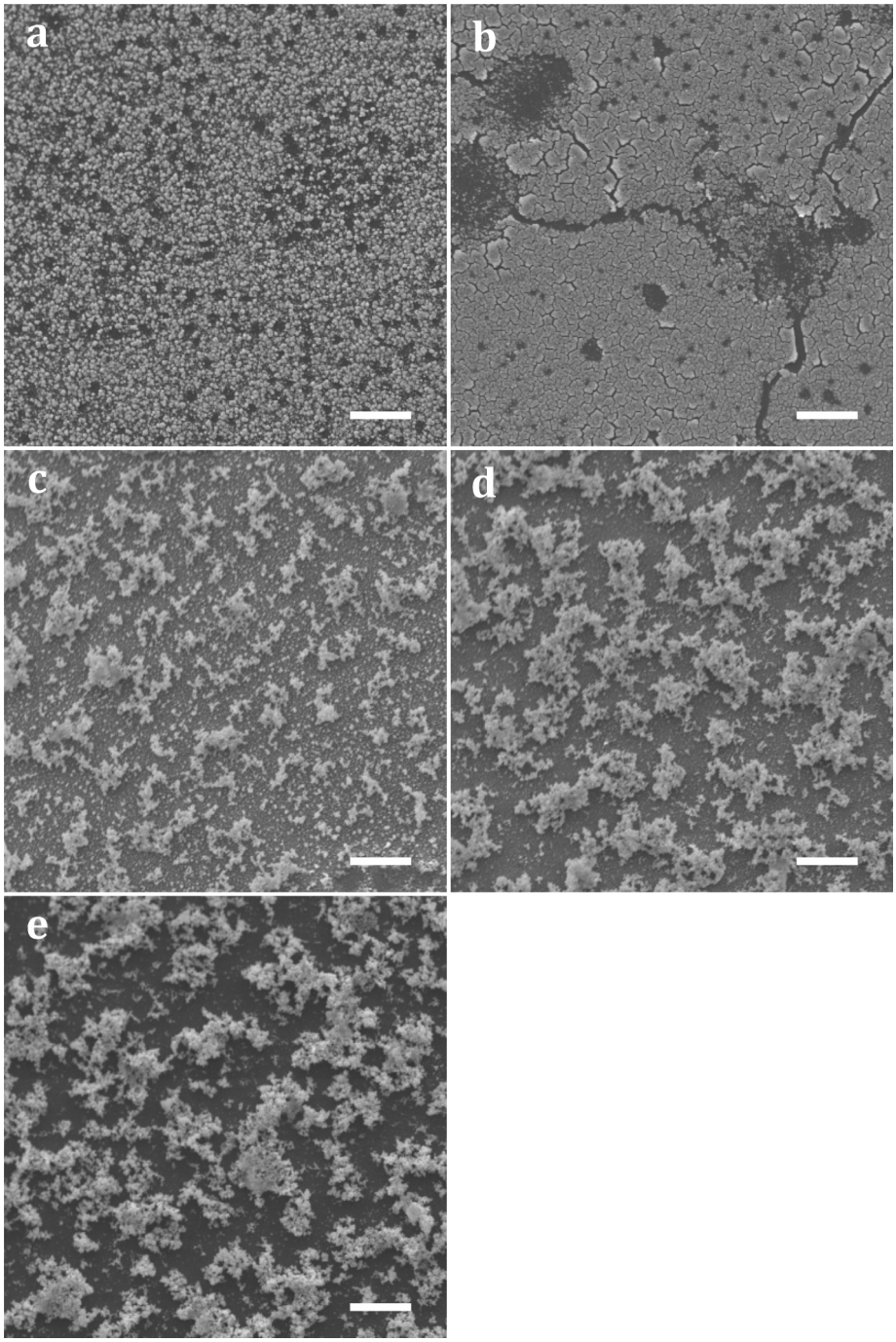

Figure 5.6: SEM images of the surface of antimony telluride electrodeposited onto TiN from oDCB containing 1.5 mM $[N^nBu_4][SbCl_4]$ and 3 mM $[N^nBu_4]_2[TeCl_6]$. a) −1.5 V, b) −1.75 V, c) −2 V, d) −2.25 V, e) −2.5 V *vs.* DMFc. Scale bar represents 10 µm.

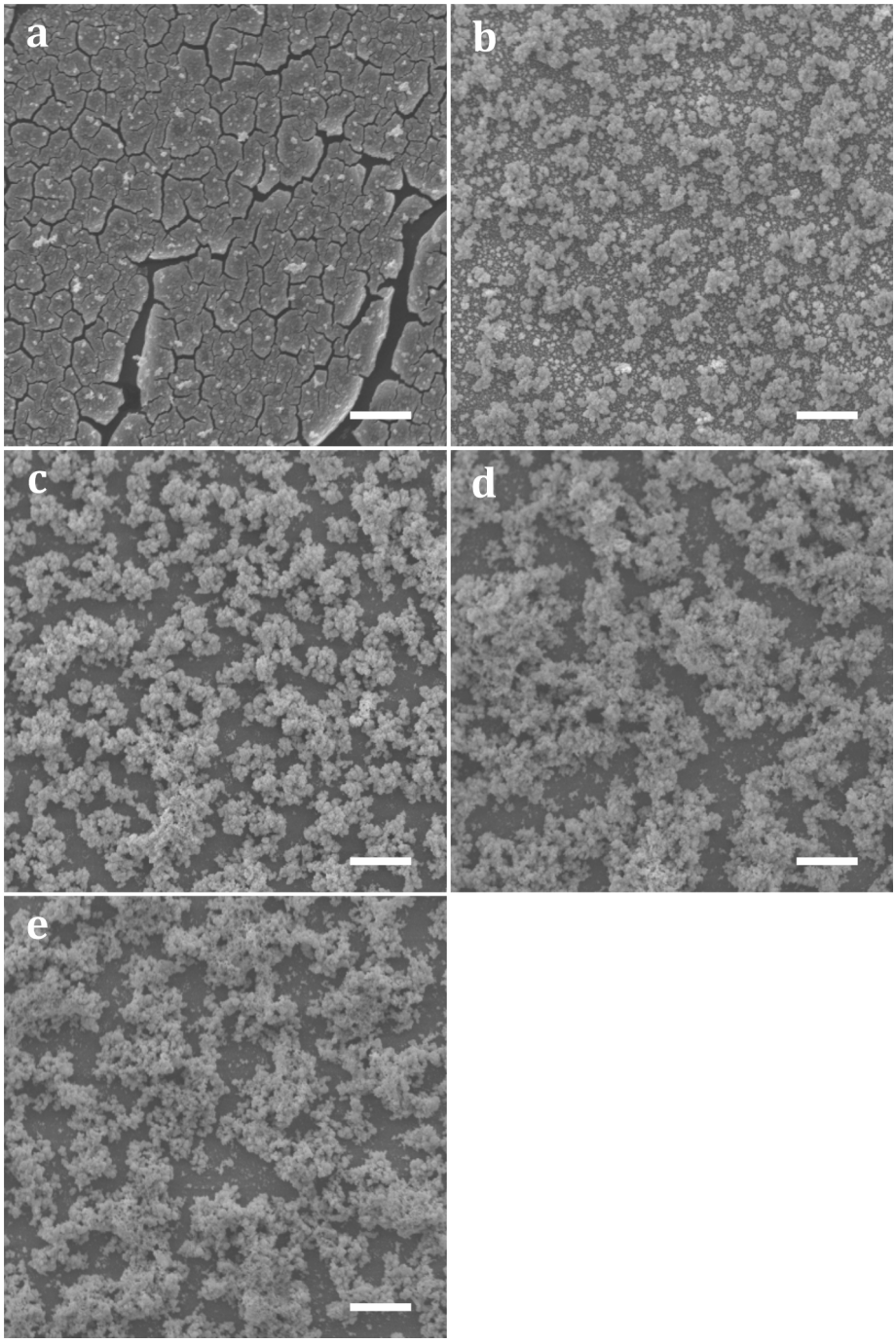

Figure 5.7: SEM images of the surface of antimony telluride electrodeposited onto TiN from DCE containing 1.75 mM $[N^nBu_4][SbCl_4]$ and 3 mM $[N^nBu_4]_2[TeCl_6]$. a) −1.5 V, b) −1.75 V, c) −2 V, d) −2.25 V, e) −2.5 V *vs.* DMFc. Scale bar represents 10 µm.

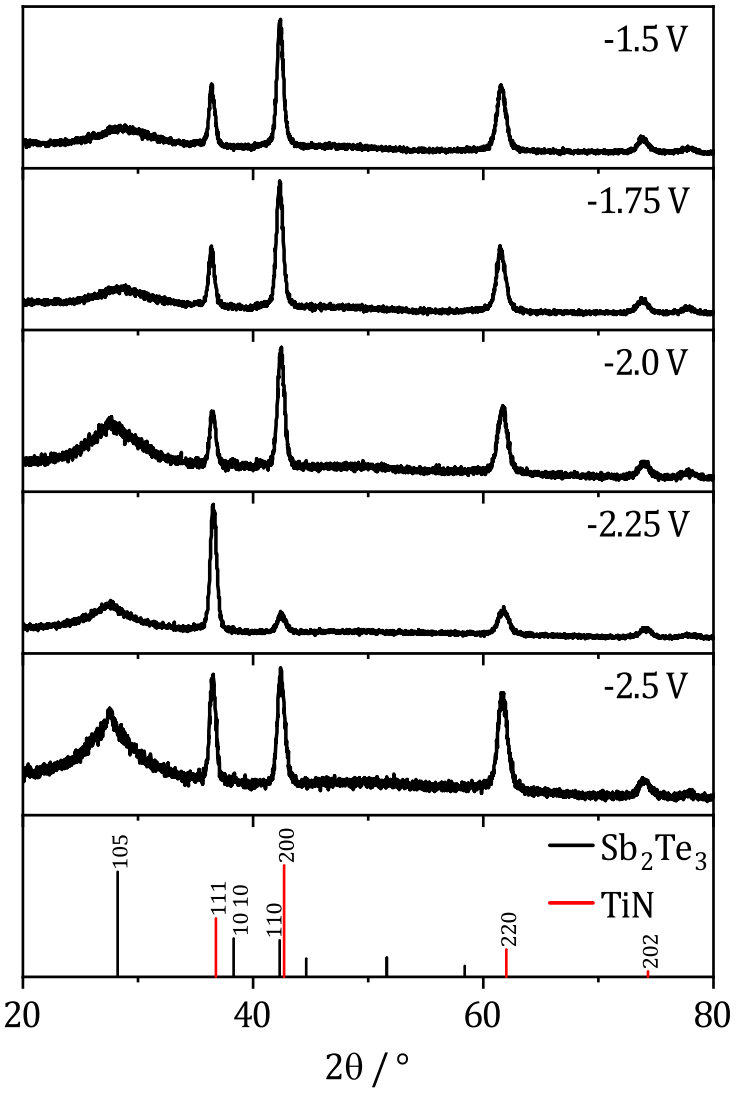

Figure 5.8: Grazing incidence XRD patterns of antimony telluride films electrodeposited at various potentials onto TiN from a bath containing 1.5 mM $[N^nBu_4][BiCl_4]$ and 3 mM $[N^nBu_4]_2[TeCl_6]$ in oDCB. The literature diffraction peaks of Sb_2Te_3 and TiN with their associated indices are shown in black and red respectively in the bottom panel. Literature Sb_2Te_3: ICSD 2084, TiN: ICSD 152807.

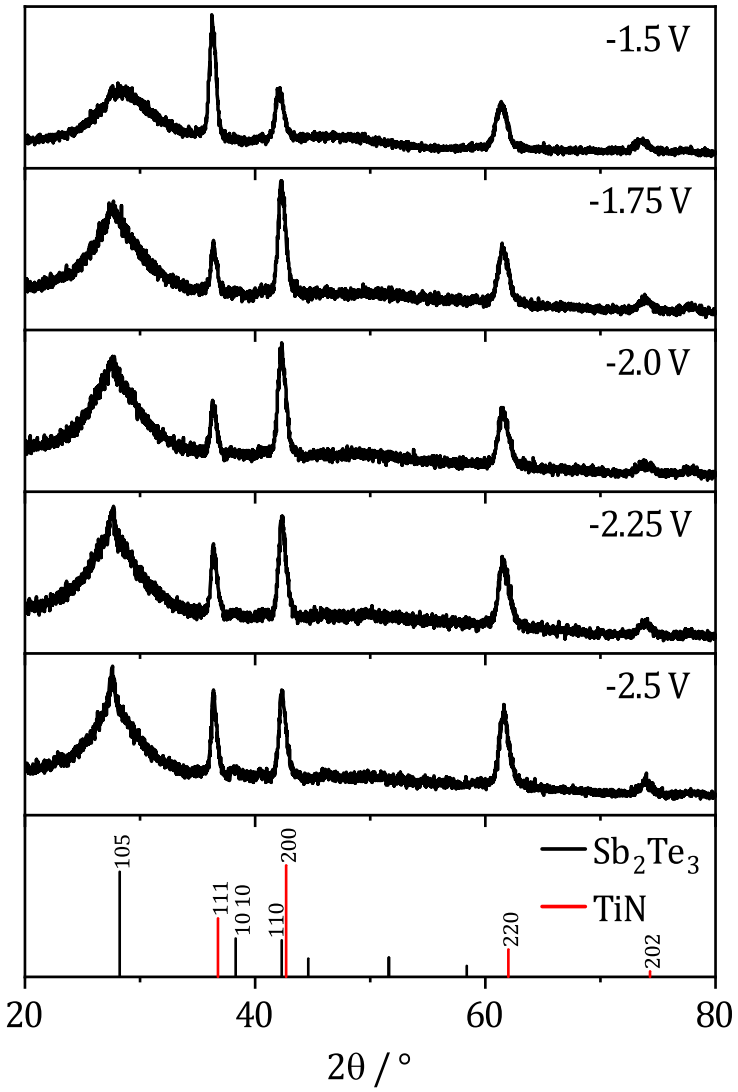

Figure 5.9: Grazing incidence XRD patterns of antimony telluride films electrodeposited at various potentials onto TiN from a bath containing 1.75 mM $[N^nBu_4][BiCl_4]$ and 3 mM $[N^nBu_4]_2[TeCl_6]$ in DCE. The literature diffraction peaks of Sb_2Te_3 and TiN with their associated indices are shown in black and red respectively in the bottom panel. Literature Sb_2Te_3: ICSD 2084, TiN: ICSD 152807.

5.4. Bismuth telluride

5.4.1. Electrochemistry

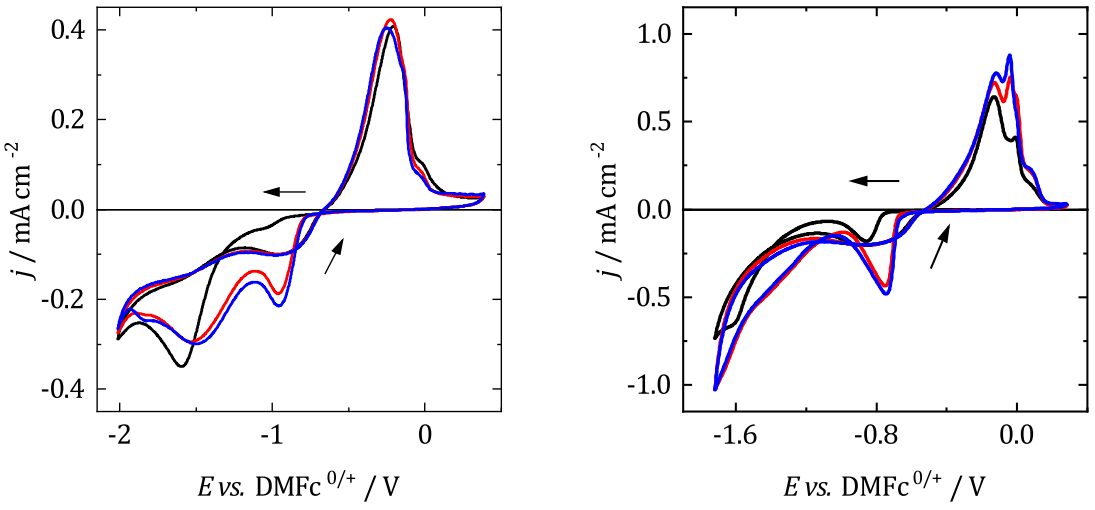

(a) oDCB (b) DCE

Figure 5.10: Voltammograms of a mixed 1 mM $[N^nBu_4][BiCl_4]$ and 1 mM $[N^nBu_4]_2[TeCl_6]$ electrolyte with 100 mM $[N^nBu_4]Cl$ in oDCB and DCE. WE was swept from 0 V *vs.* DMFc at 50 mV s^{-1} in the direction indicated by the arrows. CE: Pt grid, RE: Ag/AgCl, WE: r = 0.25 mm Pt disc. Black: scan 1, red: scan 2, blue: scan 3.

The electrochemistry of the $[BiCl_4]^-$ and $[TeCl_6]^{2-}$ was studied with a similar approach to that in 5.3.1 above. Fig. 5.10 shows voltammograms of a mixed $[N^nBu_4][BiCl_4]$ and $[N^nBu_4]_2[TeCl_6]$ electrolyte in oDCB and DCE at a Pt macroelectrode. Reduction begins in oDCB at approximately −1 V *vs.* DMFc with low levels of current before increasing to a peak at −1.6 V. On the return scan, a nucleation loop can clearly be seen, before a single oxidation peak occurs. The first scan has an oxidation efficiency of 43%. On the second and third scans the onset of reduction shifts anodically to −0.8 V and another reduction peak appears at 0.9 V. As the scan progresses a second peak emerges at −0.5 V. The anodic peak then does not changes significantly from the first scan. The presence of a nucleation loop and, a positive shift in the onset of reduction with subsequent scans, indicates the presence of the codeposition of Bi and Te.

Turning to DCE, the onset of reduction occurs at *ca.* −0.75 V, more positive than in oDCB. The remainder of the negative scan appears relatively featureless, similar to the $[SbCl_4]^-$ and $[TeCl_6]^{2-}$ above. The current increases rapidly as the potential decreases and a small peak appears at −1.6 V, which appears to be overlaid onto the start of solvent breakdown. The reduction can be attributed to the electrodeposition of a Bi and Te codeposit. On the positive scan a single stripping peak occurs, with a small shoulder, associated with the stripping of deposited Bi and Te. The oxidation efficiency of the first scan was 48%, slightly lower than from oDCB. On subsequent scans the first reduction peak

becomes more pronounced, increasing in height and shifting positively. Indicating that some material is nucleated on the electrode surface. The stripping peaks also increase in height, suggesting a larger amount of material was deposited on the surface.

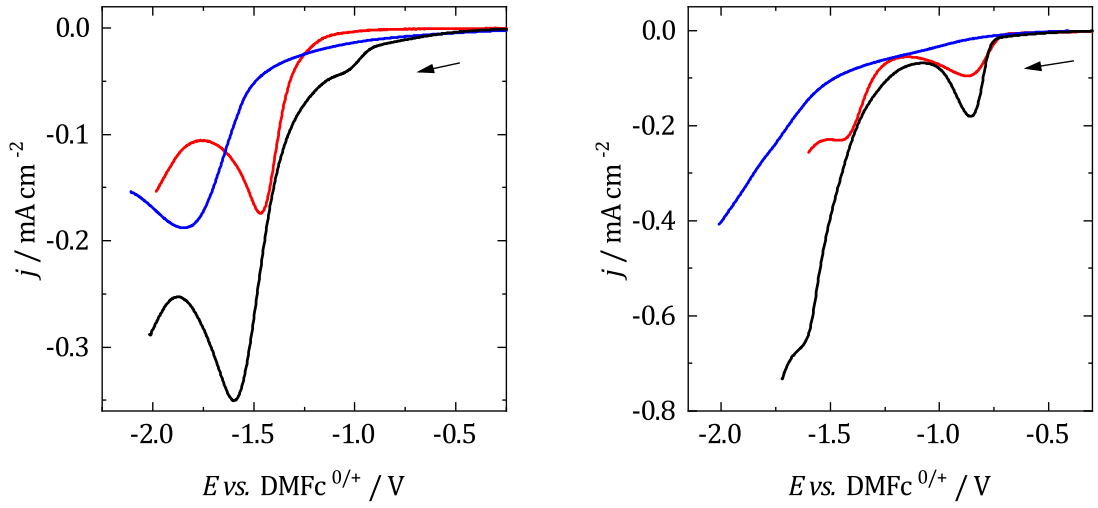

(a) oDCB (b) DCE

Figure 5.11: Voltammograms of a mixed 1 mM $[N^nBu_4][BiCl_4]$ and $[N^nBu_4]_2[TeCl_6]$ electrolyte overlaid with voltammograms of 1 mM of the individual precursors, along with 100 mM $[N^nBu_4]Cl$ in oDCB and DCE. WE was swept from 0.2 V *vs.* DMFc at 50 mV s^{-1} in the direction indicated by the arrows. CE: Pt grid, RE: Ag/AgCl, WE: $r = 0.25$ mm Pt disc. Black: 1 mM $[N^nBu_4][BiCl_4]$ and 1 mM $[N^nBu_4]_2[TeCl_6]$, red: 1 mM $[N^nBu_4][BiCl_4]$, blue: 1 mM $[N^nBu_4]_2[TeCl_6]$.

As in 5.3.1, overlaying the voltammogram of the mixed electrolyte with the voltammograms of the individual precursors can give insight into the processes taking place when both metal precursors are in solution. These are shown for oDCB and DCE in Fig. 5.11. The effect of increasing the concentration of each precursor is then given in Fig. 5.12. Reduction current can be observed in the mixed electrolyte before the onset of deposition of either metal, this is most likely evidence of Bi and Te codeposition. The first peak of the mixed electrolyte in oDCB appears to correspond to the reduction of Sb, however it also increases significantly in height when the concentration of $[TeCl_6]^{2-}$ is raised. This is also the case, by a lesser degree, when the concentration of $[BiCl_4]^-$ is increased, suggesting that the peak in the mixed electrolyte is associated with the reduction of both Bi^{3+} and Te^{4+}. When the concentration of $[BiCl_4]^-$ is increased, a second reduction peak emerges and the voltammogram now appears as the second scan when 1 mM of precursor is used.

With regards to DCE, the initial reduction step in Bi deposition matches well with the first cathodic peak of the mixed electrolyte at −0.8 V. Increasing the concentration of $[BiCl_4]^-$ in Fig. 5.12b causes a significant increase in the peak height and furthermore, its shape is independent of the concentration of $[TeCl_6]^{2-}$. Therefore, this peak can be attributed to the deposition of Bi. The are no peaks in the $[TeCl_6]^{2-}$ voltammogram which

also appear in the voltammetry of the mixed electrolyte. However, the current density at potentials more negative than the Bi deposition peak is larger than that for Bi deposition alone, suggesting the presence of Te^{4+} reduction also. The current also increases upon the addition of $[N^nBu_4]_2[TeCl_6]$, suggesting both Bi and Te deposition is taking place at these potentials.

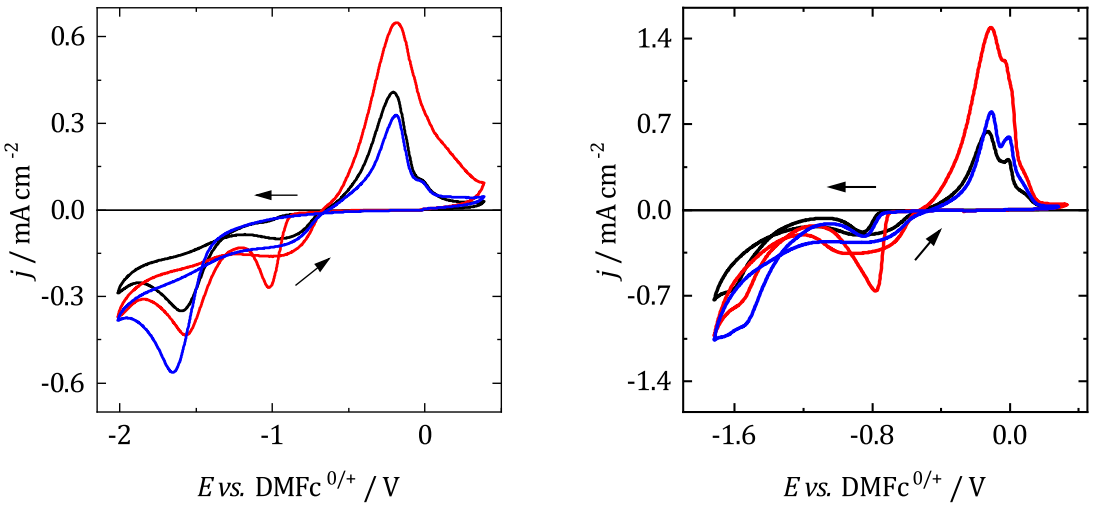

(a) oDCB (b) DCE

Figure 5.12: Voltammograms of a mixed $[N^nBu_4][BiCl_4]$ and $[N^nBu_4]_2[TeCl_6]$ electrolyte at varying concentrations, along with 100 mM $[N^nBu_4]Cl$ in oDCB and DCE. WE was swept from 0.2 V *vs.* DMFc at 50 mV s^{-1} in the direction indicated by the arrows. CE: Pt grid, RE: Ag/AgCl, WE: $r = 0.25$ mm Pt disc. Black: 1 mM $[N^nBu_4][BiCl_4]$ and 1 mM $[N^nBu_4]_2[TeCl_6]$, red: 2 mM $[N^nBu_4][BiCl_4]$ and 1 mM $[N^nBu_4]_2[TeCl_6]$, blue: 1 mM $[N^nBu_4][BiCl_4]$ and 2 mM $[N^nBu_4]_2[TeCl_6]$.

5.4.2. Electrodeposition

Electrodeposition was performed with TiN substrates using the same method as for antimony telluride above. Initial experiments in oDCB with a bath containing 2.5 mM $[N^nBu_4][BiCl_4]$ and 3 mM $[N^nBu_4]_2[TeCl_6]$, the same as required in DCM to deposit stoichiometric Bi_2Te_3,[41] gave compositions of the range 45-51% Bi and so the $[N^nBu_4][BiCl_4]$ concentration was lowered to 2 mM. In DCE, 2.5 mM $[N^nBu_4][BiCl_4]$ and 3 mM $[N^nBu_4]_2[TeCl_6]$ was found to be a satisfactory concentration. Fig. 5.13 shows a voltammograms of 2 mM $[N^nBu_4][BiCl_4]$ and 3 mM $[N^nBu_4]_2[TeCl_6]$ in oDCB, and 2.5 mM $[N^nBu_4][BiCl_4]$ and 3 mM $[N^nBu_4]_2[TeCl_6]$ in DCE at a $r = 2$ mm TiN WE. Once again, the effect of iR drop and the changing electrode material on the voltammetry is significant, and emphasises the importance of choosing deposition potentials from voltammograms at the deposition substrate. Deposits were collected at -1.5, -1.75, -2, -2.25 and −2.5 V *vs.* DMFc, covering the available deposition range from onset to solvent breakdown. Table 5.3 shows representative parameters of the collected deposits.

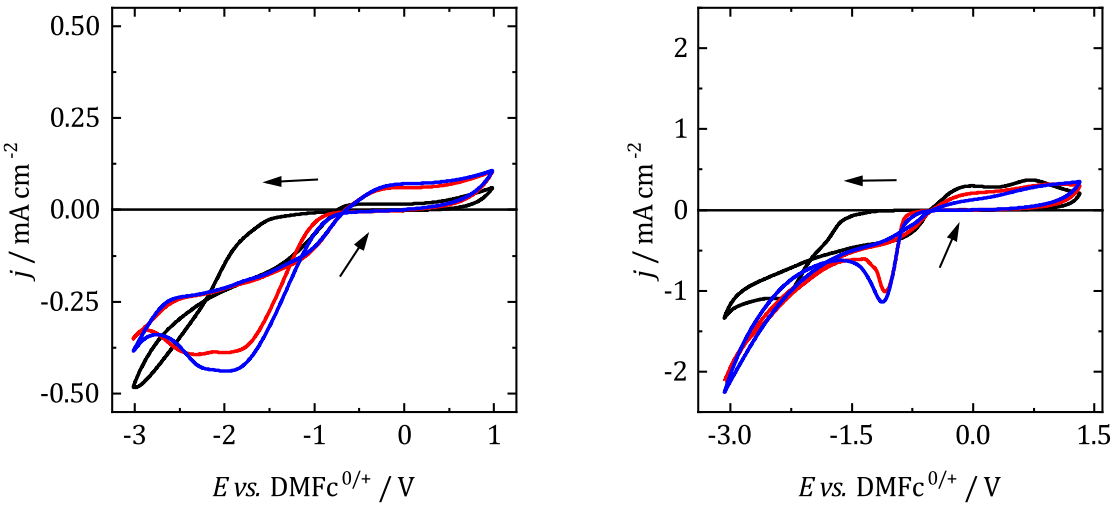

(a) oDCB (b) DCE

Figure 5.13: Voltammograms of a mixed a) 2 mM $[N^nBu_4][BiCl_4]$ and 3 mM $[N^nBu_4]_2[TeCl_6]$, b) 2.5 mM $[N^nBu_4][BiCl_4]$ and 3 mM $[N^nBu_4]_2[TeCl_6]$ with 100 mM $[N^nBu_4]Cl$ in oDCB and DCE at a r = 2 mm TiN WE. WE was swept from 0.2 V *vs.* DMFc at 50 mV s^{-1} in the direction indicated by the arrows. CE: Pt grid, RE: Ag/AgCl. Black: scan 1, red: scan 2, blue: scan 3.

CR generally increases with decreasing potential, and with DCE as a solvent instead of oDCB, as observed previously. However, it is also higher for bismuth telluride deposition than for antimony telluride deposition. The concentration of $[N^nBu_4][BiCl_4]$ was higher than $[N^nBu_4][SbCl_4]$, with the same concentration of $[N^nBu_4]_2[TeCl_6]$, which is the likely reason for this effect. Although, a faster rate of Bi deposition than Sb could also influence the rate of material growth.

Solvent	*E vs.* DMFc / V	*t* / s	$-Q$ / mC	*CR* / mC cm^{-2} min^{-1}
oDCB	−1.5	1800	39	0.6
	−1.75	1800	48	0.7
	−2	1800	52	0.8
	−2.25	1800	55	0.8
	−2.5	1800	55	0.8
DCE	−1.5	1671	105	1.7
	−1.75	983	105	2.8
	−2	711	105	3.9
	−2.25	492	105	5.7
	−2.5	408	105	6.8

Table 5.3: Representative deposition parameters of deposits collected from oDCB containing 2 mM $[N^nBu_4][BiCl_4]$ and 3 mM $[N^nBu_4]_2[TeCl_6]$, and from DCE containing 2.5 mM $[N^nBu_4][BiCl_4]$ and 3 mM $[N^nBu_4]_2[TeCl_6]$ with 100 mM $[N^nBu_4]Cl$ onto a r = 2 mm TiN substrate at 25 °C.

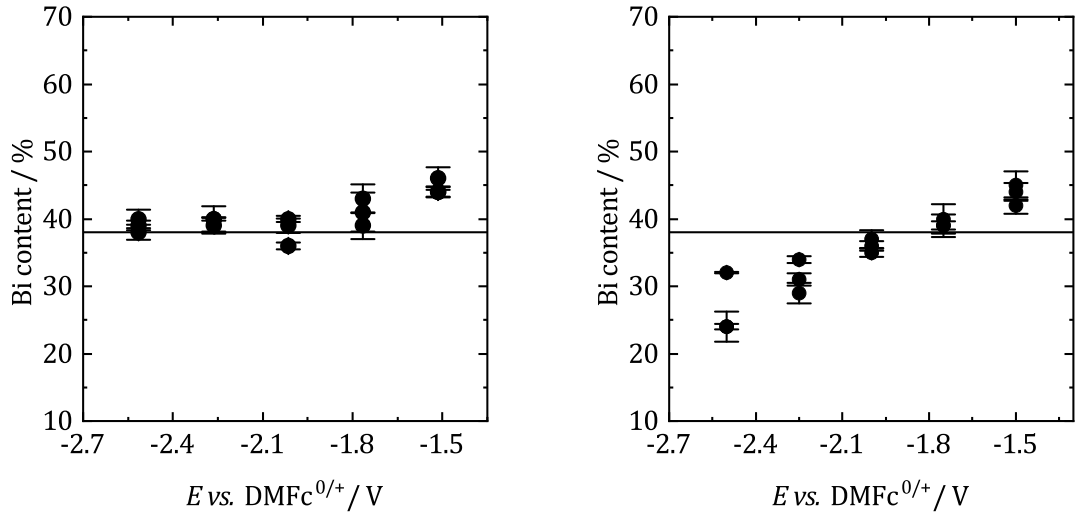

(a) oDCB (b) DCE

Figure 5.14: Bi content by EDX of electrodeposited bismuth and tellurium at various potentials on a TiN working electrode from oDCB with a bath composed of 2 mM $[N^nBu_4][BiCl_4]$ and 3 mM $[N^nBu_4]_2[TeCl_6]$, and from DCE with a bath composed of 2.5 mM $[N^nBu_4][BiCl_4]$ and 3 mM $[N^nBu_4]_2[TeCl_6]$. The horizontal line is the composition of a commercial Bi_2Te_3 sample. The composition was determined at three locations on the deposit and averaged and the error corresponds to the standard deviation.

Fig. 5.14 shows the composition by EDX of bismuth and tellurium films electrodeposited from oDCB and DCE. The horizontal line is the composition of a commercial Bi_2Te_3 reference sample, corresponding to 38% Bi. There is a small standard deviation for each deposit, indicating minimal spatial variation and the repeats are in good agreement with one another demonstrating reproducibility. Variation in Bi content with potential is minimal for the deposits collected from oDCB, and at potentials lower than −1.75 V the composition is essentially independent of potential. Furthermore, the composition of the reference sample and the electrodeposits at these potentials closely match, indicating the deposits have the correct ratio of Bi and Te for stoichiometric Bi_2Te_3. Interestingly, unlike DCM or oDCB there appears to be a relationship between composition and potential in DCE. Lowering the applied potential causes decreases in the Bi content in the deposit. This may be related to the limiting factor for Te deposition; if Te deposition is kinetically limited, as suggested by its voltammetry, then decreasing the potential may result in an increased rate of deposition. Nevertheless, it appears possible to achieve the composition for stoichiometric Bi_2Te_3 in the potential range −1.75 to −2 V *vs.* DMFc. The averaged ratio of Bi and Te in the deposits at each potential is given in Table 5.4.

Figs. 5.15 and 5.16 show representative SEM images of the electrodeposited bismuth telluride films from oDCB and DCE respectively. At −1.5 V in oDCB, the film is homogeneous and composed of round particles of material. As the potential is lowered to −1.75 V the particles appear to coalesce into a uniform compact layer, with many cracks running

through the film. As the applied potential is decreased further to −2 V, more porous material begins to grow on top of the compact layer. This continues at more negative potentials, until the entire deposited film appears spongy and porous. The morphology of these deposits is similar in appearance to those reported from DCM.[41]

The morphology of the deposits collected from DCE display similar features to those in oDCB, along with a similar relationship with potential. At −1.5 V, a smooth and homogeneous, cracked film forms. As the applied potential decreases a porous layer forms, with increasing coverage with decreasing potential. At the most negative potential, −2.5 V, the film then appears to become more compact.

XRD was used to probe the crystal structure of the bismuth telluride deposits. Figs. 5.17 and 5.18 show XRD patterns of the deposits collected at each potential from oDCB and DCE respectively. Also shown are the literature spectra for stoichiometric Bi_2Te_3 and the TiN substrate. A peak in the patterns is observed at *ca.* 28°, which corresponds to the diffraction of the bismuth telluride deposit. Similar to the Sb-Te system, stoichiometric Bi_2Te_3 forms only at 40% Bi content in the material. Therefore, only the deposits where the Bi/Te ratio is close to 0.67 can be considered to have formed Bi_2Te_3. This corresponds to the deposits collected at −1.75, −2, −2.25 and −2.5 V from oDCB, and −1.75 V from DCE. These patterns were successfully indexed as Bi_2Te_3 and the calculated lattice parameters show agreement with the literature values.

Solvent	E_{dep} *vs.* DMFc / V	Composition[a]	Phase	$a = b$ / Å	c / Å	Crystallite size / Å
oDCB	−1.5	$Bi_{0.45}Te_{0.55}$	Bi_4Te_5	4.35(14)	52.2(13)	27.3(3)
	−1.75	$Bi_{0.41}Te_{0.59}$	Bi_2Te_3	4.31(6)	31.1(11)	41(3)
	−2	$Bi_{0.38}Te_{0.62}$	Bi_2Te_3	4.42(10)	29.6(13)	15.9(8)
	−2.25	$Bi_{0.40}Te_{0.60}$	Bi_2Te_3	4.31(8)	29.3(4)	15.8(5)
	−2.5	$Bi_{0.39}Te_{0.61}$	Bi_2Te_3	4.40(5)	30.4(10)	21.9(14)
DCE	−1.5	$Bi_{0.44}Te_{0.56}$	Bi_4Te_5	4.35(2)	55.4(1)	42.1(11)
	−1.75	$Bi_{0.39}Te_{0.61}$	Bi_2Te_3	4.25(4)	31.3(7)	25.6(15)
	−2	$Bi_{0.36}Te_{0.64}$	Bi_2Te_3	4.43(4)	30.3(6)	26.5(6)
	−2.25	$Bi_{0.31}Te_{0.69}$	Bi_2Te_3	4.37(6)	31.2(15)	19.4(4)
	−2.5	$Bi_{0.27}Te_{0.73}$	Bi_2Te_3	4.31(11)	31.2(5)	16.4(3)
Lit.			Bi_4Te_5[b]	4.41	54.3	
			Bi_2Te_3[c]	4.40	30.4	

Table 5.4: Phase identification and quantitative analysis of bismuth and tellurium electrodeposited from oDCB and DCE indexed using grazing incidence XRD. Crystallite sizes obtained using the Scherrer equation. [a]average of three repeats using EDX data. [b] ICDD 00-022-0115 . [c]ICSD 74348.

Inspection of the Bi-Te binary phase diagram reveals that when the Bi content is greater than 40%, Bi_2Te_3 is no longer formed. Instead, similar to Sb and Te above, the Bi-Te system forms a homologous series of the general form $(Bi_2)_m(Bi_2Te_3)_n$ where the structure involves stacking of units of Bi_2 and Bi_2Te_3 in various ratios.[45] Of the structures

that are known to form, the phase with the composition which most closely matches that measured for −1.5 V in oDCB, and DCE is Bi_4Te_5 corresponding to $(Bi_2)_1(Bi_2Te_3)_5$ with 44% Bi.[46] It might therefore be expected that the deposits collected at −1.5 V take the form of Bi_4Te_5. The deposits were indexed against this phase and the calculated lattice parameters are given in Table 5.4. As with the Sb-Te system above, any additional Te in the material above 60% Te, takes the form of elemental Te.[45] This is presumably the case for the deposits with an applied potential of −2, −2.25 and −2.5 V in DCE. Although, no significant differences are observed in the diffraction patterns.

The average crystallite size of the deposits was estimated using the Scherrer equation for the peak at 28°, with the results given in Table 5.4. In oDCB, the crystallites are on the order of nanometres and are generally largest at positive potentials when the Bi content is highest. No trend is observed as the potential decreases further. For the deposits collected from DCE, the crystallites are largest at the most positive potentials, then generally decrease with potential.

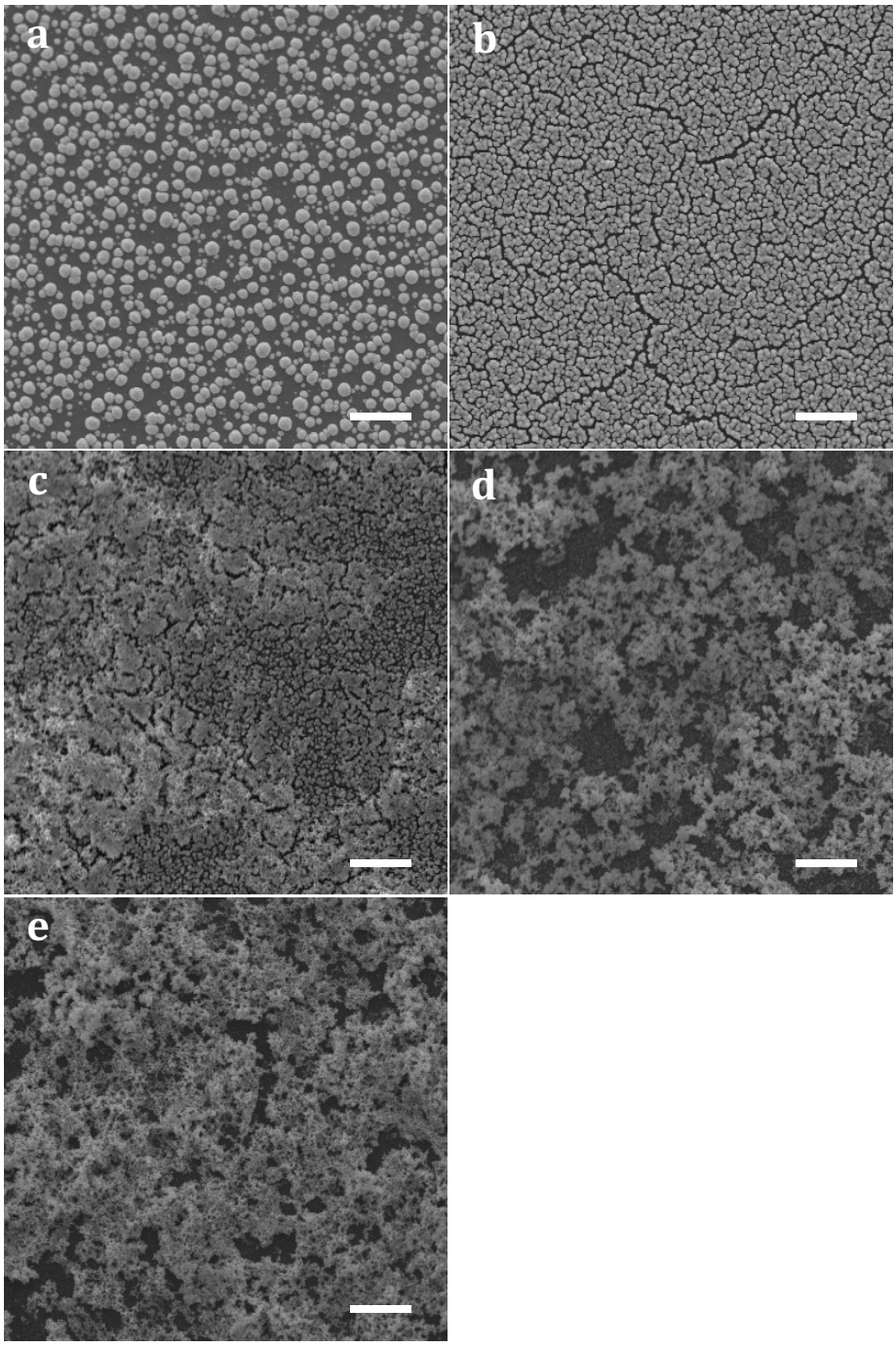

Figure 5.15: SEM images of the surface of bismuth telluride electrodeposited onto TiN from oDCB containing 2 mM $[N^nBu_4][BiCl_4]$ and 3 mM $[N^nBu_4]_2[TeCl_6]$. a) −1.5 V, b) −1.75 V, c) −2 V, d) −2.25 V, e) −2.5 V *vs.* DMFc. Scale bar represents 10 µm.

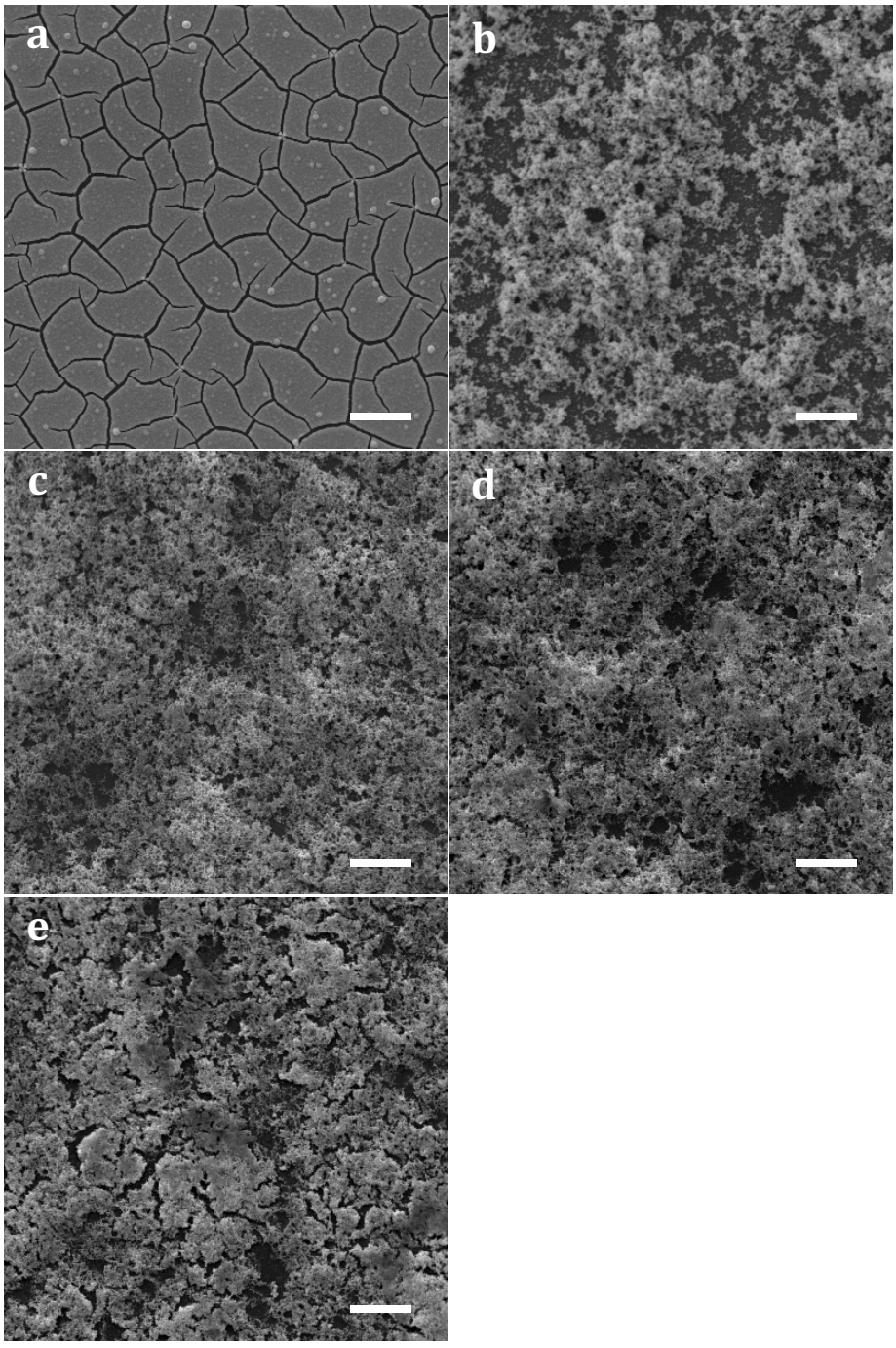

Figure 5.16: SEM images of the surface of Bi_2Te electrodeposited onto TiN from DCE containing 2.5 mM $[N^nBu_4][BiCl_4]$ and 3 mM $[N^nBu_4]_2[TeCl_6]$. a) −1.5 V, b) −1.75 V, c) −2 V, d) −2.25 V, e) −2.5 V *vs.* DMFc. Scale bar represents 10 µm.

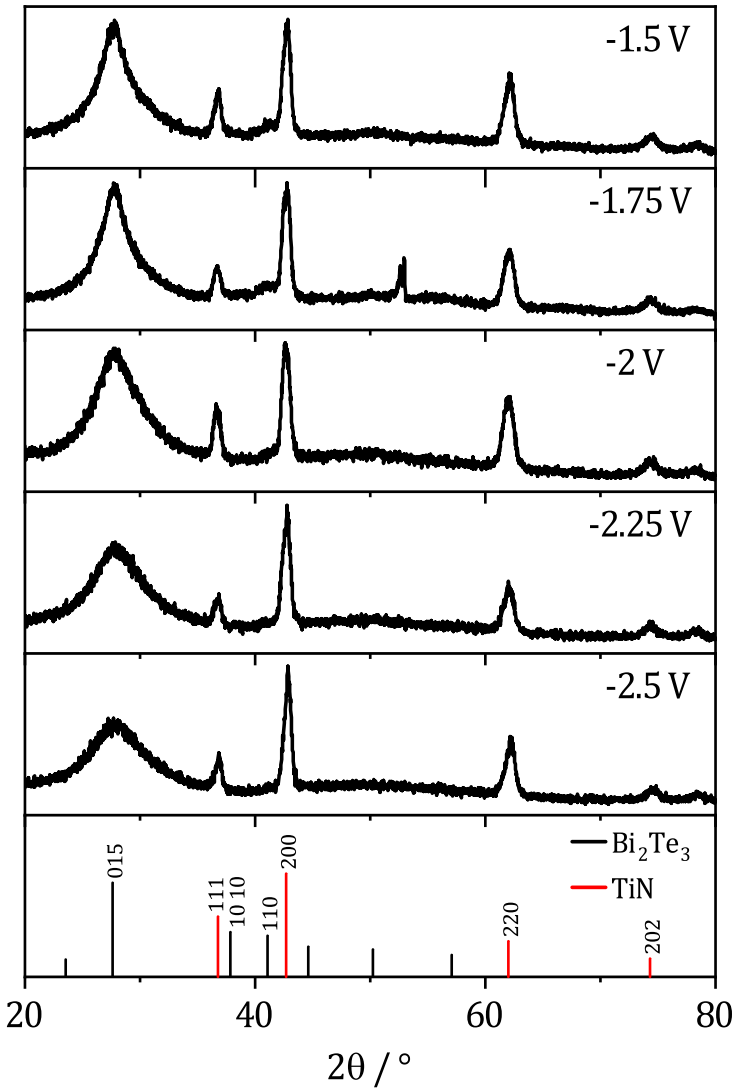

Figure 5.17: Grazing incidence XRD patterns of bismuth telluride films electrodeposited at various potentials onto TiN from a bath containing 2 mM $[N^nBu_4][BiCl_4]$ and 3 mM $[N^nBu_4]_2[TeCl_6]$ in oDCB. The literature diffraction patterns of Bi_2Te_3 and TiN with their associated indices are shown in black and red respectively in the bottom panel. Bi_2Te_3: ICSD 74348, TiN: ICSD 152807.

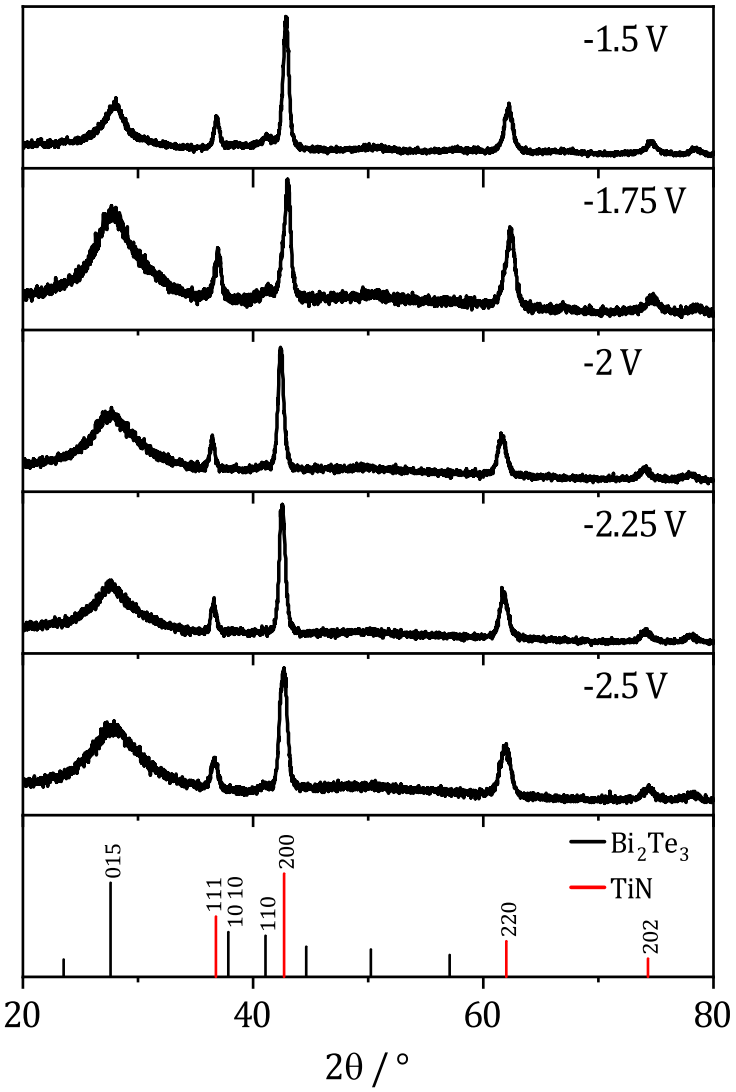

Figure 5.18: Grazing incidence XRD patterns of bismuth telluride films electrodeposited at various potentials onto TiN from a bath containing 2.5 mM $[N^nBu_4][BiCl_4]$ and 3 mM $[N^nBu_4]_2[TeCl_6]$ in DCE. The expected diffraction peaks of Bi_2Te_3 and TiN with their associated indices are shown in black and red respectively in the bottom panel. Bi_2Te_3: ICSD 74348, TiN: ICSD 152807.

5.5. Supercritical difluoromethane

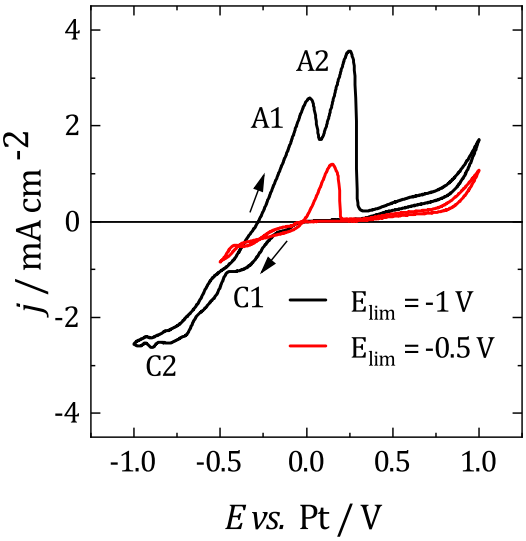

Figure 5.19: Voltammogram of 0.5 mM $[N^nBu_4][BiCl_4]$, 0.5 mM $[N^nBu_4]_2[TeCl_6]$ and 50 mM $[N^nBu_4]Cl$ in scDFM at 86 °C and 17 MPa. Working electrode was swept from 0 V at 50 mV s^{-1} in the direction indicated by the arrows. CE: Pt grid, RE: Pt disc, WE: r = 0.25 mm Pt disc.

Fig. 5.19 shows voltammograms of 0.5 mM $[N^nBu_4][BiCl_4]$ and 0.5 mM $[N^nBu_4]_2[TeCl_6]$ in scDFM. Works by Bartlett *et al.* indicate that the solubility of $[N^nBu_4]_2[TeCl_6]$ in scDFM is approximately 1.7 mM,[47] necessitating lower concentrations than those used previously. Two cathodic regions can be observed: C1 and C2. Reversing the potential before the current plateau at *ca.* −1 V shows C1 corresponds to deposition of Te only, since Te has the more positive redox potential. This was also verified by collecting a deposit at −0.4 V, shown in Fig. 5.20. The increase in current at *ca.* −0.5 V can be attributed to the onset of Bi deposition. Mass transport limited codeposition, can therefore be expected from the current plateau at *ca.* −0.7 V, C2.

Bi generally strips at more negative potentials, therefore, the peak at A1 can be attributed to the dissolution of Bi

$$Bi_xTe_y \longrightarrow xBi^{3+} + yTe_{(s)} + 3\,xe^-$$

and so A2 corresponds to the stripping of Te.

Comparison of Fig. 5.19 with voltammetry of a mixed Bi and Te electrolyte in DCM, show that the electrochemical behaviour changes in scDFM.[41] Firstly, at ambient temperatures the deposit composition is generally independent of potential, however as evidenced by Fig. 5.20 this is not the case under supercritical conditions where Te only can be deposited at the most positive potentials. It can also be seen that mass transport limited codeposition is possible in scDFM, unlike DCM, as a result of the lower viscosity in

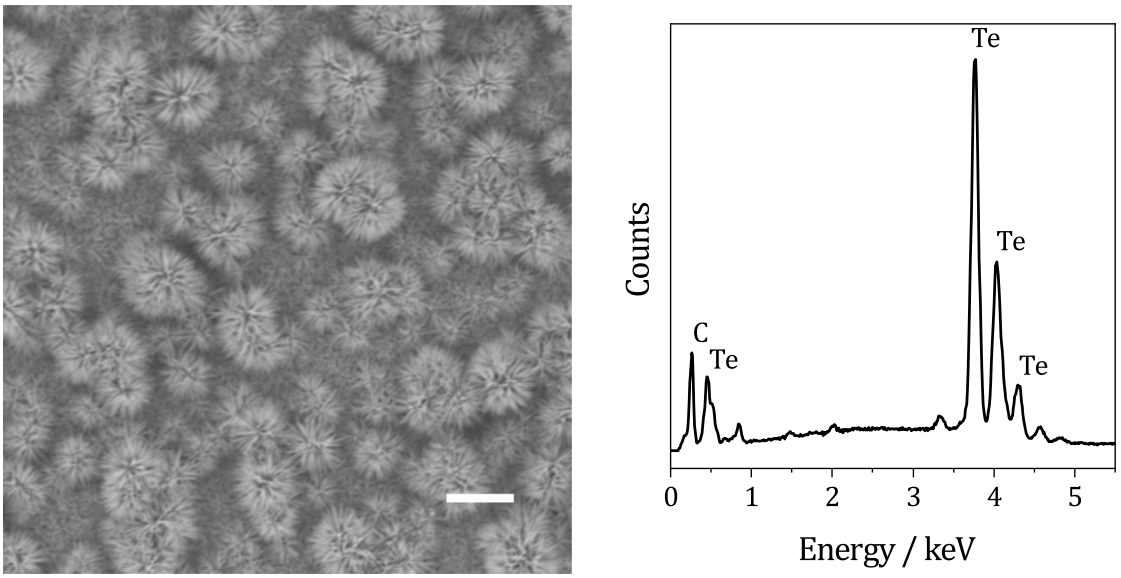

(a) SEM image (b) EDX spectrum

Figure 5.20: Deposit collected at −0.4 V *vs.* Pt for 1000 s onto a r = 0.25 mm disc from scDFM at 86 °C and 17 MPa from a mixed bismuth and tellurium electrolyte. Scale bar indicates 10 µm.

scfs. In scDMF Bi and Te appear to strip individually, unlike DCM where a single broad stripping peak is observed. This could be because the individual metals are not resolved, or it could indicate that the codeposit exists at ambient conditions as Bi_2Te_3 and strips as such, whereas in scDFM the codeposit exists as Bi and Te in separate phases.

From the work of Meng *et al.*, the electrodeposition of Bi_2Te_3 from DCM is well characterised.[41] It is therefore insightful to replicate the same deposition conditions in scDFM to understand any changes in the behaviour of the $[BiCl_4]^-$/ $[TeCl_6]^{2-}$ system upon entering the supercritical phase. In their work electrolyte ratios of Bi:Te 1:1, 1:1.2 and 1:1.5 were investigated and the same is used here. Deposits were collected at −1.5 V *vs.* Pt where both the Bi and Te precursors are expected to deposit under mass transport control. The composition information can be found in Table 5.5.

Electrolyte			Deposit		
$c(Bi^{3+})$ / mM	$c(Te^{4+})$ / mM	Bi^{3+}/Te^{4+}	Bi/Te	Average Te / %	DCM Te content[a] / %
1	1	1/1	1/0.8	45	40-50
1	1.2	1/1.2	1/1.0	50	60
1	1.5	1/1.5	1/1.1	53	70

Table 5.5: Comparison of Bi and Te composition in codeposits collected from scDFM and DCM. [a] DCM deposit data obtained by Meng *et al.* from Ref. [41], collected using a TiN substrate from electrolytes of 3 mM and 3 mM, 2.5 mM and 3 mM, 2 mM and 3 mM $[N^nBu_4][BiCl_4]$ and $[N^nBu_4]_2[TeCl_6]$ respectively.

As can be seen, the deposition behaviour in scDFM is significantly different to DCM

and it is not possible to deposit Bi_2Te_3 in scDFM with the 1/1.2 Bi/Te ratio necessary in DCM. It is possible the difference in total concentration is the cause, however based on the differences in voltammetry observed above, it is probably that a change in the nature of the precursors in solution is the cause.

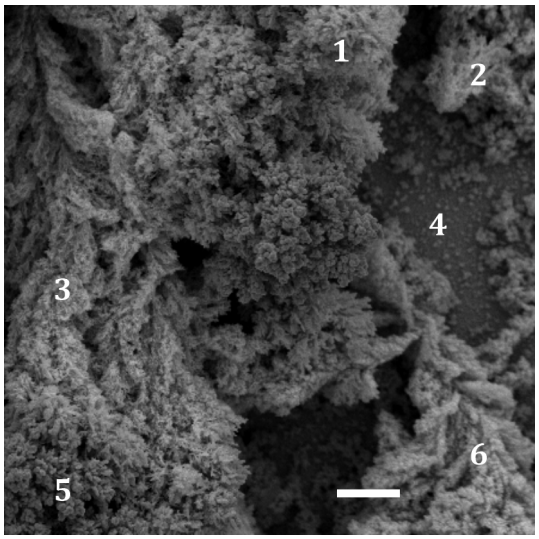

Figure 5.21: SEM image of deposit collected on a Pt substrate at −1.5 V for 1000 s from scDFM at 85 °C and 17 MPa. With an electrolyte containing 1 mM $[N^nBu_4][BiCl_4]$, 1 mM $[N^nBu_4]_2[TeCl_6]$. Scale bar indicates 10 µm.

Fig. 5.21 shows an SEM image of a typical deposit collected from scDFM. As can be seen, inhomogeneous deposits are formed from scDFM, unlike the uniform morphology observed in deposits from DCM. As shown in Table 5.6, this also results in local composition variation, from an area approx. 6×10^{-3} mm^2, five different regions with five different ratios of Bi and Te can be observed. This would suggest that there are multiple phases present in the deposit.

Number (Fig. 5.21)	Bi/Te	Te content / %
1	1/0.85	46
2	1/0.71	42
3	1/0.85	46
4	1/0.61	38
5	1/1.42	59
6	1/0.49	33

Table 5.6: Bi and Te deposit composition at locations in Fig. 5.21. Composition information obtained by EDX.

Fig. 5.22 shows a representative XRD spectrum of a deposit collected from scDFM along with literature standard spectra of Bi, Te and Bi_2Te_3. Typically, X-ray diffraction (XRD) can be used to study the phase composition of materials. However, since Bi, Te and Bi_2Te_3 all have their primary diffraction peaks at similar angles, it is not possible to

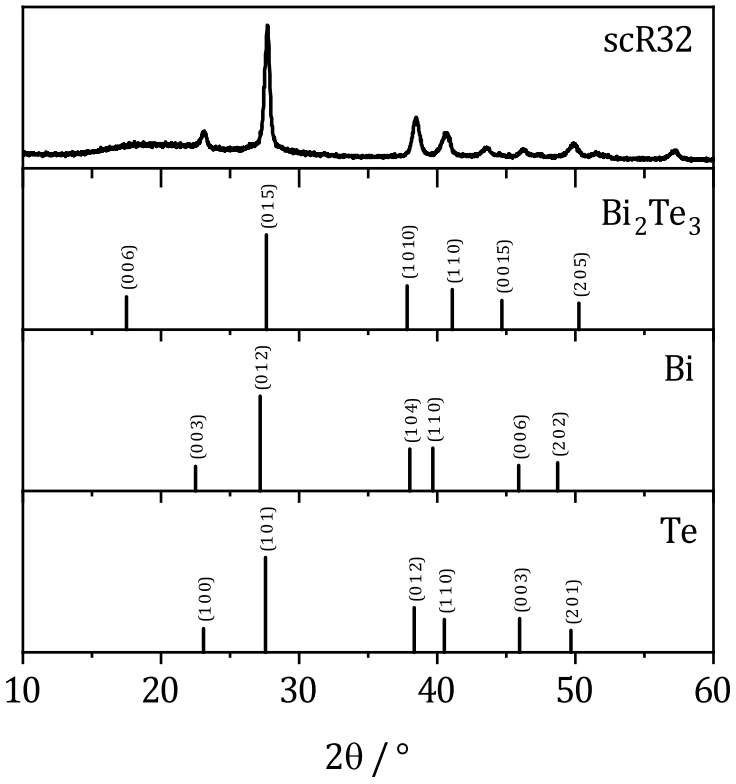

Figure 5.22: Representative XRD spectrum of a Bi and Te codeposit from scDFM along with literature standards of Bi, Te and Bi_2Te_3. Literature spectra obtained from ICSD collection codes 64703, 65692, 74348 for Bi, Te and Bi_2Te_3 respectively. Substrate peaks expected at 40° and 46°.

understand whether the deposits collected from oDCB are composed of Bi_2Te_3, elemental Bi and Te individually, or a mixture of phases.

There are also reasons to be uncertain with the bismuth telluride composition, the codeposit is unlikely to be stable at open circuit. Te^{4+} is capable of reacting with deposited Te:

$$Te^{4+} + Te_{(s)} \longrightarrow 2\,Te^{2+}$$

and Te^{4+} can also react with deposited Bi in a comproportionation reaction, driven by the difference in deposition potential:

$$Bi_2Te_{3(s)} + \frac{3}{2}\,Te^{4+} \longrightarrow 2\,Bi^{3+} + \frac{9}{2}\,Te_{(s)}$$

Since the Te reacting with itself would lower the Te content in the deposit, and the comproportionation reaction would increase it, it is possible the two effects could counteract each other. To overcome this problem, where possible, the cell was vented as soon as possible after the deposit was collected to minimise the time spent in contact with the electrolyte.

5.5.1. Application of the Kröger method

As evidenced from the work above, compound deposition does not begin immediately after the onset of cathodic activity. This does not agree with reports from the literature (Section 5.2.2), suggesting that deposition is no longer taking place *via* the Kröger Class 2 mechanism. Instead, it appears that in scDFM the Bi and Te system now is a Kröger Class 1 system. It is possible that the deposition potential of either metal has shifted, Bi cathodically or Te anodically, such that they no longer deposit at similar potentials, causing a change in deposition mechanism and so different electrolyte conditions are required for controlled deposition.

The Class 1 system of Kröger differs from Class 2 in that codeposition only takes place at a potential range which is between the deposition potential of either species individually. Although, as with Class 2, deposition of the more easily deposited species induces deposition of the other component.

To observe the Class 1 mechanism of deposition and assert control over the composition of a bismuth telluride deposit, it is necessary to use a bath containing a large concentration of $[N^nBu_4]BiCl_4$ and a low concentration of $[N^nBu_4]_2TeCl_6$. The effect of this is to reduce the concentration of Te relative to Bi^{3+} at the interface, lowering the rate of Te^{4+} deposition to the time-scale of the Bi reaction with Te. Since the deposition of Te is rate limiting, the composition of the deposit and the rate of deposition should be dependent on the concentration of Te^{4+} only.

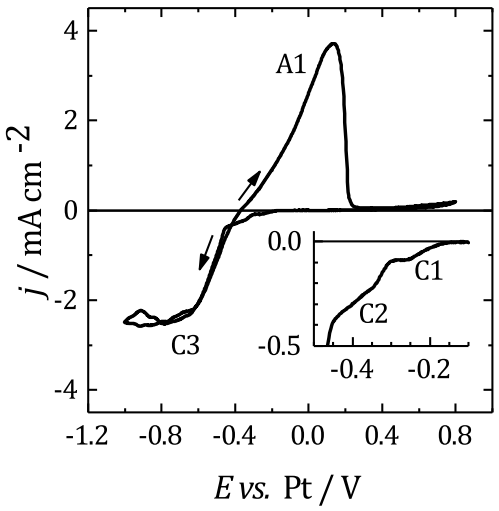

Figure 5.23: Voltammogram of 1.9 mM $[N^nBu_4][BiCl_4]$, 0.3 mM $[N^nBu_4]_2[TeCl_6]$ and 50 mM $[N^nBu_4]Cl$ in scDFM at 85 °C and 17 MPa. Working electrode was swept from 0 V at 50 mV s^{-1} in the direction indicated by the arrows. CE: Pt grid, RE: Pt disc, WE: $r = 0.25$ mm Pt disc. Inset is the cathodic scan in the range 0 V to −0.5 V.

The Class 1 model predicts three stages to the cathodic region with decreasing potential. Firstly at the most positive potentials, only the less noble species deposits. This

is then followed by a current plateau caused by Te reaching mass transport limited deposition. At this stage induced codeposition begins and is where strict composition control can be achieved, Bi content gradually increasing with decreasing potential. Meaning that, in principle, at a certain potential a compound of the desired stoichiometry can be deposited. The third stage begins at potentials more cathodic than the onset of Bi deposition, now Bi begins to deposit as a separate phase and control over composition is lost.

With the previous discussion in mind, experiments were performed with an electrolyte containing 1.9 mM $[N^nBu_4][BiCl_4]$ and 0.3 mM $[N^nBu_4]_2[TeCl_6]$, a Bi^{3+}/Te^{4+} electrolyte ratio of 6.3/1. As predicted, three cathodic regions can be observed. C1, which can be attributed to the deposition of Te. Reversing the potential at −0.3 V (Fig. 5.24a) in the C1 region, shows that the onset of deposition is at −0.01 V, similar to what was observed for Te above. Furthermore, the charge of the stripping peak is approximately half the charge passed during deposition, another feature of Te^{4+} electrochemistry.[47]

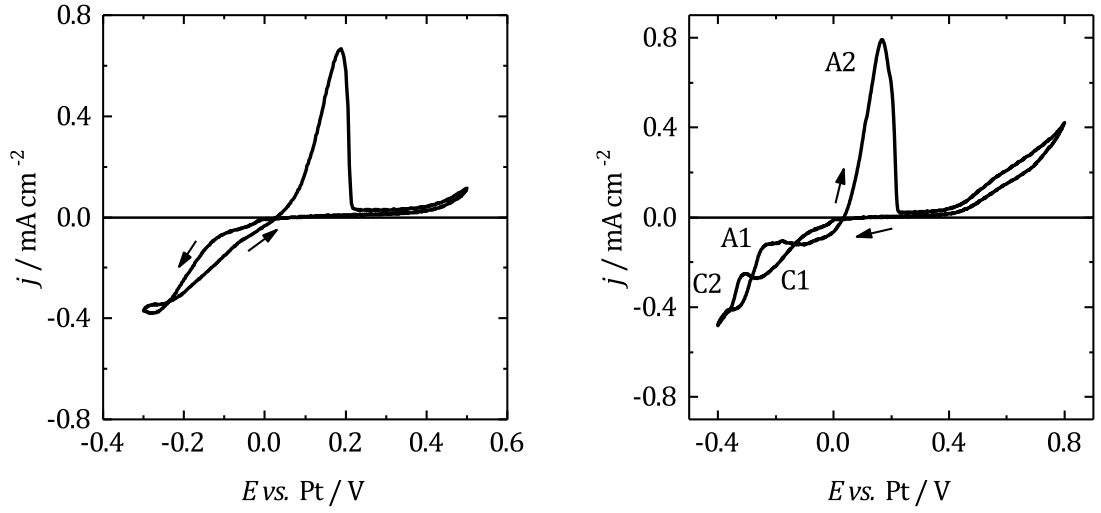

(a) Reversing potential: −0.3 V

(b) Reversing potential: −0.4 V

Figure 5.24: Voltammograms of 1.9 mM $[N^nBu_4][BiCl_4]$, 0.3 mM $[N^nBu_4]_2[TeCl_6]$ and 50 mM $[N^nBu_4]Cl$ in scDFM at 85 °C and 17 MPa. Working electrode was swept from 0 V at 50 mV s^{-1} in the direction indicated by the arrows. CE: Pt grid, RE: r = 0.25 mm Pt disc, WE: r = 0.25 mm.

The C2 region might therefore be expected to be the potential range where controlled codeposition of Bi and Te is possible. Upon extension of the reversing potential into the C2 region at −0.4 V in Fig. 5.24b, a small positive increase in current appears on the anodic sweep, labelled A1. This is possibly associated with the stripping of a bismuth telluride codeposit. On the anodic sweep only one bulk stripping peak is observed, A1, unlike a peak for each element as shown above.

Fig. 5.25 shows a deposit collected from an electrolyte containing 1.9 mM $[N^nBu_4][BiCl_4]$ and 0.3 mM $[N^nBu_4]_2[TeCl_6]$ at −0.43 V, the cathodic end of the C2 region

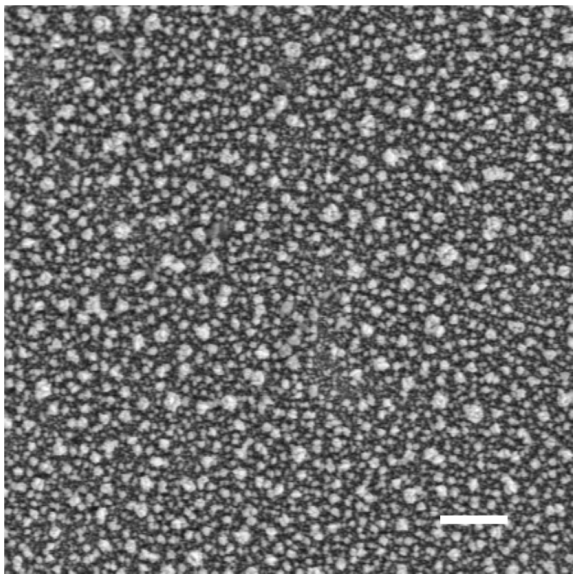

Figure 5.25: SEM image of a deposit collected at −0.43 V *vs.* Pt for 600 s onto a $r = 0.5$ mm Pt disc from scDFM at 86 °C and 17.5 MPa. Containing 1.9 mM $[N^nBu_4][BiCl_4]$, 0.3 mM $[N^nBu_4]_2[TeCl_6]$ and 50 mM $[N^nBu_4]Cl$. Scale bar indicates 10 µm.

of Fig. 5.23. The morphology indicates an initial compact layer of deposit followed by crystallites 1-5 µm in size grown on top. The average Te content is 85%, too high for the formation of stoichiometric Bi_2Te_3.

The Bi/Te electrolyte ratio was increased to 16/1, using 4 mM $[N^nBu_4][BiCl_4]$ and 0.25 mM $[N^nBu_4]_2[TeCl_6]$, with the electrochemistry remaining unchanged from Fig. 5.23. A deposit was collected from the electrolyte at −0.45 V, at a similar position to Fig. 5.25, the cathodic end of the C2 region. The morphology of the deposit appears the same as Fig. 5.25. The average Te composition was 76%, a controlled decrease from the deposit at a lower Bi/Te electrolyte ratio. But it is still not possible to deposit stoichiometric Bi_2Te_3.

It can be seen that increasing the Bi/Te ratio does increase the amount of Bi in the deposit, therefore achieving the correct composition appears to be a matter of finding the appropriate electrolyte ratio. However, then solubility must also be considered. Although it is possible to increase the density and consequently solubility by increasing the operating pressure. The Kröger approach also requires fine control over the potential, something which is not possible with a Pt pseudo RE. It is possible the applied potential drifts out of the potential window suitable for codeposition over the course of the experiment. It is also possible that thermal convection is causing uneven transport of the precursor complexes to the electrode surface.

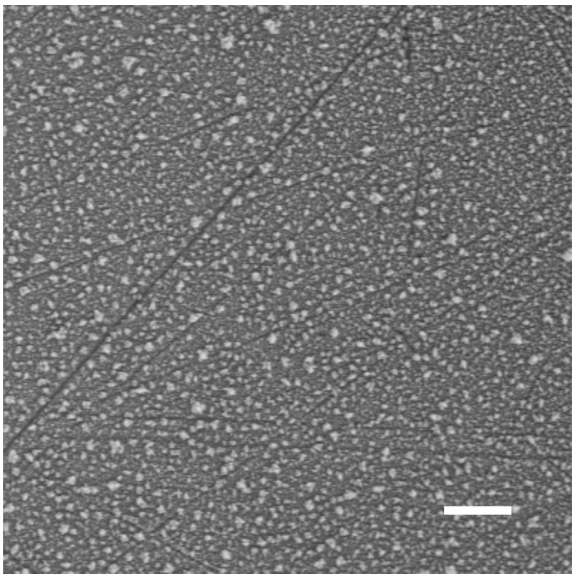

Figure 5.26: SEM image of a deposit collected at −0.45 V *vs.* Pt for 600 s onto a $r = 0.5$ mm Pt disc from scDFM at 85 °C and 17.5 MPa. Containing 1.9 mM $[N^nBu_4][BiCl_4]$, 0.3 mM $[N^nBu_4]_2[TeCl_6]$ and 50 mM $[N^nBu_4]Cl$. Scale bar indicates 10 µm.

5.6. Conclusions

This Chapter detailed investigations into the electrodeposition of Sb_2Te_3 from oDCB and DCE, and of Bi_2Te_3 from oDCB, DCE and scDFM. The purpose was to further characterise the solvents oDCB and DCE, exploring the feasibility of semiconductor electrodeposition from oDCB and DCE, and also to investigate the possibility of Bi_2Te_3 nanowire deposition from scDFM. Sb_2Te_3 and Bi_2Te_3 were used as benchmark materials due their previous demonstration as robust systems in both aqueous and non-aqueous solvents, including DCM.

Stoichiometric Sb_2Te_3 was successfully deposited onto TiN from both oDCB and DCE and characterised by EDX, SEM and XRD. In oDCB, an electrolyte composed of 1.5 mM $[N^nBu_4][BiCl_4]$ and 3 mM $[N^nBu_4]_2[TeCl_6]$ was found to be necessary, whereas in DCE a bath of 1.75 mM $[N^nBu_4][BiCl_4]$ and 3 mM $[N^nBu_4]_2[TeCl_6]$ was required. Sb/Te electrolyte ratios of 0.5 and 0.6 for oDCB and DCE respectively. Deposits were collected at five potentials between −1.5 and 2.5 V *vs.* DMFc. Sb was in excess in the deposits collected −1.5 V and −1.75 V from both oDCB and DCE. As the potential was lowered, the Sb content in the deposits decreased to that corresponding to Sb_2Te_3, and the composition became independent of potential. XRD indicated that the deposits were amorphous or partially crystalline.

For Bi_2Te_3, stoichiometric, crystalline Bi_2Te_3 was electrodeposited from oDCB and DCE, also within the potential range −1.5 to −2.5 V. In oDCB, a bath of 2 mM $[N^nBu_4][BiCl_4]$ and 3 mM $[N^nBu_4]_2[TeCl_6]$ was required for deposition of Bi_2Te_3. The composition was unaffected by the applied potential, except at −1.5 V where Bi was in excess. In DCE, 2.5 mM $[N^nBu_4][BiCl_4]$ and 3 mM $[N^nBu_4]_2[TeCl_6]$ was required for the electrodeposition of Bi_2Te_3.

This corresponds to an electrolyte Bi/Te ratio of 0.67 and 0.83 for oDCB and DCE respectively, and a linear relationship between composition and potential was found. With the deposited Bi/Te ratio decreasing with potential. Attempts at deposition of Bi_2Te_3 from scDFM were unsuccessful, it was not possible to achieve deposits of a suitable composition. This was attributed to convection affecting mass transport behaviour, poor control over the reference potential, and possibly a change in the electrochemistry of the precursors also.

It is now possible to assess the mechanism of Sb_2Te_3 and Bi_2Te_3 deposition from oDCB and DCE, and how this compares with other studied solvents. As with other non-aqueous solvents, including DCM, Te is now the more noble metal with a more negative onset of deposition than Sb and Bi. However, codeposition of Te with Sb and Bi still appears to be possible at potentials more positive than the onset of Te deposition only. Indicating that the induced deposition of Te by Sb or Bi is occurring in the studied solvents. Similar relationships with potential are also observed in the different systems, where composition was broadly independent of potential. These behaviours both point to the Kröger mechanism of induced deposition being present in oDCB and DCE also. The exception to this rule appears to be Bi-Te in DCE, where a linear decrease in Bi content is observed with potential. One possible reason for this is that the deposition of both metals is not limited by diffusion. Voltammetry of Te^{4+} in Chapter 4 suggested it was kinetically limited. The ratio of Sb and Bi to Te in stoichiometric Sb_2Te_3 and Bi_2Te_3 is 0.67. The precursor ratio in the electrolyte was Sb/Te: 0.5 and 0.58 for oDCB and DCE respectively, and Bi/Te: 0.67 and 0.83 for oDCB and DCE respectively. It appears therefore that an excess of the Te precursor, greater than 0.67, is required to deposit Sb_2Te_3, suggesting that this remains a Kröger Class 1 system, similar to other non-aqueous electrolytes. For Bi_2Te_3 on the other hand, less Te precursor is required in the electrolyte than the compound. This is the same as previous work in DCM and other solvents, and indicates that the Bi-Te system remains Class 2 in oDCB and DCE.

These results represent further characterisation of the WCS, and by electrodeposition of Sb_2Te_3 and Bi_2Te_3, demonstrate the solvent's suitability for further application to the electrodeposition of semiconductors, and also electrodeposition at elevated temperatures.

5.7. References

(1) R. Chen, J. Lee, W. Lee and D. Li, *Chem. Rev.*, 2019, **119**, 9260–9302.

(2) G. Leimkühler, I. Kerkamm and R. Reineke-Koch, *J. Electrochem. Soc.*, 2002, **149**, C474–C478.

(3) D. Del Frari, S. Diliberto, N. Stein, C. Boulanger and J. M. Lecuire, *Thin Solid Films*, 2005, **483**, 44–49.

(4) K. Park, F. Xiao, B. Y. Yoo, Y. Rheem and N. V. Myung, *J. Alloys Compd.*, 2009, **485**, 362–366.

(5) S. K. Lim, M. Y. Kim and T. S. Oh, *Thin Solid Films*, 2009, **517**, 4199–4203.

(6) H. Jung and N. V. Myung, *Electrochim. Acta*, 2011, **56**, 5611–5615.

(7) J. L. Lensch-Falk, D. Banga, P. E. Hopkins, D. B. Robinson, V. Stavila, P. A. Sharma and D. L. Medlin, *Thin Solid Films*, 2012, **520**, 6109–6117.

(8) J. Schoenleber, N. Stein and C. Boulanger, *J. Electroanal. Chem.*, 2014, **724**, 111–117.

(9) H. P. Nguyen, X. Peng, G. Murugan, R. J. M. Vullers, P. M. Vereecken and J. Fransaer, *J. Electrochem. Soc.*, 2013, **160**, D75–D79.

(10) M. Wu, K. Binnemans and J. Fransaer, *Electrochim. Acta*, 2014, **147**, 451–459.

(11) A. S. Catrangiu, I. Sin, P. Prioteasa, A. Cotarta, A. Cojocaru, L. Anicai and T. Visan, *Thin Solid Films*, 2016, **611**, 88–100.

(12) K. Cicvarić, Ph.D. Thesis, University of Southampton, 2020.

(13) F. A. Kroger, *J. Electrochem. Soc.*, 1978, **125**, 2028–2034.

(14) M. Takahashi, Y. Oda, T. Ogino and S. Furuta, *J. Electrochem. Soc.*, 1993, **140**, 2550.

(15) P. Magri, C. Boulanger and J.-M. Lecuire, *J. Mater. Chem.*, 1996, **6**, 773–779.

(16) K. Tittes, A. Bund, W. Plieth, A. Bentien, S. Paschen, M. Plötner, H. Gräfe, W. J. Fischer, M. Plotner, H. Grafe and W. J. Fischer, *J. Solid State Electrochem.*, 2003, **7**, 714–723.

(17) M. S. Martıin-Gonzalez, A. L. Prieto, R. Gronsky, T. Sands and A. M. Stacy, *J. Electrochem. Soc.*, 2002, **149**, C546.

(18) D.-W. Liu and J.-F. Li, *J. Electrochem. Soc.*, 2008, **155**, D493.

(19) Y. Ma, A. Johansson, E. Ahlberg and A. E. Palmqvist, *Electrochim. Acta*, 2010, **55**, 4610–4617.

(20) A. Zimmer, L. Broch, C. Boulanger and N. Stein, *Electrochim. Acta*, 2015, **174**, 376–383.

(21) S. Wen, R. R. Corderman, F. Seker, A.-P. Zhang, L. Denault and M. L. Blohm, *J. Electrochem. Soc.*, 2006, **153**, C595–C602.

(22) A. Zimmer, N. Stein, L. Johann, R. Beck and C. Boulanger, *Electrochim. Acta*, 2007, **52**, 4760–4766.

(23) V. Richoux, S. Diliberto, C. Boulanger and J. M. Lecuire, *Electrochim. Acta*, 2007, **52**, 3053–3060.

(24) W. Glatz, L. Durrer, E. Schwyter and C. Hierold, *Electrochim. Acta*, 2008, **54**, 755–762.

(25) C. Lei, K. S. Ryder, E. Koukharenko, M. Burton and I. S. Nandhakumar, *Electrochem. commun.*, 2016, **66**, 1–4.

(26) C. Kulsi, M. Mitra, K. Kargupta, S. Ganguly, D. Banerjee and S. Goswami, *Mater. Res. Express*, 2015, **2**, 106403.

(27) Y. Song, I. J. Yoo, N. R. Heo, D. C. Lim, D. Lee, J. Y. Lee, K. H. Lee, K. H. Kim and J. H. Lim, *Curr. Appl. Phys.*, 2015, **15**, 261–264.

(28) O. Caballero-Calero, P. Diaz-Chao, B. Abad, C. V. Manzano, M. D. Ynsa, J. J. Romero, M. M. Rojo and M. S. Martin-Gonzalez, *Electrochim. Acta*, 2014, **123**, 117–126.

(29) B. Abad, M. Rull-Bravo, S. L. Hodson, X. Xu and M. Martin-Gonzalez, *Electrochim. Acta*, 2015, **169**, 37–45.

(30) S. Michel, S. Diliberto, C. Boulanger, N. Stein and J. M. Lecuire, *J. Cryst. Growth*, 2005, **277**, 274–283.

(31) M. Bouroushian, *Electrochemistry of Metal Chalcogenides*, ed. F. Scholz, Springer, Berlin, 2010.

(32) W. M. Haynes, D. R. Lide and T. J. Bruno, *CRC Handbook of Chemistry and Physics*, CRC Press, New York, 96th edn., 2016.

(33) Y. Miyazaki and T. Kajitani, *J. Cryst. Growth*, 2001, **229**, 542–546.

(34) V. R. Sidorko, L. V. Goncharuk and R. V. Antonenko, *Powder Metall. Met. Ceram.*, 2008, **47**, 234–241.

(35) W. S. Kang, W. J. Li, W. C. Chou, M. F. Tseng and C. S. Lin, *Thin Solid Films*, 2017, **623**, 90–97.

(36) L. Qiu, J. Zhou, X. Cheng and R. Ahuja, *J. Phys. Chem. Solids*, 2010, **71**, 1131–1136.

(37) W. J. Li, *Electrochim. Acta*, 2009, **54**, 7167–7172.

(38) M. Abellan, R. Schrebler and H. Gomez, *Int. J. Electrochem. Sci.*, 2015, **10**, 7409–7422.

(39) H. P. Nguyen, M. Wu, J. Su, R. J. M. Vullers, P. M. Vereecken and J. Fransaer, *Electrochim. Acta*, 2012, **68**, 9–17.

(40) C. Agapescu, A. Cojocaru, A. Cotarta and T. Visan, *J. Appl. Electrochem.*, 2013, **43**, 309–321.

(41) L. Meng, K. Cicvarić, A. L. Hector, C. de Groot and P. N. Bartlett, *J. Electroanal. Chem.*, 2019, **839**, 134–140.

(42) G. Ghosh, *J. Phase Equilibria*, 1994, **15**, 349–360.

(43) C. Guo, C. Li and Z. Du, *J. Electron. Mater.*, 2014, **43**, 4082–4089.

(44) K. Govaerts, M. H. Sluiter, B. Partoens and D. Lamoen, *Phys. Rev. B*, 2012, **85**, 1–8.

(45) C. Mao, M. Tan, L. Zhang, D. Wu, W. Bai and L. Liu, *Calphad*, 2018, **60**, 81–89.

(46) J. W. Bos, H. W. Zandbergen, M. H. Lee, N. P. Ong and R. J. Cava, *Phys. Rev. B*, 2007, **75**, 1–9.

(47) P. N. Bartlett, D. A. Cook, M. M. Hasan, A. L. Hector, S. Marks, J. Naik, G. Reid, J. Sloan, D. C. Smith, J. Spencer and Z. Webber, *RSC Adv.*, 2017, **7**, 40720–40726.

6

The Effect of Temperature

6.1. Overview

In this Chapter the effect of temperature on electrochemistry in the weakly coordinating solvents oDCB and DCE is reported. DMFc and $CcPF_6$ are once again used as model redox species and the relationship between redox potential and diffusion coefficient, and temperature is investigated. The solvents are also used to electrodeposit antimony and antimony telluride at various temperatures, with the collected deposits characterised using SEM, XRD and Raman spectroscopy. The obtained information is then used to deduce the role of temperature in determining the properties of the deposited material.

6.2. Introduction

One of the stated aims of this project was to use the identified weakly coordinating solvents for electrodeposition at elevated temperatures. This was because of the expected improvements in crystallinity and material properties that could be achieved, relative to depositions at room temperature. Previous Chapters have detailed characterisation of the solvents at increasing levels of complexity and it has now been successfully demonstrated that the two candidate solvents: o-dichlorobenzene and 1,2-dichloroethane, are capable of electrodepositing p-block semiconductors. The work also revealed that Sb and Sb_2Te_3 appear to deposit in an amorphous form at room temperature. These two materials are therefore good candidates to investigate deposition at higher temperatures since a visible change in their material properties might be expected to be observed with increasing temperature.

In a conventional electrochemical cell, the RE is located in the same compartment as the WE and the CE. However, the reference potential of a particular RE is temperature dependent, so if a cell were heated to study the effect of temperature, the RE is also heated and no longer provides a stable reference potential. It would therefore be impossible to disentangle any changes in redox potential of a couple under investigation from that of the RE. A solution is to store the RE in a separate compartment, which is not heated, in a cell design known as a 'non-isothermal' cell.[1] With a non-isothermal cell, the main compartment which is heated contains the WE and the CE, and the RE is located in a separate compartment which is held at room temperature. In this way, the reference potential is unaffected by temperature changes, permitting reliable electrochemical measurements at higher temperatures and also allows any changes in measured redox potential to be attributed directly to the studied redox couple. A non-isothermal cell was designed and built for the purposes of this work, based upon the design by Weaver *et al.*[1] Further details of its design can be found in Chapter 2.

The change in measured redox potential of a couple with temperature, $\mathrm{d}E_{1/2}/\mathrm{d}T$, consists of three components:

$$\frac{\mathrm{d}E_{1/2}}{\mathrm{d}T} = \frac{\mathrm{d}E_{\mathrm{tlj}}}{\mathrm{d}T} + \frac{\mathrm{d}E_{\mathrm{T}}}{\mathrm{d}T} + \frac{\mathrm{d}E_{\mathrm{rc}}}{\mathrm{d}T} \tag{6.1}$$

Where E_{tlj} is the thermal liquid junction potential (tlj), arising because of the potential difference between the heated and unheated sections of the cell and E_{T} is the potential difference caused by the Thompson effect; a thermoelectric effect caused by a temperature differential in the working electrode wire.[1–3] The tlj has been measured in aqueous electrolytes using a similar non-isothermal cell arrangement and values were generally less than $25\,\mu\mathrm{V\,K^{-1}}$.[2] Similar information is not available for non-aqueous electrolytes but the magnitude can be assumed to be similar. The Thompson coefficient for Pt is $6\,\mu\mathrm{V\,K^{-1}}$,[1] suggesting that errors associated with these effects will be minimal. The third term in Eqn.

(6.1) is then the variation associated with the redox couple under investigation. Since $nFE = T\Delta S - \Delta H$, $dE_{1/2}/dT = dE_{rc}/dT = \Delta S_{rc}/nF$. Where $\Delta S_{rc} = S^0_{red} - S^0_{ox}$. Therefore, the change in redox potential of a couple with temperature is caused by the entropy change of electron transfer of the redox couple.

A major source of motivation for performing electrochemical measurements at varying temperatures has been to measure ΔS_{rc} and investigate the contribution of entropy to the driving force of electrode reactions. Major contributions to this area of study have been provided by Weaver,[1,3–5] who measured the reaction entropy of several combinations of metals and ligands in a variety of solvents. The entropy of electron transfer is generally found to be positive for cationic redox couples. The increase in charge of the oxidised form causes a relative increase in solvent polarisation around the complex as the solvent orders itself around the species. The exceptions to this rule are solvents with internal structure, such as water, in which a large degree of order already exists, arising from the H-bonding network. Reaction entropies are typically smaller in such solvents, and potentially negative, as the solvent molecules are more resistant to disturbances in the solvent structure.[3] For a given solvent, the reaction entropy has generally been found to correlate well with the radius of the reacting species and also the change in charge $\left(z^2_{ox} - z^2_{red}\right)$ for structurally diverse complexes,[5] demonstrating the importance of non-specific electrostatic interactions in determining the degree of reaction entropy. Exceptions to this rule are observed when the ligands are able to interact specifically with the solvent. For example, aquo complexes in water or electrophilic ligands in Lewis basic solvents, where a relative further increase in reaction entropy is observed.[4] The metal centre can also influence the measured reaction entropy through changes in bonding upon oxidation. As a representative example, complexes based on $Co^{2+/3+}$ show markedly higher reaction entropies than those with other metal centres under identical conditions.[6,7] This has been attributed to a large reorganisation energy caused by the loss of an anti-bonding electron upon oxidation.

The effect of electrostatics on reaction entropies has also been investigated. The dielectric constant changes with temperature so a direct correlation between ΔS_{rc} and dielectric constant is not possible. However, the theoretical reaction entropy can be calculated using the Born equation and then compared with experimental values. This has been attempted previously,[3,5] with poor agreement between the two. Typically the Born equation significantly underestimates the reaction entropy, which has been attributed to a lowering of the effective dielectric constant in the vicinity of the reacting species caused by dielectric saturation. This is not accounted for in the Born model. Instead, correlation has been observed with empirical measures of solvent structure.[5,7] Stronger electrostatic interactions between solvent molecules mean that the solvent is more resistant to polarisation by the reacting species and so the difference in entropy between the oxidised and reduced forms is less. The effect of H-bonding in water described above is a specific example of this. A modified form of the Born equation, accounting for non-continuum

effects, was used by Blum and Fawcett to estimate reaction entropies for ferrocene. The values showed improved agreement with experiment compared with the Born equation.[8]

The temperature is a commonly exploited variable in electrodeposition. For example the Watts bath for Ni electrodeposition operates in the temperature range 44-66 °C.[9] The standard/industry plating baths for other commonly electrodeposited metals, including Cu, Au and Pb, also operate at temperatures above room temperature.[9] In a general sense, increasing the temperature increases the rate of mass transport of precursor to the substrate, and also the rate of electron transfer and any associated chemical reactions. As such, the rate of metal growth is increased. Higher temperatures can also raise the solubility of the metal precursor, leading to even greater deposition rates and an improvement in throwing power. The temperature can also influence the morphology of the deposit. For example, Sn deposited from an aqueous electrolyte was reported to become smoother and brighter as the the temperature was increased.[10] Moreover, the solution temperature can influence the material properties of the electrodeposited metal. Parameters such as tensile strength, hardness and internal stress of electrodeposited Ni have all been observed to be affected by the bath temperature.[9] The situation is similar with the composition of electrodeposited alloys, with all other variables being equal the ratio of elements can vary significantly with temperature.[11]

It is clear that the bath temperature exerts significant control over the properties of an electroplated metal or alloy, and can be exploited to gain influence over them. However, examination of the literature reveals that the particular property that is affected, and the magnitude of the response, is highly system dependent. Little systematic investigation has been undertaken and, since changes in other available variables in a deposition bath manifest themselves in a similar way, the underlying principles of the effect of temperature remain unclear.

Of particular interest for the present work is the effect of the temperature on the crystallisation of the electrodeposited metal. It is generally observed that heating of the electrolyte can lead to an improvement in the crystallinity of the deposit, either by a transition from amorphous to crystalline material, or the formation of larger crystallites. Typically, a material which deposits amorphously at room temperature would need to be subsequently annealed to render it crystalline. Alternatively, by depositing at elevated temperatures, crystalline material is formed and so removing the need for annealing. Such effects have been reported by Gu *et al.* for the electrodeposition of Si from propylene carbonate.[12] Where amorphous Si forms at room temperature, heating to 80 °C achieves crystalline Si. Similarly Wu *et al.* formed crystalline Re-Ir-Ni alloys when depositing at 70 °C, which were found to be amorphous at lower temperatures.[13] Murugesan *et al.* also reported electrodeposition of amorphous MoS_2 at room temperature from ionic liquids, but crystalline deposits were collected at 100 °C.[14] Whilst this effect is regularly observed in the literature, a microscopic explanation of its origins is lacking. It does not appear to be well understood why different metals or compounds require differing temperatures

to deposit in a crystalline form. Insight can however be gained from knowledge on the mechanisms of non-electrocrystallisation. According to Ostwald's law of stages the least stable form of a system crystallises first, *i.e.* the amorphous form.[15] The transition from the amorphous to crystalline form is then a thermally activated process, the rate of crystallisation following an Arrhenius type relationship with an associated activation energy of crystallisation.[16] As such, it might be possible to say qualitatively, that when the bath temperature is raised, a greater proportion of the deposited atoms would be able to overcome the activation energy of crystallisation and therefore the deposit adopts a crystalline structure. It might also therefore be speculated that materials that are not crystalline at room temperature possess a relatively larger activation energy of crystallisation than those that do.

The aim of this Chapter is to study the effect of temperature on various electron transfer processes. Firstly the electrochemistry of model redox couples will be investigated at various temperatures to understand the role of temperature in the solvents oDCB and DCE. The electrodeposition of semiconductors will also be attempted as a method to improving their material properties.

6.3. Electrochemistry of Decamethylferrocene and Cobaltocenium Hexafluorophosphate

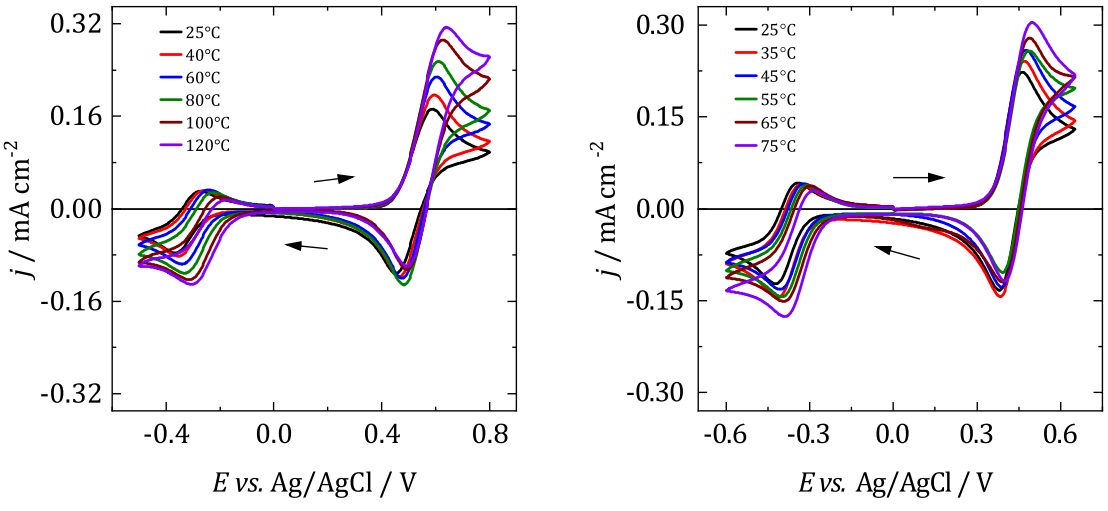

(a) oDCB (b) DCE

Figure 6.1: Representative voltammograms at various temperatures of 1 mM DMFc and 0.5 mM $CcPF_6$ with 100 mM $[N^nBu_4]Cl$ in oDCB and DCE at r = 0.25 mm Pt WE. WE was swept from 0 V *vs.* Ag/AgCl in the direction of the arrows at a scan rate of 100 mV s^{-1}. CE: Pt grid, RE: Ag/AgCl.

The electrochemistry of DMFc and $CcPF_6$ was once again used as an initial model system in order to understand the effect of temperature on electrochemistry in oDCB and

DCE. Fig. 6.1 above shows the effect of temperature on the voltammetry of DMFc and $CcPF_6$ at a macrodisc in oDCB and DCE. In oDCB voltammograms were recorded at six temperatures between 25 and 120 °C. For DCE, data was collected six temperatures between 25 and 75 °C (limited by its boiling point). Beginning at 0 V *vs.* Ag/AgCl and scanning anodically, an oxidation peak is observed corresponding to the oxidation of DMFc to $DMFC^+$, after reversing the scan, a second reduction peak can be seen, associated with the reduction of Cc^+ to Cc. With increasing temperature the peak currents also increase. Decreasing viscosity increases the rates of mass transport. It is interesting to note that the first peak for each redox couple (oxidation for DMFc and reduction for $CcPF_6$) appears to be more sensitive to temperature than the second peak. The separation between the peak potentials, ΔE_p, is proportional to RT/nF, therefore this effect is likely caused by the increase in separation between the oxidation and reduction peaks.

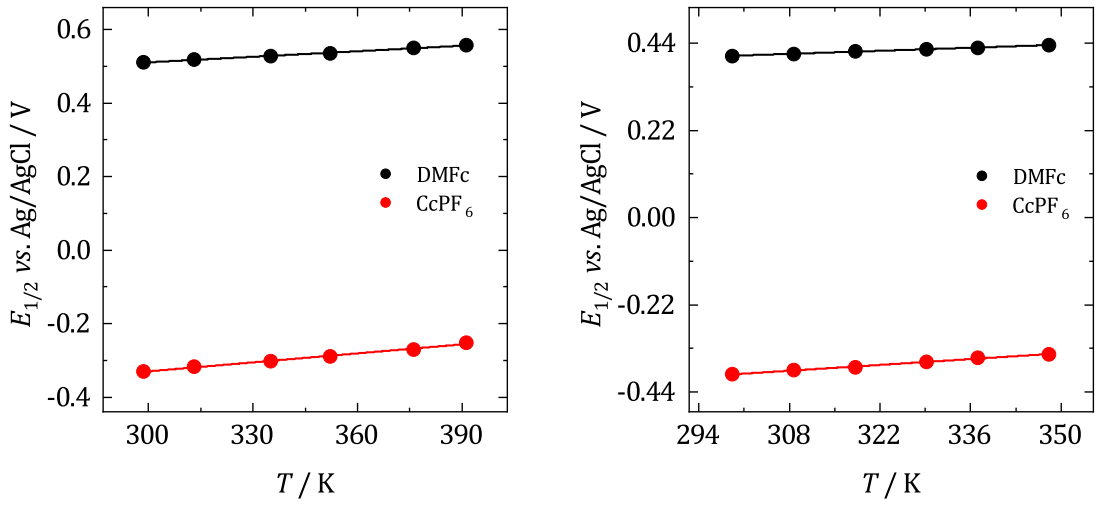

(a) oDCB (b) DCE

Figure 6.2: Representative plots of variation of $E_{1/2}$ of DMFc and $CcPF_6$ with temperature in oDCB and DCE. Data collected from macrodisc voltammograms. Black: DMFc, red: $CcPF_6$

As established in the discussion above, a plot a of $E_{1/2}$ *vs.* T should be linear with a slope equal to $\Delta S_{rc}/nF$.[3] Fig. 6.2 shows such plots for DMFc and $CcPF_6$ in oDCB and DCE. All plots show a positive correlation and a good linear fit with $R^2 > 0.99$ in all cases. The value of the slope and associated ΔS_{rc} are shown in Table 6.1. ΔS_{rc} is relatively small and positive for DMFc and $CcPF_6$ in both oDCB and DCE, with values generally larger for $CcPF_6$ than for DMFc and larger in DCE than in oDCB. The ratio $\Delta S_{rc}(DMFc)/\Delta S_{rc}(CcPF_6)$ is similar for both solvents, with values of 0.60 and 0.56 for oDCB and DCE respectively, suggesting that the relative sizes remain constant across both solvents. A positive entropy change is typical for unstructured solvents and is because of electrostriction of the solvent surrounding the species as the charge increases. Previous work, as described above,

has shown that Co(II/III) redox couples experience a relative increase in entropic effects because of the particularities of its bonding.[6,7]

	DMFc			$CcPF_6$		
	$dE_{1/2}/dT$ / mV K^{-1}	ΔS_{rc}(exp) / J K^{-1} mol^{-1}	ΔS_{rc}(calc) / J K^{-1} mol^{-1}	$dE_{1/2}/dT$ / mV K^{-1}	ΔS_{rc}(exp) / J K^{-1} mol^{-1}	ΔS_{rc}(calc) / J K^{-1} mol^{-1}
oDCB	0.50(3)	48(3)	49	0.83(7)	80(7)	64
DCE	0.56(1)	54(1)	83	0.98(8)	94(7)	108

Table 6.1: Temperature dependence of the redox potential of DMFc and $CcPF_6$ and associated experimental and theoretical reaction entropies, ΔS_{rc}. Experimental values obtained from the average of three repeats with the standard deviation as the error. ΔS_{rc} (calc) estimated from the Born equation.

ΔS_{rc} of metallocenes have been measured previously and some relevant values for aprotic, unstructured solvents are given in Table 6.2 below. As can be seen, the values generally fall in the range 10−60 J K^{-1} mol^{-1}. The exception to this is the work by Matsumoto and Swaddle who observed negative values.[17] A non-isothermal cell was not used in their work and the results can be ignored. The values for DMFc measured in the present work appear to lie within range of values observed in the literature, the value for DMFc in DCE also agrees well for that reported by Noviandri *et al.*[18] This demonstrates that the results in the present work are reasonable, and that the non-isothermal cell design used here is successful at minimising the effect of E_{tlj} and E_T. Furthermore, taking the most pessimistic estimates for dE_{tlj}/dT and dE_T/dT, 50 and 15 µV K^{-1},[1,2] gives an estimated error in ΔS_{rc} of ±6 J K mol^{-1}, which is on the order of the experimental error.

Redox couple	Solvent	Electrolyte	ΔS_{rc} / J K^{-1} mol^{-1}	Ref.
$Fc^{0/+}$	DCM	$[N^nBu_4][BF_4]$	15	[18]
$DMFc^{0/+}$	DCM	$[N^nBu_4][BF_4]$	13	[18]
$Fc^{0/+}$	DCE	$[N^nBu_4][BF_4]$	39	[18]
$DMFc^{0/+}$	DCE	$[N^nBu_4][BF_4]$	59	[18]
$Fc^{0/+}$	ACN	$[N^nBu_4][BF_4]$	47	[18]
$Fc^{0/+}$	DMF	$[N^nBu_4][BF_4]$	54	[18]
$DMFc^{0/+}$	ACN	$[N^nBu_4][BF_4]$	52	[18]
$DMFc^{0/+}$	DMF	$[N^nBu_4][BF_4]$	54	[18]
$Fc^{0/+}$	ACN	$LiClO_4$	48	[3]
$Fc^{0/+}$	DMF	$LiClO_4$	59	[3]
$DMFc^{0/+}$	ACN	$[N^nBu_4][ClO_4]$	−39	[17]
$DMFc^{0/+}$	DMF	$[N^nBu_4][ClO_4]$	−24	[17]

Table 6.2: Literature compilation of relevant ΔS_{rc} values for DMFc. Fc: ferrocene, ACN: acetonitrile, DMF: N,N-dimethylformamide.

As discussed above, ΔS_{rc} would generally be expected to decrease with increasing size of the redox couple. Interestingly, this is not consistently observed in the literature

results, with ΔS_{rc}(DMFc) often similar to or greater than the value for Fc. This might suggest that another factor that affects the entropy value is more significant and lowering Fc/increasing DMFc. It is possible this is caused by ion pairing, Fc is smaller than DMFc so would be expected to have a greater degree of ion pairing, increasing the size of the reacting species, and lowering ΔS_{rc}. Alternatively it is possible that experimental error is greater than the difference in entropy expected for the redox couples. If a small temperature range was used for example, then the slope may not be measured accurately enough to distinguish between the two. In earlier Chapters it was shown that, based upon diffusion coefficient measurements, Cc^+ was ion paired in solution and so had a larger particle size than DMFc. Since ΔS_{rc} is greater for $CcPF_6$ than DMFc, this suggests the reduction caused by ion pairing is not significant compared to the contribution from bonding effects.

Table 6.2 also shows theoretical entropies of electron transfer, ΔS_{rc}(calc), calculated from the Born equation using Eqn. (6.2).

$$\Delta S_{rc} = -\frac{N_A e^2}{8\pi\epsilon_0\epsilon_r r_i}\frac{\partial \ln \epsilon_r}{\partial T}\left(z_{ox}^2 - z_{red}^2\right) \tag{6.2}$$

Where $\partial \ln \epsilon_r / \partial T$ is the temperature dependence of the solvents' dielectric constant, and z_{ox} and z_{red} is the charge on the reduced and oxidised species respectively. The van der Waals radius was used for r_i, assuming no change in the radius between oxidised and reduced forms. For $\partial \ln \epsilon_r / \partial T$ values of -0.00297 and -0.00524, estimated from Ref. [19], were used for oDCB and DCE respectively. The estimate seems to be highly dependent on the quality of the data used for $\partial \ln \epsilon_r / \partial T$, however. When predicted using data from an alternative source, Ref. [20], values were quite different, especially for oDCB, suggesting the temperature dependence is not known with much accuracy in the literature. The theoretical reaction entropies appear to show the same trends as the experimental values, but quantitative agreement is poor. The Born value is reasonable for DMFc in oDCB, underestimated for $CcPF_6$ in oDCB, and overestimated for both couples in DCE. It must be noted that since r_{vdW} is the minimum possible radius for the molecules, the resulting ΔS_{rc} estimate represents an upper bound and the effective radius in solution is likely larger. Nevertheless in oDCB, after accounting for the larger reaction entropy expected for $Co^{2+/3+}$ complexes described above, it might be concluded that the Born estimate is reasonable and therefore little dielectric saturation is present. Conversely this cannot be said in DCE, there is no reasonable explanation for the Born equation overestimating ΔS_{rc} and so it would appear that the value used for $\partial \ln \epsilon_r / \partial T$ is too large.

The behaviour of the diffusion coefficients of DMFc and $CcPF_6$ as the solvents were heated was also of interest. To this end, microelectrode voltammograms of an electrolyte containing DMFc and $CcPF_6$ were recorded in oDCB and DCE at 10 °C intervals between 25-65 °C. These can be found in Fig. 6.3. A limiting current plateau forms at each temperature, however it can also be seen that at higher temperatures the current plateau is

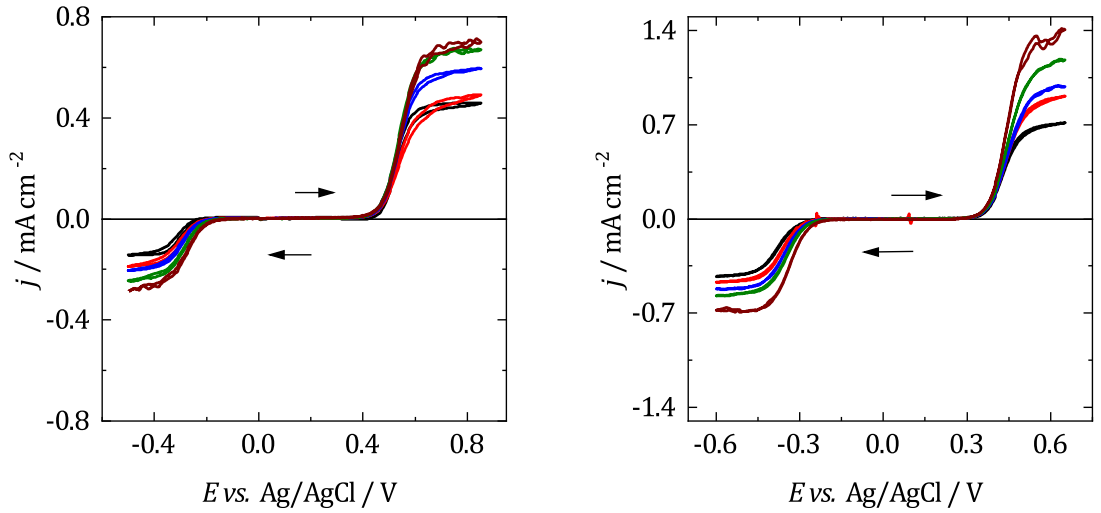

(a) oDCB (b) DCE

Figure 6.3: Representative voltammograms at various temperatures of 1 mM DMFc and 0.5 mM $CcPF_6$ with 100 mM $[N^nBu_4]Cl$ in oDCB and DCE at $r = 25\,\mu m$ WE. WE was swept from 0 V *vs.* Ag/AgCl in the direction of the arrows at a scan rate of 10 mV s^{-1}. CE: Pt grid, RE: Ag/AgCl. Black: 25 °C, red: 35 °C, blue: 45 °C, green: 55 °C, brown: 65 °C.

noisy. This is due to additional mass transport caused by thermal convection and has been observed previously for microelectrode measurements at elevated temperatures in supercritical fluids.[21] This clearly introduces an uncertainty in i_L since its value is poorly defined, and it is not clear to what extent convection contributes to the limiting current. This was resolved in supercritical fluids by the fitting of a baffle to shield the electrode.[21] However this was found to be ineffective in organic solvents because mixing of electrolyte between the baffle and the bulk solution was poor. Instead an alternate method was used, also presented by Branch, whereby multiple scans are performed and the lower bound of the current plateau was taken as i_L.[21] D was then taken from voltammograms of a $r = 12.5\,\mu m$ Pt microelectrode, without concentration correction.

The relationship between diffusion coefficient and temperature has been shown to take an Arrhenius type form, shown below.[22]

$$D = D_0 \exp\left(-\frac{E_{a,D}}{RT}\right) \tag{6.3}$$

Where D_0 is the theoretical diffusion coefficient at infinitely low temperature and $E_{a,D}$ is the activation energy of diffusion of the diffusing particle. $E_{a,D}$ is associated with the energy required to remove the particle from its surroundings, and into a a neighbouring void.[22] Representative Arrhenius plots for DMFc and $CcPF_6$ in oDCB and DCE can be found in Fig. 6.4. As can be seen the plots are linear with reasonable fits and the resulting activation energies of diffusion are summarised in Table 6.3.

There does not seem to be any significant variation in $E_{a,D}$ with solvent or diffusing particle. $E_{a,D}(CcPF_6)$ is larger than DMFc in oDCB, but this is then reversed in DCE. It has previously been shown that the radius of Cc^+ is larger than DMFc in solution because of ion pairing. Moreover, conceptually it might be expected that a larger diffusing particle has a larger activation energy of diffusion and so $E_{a,D}(CcPF_6)$ is greater than $E_{a,D}$(DMFc). This was observed in oDCB where ion pairing is significant, but not in DCE. According to Tyrell and Harris, activation energies of diffusion for liquids are typically less than 20 kJ mol^{-1}.[22] Additionally, Compton *et al.* observed that the activation energy of diffusion of metallocenes in ionic liquids agreed approximately with the activation energy of viscous flow for the solvent, $E_{a,\eta}$.[23] Table 6.3 shows $E_{a,\eta}$ for oDCB and DCE, calculated using $\eta(T)$ data from Ref. [19], assuming the relationship between solvent viscosity and temperature could be represented with an Arrhenius relationship. Fluid motion in a molecular solvent is significantly different to that in an ionic liquid but agreement with the experimental activation energies of diffusion measured here appears satisfactory, suggesting that the obtained experimental values are reasonable. It is possible that the activation energy of diffusion is not particularly sensitive to the nature of the solvent.

The foregoing discussion assumed that the radius of the diffusing particle does not change significantly with temperature. If this was the case then, from the Stokes-Einstein equation, the product $D\eta/T$ should be constant. The ratio of this product at 25 °C and 65 °C was taken for DMFc and $CcPF_6$ in oDCB and Cc. The solvent viscosity at each temperature was estimated by interpolating values taken from Ref. [19]. The ratio was approximately 1 for DMFc and $CcPF_6$ in both solvents. Indicating that the molecular size remains constant.

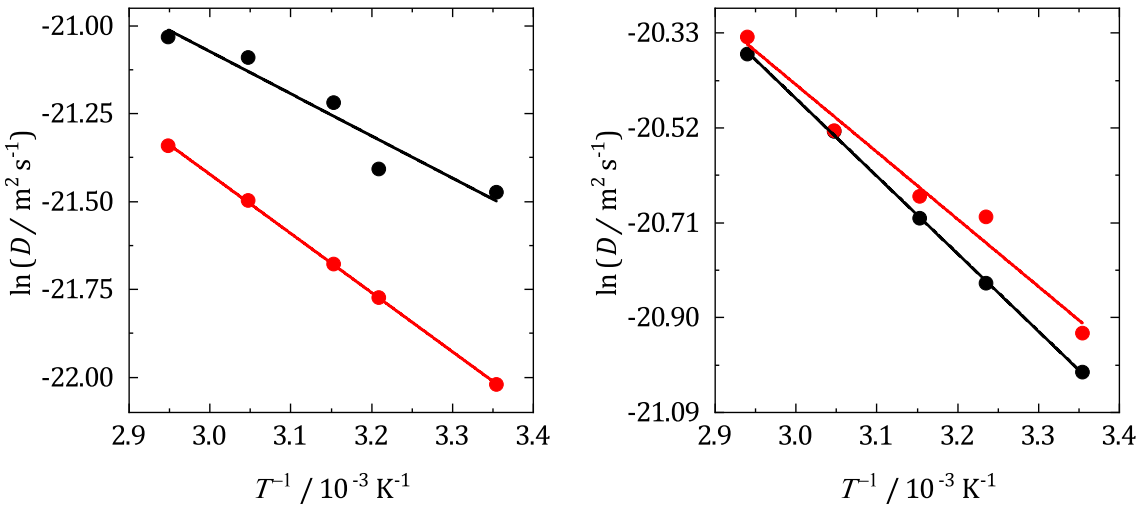

(a) oDCB (b) DCE

Figure 6.4: Representative Arrhenius plots of the diffusion coefficients of DMFc and $CcPF_6$ in oDCB and DCE over the temperature range 25-65 °C. Black: DMFc, red: $CcPF_6$.

	DMFc		$CcPF_6$		
	$\ln D/T$ / K^{-1}	$E_{a,D}$ / kJ mol^{-1}	$\ln D/T$ / K^{-1}	$E_{a,D}$ / kJ mol^{-1}	$E_{a,\eta}$ / kJ mol^{-1}
oDCB	−1031(160)	9(1)	−1593(124)	13(1)	10
DCE	−1497(67)	12(1)	−1213(140)	10(1)	10

Table 6.3: Temperature dependence of the diffusion coefficients of DMFc and $CcPF_6$ in oDCB and DCE and corresponding activation energies of diffusion. Diffusion coefficients obtained from microdisc voltammograms at temperatures in the range 25-65 °C. Values are the average of three repeats with the error the standard deviation. Activation energy of viscosity estimated using data from Ref. [19].

6.4. Electrodeposition of Sb

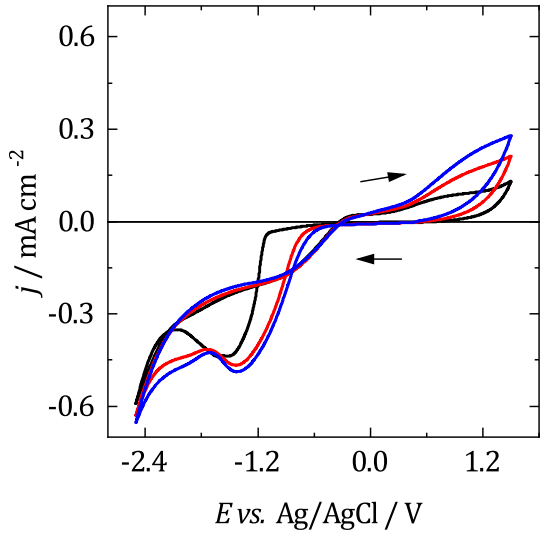

Figure 6.5: Voltammograms of 3 mM $[N^nBu_4][SbCl_4]$ and 100 mM $[N^nBu_4]Cl$ at a r = 2 mm TiN WE in oDCB at 25 °C in the high temperature cell. Scan swept from 0.5 V *vs.* Ag/AgCl at 100 mV s^{-1} in the direction indicated by the arrows. CE: Pt mesh, RE: Ag/AgCl. Black: scan 1, red: scan 2, blue: scan 3.

Fig. 6.5 shows a voltammogram of 3 mM $[N^nBu_4][SbCl_4]$ in oDCB in the high temperature cell. Naturally, the electrochemistry appears similar to that observed under similar conditions in previous Chapters. Electrodeposition was performed at −1.8 V *vs.* Ag/AgCl, the same potential as previous deposits collected from oDCB, to allow comparison. Here it was assumed that the redox potential did not change with temperature, and so the overpotential for deposition was constant. Deposits were collected at temperature increments up to 140 °C, the potential was applied until a fixed amount of charge was passed which corresponded to a 1800 s deposition of Sb from oDCB at 25 °C. This was to ensure all deposits were of approximately the same thickness. In principle, the maximum

possible deposition temperature would be *ca.* 180 °C since oDCB has a boiling point of 181 °C. However it was found that with the current practical arrangements, 140 °C was the highest achievable temperature.

Fig. 6.6 shows SEM images of Sb electrodeposited onto TiN from oDCB at temperatures of 25 °C, 80 °C, 100 °C, 120 °C and 140 °C. At room temperature, Sb deposits as a thin compact layer, on top of which small islands of Sb form. As the temperature increases, the morphology changes and Sb forms a compact, homogeneous layer which appears more uniform than deposits at lower temperatures. Finally, at 140 °C the appearance changes once again and individual clumps of Sb are observed on the bare TiN substrate.

Temperature / °C	CR / mC cm^{-2} min^{-1}
25	2.6
80	34.7
100	47.5
120	52.7
140	29.3

Table 6.4: The effect of temperature on the rate of charge passed for the electrodeposition of Sb from oDCB containing 3 mM $[N^nBu_4][SbCl_4]$ at −1.8 V *vs.* Ag/AgCl.

Table 6.4 shows CR for the deposition of Sb at different temperatures. This should give an indication of the effect of temperature on the rate of mass growth. It is notable that the value at 25 °C is greater than that reported in previous Chapters. This is most likely because it was not possible to use the front seal holder with the high temperature cell and so conducting areas on the substrate other than the WE disc, such as the edges, are now exposed to the electrolyte. Nevertheless, CR increases with temperature up to 120 °C as might be expected, because the rate of mass transport and charge transfer increases. However at 140 °C, CR decreases significantly, suggesting a change in the rate of mass growth. This phenomenon will be discussed further below.

The collected deposits were also analysed using XRD. Spectra recorded for the deposits collected at each temperature are shown in Fig. 6.7. For the room temperature deposit, as was shown previously, a single broad peak was observed at *ca.* 28° corresponding to the primary diffraction peak of Sb. Up to 100 °C the shape of the diffractogram remains unchanged. However as the temperature was increased to 120 °C and 140 °C, a sharper peak at 28° can be seen, and minor diffraction peaks begin to appear. Sb was successfully indexed for all the patterns and the lattice parameters, shown in Table 6.5, agree with the literature. Since the patterns show no difference up to 100 °C it would appear that the temperature has no effect on the crystallinity of the deposit. This is reflected in quantitative estimates of the crystallite size, given in Table 6.5, which remain unchanged. However, for the deposits collected at 120 and 140 °C the crystallite size increases significantly, indicating an improvement in the crystallinity of the deposited Sb. Changes in the crystallinity of electrodeposited Sb are also observable with Raman spectroscopy, spectra collected

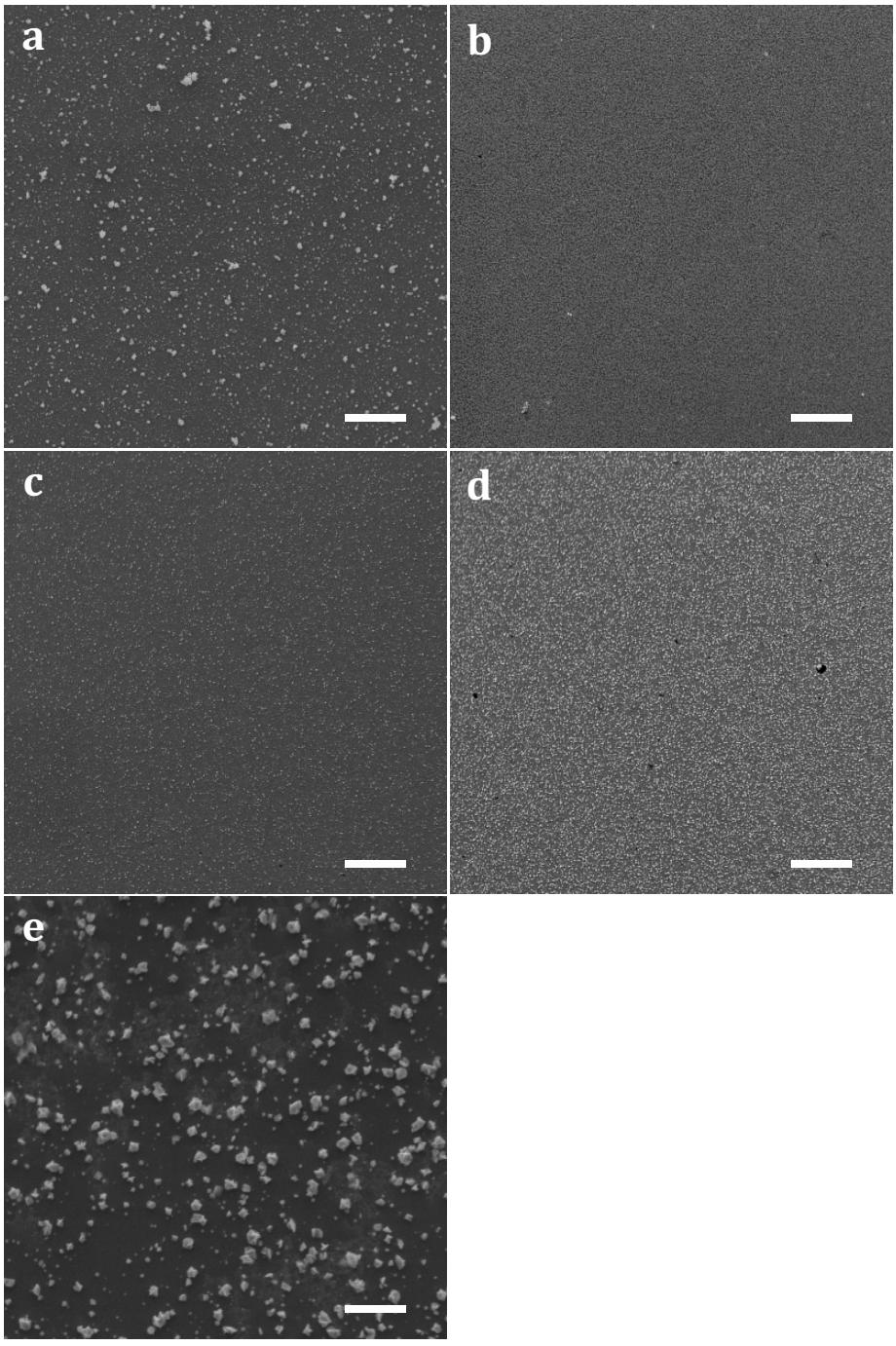

Figure 6.6: SEM images of Sb electrodeposited onto r = 2 mm TiN from oDCB containing 3 mM $[N^nBu_4][SbCl_4]$ and 100 mM $[N^nBu_4]Cl$. a) 25 °C, b) 80 °C, c) 100 °C, d) 120 °C, e) 140 °C. Scale bar indicates 10 µm.

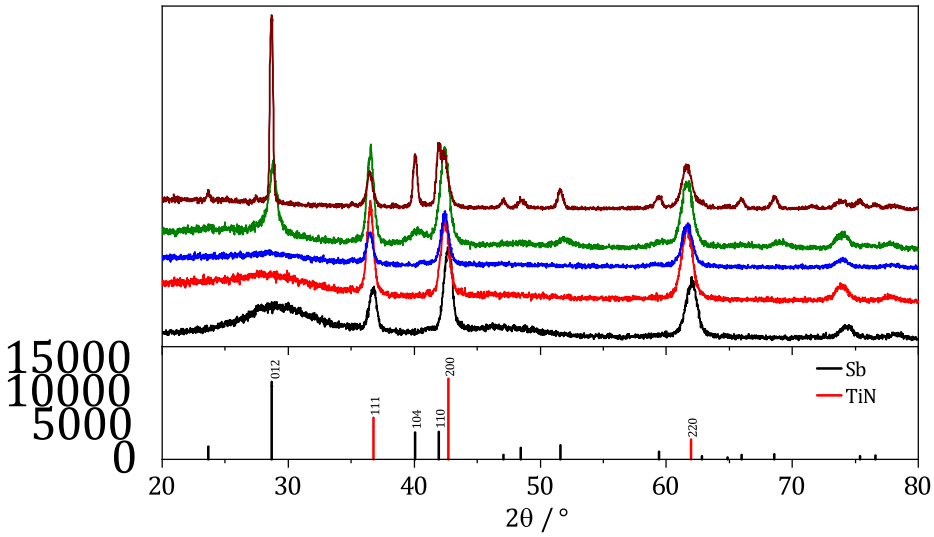

Figure 6.7: Grazing incidence XRD spectra of Sb electrodeposited onto TiN from oDCB at varying temperatures. Deposits collected from electrolyte containing 3 mM $[N^nBu_4][SbCl_4]$ and 100 mM $[N^nBu_4]Cl$. Black: 25 °C, red: 80 °C, blue: 100 °C, green: 120 °C, brown: 140 °C. Bottom panel shows in black the literature pattern for Sb (ICSD 64695) and in red the pattern of the substrate (ICSD 152807). The offset is arbitrary and added for clarity.

Temperature	$a = b$ / Å	c / Å	Average crystallite size / Å
25	4.25(5)	10.4(7)	11(1)[a]
80	4.36(15)	11.5(5)	22(2)[a]
100	4.27(14)	10.4(2)	23(3)[a]
120	4.24(4)	11.1(2)	97(24)[b]
140	4.31(1)	11.3(1)	233(30)[b]
lit.[c]	4.31	11.3	

Table 6.5: Lattice parameters and average crystallite sizes of Sb electrodeposited from oDCB at varying temperatures, refined from XRD patterns. [a]: obtained using the Scherrer method. [b]: obtained using the Halder-Wagner method. [c]: ICSD: 94695.

from the deposits at each temperature are shown in Fig. 6.8. Crystalline Sb displays two Raman peaks at 115 and 150 cm^{-1} corresponding to the TO and LO Raman modes respectively.[24] Similar to the XRD patterns, the Raman spectrum for the deposits at 25, 80 and 100 °C are comparable, with a single peak at approximately 142 cm^{-1}. This is in agreement with Raman measurements of Sb in previous Chapters and indicative of amorphous Sb. At 120 °C, a peak at 149 cm^{-1} along with a shoulder emerges, suggesting the presence of partially crystalline Sb. Finally at 140 °C, two peaks can be seen at 110 cm^{-1} and 149 cm^{-1} clearly showing the formation of crystalline Sb. In agreement with XRD data shown above.

As noted above, the rate of Sb growth appeared to decrease when the temperature was increased to 140 °C. This, combined with the change in morphology of the Sb deposit,

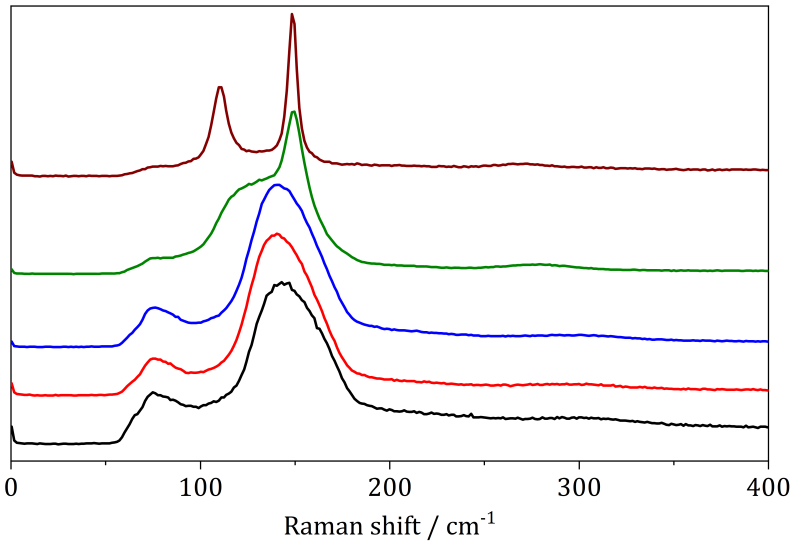

Figure 6.8: Raman spectroscopy of Sb electrodeposited onto TiN from oDCB at varying temperatures. Deposits collected from electrolyte containing 3 mM $[N^nBu_4][SbCl_4]$ and 100 mM $[N^nBu_4]$. Collected using 785 nm excitation laser. Intensity normalised by y_{max} Black: 25 °C, red: 80 °C, blue: 100 °C, green: 120 °C, brown: 140 °C. The offset is arbitrary and added for clarity.

suggests that a change in the electrolyte is taking place at temperatures above 120 °C. To investigate the effect of heating to 140 °C further, voltammograms of the electrolyte, and deposits were collected before, during and after heating.

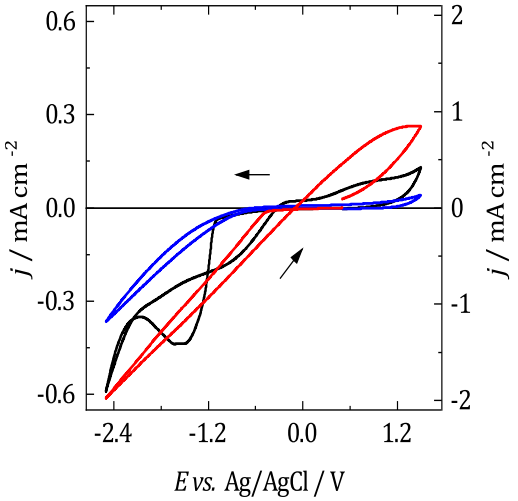

Figure 6.9: Effect of temperature on the electrochemistry of 3 mM $[N^nBu_4][SbCl_4]$ in oDCB at $r = 2$ mm TiN WE. Scan swept from 0.5 V *vs.* Ag/AgCl at 100 mV s^{-1} in the direction indicated by the arrows. CE: Pt mesh, RE: Ag/AgCl. Black: 25 °C pre-heating taken from Fig. 6.5, red: 140 °C, blue: 25 °C post-heating. Right hand axis corresponds to voltammogram at 140 °C.

Fig. 6.9 shows a voltammogram at 25 °C without any prior heating, taken from Fig. 6.5 above. Also shown is a CV of the same electrolyte at a fresh WE at 140 °C, and also once

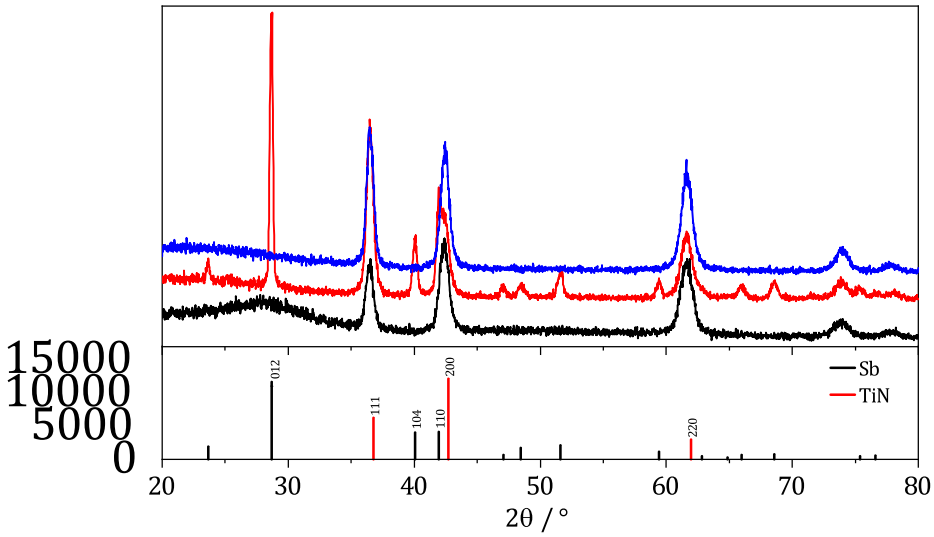

Figure 6.10: Grazing incidence XRD patterns of Sb electrodeposited onto TiN from oDCB containing 3 mM $[N^nBu_4][SbCl_4]$ before, during and after heating to 140 °C. Black: 25 °C pre-heating taken from Fig.6.7 above, red: 140 °C, blue: 25 °C post-heating. Bottom panel shows in black the literature pattern for Sb (ICSD 64695) and in red the pattern of the substrate (ICSD 152807).

it had been cooled to 25 °C, at a fresh electrode as well. The voltammogram at 140 °C is clearly quite different to that at 25 °C pre-heating, and this is also true for the CV at 25 °C post-heating. The current density increases significantly at 140 °C, because of faster rates of mass transport. But the peaks seen at room temperature can no longer be observed. After heating, the reduction current is reduced compared to the voltammogram without heating, and no oxidation current is observed also. It is not possible to understand from the voltammograms specifically what has changed in the electrolyte but it is clear heating has significant consequences for the electrochemistry of $[SbCl_4]^-$.

Figs. 6.11 and 6.10 show SEM images and XRD patterns respectively of Sb deposits collected at 25 °C without heating, at 140 °C and at 25 °C after heating, all from the same electrolyte. The SEM images and XRD spectrum of pre-heating Sb were taken from the work above. At 140 °C the morphology of the deposit is reproduced, with Sb forming small isolated clumps of material on the bare substrate. The XRD spectrum is also comparable to that shown above. After cooling, there is very little evidence of any Sb deposited onto the electrode, with growth only occurring in a few small areas. Additionally, there appears to be no evidence of any diffracted Sb from the XRD spectrum of the deposit. Clearly, the Sb precursor is changing in some way as a result of heating to 140 °C that is preventing the deposition of Sb. It is possible the complex is decomposing as a result of reaction with the solvent or the supporting electrolyte, but further work is required to reveal the mechanism of the decomposition process. Nevertheless it is still clear that Sb was deposited at 140 °C and that it was more crystalline than deposits collected at lower temperatures.

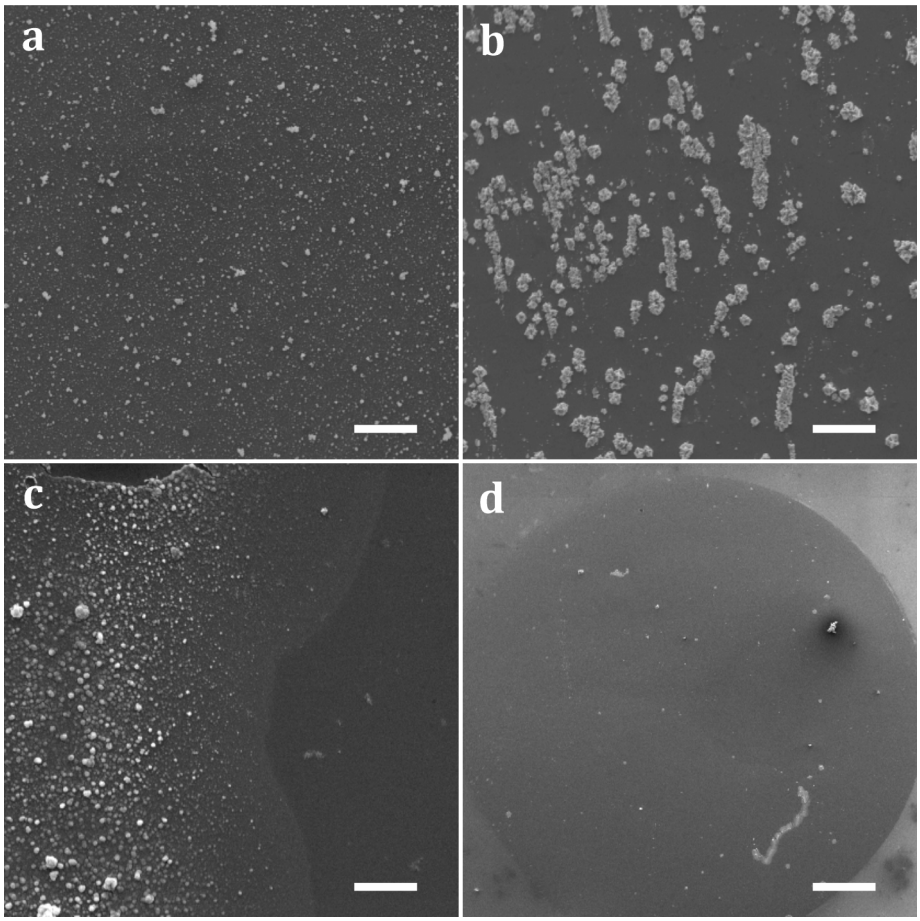

Figure 6.11: SEM images of the effect of temperature on Sb electrodeposited onto r =2 mm TiN from oDCB containing 3 mM $[N^nBu_4][SbCl_4]$. a) 25 °C pre-heating taken from Fig.6.6 above, b) 140 °C, c) 25 °C post-heating, d) 25 °C post-heating at a lower magnification. Scale bar corresponds to 10 µm except d) which is 1 mm.

6.5. Electrodeposition of Sb_2Te_3

Since previous Chapters have shown that Sb_2Te_3 deposits with partial crystallinity at room temperature, it would also be interesting to attempts its electrodeposition at elevated temperatures, in an effort to improve the material properties of a system more complicated than a single metal. Deposits were collected at −1.75 V *vs.* Ag/AgCl, the potential required to achieve stoichiometric Sb_2Te_3 from oDCB at room temperature. As with Sb deposition, a cutoff charge was applied corresponding to the charge passed after a 1800 s deposition at room temperature.

Fig. 6.12 shows how the composition of an antimony telluride codeposit varies with temperature. The composition of the deposit remains approximately stoichiometric at 40 °C, but with continued heating the Sb content decreases approximately linearly and it appears no longer possible to deposit stoichiometric Sb_2Te_3 at elevated temperatures with the same electrolyte composition as at 25 °C. As the temperature increases the rates of mass transport and electron transfer will increase, and it is possible that the relative rates for the two metal complexes change with temperature, affecting the composition of

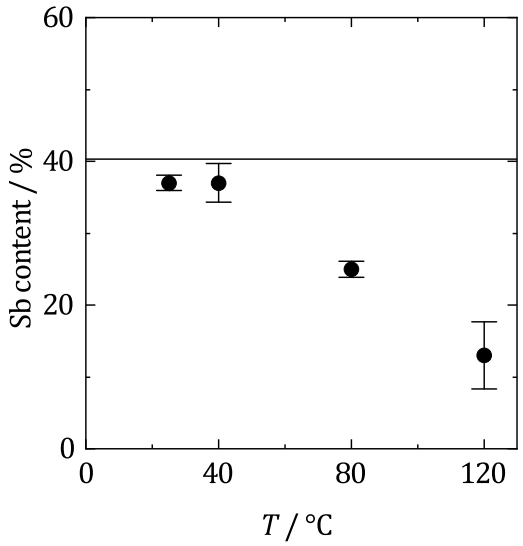

Figure 6.12: The effect of temperature on the composition by EDX of Sb and Te deposited on to r = 2 mm TiN WE from oDCB containing 1.5 mM $[N^nBu_4][SbCl_4]$, 3 mM $[N^nBu_4]_2[TeCl_6]$ and 100 mM $[N^nBu_4]Cl$. Values are the average composition of three locations on the deposit with the error the standard deviation. Horizontal line indicates the composition of a commercial standard.

the deposit. It might therefore be possible to optimise the precursor concentrations in the electrolyte for a particular temperature, in order to once again achieve stoichiometric Sb_2Te_3. It is also possible that the Sb complex is decomposing at these temperatures, as described above.

Despite issues with the composition, there does appear to be noticeable improvements in the quality of the deposit with temperature. SEM images of the deposits at each temperature are given in Fig. 6.13, and XRD spectra in Fig. 6.14. The morphology of the deposit changes little up to 80 °C, but at 120 °C the film grows in a denser and more uniform fashion. The crystallinity also appears to improve, with a sharper (105) peak observed at 80 °C and 120 °C. An associated increase in crystallite size is observed, as can be seen in Table 6.6. Showing that increasing the bath temperature can have a beneficial effect on the electrodeposition of semiconductors as well as metals. This is in agreement with previous reports on the effect of temperature on antimony telluride electrodeposition. As was described in previous Chapters, Sb_2Te_3 typically deposits amorphously at room temperature. This was also reported by Leimkühler *et al.* with work into Sb_2Te_3 deposition from acidic aqueous electrolytes.[25] When depositing at 98 °C however, the deposits were found to be crystalline. Sb_2Te_3 electrodeposited from molten salts at 150 °C was also crystalline.[26] Huang *et al.* deposited Sb_2Te_3 amorphously at room temperature and then annealed the deposit with a temperature ramp.[27] It was found that Sb_2Te_3 crystallised at *ca.* 120 °C, similar to the results observed here.

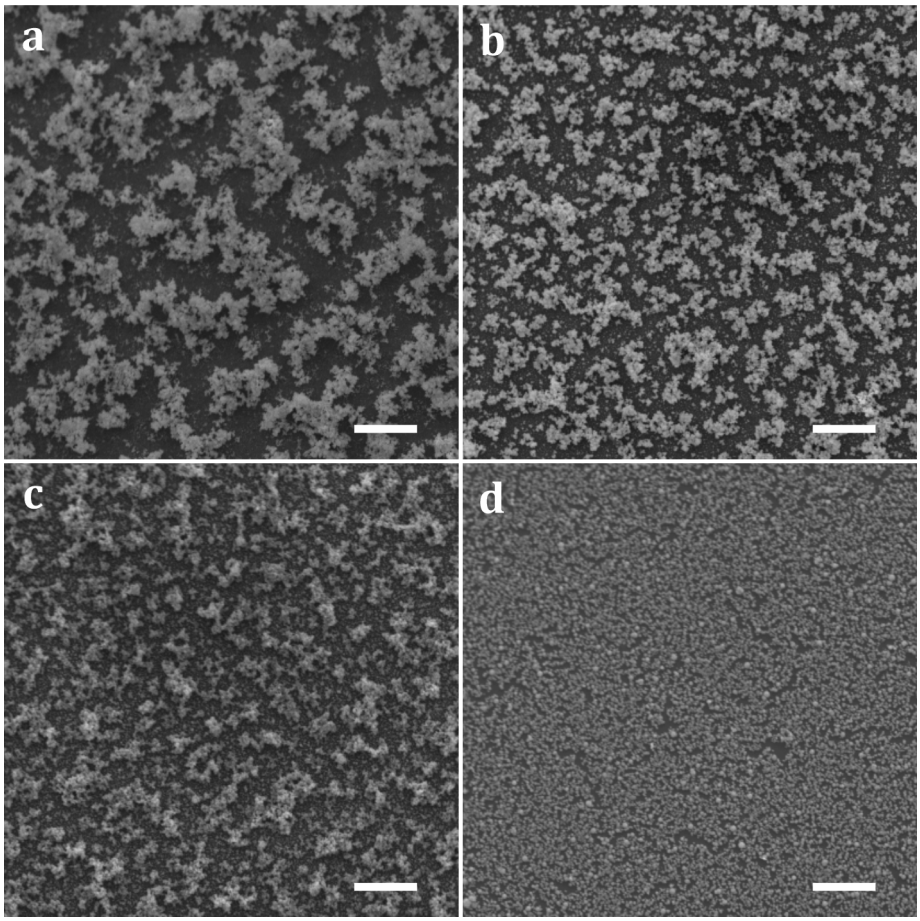

Figure 6.13: SEM images of Sb and Te codeposit at varying temperatures on a r = 2 mm TiN WE. Deposited from oDCB containing 1.5 mM $[N^nBu_4][SbCl_4]$ and 3 mM $[N^nBu_4]_2[TeCl_6]$. a) 25 °C taken from Chapter 5, b) 40 °C, c) 80 °C, d) 120 °C. Scale bar indicates 10 µm.

Temperature	$a = b$ / Å	c / Å	Average crystallite size / Å
25[a]	4.28(4)	31.1(3)	21(3)[b]
40	4.23(6)	30.7(4)	23(1)[b]
80	4.28(2)	30.2(2)	55(3)[c]
120	4.28(2)	30.8(1)	56(12)[c]
lit.[d]	4.26	30.5	

Table 6.6: Lattice parameters and average crystallite sizes of antimony telluride electrodeposited from oDCB onto TiN at varying temperatures, refined from XRD patterns. [a]: taken from Chapter 5 [b]: obtained using the Scherrer method. [c]: obtained using the Halder-Wagner method. [d]: ICSD: 2084.

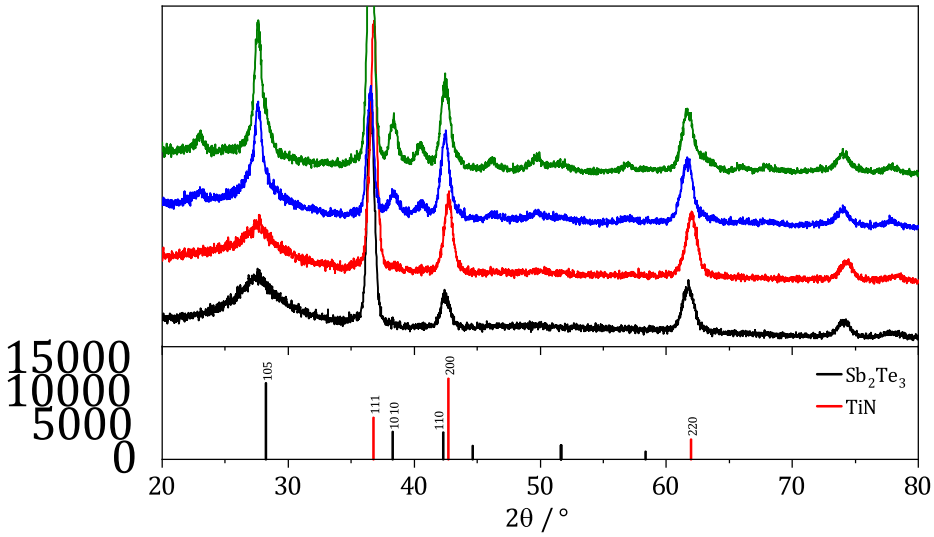

Figure 6.14: Grazing incidence XRD patterns of a mixed Sb and Te deposit at various temperatures. Deposited onto $r = 2$ mm TiN WE at -1.75 V *vs.* Ag/AgCl from oDCB containing 1.5 mM $[N^nBu_4][SbCl_4]$ and 3 mM $[N^nBu_4]_2[TeCl_6]$. Black: 25 °C taken from Chapter 5, red: 40 °C, blue: 80 °C, green: 120 °C. Bottom panel shows in black the literature pattern for Sb_2Te_3 (ICSD 2084) and in red the pattern of the substrate (ICSD 152807).

6.6. Conclusions

The intention of this Chapter was to study the effect of temperature on electrochemistry in weakly coordinating solvents, and to apply the solvents to the elevated temperature electrodeposition of metals to achieve improved material properties. In pursuit of this, the redox potential and diffusion coefficients of DMFc and $CcPF_6$ were measured as a function of temperature in oDCB and DCE. From these, the reaction entropy and activation energy of diffusion was calculated. The resulting values were in agreement with theory and previous measurements in the literature. oDCB was then used to electrodeposit Sb, previous work had shown it to be amorphous at room temperature and so it was a good candidate to observe any possible effects of temperature. Deposits were successfully collected at a range of temperatures between 25 °C and 140 °C and characterised using SEM, XRD and Raman spectroscopy. SEM images showed that up to 120 °C, the deposited Sb became smoother and more homogeneous. At higher temperatures the deposit morphology changed and the Sb formed islands instead. XRD and Raman spectroscopy also showed an improvement in crystallinity of the deposit at 120 °C and above. Crystallite sizes calculated from the XRD patterns increased significantly, and the Raman spectra showed peaks in agreement with that expected for crystalline Sb. However, evidence was also found of apparent decomposition of the precursor when the bath was heated above 120 °C. This resulted in lower growth rates and was also the likely cause of the change in morphology. Electrodeposition of Sb_2Te_3 was also attempted, with similar improvements in deposit appearance and crystallinity. However the Sb content decreased

with temperature, so that stoichiometric antimony telluride was no longer formed. Electrodeposition from DCE was not attempted, because the observed changes in material properties occurred above its boiling point.

The decomposition of the plating bath likely presents a significant barrier to the successful application of oDCB as a solvent for electrodeposition at elevated temperatures. The decomposition of the Sb precursor appears to begin at the temperature which shows the greatest improvements in morphology and crystallinity. This is likely to be the case for other metals also and further investigation into the causes of the decomposition is therefore essential. It might also be possible to design a plating bath which is more stable at higher temperatures, by changing the metal's ligands for example. It would also be interesting to see if the decomposition is specific to the $[SbCl_4]^-$ precursor, or occurs for other metals such as Bi^{3+} and is a more general issue.

For semiconductor electrodeposition it is also important that the stoichiometric composition is maintained when depositing at elevated temperatures. As the temperature increases, the relative rates of mass transport and electron transfer will change and this is the probable cause for the change in composition ratio for antimony telluride. It is possible that the electrolyte composition simply requires re-optimising at the relevant temperature. This is likely to be necessary when the codeposition of other metals is attempted as well.

6.7. References

(1) E. L. Yee, R. J. Cave, K. L. Guyer, P. D. Tyma and M. J. Weaver, *J. Am. Chem. Soc.*, 1979, **101**, 1131–1137.

(2) A. J. DeBethune, T. S. Licht and N. Swendeman, *J. Electrochem. Soc.*, 1959, **106**, 616–625.

(3) S. Sahami and M. J. Weaver, *J. Electroanal. Chem.*, 1981, **122**, 155–170.

(4) S. Sahami and M. J. Weaver, *J. Electroanal. Chem.*, 1981, **122**, 171–181.

(5) J. T. Hupp and M. J. Weaver, *Inorg. Chem.*, 1984, **23**, 3639–3644.

(6) D. E. Richardson and P. Sharpe, *Inorg. Chem.*, 1991, **30**, 1412–1414.

(7) J. W. Turner and F. A. Schultz, *Inorg. Chem.*, 1999, **38**, 358–364.

(8) L. Blum and W. R. Fawcett, *J. Chem. Soc. Faraday Trans.*, 1992, **88**, 3339–3344.

(9) M. Schlesinger and M. Paunovic, *Modern Electroplating*, Wiley, Hoboken, NJ, 5th edn., 2010.

(10) U. Sahaym, S. L. Miller and M. G. Norton, *Mater. Lett.*, 2010, **64**, 1547–1550.

(11) A. Brenner, *Electrodeposition of Alloys I*, Academic Press, London, 1963.

(12) J. Gu, E. Fahrenkrug and S. Maldonado, *J. Am. Chem. Soc.*, 2013, **135**, 1684–1687.

(13) W. Wu, N. Eliaz and E. Gileadi, *J. Electrochem. Soc.*, 2015, **162**, D20–D26.

(14) S. Murugesan, A. Akkineni, B. P. Chou, M. S. Glaz, D. A. Vanden Bout and K. J. Stevenson, *ACS Nano*, 2013, **7**, 8199–8205.

(15) W. Beckmann, *Crystallization*, Wiley-VCH Verlag GmbH, Weinheim, 2013.

(16) N. Mehta and A. Kumar, *J. Phys. Chem. B*, 2016, **120**, 1175–1182.

(17) M. Matsumoto and T. W. Swaddle, *Inorg. Chem.*, 2004, **43**, 2724–2735.

(18) I. Noviandri, K. N. Brown, D. S. Fleming, P. T. Gulyas, P. A. Lay, A. F. Masters and L. Phillips, *J. Phys. Chem. B*, 1999, **103**, 6713–6722.

(19) W. M. Haynes, D. R. Lide and T. J. Bruno, *CRC Handbook of Chemistry and Physics*, CRC Press, New York, 96th edn., 2016.

(20) Y. Marcus, *The Properties of Solvents*, Wiley, Chichester, 1998.

(21) J. A. Branch, Ph.D. Thesis, University of Southampton, 2015.

(22) H. J. V. Tyrell and K. R. Harris, *Diffusion in Liquids*, Butterworths, London, 1984.

(23) E. I. Rogers, D. S. Silvester, D. L. Poole, L. Aldous, C. Hardacre and R. G. Compton, *J. Phys. Chem. C*, 2008, **112**, 2729–2735.

(24) P. N. Bartlett, J. Burt, D. A. Cook, C. Y. Cummings, M. W. George, A. L. Hector, M. M. Hasan, J. Ke, W. Levason, D. Pugh, G. Reid, P. W. Richardson, D. C. Smith, J. Spencer, N. Suleiman and W. Zhang, *Chem. - A Eur. J.*, 2016, **22**, 302–309.

(25) G. Leimkühler, I. Kerkamm and R. Reineke-Koch, *J. Electrochem. Soc.*, 2002, **149**, C474–C478.

(26) M. Ueda, Y. Mito and T. Ohtsuka, *Mater. Trans.*, 2008, **49**, 1720–1722.

(27) Q. Huang, A. J. Kellock and S. Raoux, *J. Electrochem. Soc.*, 2008, **155**, D104–D109.

7

Conclusions and Further Work

This work used solvent descriptors to identify alternative weakly coordinating solvents (WCS) to dichloromethane (DCM) that behave similarly but with higher boiling points. This was in order to further the knowledge of electrochemistry in weakly coordinating solvents and to attempt electrodeposition at elevated temperatures. The solvents were characterised with electrochemical techniques and the behaviour of model redox couples was studied. The two most promising solvents, o-dichlorobenzene (oDCB) and 1,2-dichloroethane (DCE) were then investigated further with the successful electrodeposition of Sb, Bi, Te, antimony telluride and bismuth telluride, the first report of electrodeposition from these solvents. Finally, Sb was electrodeposited from oDCB at 140 °C and antimony telluride at 120 °C. The resulting deposits were smoother and more crystalline than deposits collected at room temperature.

In the first results Chapter, Chapter 3, the properties of a suitable alternative solvent to DCM were outlined. Such a solvent would have a high polarity; to dissolve charged species, aprotic; to extend the solvent window, and weakly coordinating; for minimal interaction between solvent and solute. The solvent descriptors of Kamlet and Taft were used to quantify these features and five alternative solvents were identified: trifluorotoluene, o-dichlorobenzene, p-fluorotoluene, chlorobenzene and 1,2-dichloroethane. The five solvents, and DCM, were characterised with measurements of the solvent potential window, conductivity and double-layer capacitance. It was found that the negative limit of the candidate solvents were comparable to DCM because the window was limited by decomposition of the supporting electrolyte cation, excepting DCE where the solvent itself appeared to be the limiting factor. Measures of the solvents' polarity could not fully account for variations in the conductivity of the solvents. Despite similarities in dielectric constant, differing degrees of ion pairing were apparent in the solvents. This was attributed to some form of intermolecular interactions between solvent molecules which was preferable to ion solvation. Furthermore, the electrochemistry of the model redox couples decamethylferrocene (DMFc) and cobaltocenium hexafluorophosphate ($CcPF_6$) was investigated with microelectrodes. The redox potential of $CcPF_6$ was solvent dependent, which was attributed to the presence of ion pairing. In addition, diffusion coefficient measurements agreed with theoretical predictions for the neutral DMFc but were lower than expected for the charged $CcPF_6$ and $DMFcPF_6$, further evidence of ion pairing. Ultimately, oDCB and DCE were chosen as the most promising solvents for application to electrodeposition because of their polarity.

Subsequently in Chapter 4, the nature of electrodeposition in the WCS was studied. The electrochemistry of Sb^{3+}, Bi^{3+} and Te^{4+} was characterised with voltammetry at macro- and microelectrodes, and the electrochemical quartz crystal microbalance. Sb^{3+} and Bi^{3+} both broadly displayed simple deposition and stripping, whereas the redox behaviour of Te^{4+} was more complex, with evidence suggesting the presence of cathodic stripping and also chemical reactions in solution. Sb, Bi and Te were successfully deposited from oDCB and DCE. Analysis by X-ray diffraction (XRD) and Raman spectroscopy suggested that Sb deposited amorphously, but Bi and Te were crystalline.

This was progressed in Chapter 5 to attempts at the electrodeposition of antimony telluride and bismuth telluride from oDCB and DCE. The electrodeposition of stoichiometric Sb_2Te_3 was possible from an electrolyte containing 1.5 mM $[N^nBu_4][BiCl_4]$ and 3 mM $[N^nBu_4]_2[TeCl_6]$ in oDCB, and 1.75 mM $[N^nBu_4][BiCl_4]$ and 3 mM $[N^nBu_4]_2[TeCl_6]$ in DCE. For the electrodeposition of Bi_2Te_3 from oDCB, a bath composed of 2 mM $[N^nBu_4][BiCl_4]$ and 3 mM $[N^nBu_4]_2[TeCl_6]$ was required, and for DCE 2.5 mM $[N^nBu_4][BiCl_4]$ and 3 mM $[N^nBu_4]_2[TeCl_6]$. Compositional information of the resulting deposits was obtained with EDX measurements, SEM showed the morphology of the deposits, and XRD was used to probe the crystal structure of the deposits. The XRD patterns indicated that the antimony deposits were amorphous, and the bismuth telluride nanocrystalline. The mechanism of

the deposition of both compounds was also discussed.

In the final results Chapter, Chapter 6, the effect of temperature on electrochemistry in oDCB and DCE was explored. This was first achieved by using macro- and microelectrode voltammograms of DMFc and $CcPF_6$ to measure ΔS_{rc}, the entropy of electron transfer, and $E_{a,D}$, the activation energy of diffusion. Subsequently, Sb was electrodeposited at varying temperatures between 25 °C and 140 °C. The effect of temperature on the deposits was probed with SEM and XRD measurements. Increasing the temperature appeared to produce smoother and more homogeneous films, with larger crystallites. The transition from amorphous to crystalline material occurred between 120 and 140 °C. However, the Sb precursor appeared to decompose at temperatures greater than 120 °C. The reason for the breakdown was not established, but reaction with the solvent or supporting electrolyte cations were speculated as possible reaction pathways. The electrodeposition of antimony telluride was also attempted at temperatures up to 120 °C. The deposits appeared to show similar improvements in their material properties as for Sb, but the Sb content in the deposits decreased with increasing temperature and it was no longer possible to grow films of stoichiometric Sb_2Te_3.

The work on diffusion coefficient measurements in Chapters 3 and 4 emphasised the importance of taking into account the modifications of the Stokes-Einstein equation when interpreting diffusion coefficients. It must not be assumed that the diffusing particle is spherical, or that the solvent is a continuum. Otherwise this may lead to misinterpretation of diffusion coefficients. The potential effects of not properly considering the electrode radius and reagent concentration on the accuracy of the calculated diffusion coefficient were also highlighted. Errors in these can lead to inaccurate values of the calculated diffusion coefficient, and this has previously been poorly recognised in electrochemistry. For example, microelectrodes are sometimes 'calibrated' by measuring the limiting current of a well known redox couple and then the microelectrode radius is calculated using a diffusion coefficient of the species from the literature. However in this case, it is not certain that the literature diffusion coefficient has been determined with appropriate accuracy, and this may lead to errors being carried forward into the estimation of the microelectrode radius.

What also became clear from this thesis was, due to the low polarity of the WCS, the influence ion pairing has on determining measured electrochemical properties. Evidence of its effects were observed in conductivity, redox potential and diffusion coefficient measurements in both Chapters 3 and 4. Its presence can cause departures from ideality and should be considered when interpreting measurements in WCS. Since there was evidence to suggest that $[SbCl_4]^-$ and $[BiCl_4]^-$ were ion paired, it is feasible that ion pairing could change the deposition potential of metal precursors and cause changes in the mechanism of semiconductor electrodeposition.

In summary, this work has advanced the understanding of electrochemistry in WCS, a previously poorly studied field, and also demonstrated the beneficial effect of temper-

ature on the crystallinity of electrodeposited metals and semiconductors. Furthermore, this work has created a framework for further studies into the electrodeposition of semiconductors at elevated temperatures and it is hoped that these solvents will be used more widely in electrochemistry to deposit materials with improved material properties.

7.1. Further Work

The obvious direction for future experiments is towards further investigation of electrodeposition at elevated temperatures. The highest temperature achieved in the present work was 140 °C. In principle it should be possible to reach temperatures up to 180 °C, close to the boiling point of oDCB, by changing the heating source from a static oil bath with a hot plate as used here, to a recirculating oil bath. This thesis has also demonstrated the benefits of electrodeposition at elevated temperatures from WCS, and there is now the possibility of application to other systems. For example, other work in the group has focussed on the electrodeposition of transition metal dichalcogenides (TMDCs) such as MoS_2 or WS_2.[1,2] These materials deposit amorphously at room temperature, and are crystallised by annealing. Therefore, raising the temperature of electrodeposition could remove the need for annealing and simplify the route to fabricating crystalline TMDC devices. Since these materials are deposited from a single source precursor, reoptimisation of the bath composition would not be necessary and translation of the work from DCM to oDCB should be simple. Moreover, the relationship between metal crystallisation and temperature remains unclear. It does not appear to be known, for example, why metals vary in the temperature at which they crystallise, nor the role temperature has in the transition between amorphous and crystalline material during electrodeposition. Theoretical and/or experimental work considering this would be interesting.

As discussed above, the evidence in Chapters 3 and 4 suggest that ion pairs of the supporting electrolyte and reagents are present in significant quantities in the studied solvents. There was also reason to believe that the aromatic solvents adopt a form of internal structure. Therefore, further work into the electrolyte structure in some of the WCS would be of interest, and it is also important to fully understand electrochemical behaviour in the solvents. There are several methods for measuring the degree of ion pairing in the solvents, including, conductivity measurements and various spectroscopies.[3] Other spectroscopies can also be used to measure the type of internal structure that was speculated to be present in the aromatic WCS.[4]

Finally, there were some features in the voltammetry of the individual metals in Chapter 4 that it was not possible to fully account for. The kinetics of the $Sb^{3+/0}$ redox couple appeared to be slower than $Bi^{3+/0}$, so kinetics measurements such as Tafel analysis would be interesting to explore this further. In addition, Bi^{3+} voltammetry displays a high nucleation overpotential in oDCB and DCE, perhaps due to a some form of blocking layer on the electrode surface. Further experiments changing the supporting electrolyte ions

may help improve understanding of this.

7.2. References

(1) S. Thomas, D. E. Smith, V. K. Greenacre, Y. J. Noori, A. L. Hector, C. H. de Groot, G. Reid and P. N. Bartlett, *J. Electrochem. Soc.*, 2020, **167**, 106511.

(2) S. Thomas, V. K. Greenacre, D. E. Smith, Y. J. Noori, N. M. Abdelazim, A. L. Hector, C. H. de Groot, W. Levason, P. N. Bartlett and G. Reid, *Chem. Commun.*, 2021, **57**, 10194–10197.

(3) Y. Marcus and G. Hefter, *Chem. Rev.*, 2006, **106**, 4585–4621.

(4) T. Shikata, N. Sugimoto, Y. Sakai and J. Watanabe, *J. Phys. Chem. B*, 2012, **116**, 12605–12613.

Appendices

A.1 Appendix to Chapter 3

Simulated Diffusion Coefficients

	DMFc / 10^{-5} cm^2 s^{-1}		Cc^+ / 10^{-6} cm^2 s^{-1}	
Solvent	D_{min}	D_{max}	D_{min}	D_{max}
DCM	1.01	1.73	1.29	2.24
TFT	0.82	1.39	1.04	1.80
oDCB	0.31	0.54	0.40	0.70
pFT	0.67	1.14	0.85	1.48
CB	0.55	0.93	0.70	1.21
DCE	0.53	0.91	0.68	1.18

Table A.1: Simulated diffusion coefficients using the Stokes-Einstein equation for DMFc and Cc^+. Where D_{min}: $c = 6$ and $r = r_{crs}$, and D_{max}: $c = 4$ and $r = r_{vDW}$ at 25 °C. See Chapter 3 for further details.

DMFc Diffusion Coefficient Compilation

Solvent	Electrolyte	Concentration / mM	Electrode material	Method	Temperature / °C	D / 10^{-5} cm^2 s^{-1}	Ref.
ACE	$[N^nBu_4][PF_6]$	100	Hg	DC polarography	23	1.50	[1]
ACE	$[N^nBu_4][ClO_4]$	500	Pt	macrodisc CV	25	1.41	[2]
ACN	$[N^nBu_4][PF_6]$	100	Hg	DC polarography	23	1.30	[1]
ACN	Na[OTf]	200	W	macrodisc CV	25	1.80	[3]
ACN	$[N^nBu_4][ClO_4]$	500	Pt	macrodisc CV	25	1.26	[2]
ACN	$[N^nBu_4][PF_6]$	100	GC	macrodisc CV	23[a]	1.30	[4]
ACN	$[N^nBu_4]$[BARF]	100	GC	macrodisc CV	23[a]	1.30	[4]
ACN	$[N^nBu_4][ClO_4]$	100	Au	microdisc CV	23	1.90	[5]
ACN	$[N^nBu_4][BF_4]$	20	Pt	microdisc CV	25	1.69	[6]
ACP	$[N^nBu_4][PF_6]$	200	Pt	microdisc CV	25	0.32	[7]
CB	$[N^nBu_4][BF_4]$	100	Pt	microdisc CV	25	0.87	This work
DCE	$[N^nBu_4]Cl$	100	Pt	microdisc CV	25	0.88	This work
DCM	$[N^nBu_4]Cl$	100	Pt	microdisc CV	25	1.68	This work
DCM	$[N^nBu_4][PF_6]$	100	Hg	DC polarography	23	1.30	[1]
DCM	$[N^nBu_4][ClO_4]$	500	Pt	macrodisc CV	25	1.07	[2]
DCM	$[N^nBu_4][PF_6]$	100	GC	macrodisc CV	23[a]	0.56	[4]
DCM	$[N^nBu_4]$[BARF]	100	GC	macrodisc CV	23[a]	0.37	[4]
DCM	$[N^nBu_4]Cl$	100	Pt	microdisc CV	25	1.45	[8]
DMF	$[N^nBu_4][PF_6]$	100	Hg	DC polarography	23	0.77	[1]
DMF	$[N^nBu_4][ClO_4]$	500	Pt	macrodisc CV	25	0.69	[2]
DMF	$[N^nBu_4][PF_6]$	100	GC	RDE CV	25	0.61	[9]
DMSO	$[N^nBu_4][PF_6]$	100	Hg	DC polarography	23	0.32	[1]
DMSO	$[N^nBu_4][ClO_4]$	500	Pt	macrodisc CV	25	0.35	[2]

EtOH	$[N^nBu_4][ClO_4]$	500	Pt	macrodisc CV	25	0.46	[2]
MeTHF	$[N^nBu_4]$[BARF]	100	GC	macrodisc CV	23[a]	0.48	[4]
NB	$[N^nBu_4][PF_6]$	200	Pt	microdisc CV	25	0.31	[10]
NB	$[N^nBu_4][ClO_4]$	250	graphite	microdisc CV	23	0.60	[11]
NMF	$[N^nBu_4][PF_6]$	100	Hg	DC polarography	23	0.14	[1]
oDCB	$[N^nBu_4]Cl$	100	Pt	microdisc CV	25	0.52	This work
oDCB	[PNP][BARF]	5	W	microdisc CV	20	0.45	[12]
PC	$[N^nBu_4][ClO_4]$	500	Pt	macrodisc CV	25	0.18	[2]
PC	$[N^nBu_4][BF_4]$	100	GC	macrodisc CV	22	0.24	[13]
pFT	$[N^nBu_4][BF_4]$	100	Pt	microdisc CV	25	1.10	This work
PhCN	$[N^nBu_4][ClO_4]$	500	Pt	macrodisc CV	25	0.36	[2]
Py	$[N^nBu_4][ClO_4]$	500	Pt	macrodisc CV	25	0.50	[2]
TFT	$[N^nBu_4][BF_4]$	100	Pt	microdisc CV	25	1.18	This work
TFT	$[N^nBu_4][BF_4]$	100	GC	macrodisc CV	23	1.20	[14]

Table A.2: Literature compilation of known diffusion coefficients of DMFc, along with useful experimental parameters. ACE: acetone, ACN: acetonitrile, ACP: acetophenone, CB: chlorobenzene, DCE: 1,2-dichloroethane, DCM: dichloromethane, DMF: N,N-dimethylformamide, DMSO: dimethylsulphoxide, EtOH: ethanol, MeTHF: 2-methyltetrahydrofuran, NB: nitrobenzene, NMF: N-methylformamide, oDCB: 1,2-dichlorobenzene, PC: propylene carbonate, pFT: p-fluorotoluene, PhCN: benzonitrile, Py: pyridine, TFT: trifluorotoluene. OTf: $[CF_3SO_3]^-$, BARF: $[B(C_6F_5)_4]^-$, PNP: $[((C_6H_5)_3P)_2N]^+$. [a]: Temperature value not given, assumed to be 23 °C.

A.2 Appendix to Chapter 4

Simulated Diffusion Coefficients

	$[SbCl_4]^-$ / 10^{-5} cm^2 s^{-1}		$[BiCl_4]^-$ / 10^{-5} cm^2 s^{-1}	
Solvent	D_{min}	D_{max}	D_{min}	D_{max}
DCM	2.16	1.44	2.13	1.42
oDCB	0.67	0.45	0.66	0.44
DCE	1.14	0.76	1.12	0.75

Table A.3: Simulated diffusion coefficients using the Stokes-Einstein equation for $[SbCl_4]^-$ and $[BiCl_4]^-$. Where D_{min}: $c = 6$ and $r = r_{crs}$, and D_{max}: $c = 4$ and $r = r_{vDW}$ at 25 °C. See Chapter 4 for further details.

A.3 References

(1) M. J. Weaver and T. Gennett, *Chem. Phys. Lett.*, 1985, **113**, 213–218.

(2) M. Matsumoto and T. W. Swaddle, *Inorg. Chem.*, 2004, **43**, 2724–2735.

(3) C. R. Cabrera and A. J. Bard, *J. Electroanal. Chem.*, 1989, **273**, 147–160.

(4) F. S. T. Khan, A. L. Waldbusser, M. C. Carrasco, H. Pourhadi and S. Hematian, *Dalt. Trans.*, 2021, **50**, 7433–7455.

(5) N. Leventis, W. S. Oh, X. Gao and A. M. M. Rawashdeh, *Anal. Chem.*, 2003, **75**, 4996–5005.

(6) J. A. Branch, Ph.D. Thesis, University of Southampton, 2015.

(7) K. J. Stevenson and H. S. White, *J. Phys. Chem.*, 1996, **100**, 18818–18822.

(8) S. J. Reeves, Y. J. Noori, W. Zhang, G. Reid and P. N. Bartlett, *Electrochim. Acta*, 2020, **354**, 136692.

(9) G. Macfie and R. G. Compton, *J. Electroanal. Chem.*, 2001, **503**, 125–132.

(10) W. K. Stephenson and R. Fuchs, *Can. J. Chem.*, 1985, **63**, 2535–2539.

(11) C. Shi and F. C. Anson, *J. Phys. Chem. B*, 1998, **102**, 9850–9854.

(12) P. Peljo, T. Rauhala, L. Murtomäki, T. Kallio and K. Kontturi, *Int. J. Hydrogen Energy*, 2011, **36**, 10033–10043.

(13) J. Li, G. F. Kennedy, A. M. Bond and J. Zhang, *J. Phys. Chem. C*, 2018, **122**, 9009–9014.

(14) C. Ohrenberg and W. E. Geiger, *Inorg. Chem.*, 2000, **39**, 2948–2950.

PCCP

ROYAL SOCIETY OF CHEMISTRY

PAPER

View Article Online
View Journal

Cite this: DOI: 10.1039/d2cp00696k

Selection and characterisation of weakly coordinating solvents for semiconductor electrodeposition†

Alexander W. Black and Philip N. Bartlett *

Received 11th February 2022,
Accepted 14th March 2022

DOI: 10.1039/d2cp00696k

rsc.li/pccp

Weakly coordinating solvents, such as dichloromethane, have been shown to be attractive for the electrodeposition of functional p-block compound and alloy semiconductors for electronic device applications. In this work the use of solvent descriptors to define weakly coordinating solvents and to identify new candidates for electrochemical applications is discussed. A set of solvent selection criteria are identified based on Kamlet and Taft's π^*, α and β parameters: suitable solvents should be polar ($\pi^* \geq 0.55$), aprotic and weakly coordinating (α and $\beta \leq 0.2$.). Five candidate solvents were identified and compared to dichloromethane: trifluorotoluene, *o*-dichlorobenzene, *p*-fluorotoluene, chlorobenzene and 1,2-dichloroethane. The solvents were compared using a suite of measurements including electrolyte voltammetric window, conductivity, and differential capacitance, and the electrochemistry of two model redox couples (decamethylferrocene and cobaltocenium hexafluorophosphate). Ion pairing is identified as a determining feature in weakly coordinating solvents and the criteria for selecting a solvent for electrochemistry is considered. *o*-dichlorobenzene and 1,2-dichloroethane are shown to be the most promising of the five for application to electrodeposition because of their polarity.

Introduction

Compound semiconductors and alloys based upon main group elements are of considerable interest for use in advanced electronic devices and memory. The possible combination of elements is significant and comprises binary compounds as well as ternary or quaternary alloys of elements from groups II to VI of the periodic table. These materials have a wide range of properties and band-gaps that permits a diversity of applications. For example: infra-red detection (indium antimonide), phase change memory (germanium antimony telluride), photovoltaics (cadmium telluride) and thermoelectrics (bismuth telluride) are all types of devices where compound p-block semiconductors have been used.[1]

The particular features of electrodeposition offer distinct advantages over other common methods such as chemical vapour deposition, sputtering, ALD, *etc.* In electrodeposition, deposition only occurs in areas with electrical contact, allowing precise control over the size and shape of the deposit, and deposition occurs under the control of the potential or current providing a tuneable composition, and it occurs outwards from the electrode surface, in other words 'bottom up', permitting growth of large aspect ratio nanostructures. In contrast, with 'top down' approaches such as vapour deposition, it is not possible to reliably penetrate the entire depth of high aspect ratio structures such as deep pores due to blocking at the pore mouth.

Complexes of the p-block elements are particularly labile and undergo facile ligand exchange. For example, for all p-block elements that form aqua complexes, the mean lifetime for a primary shell water molecule is less than 1 s,[2] and they lie on the labile side of Taube's inert/labile boundary.[3] In solution the solvent molecules can compete with the ligands present in the initial complex for coordination to the metal cation. As such, a complex with labile ligands in a Lewis basic solvent is vulnerable to displacement by the solvent molecule. Different metal cations differ in their interaction with the solvent, and therefore in a donor solvent differences in speciation across different metal precursors and oxidation states will occur. For electrodeposition of alloys and compounds this is a problem because more than one metal complex must be present and because speciation affects all aspects of an electron transfer reaction. Unpredictable changes in metal speciation greatly complicates the process of metal codeposition. Hence, a plating bath composed of metal precursors sharing common ligands in a weakly coordinating solvent is an attractive proposition.

The interactions between an ion and its solvent can broadly be divided into two classes: non-specific and specific interactions.[4]

School of Chemistry, University of Southampton, Southampton, SO17 1BJ, UK. E-mail: p.n.bartlett@soton.ac.uk

† Electronic supplementary information (ESI) available. See DOI: 10.1039/d2cp00696k

Non-specific interactions are electrostatic in nature and collectively known as van der Waals interactions. Specific interactions are of a chemical type and include hydrogen bonding and Lewis acid/base interactions. Quantifying the myriad and dynamic nature of interactions between solvents and solutes is difficult. However, insight can be achieved with the use of solvent descriptors: quantitative measures of some property of a solvent, for example using dielectric constant as an estimate of solvent polarity.

Dichloromethane (DCM) has been used recently as a weakly coordinating solvent in the electrodeposition of p-block metals and semiconductors. A generalised plating bath composed of $[N^nBu_4]Cl$ as the supporting electrolyte and halometallate, $[N^nBu_4]_{y-x}[M^{x+}Cl_y]$, based metal precursors was developed and used with success.[5–8] However, the use of this category of solvent for electrochemistry in general, and electrodeposition in particular, is relatively poorly explored. Furthermore, DCM has a low boiling point (40 °C) and performing electrodeposition in a less volatile solvent and at elevated temperatures would be of interest because of the expected improvement in deposit properties.

In the present work, a method using solvent descriptors is presented and used to make informed choices about solvent selection. This method was used to select several potential weakly coordinating solvents for application to p-block electrodeposition. Subsequently, the candidate solvents were characterised in a variety of ways to understand the nature of electrochemistry in these solvents. The potential window, conductivity and double layer properties were all examined. Additionally, the electrochemistry of the model redox couples decamethylferrocene and cobaltocenium hexafluorophosphate was investigated. From this, the understanding of electrochemistry in weakly coordinating solvents can be improved and weakly coordinating solvents suitable for electrodeposition at elevated temperatures can be identified.

Experimental

Chemicals

Dichloromethane, CH_2Cl_2 (95%, Sigma-Aldrich), α,α,α-trifluorotoluene, $C_7H_5F_3$ (>99%, Sigma-Aldrich), *o*-dichlorobenzene, $C_6H_4Cl_2$ (>99%, Sigma-Aldrich), *p*-fluorotoluene, C_7H_7F (97%, Sigma-Aldrich) were dried and degassed by refluxing with CaH_2 followed by distilling, and were stored in an inert atmosphere of N_2. The water content in the solvents was measured with Karl–Fischer titration (KF 899 Coloumeter, Metrohm, UK). There was less than 35 ppm of water in all solvents. Tetrabutylammonium chloride, $[N^nBu_4]Cl$ (Sigma-Aldrich, >99%) and tetrabutylammonium tetrafluoroborate, $[N^nBu_4][BF_4]$ (Sigma-Aldrich, >99%) were dried by heating at 100 °C under vacuum for several hours. Decamethylferrocene, $(C_5(CH_3)_5)_2Fe$ (Sigma-Aldrich, 97%) and cobaltocenium hexafluorophosphate, $[(C_5H_5)_2Co][PF_6]$ (Sigma-Aldrich, 98%) were purified by sublimation. All solvents and reagents were stored in a glovebox.

Electrodes

Working electrodes used were inlaid Pt macrodiscs of radius 0.5 mm, and microdiscs of radii 5, 12.5 and 25 μm, sealed in glass. The working electrodes were polished sequentially with 5, 1 and 0.3 μm alumina pastes on a microcloth polishing pad (Buehler, USA). Microelectrodes were calibrated using SEM (Philips XL30 ESEM). A Pt grid was used as a counter electrode, the reference electrode was Ag/AgCl immersed in a storage solution of 100 mM $[N^nBu_4]Cl$ for dichloromethane, *o*-dichlorobenzene and 1,2-dichloroethane, separated from the electrolyte by a porous glass frit, and a Pt wire pseudo reference for α,α,α-trifluorotoluene, *p*-fluorotoluene and chlorobenzene.

Electrochemical measurements

All glassware was cleaned by soaking in Decon 90 (Decon Laboratories Ltd, UK) for at least 24 h, followed by rinsing with ultrapure water, 0.055 μS cm^{-1} and then dried in an oven for a further 24 h.

All experiments were performed with a standard pear shaped cell in a glovebox (Belle Technology, UK) under an inert atmosphere of N_2 in the presence of <5 ppm O_2 and H_2O. Measurements were performed with a PGSTAT μIII or PGSTAT 302N (Metrohm Autolab, UK) potentiostat. Data was recorded with NOVA 1.11 (Metrohm Autolab, UK). The ambient temperature in the glovebox was monitored using a digital thermometer to an accuracy of ±0.05 °C (Hama, UK).

Conductivity measurements were performed in a two electrode cell with electrodes of 0.25, 0.375 and 1 mm radius Pt and a Pt grid. The electrolyte contained supporting electrolyte only. The measurements were performed using a PGSTAT 302N with a FRA32M module. Electrochemical impedance spectroscopy was used potentiostatically at open circuit with 50 frequencies logarithmically spaced between 40 kHz and 10 Hz at an amplitude of 5 mV RMS. Data was fitted using ZView 3.5 (Scribner) to an equivalent circuit of a resistor in series with a constant phase element (CPE). The CPE exponent, α, was greater than 0.9 for all measurements. The uncompensated resistance, R_u, was converted to the specific conductivity, κ, with Newman's equation: $R_u = 1/4a\kappa$, where a is the electrode radius using a plot of R_u *vs.* $1/a$.[9] The molar conductivity, Λ_m, was calculated using $\Lambda_m = \kappa/c$, where c is the electrolyte concentration. For double layer capacitance measurements, electrochemical impedance spectroscopy was performed as described above with 20 frequencies. However, a three electrode cell was used, with sat. Ag/AgCl used as the reference for TFT, pFT and CB. Additionally, a 100 nF capacitor and 0.25 mm radius Pt wire was used in parallel with the reference electrode.[10] Measurements were performed as a function of potential within the potential window of the electrolyte, at intervals of 200 mV with a wait time of 30 s between each potential.

Results and discussion

Weakly coordinating solvents

Kamlet and Taft's (KT) set of empirical solvent descriptors have been extensively used to understand the effect of the solvent on a variety of chemical processes. They are composed of three descriptors: π^*, α and β which describe the polarity, Lewis

acidity and Lewis basicity respectively.[11] By definition, therefore, a weakly coordinating solvent might be expected to have a negligible or zero β. There are however, other requirements if a solvent is to be suitable for electrochemistry. The solvent must be to some extent polar; to permit the dissolution and separation of charged species so that a conducting electrolyte solution is formed. It must also be aprotic to give a large potential window for the reduction of more stable elements. As such, within the framework of the KT parameters a useful weakly coordinating solvent for electrodeposition would have a large π^* parameter, and a zero, or low, value for the α and β parameters.

Fig. 1 shows in red a plot of solvents with KT parameter values of $\pi^* \geq 0.55$, $\alpha \leq 0.2$ and $\beta \leq 0.2$. These represent solvents with properties expected to be useful based upon the above criteria. As can be seen, the solvents occupy a specific volume of the 3D solvent descriptor space. The solvents in this region are primarily halogenated aromatics or short chain aliphatics. Also shown in the same plot are a selection of solvents commonly used in electrochemistry (in blue) and some typical ionic liquids (in yellow). Details of the solvents and their KT parameters are given in Table S1 (ESI†). Clearly the weakly coordinating solvents form a separate group distinct from the ionic liquids and solvents commonly used in electrochemistry. Interpretation of the absolute values of the KT descriptors must be done with caution. The methods of acquiring the descriptors have been criticised,[4] nevertheless they have been shown to correlate well with other solvent descriptors, suggesting that they all measure broadly the same property.[12] Furthermore with the advent of high powered computing, more advanced models, such as CODESSA or COSMO-RS,[13,14] have emerged. These allow the accurate prediction of solute and solvent properties and deepen understanding of the underlying factors affecting solute–solvent interactions. Empirical solvent descriptors may have been superseded, but they remain an accessible tool for quick understanding of the properties of a solvent to the chemist.

Of the solvents in the correct region of solvent space, six were selected as candidate solvents for study: dichloromethane (DCM), α,α,α-trifluorotoluene (TFT), *o*-dichlorobenzene (*o*DCB), *p*-fluorotoluene (pFT), chlorobenzene (CB) and 1,2-dichloroethane (DCE). DCM is included for comparison since it has previously been examined in the literature. A compilation of relevant physical properties of these solvents is given in Table 1. The candidate solvents all possess boiling points higher than DCM. Additionally, all have similar α and β values but vary in their π^*. Therefore it would be expected that the solvents behave similarly, except for properties determined by their polarity. All solvents are readily available at a low cost from standard chemical suppliers. There are varying degrees of safety considerations associated with the solvents (see Table 1), *o*DCB is fairly

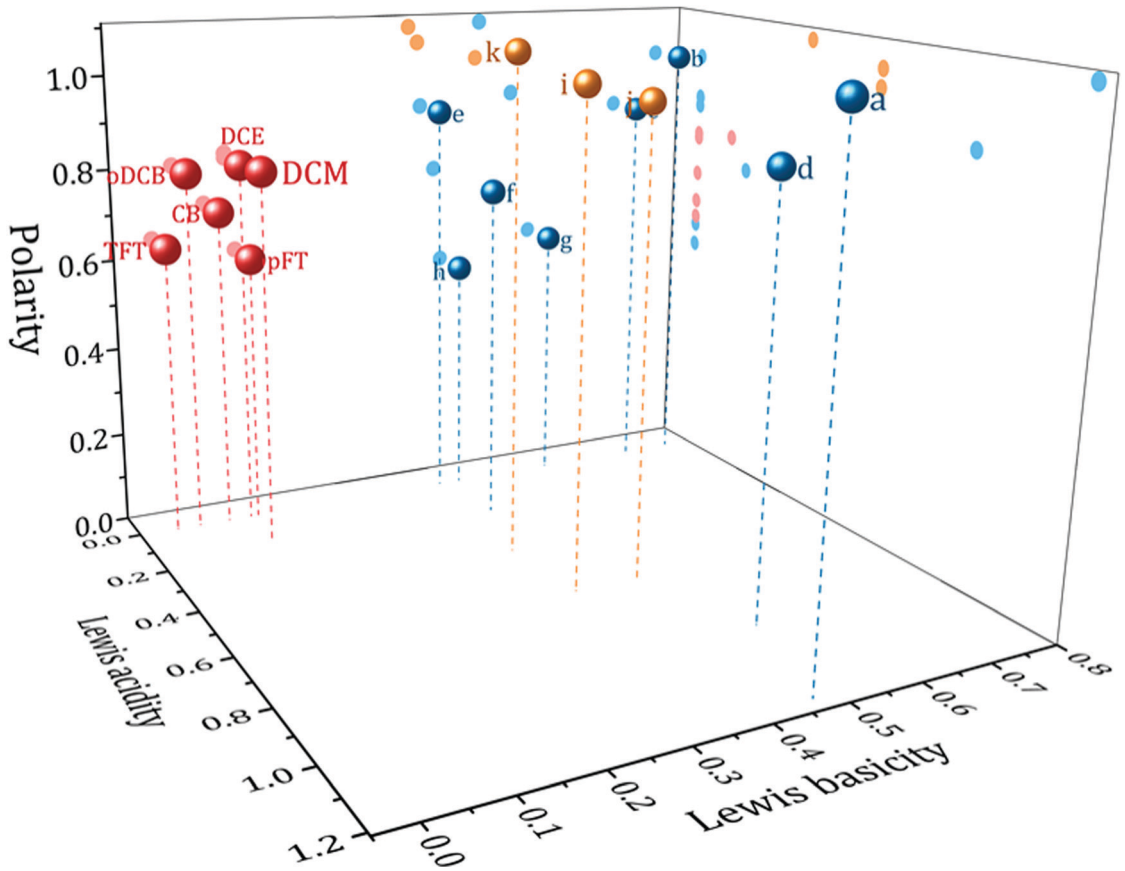

Fig. 1 Weakly coordinating solvent selection map. Showing Kamlet and Taft's descriptors solvent polarity, π^*, Lewis acidity, α and Lewis basicity, β, for red: weakly coordinating solvents, blue: common electrochemical solvents, yellow: typical ionic liquids. Solvent identities can be found in Table S1 (ESI†).

Table 1 Physical properties of weakly coordinating solvents. T_b: boiling point, p_v: vapour pressure, η: viscosity, ρ: density, ε_r: dielectric constant, n: refractive index, μ: dipole moment in the gas phase. All values at 25 °C

Solvent	T_b/°C	p_v/kPa	η/mPa s	ρ/g cm^{-3}	ε_r	n	μ/D	Hazards[a]
DCM[b]	40	58.3	0.41	1.39	8.9	1.42	1.1	Suspected carcinogen
TFT	102[c]	5.3[c]	0.47[d]	1.18[c]	9.2[e]	1.48[e]	2.9[c]	Highly flammable Harmful to the environment
*o*DCB[b]	181	0.2	1.32	1.30	9.9	1.55	2.5	Harmful to the environment
pFT	117[e]	3.0[f]	0.62[g]	1.00[e]	5.9[e]	1.47[e]	2.0[e]	Highly flammable
CB[b]	132	1.6	0.76	1.10	5.6	1.52	1.7	Flammable Harmful to the environment
DCE[b]	83	10.6	0.78	1.25	10.4	1.44	1.8	Highly flammable Suspected carcinogen Toxic

[a] From safety data sheet available at www.sigmaaldrich.com, accessed 03/2022. [b] Ref. 50. [c] Ref. 51. [d] Ref. 52. [e] Ref. 53. [f] Ref. 54. [g] Ref. 55.

benign whereas DCE is restricted by the European Union's REACH regulations for example. But the risks are no greater than for other solvents regularly used in chemistry.

Potential window

The definition of the electrolyte potential window is somewhat arbitrary since the current generally increases approximately exponentially at the anodic and cathodic limit. In this work the potential window of each solvent was determined with the use of decamethylferrocene (DMFc) as an internal current reference. The electrolyte was considered to have reached its solvent limit, anodic or cathodic, when the current was equal to the anodic or cathodic peak current for 1 mM DMFc. All measurements were made using a 0.25 mm radius Pt disc at a scan rate of 50 mV s^{-1}. The results are shown in Table 2. In those cases where 100 mM [N^{n}Bu$_4$]Cl was insoluble in the solvent (TFT, pFT and CB) 100 mM [N^{n}Bu$_4$][BF$_4$] was used instead. The voltammograms used to measure the solvent potential window, along with windows at Au and glassy carbon (GC) electrodes are shown in Fig. S1 (ESI†).

For the majority of solvents, the available potential window, E_{window}, is similar for the solvents with the same electrolyte. Additionally, all solvents have a similar cathodic limit, E_c, and those that share a common anion have a similar anodic limit, E_a. E_a is greater when [BF$_4$]$^-$ is used, indicating that Cl$^-$ is more easily oxidised. It has been shown that the addition of strongly withdrawing groups in the anion can increase its resistance to oxidation.[15] The electrochemistry of the chloride/chlorine system at a Pt surface was studied by Sereno *et al.* in the aprotic solvent acetonitrile.[16] The overall redox reaction appeared to be

$$2Cl^- + 2e^- \rightarrow Cl_2(g)$$

which proceeded *via* a Volmer–Heyrovsky mechanism. Xiao and Johnson performed bulk electrolysis of the ionic liquid [bmim][BF$_4$] at Pt electrodes.[17] The anodic product was found to be primarily BF$_3$. With [N^{n}Bu$_4$][BF$_4$], it might therefore be expected that the anodic decomposition reaction is

$$[BF_4]^- \rightarrow BF_3(g) + e^-.$$

The similarity of the windows suggest that the available window of the system is limited by decomposition of the supporting electrolyte rather than the solvent itself. The exception to this rule is DCE which has a much lower cathodic limit, suggesting the solvent itself is decomposing. The electrochemical reduction of DCE has been studied at GC and Ag electrodes in acetonitrile and dimethylformamide.[18,19] The proposed mechanism is one of stepwise dechlorination forming a carbon radical followed by a carbanion, with the reaction terminated by the formation of ethylene.[19] Protonation of the anion by trace water to give chloroethane or ethane is also possible. However considering the minimal water content in the solvents (see above), this is likely to only be a very minor product.

Slight variations of the limits can still be observed between solvents, this could be the effect of trace water impurities, which have been observed to narrow the potential window of ionic liquids.[20] Nevertheless, the key consideration for electrodeposition is the cathodic limit, which is comparable to DCM for all solvents and indicates that the candidate solvents have a useful window for cathodic semiconductor deposition.

Table 2 Anodic and cathodic limits, and available electrolyte window determined using 1 mM DMFc at 0.25 mm Pt WE at 50 mV s^{-1}. Electrolyte composed of 100 mM [N^{n}Bu$_4$]Cl in DCM, *o*DCB and DCE, and 100 mM [N^{n}Bu$_4$][BF$_4$] in TFT, pFT and CB

Solvent	E_a *vs.* DMFc$^{0/+}$/V	E_c *vs.* DMFc$^{0/+}$/V	E_{window}/V
DCM	0.89	−2.18	3.07
TFT	1.45	−2.30	3.76
*o*DCB	0.78	−2.31	3.09
pFT	1.40	−2.56	3.97
CB	1.45	−2.51	3.95
DCE	0.75	−1.77	2.52

Conductivity

Table 3 shows conductivities of the selected solvents with 100 mM [N^{n}Bu$_4$]Cl and [N^{n}Bu$_4$][BF$_4$], except from TFT, pFT and CB where 100 mM [N^{n}Bu$_4$]Cl was insoluble, as noted above. Its insolubility is presumably caused by the lower polarity of the solvents ($\pi^* \leq 0.71$). Also shown is the conductivity viscosity product, $\Lambda_m\eta$, in an attempt to account for the effect of gross difference in solvent viscosity on conductivity; $\Lambda_m\eta$ should be approximately proportional to the degree of ion pairing in the

Table 3 Normalised uncompensated resistance and conductivities of 100 mM electrolyte at 25 °C obtained from impedance spectroscopy. Blank cell indicates insolubility. Each value is the average of three repeats and the error the standard deviation

Electrolyte	Solvent	$R_u a$/kΩ cm	Λ_m/S cm^2 mol^{-1}	$\Lambda_m\eta$/S cm^2 mPa s mol^{-1}
[N^{n}Bu$_4$]Cl	DCM	0.28(1)	9.04(2)	3.71(8)
	TFT	—	—	—
	*o*DCB	2.33(3)	1.07(2)	1.42(2)
	pFT	—	—	—
	CB	—	—	—
	DCE	0.34(1)	7.42(11)	5.78(8)
[N^{n}Bu$_4$][BF$_4$]	DCM	0.22(1)	11.61(38)	4.76(16)
	TFT	0.43(2)	2.30(5)	1.17(2)
	*o*DCB	1.44(1)	1.74(2)	2.29(3)
	pFT	3.50(15)	0.71(3)	0.44(2)
	CB	3.22(7)	0.78(2)	0.59(1)
	DCE	0.23(1)	10.69(12)	8.33(10)

solvent. The values obtained are comparable with those previously reported in the literature under the same or similar conditions for DCM,[21–24] TFT,[21,25] *o*DCB[24] and DCE.[22,24]

In the solvents where both salts are soluble, [N^{n}Bu$_4$][BF$_4$] imparts greater conductivity than does [N^{n}Bu$_4$]Cl. This can be rationalized in less polar solvents since the larger [BF$_4$]$^-$ anion has a lower charge density than Cl$^-$ and, consequently is expected to be less strongly ion paired.[26] The increased size of the anion does reduce mobility but this is compensated by the increase in free ions. The ratio of conductivity, $\Lambda_m\eta$ ([N^{n}Bu$_4$][BF$_4$])/$\Lambda_m\eta$ ([N^{n}Bu$_4$]Cl) is similar for DCM, *o*DCB and DCE with values of 1.3, 1.6 and 1.4 respectively; indicating that the relative strength of the electrolyte remains the same. Such effects have been previously observed in DCM and TFT by Geiger *et al.*[21] When measuring the conductivity of various tetrabutylammonium salts, they found that the conductivity was increased and K_A, the association constant, lowered for larger anions.

It is also interesting to note that although many of the solvents have similar dielectric constants, the measured conductivities are not similar. The experimental order of $\Lambda_m\eta$ is pFT < CB < TFT < *o*DCB < DCM < DCE, however that predicted by ε_r is CB < pFT < DCM ≈ TFT < *o*DCB < DCE (Fig S2, ESI†). The conductivities for TFT and *o*DCB solutions appear to be significantly lower than those for DCM and DCE with similar dielectric constants. This suggests that the isodielectric rule, which states that for a given electrolyte salt the ion pair association constant should be the same in solvents of the same electrolyte,[27] breaks down here due to short range specific interactions in these aromatic solvents.[28] The formation of ion pairs is ultimately a competition between solvent and counter ion for interaction with the ion. Such an effect has been observed in water where ion pairing increases with size since larger ions disrupt the H bonding network of water and so are forced into ion pairs to preserve it.[26] One measure of the structure of a solvent is the Kirkwood correlation parameter, g_K, which gives information on the orientation of the solvent molecule's dipole.[29] For a solvent with no alignment: $0.7 \leq g_K \leq 1.3$ and it is considered unstructured. When $g_K > 1.3$, the dipoles are oriented parallel to each other. $g_K < 0.7$ corresponds to neighbouring dipoles oriented in an antiparallel fashion. Values for the present solvents can be taken from the literature (ref. 29) or calculated, giving values for DCM, TFT, *o*DCB and DCE of 1.04, 0.56, 0.68 and 1.17 respectively. This would suggest DCM and DCE are unstructured, but in TFT and *o*DCB some of the solvent molecules are oriented in an antiparallel manner and this arrangement is preferred to ion solvation, causing a greater degree of ion pairing. There is no direct evidence of such structures in TFT or *o*DCB but dielectric measurements of bromobenzene and benzonitrile, two solvents with $g_K < 0.7$, have shown them to form stable antiparallel dimers.[30] Furthermore, crystal structures of TFT and *o*DCB showed TFT molecules arranged in a head to tail fashion, and favourable Cl-Cl interactions leading to a 'zig-zag' structure in *o*DCB,[31,32] suggesting that associations of this type are energetically favourable in solution.

Double-layer structure

Fig. 2 shows differential capacitance curves for 100 mM [N^{n}Bu$_4$][BF$_4$] at a Pt electrode. A simple model of the electrical double layer (EDL) describes the total capacitance, C_{DL}, as the sum of two capacitors in series

$$\frac{1}{C_{DL}} = \frac{1}{C_H} + \frac{1}{C_D}$$

where C_H is the capacitance of the Helmholtz layer and C_D is the capacitance of the diffuse layer.[33] At high electrolyte concentrations such as that in Fig. 2, C_D becomes large enough so that it no longer contributes to C_{DL}, which is then primarily determined by C_H.[34] C_H can be described as a parallel plate capacitor, such that

$$\frac{C_H}{A} = \frac{\varepsilon_i \varepsilon_0}{d}$$

where A is the area of the electrode, ε_i is the dielectric constant of the inner layer, ε_0 is the permittivity of free space and d is the

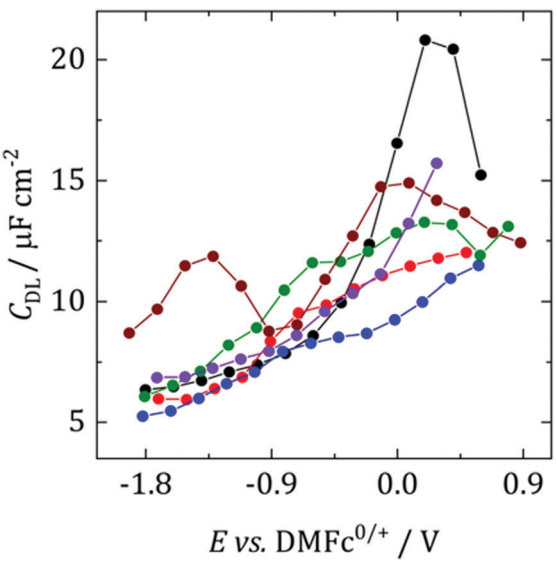

Fig. 2 Differential capacitance curves for 100 mM [N^{n}Bu$_4$][BF$_4$] at a r = 0.25 mm Pt electrode, scanning in the anodic direction. Black: DCM, red: TFT, blue: oDCB, green: pFT, brown: CB, purple: DCE.

distance between the two plates. This model predicts capacitance to be independent of potential, which is clearly not the case here. Instead, generally, a decrease in C_{DL} with potential is observed, before plateauing at the most negative potentials. Curves measured by scanning in the opposite direction showed no changes (see Fig. S3, ESI†). This appears to be in agreement with the work of Fawcett at the Hg/propylene carbonate interface with 100 mM $[N^nBu_4][ClO_4]$. As the potential decreases, solvent molecules are replaced by $[N^nBu_4]^+$ on the electrode and ε_i decreases. Taking a value of 6.5 μF cm^{-2} for the capacitance of the plateau, and assuming a dielectric constant of the inner layer of 3.2,[35] gives a thickness of 0.44 nm. This is comparable to 0.41 nm, the crystallographic radius of the $[N^nBu_4]^+$ cation,[36] indicating that the inner layer is populated by $[N^nBu_4]^+$ at negative potentials. Although, since the size reported here is larger than the crystallographic radius, this might suggest that the dielectric constant of the inner layer is less than 3.2. Abbott reported a value of 2.6 in DCE for example.[37]

The exception to this rule appears to be CB, where two humps are observed. This was also observed by Abbott

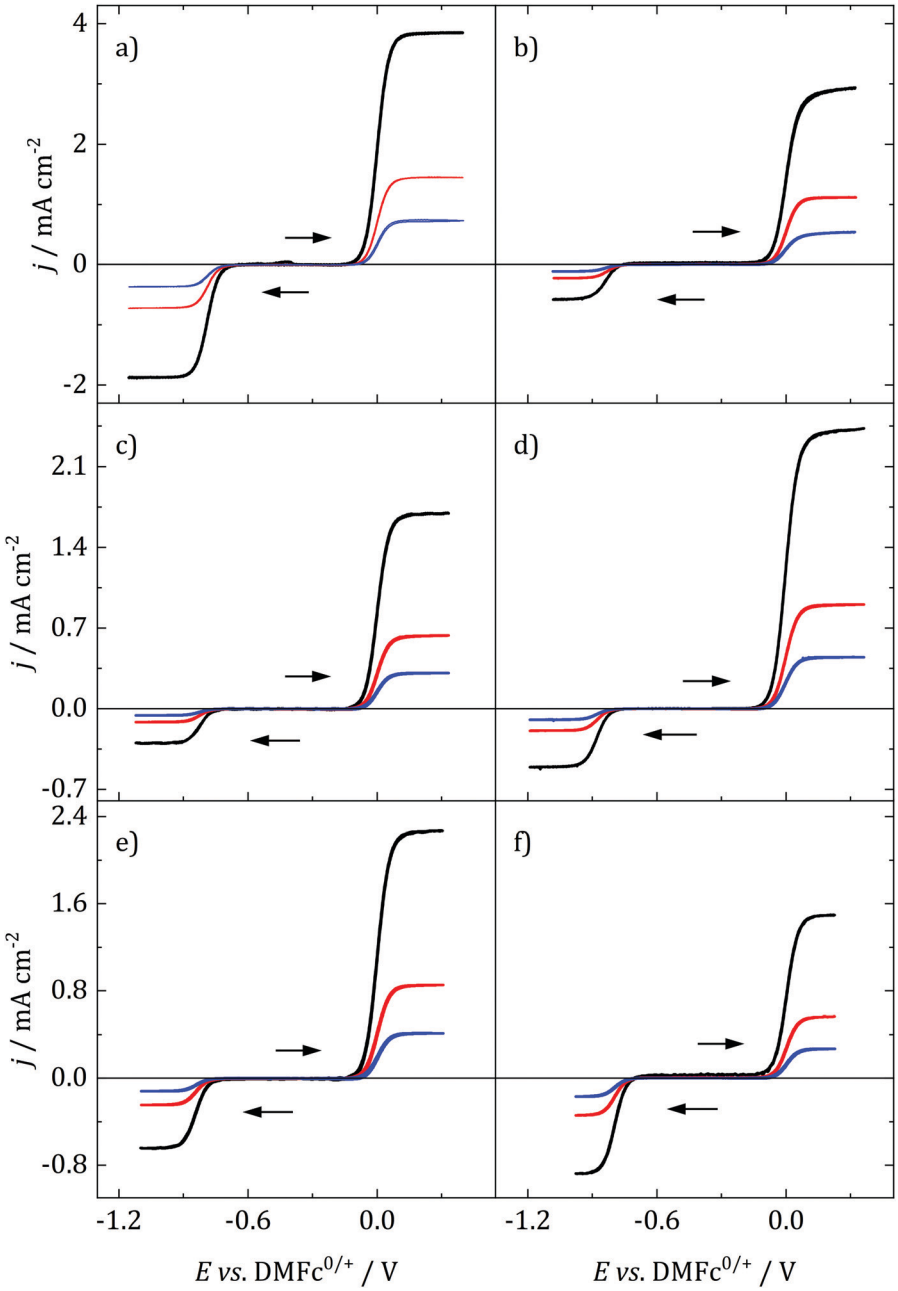

Fig. 3 Representative microdisc voltammograms for 1 mM DMFc and 0.5 mM $CcPF_6$ at various electrode materials with 100 mM (a, c and f): $[N^nBu_4]Cl$ and (b, d and e) $[N^nBu_4][BF_4]$. Scan swept from −0.3 V *vs.* DMFc at (a, b and d–f): 5 mV s^{-1}, (c) 2 mV s^{-1} in the direction indicated by the arrows. CE: Pt mesh, RE: (a, c and f): Ag/AgCl, (b, d and e): Pt PRE. (a) DCM, (b) TFT, (c) *o*DCB, (d) pFT, (e) CB, (f) DCE. Black: r = 5 μm, red: 12.5 μm, blue: 25 μm.

for 300 mM $[N^nBu_4][BF_4]$ in DCE at a Pt surface.[37] These humps were demonstrated to be caused by adsorption of ions or ion aggregates onto the electrode surface. Although it is not clear why it is only observed in CB.

Fawcett also investigated the structure of the double layer with a dropping mercury electrode (DME) in tetrahydrofuran (THF), a solvent of similar polarity to those studied here.[38] In their work diffuse layer effects were observed in the form of a capacitance minimum, caused by a decrease in effective ionic strength due to ion pairing. Ion pairing is undoubtedly present in the studied solvents but it does not appear to be observable here. It could point to the advantage of using a DME for EDL studies, where the history of the electrode is not a factor.

Electrochemistry of decamethylferrocene and cobaltocenium hexafluorophosphate

Decamethylferrocene (DMFc) and cobaltocenium hexafluorophosphate ($CcPF_6$) were used as model redox probes to investigate the nature of electrochemistry in the candidate solvents. Metallocene electron transfer is an outer sphere, mechanistically simple electron transfer process with a low inner and outer sphere reorganisation energy. They are characterised by fast, stable electrochemistry and as such are regularly used for the characterisation of unknown solvents. For example, metallocenes have been used to understand behaviour in novel media such as ionic liquids.[39] It was also imprtant to understand the behaviour of DMFc since it was to be used as a solvent independent internal reference; DMFc has been shown to be a superior internal reference to the commonly used ferrocene.[40]

Fig. 3 shows voltammograms for DMFc and $CcPF_6$ at three different sizes of microelectrode in the selected solvents. One major advantage of microelectrodes is that their smaller size results in smaller currents and therefore minimisation of distortions associated with *iR* drop. This feature becomes particularly important in low polarity solvents such as those studied here, and was exploited to achieve artefact free, quantitative analysis of voltammograms.

Starting from −0.3 V *vs.* $DMFc^{0/+}$, one oxidation process can be observed, corresponding to the oxidation of decamethylferrocene to decamethylferricenium

$$[(Me_5Cp)_2Fe(II)] \rightarrow [(Me_5Cp)_2Fe(III)]^+ + e^-$$

where Cp is the cyclopentadienyl anion. On the reverse sweep, a cathodic process occurs, associated with the reduction of cobaltocenium to cobaltocene

$$[(Cp)_2Co(III)]^+ + e^- \rightarrow [(Cp)_2Co(II)]$$

As can be seen, a limiting current plateau forms for both DMFc and $CcPF_6$ at all electrode sizes in all solvents, indicative of a diffusion limited process. This is also supported by the observation of linear Randles-Sevčik plots at larger electrodes (Fig. S4, ESI†). The behaviour was investigated at different electrode materials, with voltammograms recorded at Au and glassy carbon (GC) macroelectrodes, shown in Fig. S5 (ESI†). No changes are observed, as would be expected for an outer-sphere electron transfer.

Thermodynamics. Mass transport corrected Tafel plots were used to obtain the half wave potential, $E_{1/2}$, for DMFc and $CcPF_6$

$$E = E_{1/2} + \frac{RT}{nF}\ln\left(\frac{i_L}{i} - 1\right)$$

where R is the gas constant, T absolute temperate, n the number of electrons transferred, F the Faraday and i_L the limiting current. Therefore, plots of E *vs.* $\ln(i_L/i - 1)$ should be linear with an intercept of $E_{1/2}$. Such plots are shown in Fig. S5 (ESI†) and the obtained values *vs.* Ag/AgCl and $DMFc^{0/+}$, averaged over three electrode sizes and three repeats are shown in Table 4. No relationship between $E_{1/2}$ and electrode size was observed, demonstrating the absence of any *iR* drop effects. Some shifts in the redox potential of DMFc *vs.* Ag/AgCl are evident, we attribute these to solvent shifts in the Ag/AgCl reference electrode potential. It is then possible to reference $E_{1/2}(CcPF_6)$ against DMFc, so now all changes in the $CcPF_6$ redox potential can be attributed to the effect of the solvent.

According to the Born equation for the electrostatic solvation energy of an ion, $E_{1/2}$ should be proportional to $1/\varepsilon_r$.[41] With DMFc as an internal reference it is possible to examine this relationship for $CcPF_6$. Based upon the solvent descriptors above, it should be expected that there are minimal specific interactions between solvent and solute, and the primary form is electrostatic in nature. Consequently, simplistically the Born equation might be expected to be a reasonable descriptor of solvent solute interactions. Fig. 4a shows such a plot for the selected solvents. A weak linear relationship is observed (R^2 = 0.65), with redox potential decreasing with solvent polarity. Clearly in this case the Born equation is not a good descriptor; previous attempts at correlation in the literature have been similarly unsuccessful.[41] Also shown in Fig. 4b is the

Table 4 Thermodynamic, kinetic and mass transport parameters of 1 mM DMFc and 0.5 mM $CcPF_6$ in various solvents at 25 °C using microelectrodes. Obtained with 100 mM $[N^nBu_4]Cl$ in DCM, *o*DCB and DCE and 100 mM $[N^nBu_4][BF_4]$ in TFT, pFT and CB. Values are the average of three repeats with the error the standard deviation

	DMFc				$CcPF_6$				
Solvent	$E_{1/2}$ *vs.* Ag/AgCl/V	$\lvert E_{3/4}-E_{1/4}\rvert$/mV	b/mV	$D/10^{-5}$ cm^2 s^{-1}	$E_{1/2}$ *vs.* Ag/AgCl/V	$E_{1/2}$ *vs.* $DMFc^{0/+}$/V	$\lvert E_{3/4}-E_{1/4}\rvert$/ mV	b/mV	$D/10^{-5}$ cm^2 s^{-1}
DCM	0.438(10)	58(1)	26.6(3)	1.68(2)	−0.350(10)	−0.788(1)	56(1)	25.4(3)	1.35(1)
TFT	0.192(4)	63(2)	28.6(6)	1.18(3)	−0.637(2)	−0.830(1)	57(1)	26.0(1)	0.38(2)
*o*DCB	0.499(20)	59(1)	26.8(1)	0.52(1)	−0.323(20)	−0.822(1)	55(2)	24.8(8)	0.24(1)
pFT	0.198(7)	62(1)	28.9(8)	1.10(11)	−0.678(7)	−0.875(2)	57(1)	26.2(1)	0.31(3)
CB	0.145(1)	62(2)	28.2(8)	0.87(3)	−0.692(1)	−0.840(4)	58(1)	26.3(9)	0.32(3)
DCE	0.376(1)	57(1)	26.1(2)	0.88(3)	−0.418(1)	−0.795(2)	55(1)	25.0(1)	0.61(3)

relationship with π*, where the correlation is improved, R^2 = 0.77. Suggesting that π* is the superior descriptor of solvent polarity. Correlations of redox potential with π* have previously proved successful.[42]

The direction of the correlation is, however, opposite to what is expected. For a cation that is reduced to a neutral species, more polar solvents would more strongly solvate the cation and decrease the redox potential. One effect that potentially could cause a reversal of this trend is ion pairing. If the Cc^+ ion was paired with $[BF_4]^-$ or Cl^- then this could stabilise the cation, thus decreasing the redox potential. As the polarity of the solvent decreases, the degree of ion pairing is greater and so is the stabilisation. The presence of ion pairing effects on voltammetry has been reported in DCM for ferrocene and DMFc.[43,44]

Kinetics. Steady-state voltammograms can also be used to investigate the kinetics of electron transfer. For an electrochemically reversible one electron redox couple at 25 °C the difference between the third and first quartile potential, $E_{3/4}$ and $E_{1/4}$ respectively, should be 56 mV. Additionally, the slope of a mass transport corrected Tafel plot, b, is equal to RT/nF, corresponding to 25.7 mV for a one electron transfer at 25 °C. Values for each method are given in Table 4 for DMFc and $CcPF_6$. Tafel plots can be found in the ESI† (Fig. S6). As can be seen, both redox couples are reversible, or near reversible, in all of the solvents. This is in agreement with previous observations in the literature for DMFc.[40,45–47]

Mass transport. The limiting current at a microelectrode is given by

$$i_L = 4nFDca$$

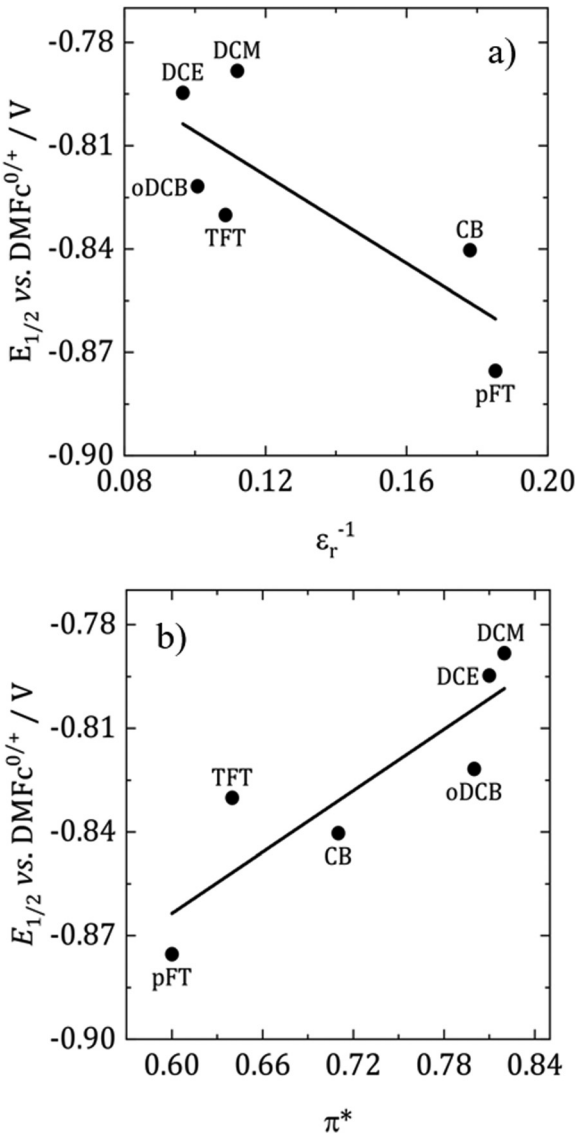

Fig. 4 Solvent dependence of $E_{1/2}(CcPF_6)$ with solvent polarity. (a) Dielectric constant and (b) KT polarity descriptor. Obtained from microelectrode voltammograms for 0.5 mM $CcPF_6$ with 100 mM $[N^nBu_4]Cl$ in DCM, *o*DCB and DCE, and 100 mM $[N^nBu_4][BF_4]$ in TFT, pFT and CB.

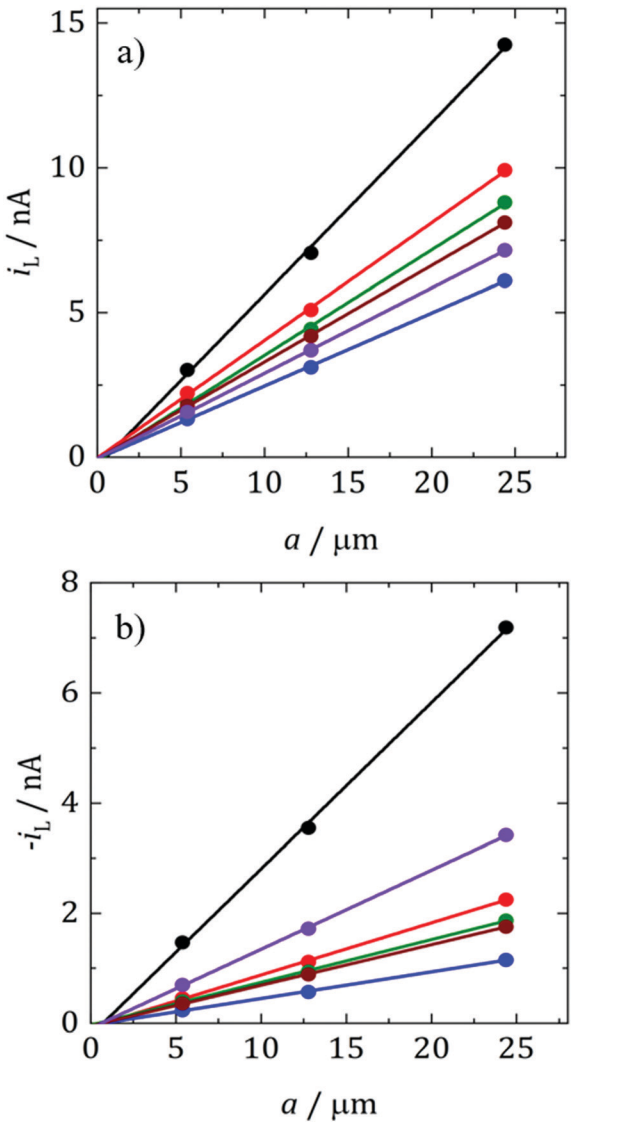

Fig. 5 Representative plots of i_L *vs.* a for (a) 1 mM DMFc and (b) 0.5 mM $CcPF_6$ at electrodes of r = 5 μm, 12.5 μm and 25 μm at 25 °C. Black: DCM, red: TFT, blue: *o*DCB, green: pFT, brown: CB, purple: DCE.

where D is the diffusion coefficient, c is the concentration of electroactive species in the bulk and a is the radius of the microelectrode. Consequently, plots of i_L *vs.* a for different sizes of microelectrode should be linear and D can be obtained from the slope. Fig. 5 shows such plots for DMFc and $CcPF_6$. Uncertainty in the concentration was alleviated by performing a potential step at a microelectrode. The resulting transient was fitted to the Shoup–Szabo equation, giving c.[48] The average value for all three electrode sizes was taken and used as c in calculating D. The resulting D values are shown in Table 4. Diffusion coefficients obtained from potential steps at a microelectrode corroborate the results here and are shown in Table S2 (ESI†). Where available, the values here agree with those in the literature. In DCM Weaver obtained a value of 1.30×10^{-5} cm^2 s^{-1} for DMFc using DC polarography at 23 °C.[49] Matsumoto and Swaddle reported a mean value of 1.07×10^{-5} cm^2 s^{-1} using peak currents of voltammograms at 25 °C.[46] Branch obtained a value for DMFc of 1.48×10^{-5} cm^2 s^{-1} from a microelectrode voltammogram and a mean value of 7.95×10^{-6} cm^2 s^{-1} from macrodisc voltammograms at 25 °C.[45] Tsierkezos reported a value of 1.35×10^{-5} cm^2 s^{-1} for the neutral Cc species in DCM, similar to the value obtained here.[47] There appears to be no literature data of measurements for DMFc nor $CcPF_6$ in the remaining solvents.

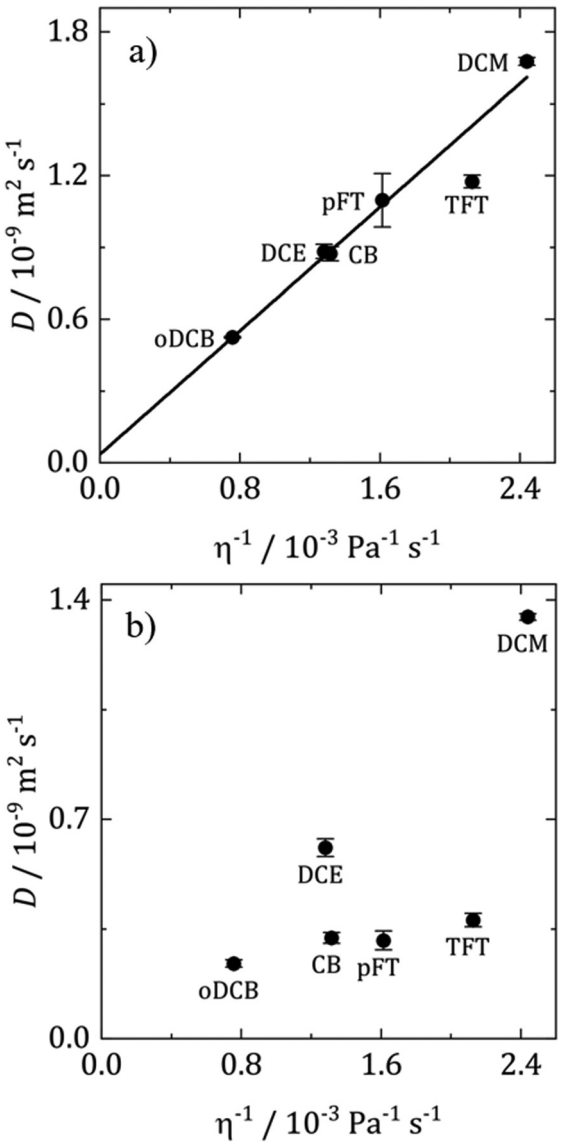

Fig. 6 Stokes–Einstein plots of (a) DMFc and (b) $CcPF_6$ at 25 °C. D obtained from microelectrode voltammograms. Values are the average of three repeats and the error bars the standard deviation.

Diffusion coefficients are often interpreted using the Stokes–Einstein (SE) equation

$$D = \frac{k_B T}{6\pi\eta r_S}$$

where k_B is Boltzmann's constant, η the solvent viscosity and r_S the Stokes radius, the size of the diffusing particle. The Stokes–Einstein equation assumes that the diffusing particle is spherical and travelling through a continuum. Therefore, a plot of D *vs.* $1/\eta$ should be linear with an intercept at the origin. Fig. 6 shows such plots for DMFc and $CcPF_6$.

In Fig. 6a for DMFc it can be seen that the plot is linear ($R^2 = 0.98$) with an intercept close to the origin, demonstrating that DMFc obeys the Stokes Einstein equation. For the charged Cc^+ in Fig. 6b the situation is markedly different. Assuming that the choice of redox couples does not significantly affect the solution viscosity, the most likely explanation for this lack of correlation is the presence of ion pairing increasing the size of the diffusing particle, r_S. This has been observed before for diffusion coefficients of $DMFc^+$ in DCM by Goldfarb and Corti.[44] The interpretation of diffusion coefficients in weakly coordinating solvents is complicated and will be discussed further in a subsequent publication.

Conclusions

The aim of this study was to improve the understanding of electrochemistry in weakly coordinating solvents and identify alternative solvents to DCM that might be useful for electrodeposition. To this end, Kamlet and Taft solvent descriptors were employed to identify solvents with similar properties to DCM. As a part of this method it was established that other solvents commonly used in electrochemistry were not suitable and would not be useful. The selected solvents were subjected to thorough characterisation, comprised of measurements of potential window, conductivity, double-layer capacitance and behaviour of model redox couples. Earlier, a prediction was made that all solvents would behave similarly except for those properties determined by polarity and this appears partially true. Whilst the advantage of solvent descriptors and Kamlet Taft parameters for choosing a solvent has been demonstrated, it was also shown that they do not tell the whole story which leaves an element of uncertainty. Increasing the number of descriptors considered would be a solution but this greatly increases the complexity of the selection process and it is not plausible to identify them all *a priori*. The most profitable approach would seem to be to choose 2–4 key descriptors and

use those to identify several candidate solvents for investigation, then choosing the optimum solvent(s). This may be more resource intensive but allows for the possibility of unforeseen behaviours.

In a general sense, all solvents investigated appear to be useful as weakly coordinating solvents for electrochemistry. However due to the low polarity of some, they are unlikely to be useful for electrodeposition. The ability to dissolve and dissociate salts in reasonable quantities is a key requirement for a useful plating bath. Therefore, *o*DCB and DCE as the most polar solvents appear the most promising for application to electrodeposition. This will be the subject of future research.

Finally, in solvents with a low polarity such as those studied here, ion pairing is clearly an important factor in determining the electrochemical response. The consequences of ion pairing were observed in measurements of conductivity, redox potential and diffusion coefficient and must be considered when interpreting electrochemical data in solvents of intermediate or low polarity. Furthermore, charged species are likely to exist in a combination of forms including free ions, ion pairs and potentially triple ions. Meaning the experimental response is an average of the species' behaviour in all its arrangements.

Author contributions

AWB: conceptualization, methodology, validation, formal analysis, investigation, data curation, writing – original draft, visualization. PNB: conceptualization, methodology, validation, formal analysis, writing – review & editing, supervision, funding acquisition, project administration.

Conflicts of interest

There are no conflicts to declare.

Acknowledgements

Dr Wenjian Zhang is thanked for the supply of solvents and reagents. This work was supported by EPSRC through the Advanced Devices by Electroplating program grant (ADEPT; EP/N035437/1).

Notes and references

1 *Nanoelectronics and Information Technology:Advanced Electronic Materials and Novel Devices*, ed. R. Waser, Wiley-VCH, Weinheim, 3rd edn, 2012.
2 D. T. Richens, *Chem. Rev.*, 2005, **105**, 1961–2002.
3 H. Taube, *Chem. Rev.*, 1952, **50**, 69–126.
4 C. Reichardt and T. Welton, *Solvents and Solvent Effects in Organic Chemistry*, Wiley-VCH Verlag GmbH, Weinheim, 4th edn, 2011.
5 P. N. Bartlett, D. Cook, C. H. de Groot (Kees), A. L. Hector, R. Huang, A. Jolleys, G. P. Kissling, W. Levason, S. J. Pearce and G. Reid, *RSC Adv.*, 2013, **3**, 15645–15654.
6 G. P. Kissling, R. Huang, A. Jolleys, S. L. Benjamin, A. L. Hector, G. Reid, W. Levason, C. H. K. De Groot and P. N. Bartlett, *J. Electrochem. Soc.*, 2018, **165**, D557–D567.
7 L. Meng, K. Cicvarić, A. L. Hector, C. H. de Groot and P. N. Bartlett, *J. Electroanal. Chem.*, 2019, **839**, 134–140.
8 G. P. Kissling, M. Aziz, A. W. Lodge, W. Zhang, M. Alibouri, R. Huang, A. L. Hector, G. Reid, C. H. de Groot, R. Beanland, P. N. Bartlett and D. C. Smith, *J. Electrochem. Soc.*, 2018, **165**, D802–D807.
9 J. Newman, *J. Electrochem. Soc.*, 1966, **113**, 501–502.
10 C. C. Herrmann, G. G. Perrault and A. A. Pilla, *Anal. Chem.*, 1968, **40**, 1173–1174.
11 M. J. Kamlet, J. L. M. Abboud, M. H. Abraham and R. W. Taft, *J. Org. Chem.*, 1983, **48**, 2877–2887.
12 Y. Marcus, *Chem. Soc. Rev.*, 1993, **22**, 409–416.
13 A. Klamt, *J. Phys. Chem.*, 1995, **99**, 2224–2235.
14 A. R. Katritzky, V. S. Lobanov and M. Karelson, *Chem. Soc. Rev.*, 1995, **24**, 279–287.
15 J. Barthel and H. J. Gores, in *Handbook of Battery Materials*, ed. C. Daniel and J. O. Besenhard, Wiley-VCH Verlag GmbH, Weinheim, 2nd edn, 2011, pp. 457–497.
16 L. Sereno, V. A. Macagno and M. C. Giordano, *Electrochim. Acta*, 1972, **17**, 561–575.
17 L. Xiao and K. E. Johnson, *J. Electrochem. Soc.*, 2003, **150**, E307–E311.
18 O. Scialdone, C. Guarisco, A. Galia and R. Herbois, *J. Electroanal. Chem.*, 2010, **641**, 14–22.
19 G. Fiori, S. Rondinini, G. Sello, A. Vertova, M. Cirja and L. Conti, *J. Appl. Electrochem.*, 2005, **35**, 363–368.
20 A. M. O'Mahony, D. S. Silvester, L. Aldous, C. Hardacre and R. G. Compton, *J. Chem. Eng. Data*, 2008, **53**, 2884–2891.
21 R. J. LeSuer, C. Buttolph and W. E. Geiger, *Anal. Chem.*, 2004, **76**, 6395–6401.
22 K. M. Kadish, J. Q. Ding and T. Malinski, *Anal. Chem.*, 1984, **56**, 1741–1744.
23 I. Svorstol and J. Songstad, *Acta Chem. Scand., Ser. B*, 1985, **39**, 639–655.
24 T. Sigvartsen, B. Gestblom, E. Noreland and J. Songstad, *Acta Chem. Scand., Ser. B*, 1989, **43**, 103–115.
25 S. Boitsov, K. J. Borve, S. Rayyan, K. W. Tornroos and J. Songstad, *J. Mol. Liq.*, 2003, **103–104**, 221–233.
26 Y. Marcus and G. Hefter, *Chem. Rev.*, 2006, **106**, 4585–4621.
27 R. M. Fuoss, *Proc. Natl. Acad. Sci. U. S. A.*, 1978, **75**, 16–20.
28 R. M. Fuoss, *J. Solution Chem.*, 1986, **15**, 231–235.
29 Y. Marcus, *J. Solution Chem.*, 1992, **21**, 1217–1230.
30 T. Shikata, N. Sugimoto, Y. Sakai and J. Watanabe, *J. Phys. Chem. B*, 2012, **116**, 12605–12613.
31 K. Merz, M. V. Evers, F. Uhl, R. I. Zubatyuk and O. V. Shishkin, *Cryst. Growth Des.*, 2014, **14**, 3124–3130.
32 M. Bujak, K. Dziubek and A. Katrusiak, *Acta Crystallogr., Sect. B: Struct. Sci.*, 2007, **63**, 124–131.
33 B. B. Damaskin and O. A. Petrii, *J. Solid State Electrochem.*, 2011, **15**, 1317–1334.
34 A. J. Bard and L. R. Faulkner, *Electrochemical Methods: Fundamentals and Applications*, Wiley-VCH, Hoboken, NJ, 2nd edn, 2001.

35 W. R. Fawcett, M. Fedurco and M. Opallo, *J. Phys. Chem.*, 1992, **96**, 9959–9964.
36 Y. Marcus, *Ions in Solution and Their Solvation*, Wiley, Hoboken, NJ, 2015.
37 A. P. Abbott and J. C. Harper, *J. Chem. Soc., Trans.*, 1997, **93**, 3981–3984.
38 M. A. Drogowska and W. R. Fawcett, *J. Electroanal. Chem.*, 1987, **222**, 293–303.
39 E. I. Rogers, D. S. Silvester, D. L. Poole, L. Aldous, C. Hardacre and R. G. Compton, *J. Phys. Chem. C*, 2008, **112**, 2729–2735.
40 I. Noviandri, K. N. Brown, D. S. Fleming, P. T. Gulyas, P. A. Lay, A. F. Masters and L. Phillips, *J. Phys. Chem. B*, 1999, **103**, 6713–6722.
41 G. Gritzner, *Rev. Inorg. Chem.*, 1990, **11**, 81–122.
42 P. A. Lay, N. S. McAlpine, J. T. Hupp, M. J. Weaver and A. M. Sargeson, *Inorg. Chem.*, 1990, **29**, 4322–4328.
43 T. Kondo, M. Okamura and K. Uosaki, *J. Organomet. Chem.*, 2001, **637–639**, 841–844.
44 D. L. Goldfarb and H. R. Corti, *J. Electroanal. Chem.*, 2001, **509**, 155–162.
45 J. A. Branch, *Electrochemical Studies of Diffusion in Supercritical Fluids*, PhD Thesis, University of Southampton, 2015.
46 M. Matsumoto and T. W. Swaddle, *Inorg. Chem.*, 2004, **43**, 2724–2735.
47 N. G. Tsierkezos, *J. Mol. Liq.*, 2008, **138**, 1–8.
48 D. Shoup and A. Szabo, *J. Electroanal. Chem.*, 1982, **140**, 237–245.
49 T. Gennett, D. F. Milner and M. J. Weaver, *J. Phys. Chem.*, 1985, **89**, 2787–2794.
50 Y. Marcus, *The Properties of Solvents*, Wiley, Chichester, 1998.
51 J. J. Maul, P. J. Ostrowski, G. A. Ublacker, B. Linclau and D. P. Curran, in *Modern Solvents In Organic Synthesis*, ed. P. Knochel, Springer-Verlag, Berlin, 1999, pp. 79–105.
52 L. De Lorenzi, M. Fermeglia and G. Torriano, *J. Chem. Eng. Data*, 1996, **41**, 1121–1125.
53 W. M. Haynes, D. R. Lide and T. J. Bruno, *CRC Handbook of Chemistry and Physics*, CRC Press, New York, 96th edn, 2016.
54 D. R. Lide, *Basic Laboratory and Industrial Chemicals: A CRC Quick Reference Handbook*, CRC Press, Boca Raton, 1993.
55 O. Ivanciuc, T. Ivanciuc, P. A. Filip and D. Cabrol-Bass, *J. Chem. Inf. Comput. Sci.*, 1999, **39**, 515–524.

Electrochimica Acta 425 (2022) 140720

Contents lists available at ScienceDirect

Electrochimica Acta

journal homepage: www.journals.elsevier.com/electrochimica-acta

Diffusion in weakly coordinating solvents

Alexander W. Black, Wenjian Zhang, Gillian Reid, Philip N. Bartlett *

School of Chemistry, University of Southampton, Southampton SO17 1BJ, United Kingdom

ARTICLE INFO

Keywords:
Weakly coordinating solvents
Diffusion coefficients
Ion pairing
Microelectrodes

ABSTRACT

Weakly coordinating solvents are of interest for the electrodeposition of p-block semiconductors for application in electronic devices. p-block complexes typically have weakly coordinated ligands that are easily displaced, making them incompatible with strongly Lewis basic solvents. In this work we use electrochemical measurements at microelectrodes to study diffusion in weakly coordinating solvents. Diffusion coefficients of the metallocenes decamethylferrocene, decamethylferrocenium hexafluorophosphate, cobaltocenium hexafluorophosphate, and the electrodeposition precursors tetrachloroantimonate(III) and tetrachlorobismuthate(III) were measured. The values are analyzed using the modified Stokes-Einstein equation and compared with the theoretical upper, D_{max}, and lower, D_{min}, bounds of the diffusion coefficients. This approach allows the interpretation of D values, whilst avoiding dealing with some of the uncertainties associated with molecular size in the Stokes-Einstein equation. The neutral decamethylferrocene was found to obey the Stokes-Einstein equation whereas the charged metallocene species had values which were less than the theoretical minimum, which was attributed to a larger than expected particle size caused by ion pairing. The importance of considering the modifications of the Stokes-Einstein equation is also highlighted.

1. Introduction

Weakly coordinating solvents are a category of solvent where the molecules are weakly Lewis basic [1]. This means that they are poor ligands and are unlikely to coordinate to a metal cation in a complex. Dichloromethane is one such solvent and its properties as a weakly coordinating solvent have been exploited recently to electrodeposit p-block semiconductors [2–4]. p-block element electrodeposition precursors tend to be labile and hence their ligands are easily displaced, meaning it is important that the solvent will not coordinate to dissolved metal ions. Additional weakly coordinating solvents have also been identified, in order to further the understanding of the nature of electrochemistry in weakly coordinating solvents and to identify alternative solvents to the volatile DCM [1]. The solvents were: α,α,α-trifluorotoluene (TFT), o-dichlorobenzene (oDCB), p-fluorotoluene (pFT), chlorobenzene (CB) and 1,2-dichloroethane (DCE) and these were electrochemically characterised in a recent study.

The diffusion coefficient, D, is a constant of proportionality between the flux and the concentration gradient of a diffusing species, and represents the rate of translational movement of a particle. It has a particular importance in electrochemistry since the current response depends on the flux of the electroactive species to the electrode surface. Quantitative descriptions of the current at an electrode require knowledge of the diffusion coefficient and its experimental calculation represents an essential component of the characterisation of a redox couple.

In the present work, the diffusion of neutral and charged species is investigated in the six weakly coordinating solvents: DCM, TFT, oDCB, pFT, CB and DCE in order to improve the understanding of diffusion in this category of solvent. Diffusion coefficients are reported for the neutral decamethylferrocene (DMFc), the cationic decamethylferrocenium hexafluorophosphate ($DMFcPF_6$) and cobaltocenium hexafluorophosphate ($CcPF_6$), and the electrodeposition salts $[N^nBu_4][SbCl_4]$ and $[N^nBu_4][BiCl_4]$. $[SbCl_4]^-$ and $[BiCl_4]^-$ are precursors for the electrodeposition of Sb and Bi that have been used in the electrodeposition of various materials from DCM [3,5,6]. Additionally, oDCB and DCE were recently identified as promising weakly coordinating solvents for semiconductor electrodeposition [1]. Diffusion to the electrode surface is an important factor in the electrodeposition process and it is therefore interesting to study this in greater detail in DCM, oDCB and DCE. Another significant motivation for this work was the desire to be able to predict the diffusion coefficients for new electrodeposition precursors from structural data. The results are examined in the context of the Stokes-Einstein equation, and they are used to understand the nature of diffusion in these solvents. The importance of

* Corresponding author.
E-mail address: P.N.Bartlett@soton.ac.uk (P.N. Bartlett).

https://doi.org/10.1016/j.electacta.2022.140720
Received 6 May 2022; Received in revised form 25 May 2022; Accepted 13 June 2022
Available online 16 June 2022

considering the modifications of the Stokes-Einstein equation when interpreting diffusion coefficients is also discussed.

1.1. The Stokes-Einstein equation

An accessible approach to the interpretation of diffusion coefficients is with classical hydrodynamic theory and the Stokes-Einstein equation [7]

$$D = \frac{k_B T}{f_{tot}} \quad (1)$$

where k_B is Boltzmann's constant, T is the absolute temperature and f_{tot} is the total friction factor. The term $k_B T$ represents the thermal energy driving force for particle motion, and f_{tot} the friction that impedes it. f_{tot} is then given by

$$f_{tot} = 6\pi\eta r_S \quad (2)$$

where η is the solvent viscosity and r_S is the Stokes radius, the radius of the diffusing species.

However, the Stokes-Einstein equation in its form above carries with it several assumptions that are not always fully appreciated. Firstly, the equation assumes infinite dilution *i.e.* that there are no interactions between diffusing particles. It is also assumed that the solvent is a continuum described only by its viscosity, and finally that the diffusing species is a hard sphere. The Stokes-Einstein equation has proven remarkably effective for large particles, *e.g.* colloids or proteins, but as the size of the particle decreases, theory and experiment begin to diverge, and for molecules of a similar size to the solvent, such as those encountered in electrochemistry, the equation performs poorly [8].

This has resulted in the development of corrections to the Stokes-Einstein equation to improve its description of small molecules. Infinite dilution can be approximated by using low concentrations of analyte. The constant 6 in Eq. (2) can be replaced by the variable β, which describes the nature of the movement of the diffusing particle past solvent molecules and is proportional to the ratio of the radii of the solvent and solute molecules. β decreases as the ratio increases, to the lower limit of 4, such that $4 \leq \beta \leq 6$, therefore accounting for non-continuum effects. The motion when $\beta = 4$ is commonly referred to as 'slipping', and when $\beta = 6$ as 'sticking'. Expressions for its exact estimation have been provided by Gierer and Wirtz, and Chen and Chen [9]. Corrections for a diffusing species that is non-spherical can also be found. Perrin provided corrections for ellipsoids of revolution, a more common shape in electrochemistry [10]. f_{tot} then becomes

$$f_{tot} = f_{HS} f_P \quad (3)$$

where f_{HS} is the hard-sphere friction factor, equal to $c\pi\eta r_S$, and f_P is the Perrin correction.

There is also the question of how best to estimate the radius of the particle in solution. There are several radii that can be found in the literature for polyatomic molecules, obtained using different methods and it is not clear which most accurately describes their size in solution [11]. Furthermore, molecules can be uneven and irregular, creating a non-uniform surface and variations in their radius across it. From experiments, Macchioni et al. concluded that the upper and lower limits of r_S are the crystallographic radius, r_{crs}, and the van der Waals radius, r_{vdW}, respectively [12]. r_{crs} is obtained from X-ray crystal structure measurements, the calculated unit cell volume can be converted into a radius by assuming sphericity [12]. r_{crs} describes the space occupied by the molecule plus void spaces between molecules due to repulsive forces. r_{vdW} is taken from the van der Waals volume, V_{vdW}, which is the sum of the spheres occupied by the constituent atoms, after accounting for bonding. V_{vdW} is obtained from computational calculations, or from correlation with other radii [11].

Another common approach to correlating diffusion coefficients is with the Wilke-Chang equation [13]. This is an empirical modification of the Stokes-Einstein equation, obtained from data for a range of (typically organic) solutes and solvents. Here, D is proportional to $(M_r)^{1/2}/\eta V^{0.6}$, where M_r is the relative molecular mass of the diffusing species, and V is its molal volume. The Wilke-Chang equation is often used in electrochemistry, as an alternative to the Stokes-Einstein equation, to predict and analyze experimental diffusion coefficients, as in Refs. [14–16] for example. The Wilke-Chang equation also requires a 'solvent association parameter', which describes the strength of interactions between solvent molecules *e.g.* hydrogen bonding [13,17]. This property must be determined experimentally, and so makes it difficult to apply the equation to solvents for which little data is available. The molecular mass approach has also been extended to allow diffusion coefficients to be directly correlated with M_r, using a method developed by Valencia and Gonzalez which was based upon electrochemical measurements of various organic molecules in acetonitrile, dimethylsulfoxide and N,N-dimethylformamide [18,19].

Approaches based on correlation with M_r assume that, for a given solvent, the density remains constant across the measured dataset. This is likely to be true for organic molecules, as evidenced by the success of the Wilke-Chang equation for such compounds, however in this work where organometallic complexes and p-block halometallate complexes are studied, it cannot be known with any certainty that this is the case. Furthermore, Zaccaria et al. measured the diffusion of multiple organometallic complexes with approximately the same size and shape, but differing metal centres and so different molecular masses [20]. It was found that the size of the molecule, rather than weight, was the determining factor in their diffusion properties. As such, correlations based on molecular mass are not considered appropriate for the compounds under investigation here, and the more general Stokes-Einstein equation is preferred.

2. Experimental

2.1. Chemicals

Dichloromethane, CH_2Cl_2 (95%, Sigma-Aldrich), α, α, α-trifluorotoluene, $C_7H_5F_3$ (>99%, Sigma-Aldrich), *o*-dichlorobenzene, $C_6H_4Cl_2$ (>99%, Sigma-Aldrich), *p*-fluorotoluene, C_7H_7F (97%, Sigma-Aldrich), chlorobenzene, C_6H_5Cl (>99%, Sigma-Aldrich) and 1,2-dichloroethane, H_2ClCCH_2Cl (>99%, Sigma-Aldrich) were dried and degassed by refluxing with CaH_2 under a dinitrogen atmosphere followed by distillation, and were stored in an inert atmosphere of N_2. The water content in the solvents was measured with Karl–Fischer titration (KF 899 Coulometer, Metrohm, UK). There was less than 35 ppm of water in all solvents. Tetrabutylammonium chloride, $[N^nBu_4]Cl$ (Sigma-Aldrich, >99%) and tetrabutylammonium tetrafluoroborate, $[N^nBu_4][BF_4]$ (Sigma-Aldrich, >99%) were dried by heating at 100 °C under vacuum for several hours. Decamethylferrocene, $[\{C_5(CH_3)_5\}_2Fe]$ (Sigma-Aldrich, 97%) and cobaltocenium hexafluorophosphate, $[(C_5H_5)_2Co][PF_6]$ (Sigma-Aldrich, 98%) were purified by sublimation. Decamethylferrocenium hexafluorophosphate, $[\{C_5(CH_3)_5\}_2Fe][PF_6]$, was synthesised according to a procedure by Duggan and Hendrickson [21]. Tetrabutylammonium tetrachloroantimonate(III), $[N^nBu_4][SbCl_4]$ and tetrabutylammonium tetrachlorobismuthate(III), $[N^nBu_4][BiCl_4]$ were prepared using methods previously described in the literature [22]. All solvents and reagents were stored in a dry, N_2 purged glovebox.

2.2. Electrodes

Working electrodes used were inlaid Pt microdiscs of radii 5, 12.5 and 25 μm, sealed in glass. The working electrodes were polished sequentially with 5, 1 and 0.3 μm alumina pastes on a microcloth polishing pad (Buehler, USA). Microelectrodes were calibrated using SEM (Philips XL30 ESEM). A Pt grid was used as a counter electrode, the

reference electrode was Ag/AgCl immersed in a storage solution of 100 mM $[N^nBu_4]Cl$ for dichloromethane, *o*-dichlorobenzene and 1,2-dichloroethane, separated from the electrolyte by a porous glass frit, and a Pt wire pseudo reference for α, α, α-trifluorotoluene, *p*-fluorotoluene and chlorobenzene.

2.3. Electrochemical measurements

All glassware was cleaned by soaking in Decon 90 (Decon Laboratories Ltd., UK) for at least 24 h, followed by rinsing with ultrapure water, 0.055 μS $cm^{-1,}$ and then dried in an oven for a further 24 h. All experiments were performed with a standard pear-shaped cell in a glovebox (Belle Technology, UK) under an inert atmosphere of N_2 in the presence of <5 ppm O_2 and H_2O. Measurements were performed with a PGSTAT μIII (Metrohm Autolab, UK) potentiostat. Data was recorded with NOVA 1.11 (Metrohm Autolab, UK). The ambient temperature in the glovebox was monitored using a digital thermometer to an accuracy of ±0.05 °C (Hama, UK).

3. Results

Diffusion coefficients of DMFc and $CcPF_6$ have been reported previously in the studied weakly coordinating solvents and were taken from Ref. [1], with their values given in Table 1. Voltammograms of $DMFc^+$, $[SbCl_4]^-$ and $[BiCl_4]^-$ were collected at Pt microelectrodes of radii 5, 12.5 and 25 μm. Representative microelectrode voltammograms for $DMFcPF_6$ can be found in Fig. 1. As can be seen, a limiting current plateau is present for the voltammograms at every size of electrode in every solvent, indicating a mass transport limited redox reaction. Voltammograms for $[SbCl_4]^-$ and $[BiCl_4]^-$ can be found in Fig. S1. Diffusion coefficients were then obtained from the slope of a plot of limiting current *vs.* microelectrode radius for three different sizes of microelectrode, since

$$i_L = 4nFDca \quad (4)$$

where i_L is the limiting current, n is the number of electrons transferred, F is the Faraday, c is concentration of electroactive species and a is the radius of the electrode. n was taken as 1 for $DMFcPF_6$, and 3 for $[SbCl_4]^-$ and $[BiCl_4]^-$. Representative plots of i_L *vs.* a are shown in Fig. 2 for $DMFcPF_6$, clearly the plots are linear with intercepts close to the origin demonstrating the validity of Eq. (4). Plots for $[SbCl_4]^-$ and $[BiCl_4]^-$ are then given in Fig. S2. The microelectrode radii were calibrated using SEM to give the effective geometric radius of the microelectrode, and the effective concentration in solution was obtained from a potential step at a microelectrode and fitting to the Shoup-Szabo equation [23]. The average of the concentration at each microelectrode was then used as c. Calculating diffusion coefficients in this way improves the accuracy of the resulting value because it can smooth out any individual errors associated with i_L, c or a. Potential steps were not performed for $[SbCl_4]^-$ and $[BiCl_4]^-$ and so the weighed concentration was used.

Table 1
Selected physical properties and experimental diffusion coefficients at 25 °C of redox couples in weakly coordinating solvents. Diffusion coefficients obtained from the limiting current at a microelectrode. Each value is the average of three repeats and the error the standard deviation.

Solvent	ε_r[a]	η / mPa s	D / 10^{-5} cm^2 s^{-1}				
			$DMFc$[d]	$DMFc^+$	Cc^+[d]	$[SbCl_4]^-$	$[BiCl_4]^-$
DCM	8.9	0.41[a]	1.68(2)	1.21 (3)	1.35 (1)	0.83(7)	0.73(3)
TFT	9.2	0.47[b]	1.18(3)	0.76 (1)	0.38 (2)	–	–
oDCB	9.9	1.32[a]	0.52(1)	0.35 (1)	0.24 (1)	0.18(1)	0.19(1)
pFT	5.9	0.62[c]	1.10 (11)	0.47 (2)	0.31 (3)	–	–
CB	5.6	0.76[a]	0.87(3)	0.46 (1)	0.32 (2)	–	–
DCE	10.4	0.78[a]	0.88(3)	0.53 (1)	0.61 (3)	0.43(1)	0.37(2)

[a] Ref. [26].
[b] Ref. [27].
[c] Ref. [28].
[d] Ref. [1].

Measured diffusion coefficients, along with some relevant physical properties for the solvents can be found in Table 1. D was also calculated from potential step data for $DMFcPF_6$, and corroborates the values in Table 1 (see Table S1). Work has shown previously that CVs and potential steps at a microelectrode are two of the most accurate and precise methods for measuring diffusion coefficients [24]. Microelectrodes are also particularly useful in solvents of relatively low polarity, such as those studied here. The small current response minimises distortions associated with *iR* drop.

The measured diffusion coefficients are in agreement with those reported in the literature, Goldfarb and Corti also reported a value of 1.07×10^{-5} cm^2 s^{-1} for $DMFcPF_6$ in DCM at 25 °C [25]. Reeves et al. found D for $[N^nBu_4][SbCl_4]$ in DCM at 25 °C to be 9.2×10^{-6} cm^2 s^{-1}. [5].

4. Discussion

The first step towards analysing diffusion coefficients in multiple solvents with the Stokes Einstein equation is to make a plot of D *vs.* η^{-1}. If the plot is linear with an intercept close to the origin, the equation can be considered valid and insight can be gained into the size of the diffusing species from the slope of the plot. However, addition of electrolyte to a solvent increases the viscosity of the solution relative to the pure solvent and this must be taken into account. The increase in solvent viscosity with electrolyte addition is described by the Jones-Dole equation [29]. This was used to estimate the relative viscosity, η_{rel}, where data was available, for the electrolyte solutions studied here. Further details and values can be found in Section S4 of the SI. The ratio of electrolyte to solvent viscosity is taken as 1.102 for all solvents and electrolytes.

Calculation of the Perrin correction for non-sphericity, f_P, requires knowledge of the dimensions of the molecules. These were obtained from crystal structure data using visualisation software. The resulting values for f_P were 1.002 and 1.004 for DMFc and Cc^+, respectively, indicating that the molecules are essentially spherical and the Perrin correction can be ignored. Details of the calculation of f_P are given in SI Section S3. The size of DMFc does not change significantly upon oxidation and so $DMFc^+$ can also be considered spherical. Moments of inertia measurements additionally suggest that $DMFc^+$ is spherical [30]. Reeves et al. used bond lengths and the geometry of the $[SbCl_4]^-$ anion to calculate f_P and concluded that the ion was spherical and that no correction was required [5], and this is also assumed to be true in the present work. Spectroscopic measurements indicate that $[BiCl_4]^-$ has a similar geometry to $[SbCl_4]^-$ and so is not expected to need correcting either [31].

Beginning with the neutral DMFc, a Stokes-Einstein plot of D_{exp} *vs.* η^{-1}, where D_{exp} is the experimental diffusion coefficient, is shown in Fig. 3 in black, using the corrected viscosity values. As can be seen, the plot is linear with an intercept close to zero and so it can be concluded that DMFc obeys the Stokes-Einstein equation in these weakly coordinating solvents.

As described above: $4 \leq \beta \leq 6$ and $r_{vdW} \leq r_S \leq r_{crs}$. Therefore, the experimental diffusion coefficient can be expected to lie within the upper bound, D_{max}, when $\beta = 4$, $r = r_{vdW}$ and the lower bound, D_{min} when $\beta = 6$ and $r = r_{crs}$. D_{min} and D_{max} were calculated for DMFc in the studied solvents and the results are also plotted on Fig. 3. Further details of the methods to obtain the molecular radii and the resulting diffusion coefficients can be found in Sections S5 and S6 of the SI, respectively. As

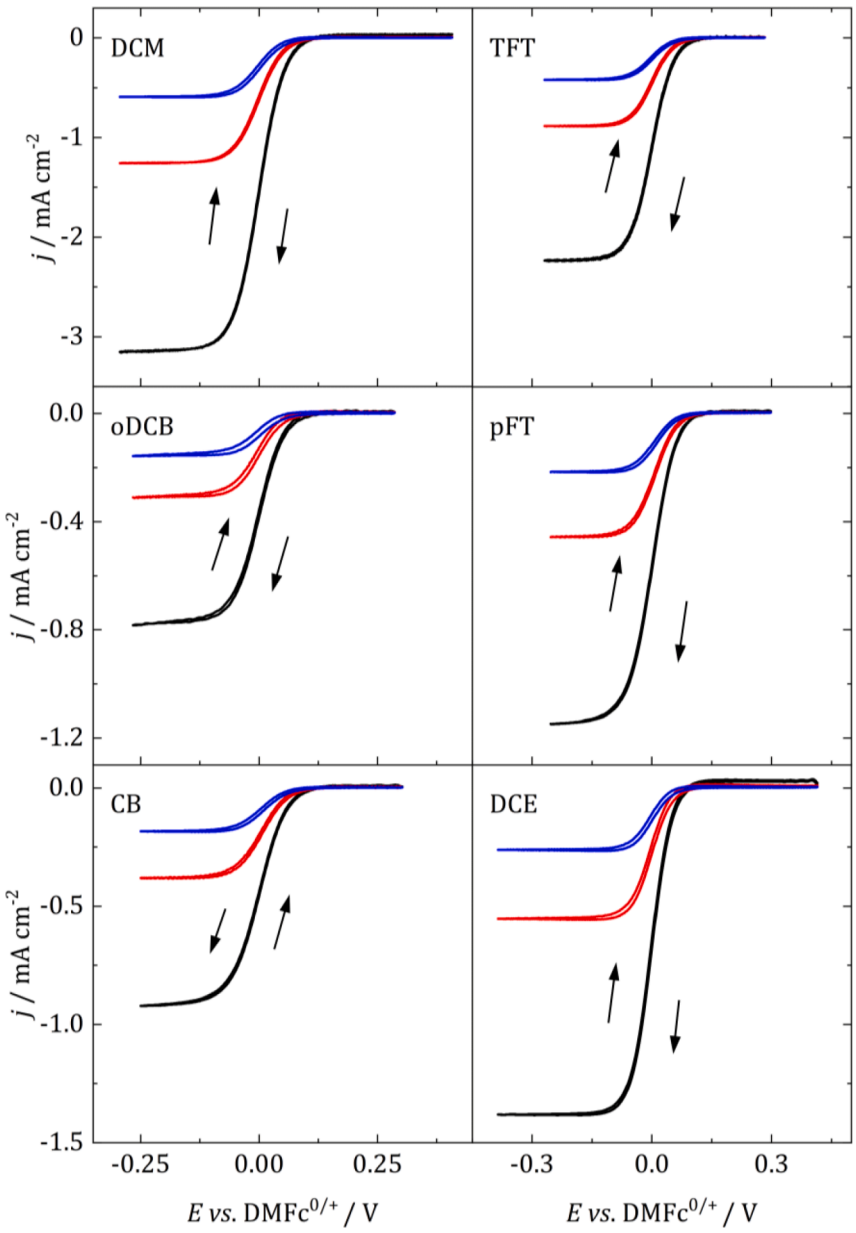

Fig. 1. Representative microelectrode voltammograms for 1 mM $DMFcPF_6$ with 100 mM $[N^nBu_4]Cl$ at a Pt WE. Potential scanned in the direction of the arrows at a sweep rate of 5 mV s^{-1}. CE: Pt grid, DCM, oDCB, DCE: Ag/AgCl RE, TFT, pFT, CB: Pt QRE. Black: $r = 5$ μm, red: $r = 12.5$ μm, blue: $r = 25$ μm.

can be seen, D_{exp}(DMFc) matches closely with D_{max}, suggesting that for DMFc, $\beta \approx 4$ and $r_S \approx r_{vdW}$. This can readily be rationalised since β approaches four as the radius of the solvent molecule and the diffusing particle become similar in size. Taking the radius of DCM as 2.5 Å for example [5], this is similar to the vDW radius for DMFc of 4.2 Å (see SI). Additionally, r_S is typically found to be close to r_{vdW} for small, compact molecules [12].

This approach to analysing the diffusion coefficient makes no assumptions about β or r and so avoids any of the uncertainties associated with these values, whilst also giving insight into the size of the particle in solution and its interaction with the solvent. It also emphasises the importance of considering modifications to the Stokes-Einstein equation when analysing diffusion coefficients. Often, r_S is calculated from the slope of the Stokes-Einstein plot, if β was taken as six then this would lead to a misleading value of r_S for DMFc.

To prove that the approach outlined above is a useful method of analysis rather than simply fortuitous agreement for the solvents studied here, diffusion coefficients of DMFc in different solvents were compiled from the literature and plotted along with their D_{min} and D_{max}, in Fig. 4. The values are tabulated in Table S7. As can be seen, excepting a few outliers, all the reported values for the diffusion coefficient of DMFc lie within D_{min} and D_{max}. The three data points with the largest discrepancy, one for THF and two from DCM, are all from the same source, Ref. [32], suggesting there may have been a systematic difference in the measurement of D.

It is noteworthy that where there are multiple data points for the same solvent that, even for DMFc a relatively simple system, a large variation in D is observed in the literature values determined electrochemically. This emphasises the importance of careful attention to details including temperature control, accurate measurement of electrode dimensions and solute concentration. It is also worth pointing out that the use of microelectrodes, as opposed to macrodisc cyclic voltammetry, avoids problems of iR drop and gives currents that are proportional to D rather than to $D^{1/2}$.

It is also interesting to investigate the diffusion of charged species to study any changes in behavior as a result of ion formation. The cationic

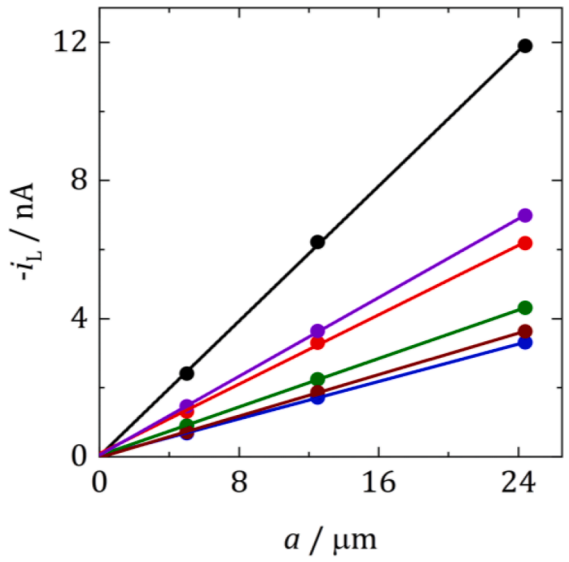

Fig. 2. Limiting currents for 1 mM $DMFcPF_6$ at Pt microelectrodes of radii r = 5 μm, 12.5 μm and 25 μm. Black: DCM, red: TFT, blue: oDCB, green: pFT, brown: CB, purple: DCE.

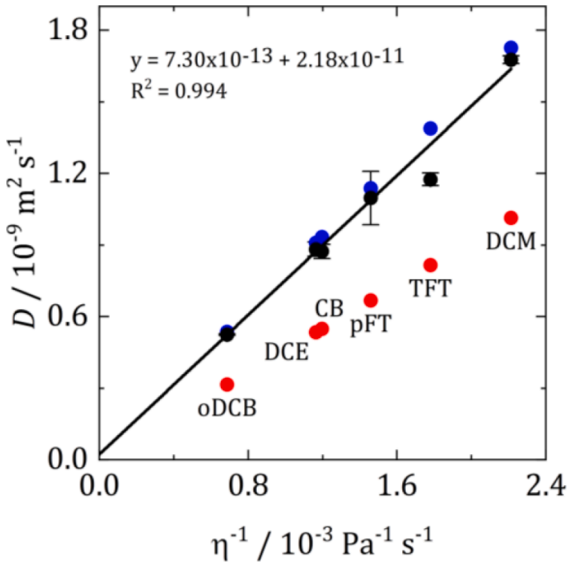

Fig. 3. Stokes-Einstein plot of experimental diffusion coefficients for DMFc in weakly coordinating solvents at 25 °C along with simulated D_{min} and D_{max}. Black: D_{exp}, red: D_{min}, blue: D_{max}.

metallocenes, decamethylferrocenium hexafluorophosphate ($DMFcPF_6$) and cobaltocenium hexafluorophosphate ($CcPF_6$) were initially used for this purpose. Stokes-Einstein plots for both, along with D_{min} and D_{max} are shown in Fig. 5. For $DMFc^+$ the same D_{min} and D_{max} as DMFc was used, and details for Cc^+ can be found in the SI. Clearly, the situation is different for charged species, and linear Stokes-Einstein behavior is no longer observed for $DMFc^+$ nor Cc^+. The measured diffusion coefficients for both redox couples are now lower than their minimum theoretical value of D_{max}. A dramatic increase in viscosity as a result of the addition of the redox couples at these concentrations (100 mM) is not plausible. Therefore, it appears that the radius of the diffusing species, r_S, is larger than that predicted by theory.

There are no major changes to the structure of DMFc and Cc upon oxidation, except for the fact that they are now charged. Therefore, the most plausible explanation for r_S to be greater than expected is the presence of ion pairing. If $DMFc^+$ and Cc^+ were associating with the Cl^-

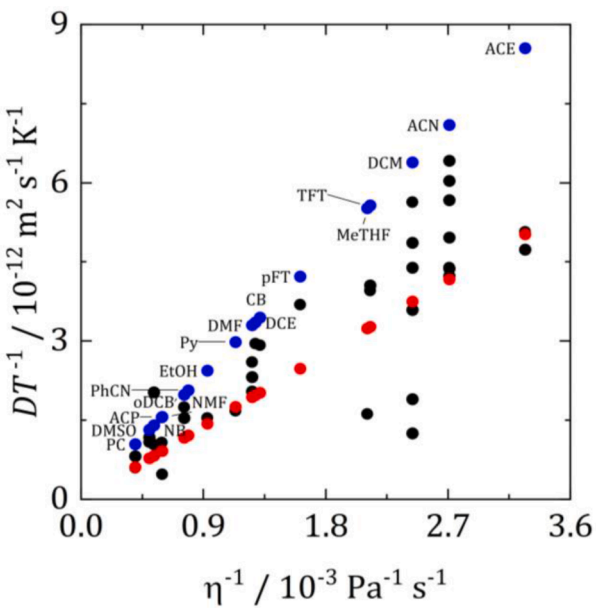

Fig. 4. Stokes-Einstein plot of experimental DMFc diffusion coefficients normalised with respect to temperature compiled from the literature together with calculated D_{min} and D_{max} values. See text for details of D_{min} and D_{max}, and SI for compilation. Black: D_{exp}, red: D_{min}, blue: D_{max}.

or $[BF_4]^-$ ion then this would form a larger diffusing particle. This is reasonable when considering the low polarity of the solvents, where the degree of ion pairing is expected to be high. $DMFc^+$ was found to have a lower diffusion coefficient than DMFc in DCM by Goldfarb and Corti, in agreement with the results presented here [25]. Conductivity measurements in the literature also indicate the presence of ion pairing in these solvents. The association constant, K_A, describes the position of the equilibrium between free ions and ion pairs. The greater K_A is above 1, the more that ion pairs are favoured in the electrolyte. Table S9 shows a compilation of relevant association constants from the literature. K_A is significantly greater than 1 for all the electrolytes where data is available, therefore clearly showing that a significant fraction of ions can be expected to be paired in the solvents studied here.

The presence of triple ions is also possible. Fuoss [33] provided a rule of thumb for the maximum concentration, c_{max}, at which only ion pairs are expected for a symmetrical electrolyte, and above which triple ions could be expected to be observed:

$$c_{max} = 1.2x10^{-14}(\varepsilon_r T)^3 \quad (5)$$

taking the largest dielectric constant of 10.4 for DCE at 298 K gives c_{max} of 0.4 mM. This is of a similar order to the concentrations used here, meaning the presence of triple ions in these solvents is probable. The measured diffusion coefficients can then be considered as a weighted average of the diffusion coefficient of all forms of the electroactive species in solution.

The presence of any ion pairs or triplets can be explored by calculating r_S from the diffusion coefficients of $DMFc^+$ and Cc^+. This was achieved by taking β as 4 (a reasonable assumption considering the data for DMFc above) and results are given in Table 2. These values represent an upper bound for r_S, since β would increase above 4 if it was estimated using the radii of the diffusing particle and the solvent. Using 0.48 nm as a value of $r(DMFc^+)$ and $r(Cc^+)$ as 0.38 nm (see SI), and also $r(Cl^-)$ as 0.18 nm and $r([BF_4]^-)$ as 0.23 nm (Ref. [34]), the approximate size of an ion pair can be estimated (Table 2). The experimental r_S can then be compared with the radii of the bare ions and also the ion pair. For $DMFc^+$ and Cc^+ in DCM, r_S is in between the free ion and the estimate for the ion pair, suggesting that here the ions exist as a mixture of both forms. For $DMFc^+$ in oDCB, and also both species in DCE, r_S is similar to

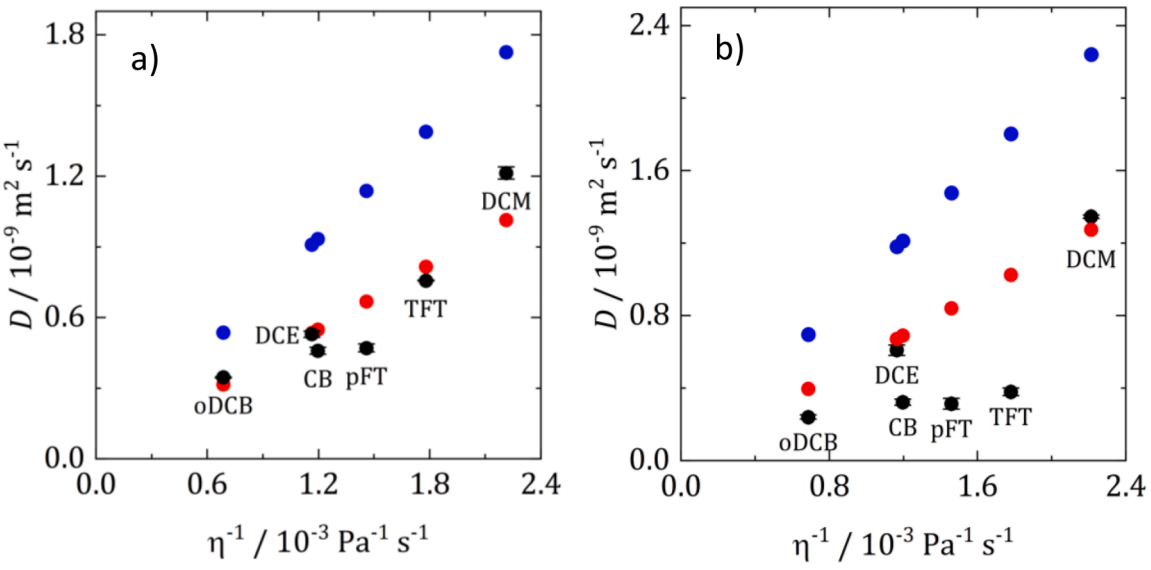

Fig. 5. Experimental Stokes-Einstein plots for (a) $DMFcPF_6$ and (b) $CcPF_6$ at 25 °C along with simulated D_{max} and D_{min} for Cc^+ and DMFc. Black: D_{exp}, red: D_{min}, blue: D_{max}.

Table 2
The Stokes radii, r_S, of $DMFc^+$ and Cc^+, determined from diffusion coefficients, and an estimate of the size of an ion pair for each species.

Solvent	$r_S(DMFc^+)$ / nm	$r_S(Cc^+)$ / nm	Estimated radius	
DCM	0.60	0.54	$r(DMFc^+)$ 0.48 nm	$r(Cc^+)$ 0.38 nm
oDCB	0.65	0.94	$r(DMFc^+ + Cl^-)$	$r(Cc^+ + Cl^-)$
DCE	0.72	0.63	0.66 nm	0.56 nm
TFT	0.77	1.54	$r(DMFc^+)$ 0.48 nm	$r(Cc^+)$ 0.38 nm
pFT	1.02	1.52	$r(DMFc^+ + [BF_4]^-)$	$r(Cc^+ + [BF_4]^-)$
CB	0.85	1.22	0.71 nm	0.61 nm

the estimate for the size of the ion pair so these are probably mostly present in the form of ion pairs. r_S is then greater than the ion pair radius in the remaining electrolytes, which could point to the presence of triple ions. It is noticeable that r_S for Cc^+ is larger than that for $DMFc^+$ in oDCB, CB, TFT and pFT consistent with greater ion association for the smaller, and therefore higher charge density, Cc^+ ion. It must also be noted that interpretation of Stokes radii in this way must be done with caution and care must be taken not to over interpret the data [35].

Fig. 6 shows Stokes-Einstein plots for $[SbCl_4]^-$ and $[BiCl_4]^-$ in the three solvents. Also shown are their simulated D_{max} and D_{min} values. r_{vdW} and r_{crs} were not available for either metal complex so the McGowan radius, r_{McG}, from the McGowan volume was used instead [26]. This is an intrinsic volume based upon the additive volumes of the constituent atoms and is intermediate between r_{vdW} and r_{crs} [26]. The simulated D_{max} and D_{min} are given in Table S6.

The plots in Fig. 6 appear linear, however the intercept is much less than zero, suggesting that the precursors are not behaving according to the Stokes-Einstein equation. Furthermore, as was the case for the cationic species above, D_{exp} of these anionic complexes is lower than the simulated D_{min}, indicating that r_S is greater than expected. This can be attributed to the presence of ion pairing once again, where now the anions are paired with the $[N^nBu_4]^+$ cation. The formation of chloride

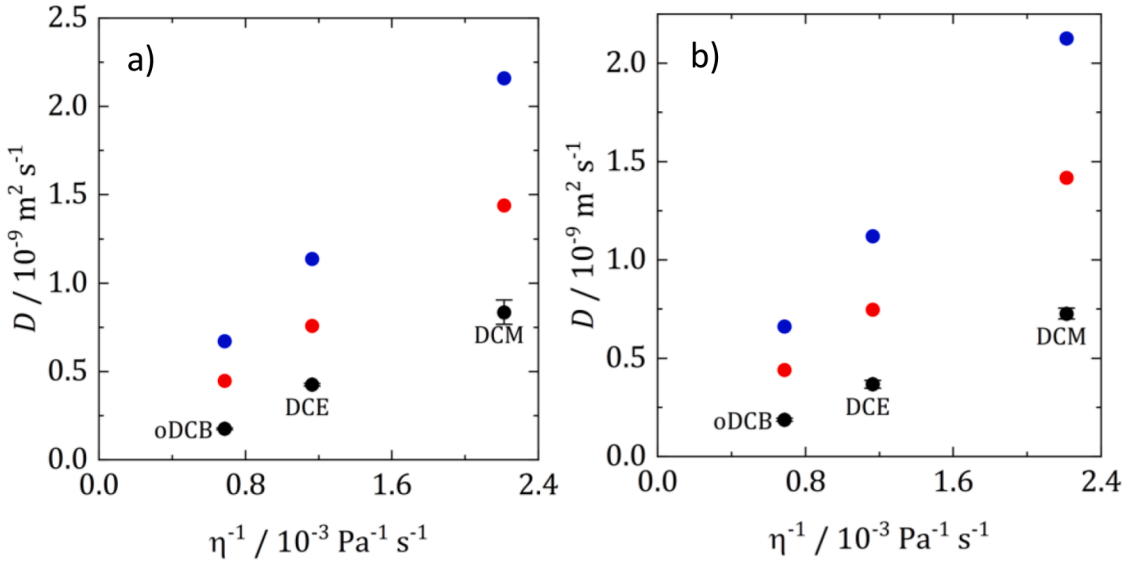

Fig. 6. Experimental Stokes-Einstein plots for (a) $[N^nBu_4][SbCl_4]$ and (b) $[N^nBu_4][BiCl_4]$ in DCM, oDCB and DCE at 25 °C along with simulated D_{max} and D_{min}. Black: D_{exp}, red: D_{min} and blue: D_{max}.

bridged dimers and higher oligomers of the metal complexes in solution is also possible [36], and has been observed previously in crystal structures of the chlorometallate salts [37,38]. These would be in equilibrium with the monomer and could also cause a larger than predicted diffusing species, similar to ion pairing. Although the two effects are likely to be indistinguishable from each other with diffusion coefficient measurements.

5. Conclusion

This work used electrochemical methods to measure the diffusion coefficients of neutral, cationic and anionic redox couples in weakly coordinating solvents. The resulting values were then analyzed using the Stokes-Einstein equation, and plots of D *vs.* η^{-1}. For the neutral DMFc, a linear plot was observed, indicating that the Stokes-Einstein equation was obeyed. The theoretical upper and lower bounds, D_{max} and D_{min}, respectively, were also calculated and compared to the experimental values. The experimental measurements were similar to D_{max} and it was possible to conclude that r_S(DMFc) was close to r_{vdW} in these solvents, and that the particles moved through the solvent with 'slipping' motion. This approach allows analysis of diffusion coefficients, and the comparison of theory with experiment, whilst avoiding the assignment of definite values to the radii of the solvent or particle in solution, which can often be uncertain.

The cationic $DMFc^+$ and Cc^+, and the anionic $[SbCl_4]^-$ and $[BiCl_4]^-$ were also studied. In contrast with neutral DMFc, these charged species had diffusion coefficients that were less than their theoretical lower bound. Due to the low polarity of the weakly coordinating solvents, this was attributed to a larger than expected r_S caused by ion pairing with the anions or cations of the supporting electrolyte.

When interpreting diffusion coefficients with the Stokes-Einstein equation, it is clearly essential to consider its modifications in order to properly understand diffusion behavior and draw robust conclusions. Improper consideration of them has the potential to lead to the calculation of erroneous values for r_S, which can lead to misinterpretation of the size of the diffusing species in solution. It is also important for the calculation of accurate diffusion coefficients to ensure that the electrode size and solute concentration are properly measured.

Conceptually, radii taken from the partial molar volume, $V_{m,i}$, would appear to be the most accurate measure of the size of a species, since this is its volume contribution measured at exactly the same electrolyte composition as that used to measure the diffusion coefficient [39]. Knowledge of this would negate the approach using r_{vdW} and r_{crs} and would improve the accuracy of diffusion coefficient predictions. However, $V_{m,i}$ is an experimentally derived parameter that is difficult to measure and also to predict. Furthermore, ideally an exact value for β would be calculated, however finding a consistent method of measuring the sizes of organic molecules, metal complexes and salts is not a simple task. Meaning it is difficult to obtain uniform values of the radius of the solvent as well as the electroactive species. Some of the solvent molecules are also aromatic, and so disc shaped rather than spherical. Their size would most accurately be described by two axes, and it is currently not possible to incorporate this into the available methods of estimating β.

CRediT authorship contribution statement

Alexander W. Black: Conceptualization, Methodology, Validation, Formal analysis, Investigation, Data curation, Writing – original draft, Visualization. **Wenjian Zhang:** Resources. **Gillian Reid:** Methodology, Conceptualization, Resources, Writing – review & editing, Supervision. **Philip N. Bartlett:** Conceptualization, Methodology, Validation, Formal analysis, Writing – review & editing, Supervision, Funding acquisition, Project administration.

Declaration of Competing Interest

None.

Acknowledgments

This work was supported by the EPSRC through the Advanced Devices by Electroplating program grant (ADEPT; EP/N035437/1). All data supporting this study are openly available from the University of Southampton repository at https://doi.org/10.5258/SOTON/D2211.

Supplementary materials

Supplementary material associated with this article can be found, in the online version, at doi:10.1016/j.electacta.2022.140720.

References

[1] A.W. Black, P.N. Bartlett, Selection and characterisation of weakly coordinating solvents for semiconductor electrodeposition, Phys. Chem. Chem. Phys. 24 (2022) 8093–8103, https://doi.org/10.1039/D2CP00696K.
[2] A.H. Jaafar, L. Meng, Y.J. Noori, W. Zhang, Y. Han, R. Beanland, D.C. Smith, G. Reid, K. De Groot, R. Huang, P.N. Bartlett, Electrodeposition of GeSbTe-based resistive switching memory in crossbar arrays, J. Phys. Chem. C 125 (2021) 26247–26255, https://doi.org/10.1021/acs.jpcc.1c08549.
[3] Y.J. Noori, L. Meng, A.H. Jaafar, W. Zhang, G.P. Kissling, Y. Han, N. Abdelazim, M. Alibouri, K. Leblanc, N. Zhelev, R. Huang, R. Beanland, D.C. Smith, G. Reid, K. De Groot, P.N. Bartlett, Phase-change memory by GeSbTe electrodeposition in crossbar arrays, ACS Appl. Electron. Mater. 3 (2021) 3610–3618, https://doi.org/10.1021/acsaelm.1c00491.
[4] N.M. Abdelazim, Y.J. Noori, S. Thomas, V.K. Greenacre, Y. Han, D.E. Smith, G. Piana, N. Zhelev, A.L. Hector, R. Beanland, G. Reid, P.N. Bartlett, C.H. de Groot, Lateral growth of MoS2 2D material semiconductors over an insulator via electrodeposition, Adv. Electron. Mater. 7 (2021), 2100419, https://doi.org/10.1002/aelm.202100419.
[5] S.J. Reeves, Y.J. Noori, W. Zhang, G. Reid, P.N. Bartlett, Chloroantimonate electrochemistry in dichloromethane, Electrochim. Acta 354 (2020), 136692, https://doi.org/10.1016/j.electacta.2020.136692.
[6] K. Cicvarić, L. Meng, D.W. Newbrook, R. Huang, S. Ye, W. Zhang, A.L. Hector, G. Reid, P.N. Bartlett, C.H.K. De Groot, Thermoelectric properties of bismuth telluride thin films electrodeposited from a nonaqueous solution, ACS Omega 5 (2020) 14679–14688, https://doi.org/10.1021/acsomega.0c01284.
[7] H.J.V. Tyrell, K.R. Harris, Diffusion in Liquids, Butterworths, London, 1984.
[8] D. Fennell Evans, T. Tominaga, C. Chan, Diffusion of symmetrical and spherical solutes in protic, aprotic, and hydrocarbon solvents, J. Solut. Chem. 8 (1979) 461–478, https://doi.org/10.1007/BF00716005.
[9] R. Evans, G. Dal Poggetto, M. Nilsson, G.A. Morris, Improving the interpretation of small molecule diffusion coefficients, Anal. Chem. 90 (2018) 3987–3994, https://doi.org/10.1021/acs.analchem.7b05032.
[10] P.F. Perrin, Mouvement brownien d'un ellipsoide - I. Dispersion diélectrique pour des molécules ellipsoidale, J. Phys. Radium 5 (1934) 497–511, https://doi.org/10.1051/jphysrad:01934005010049700.
[11] Y. Marcus, The sizes of molecules - revisited, J. Phys. Org. Chem. 16 (2003) 398–408, https://doi.org/10.1002/poc.651.
[12] A. Macchioni, G. Ciancaleoni, C. Zuccaccia, D. Zuccaccia, Determining accurate molecular sizes in solution through NMR diffusion spectroscopy, Chem. Soc. Rev. 37 (2008) 479–489, https://doi.org/10.1039/b615067p.
[13] C.R. Wilke, P. Chang, Correlation of diffusion coefficients in dilute solutions, AIChE J. 1 (1955) 264–270, https://doi.org/10.1002/aic.690010222.
[14] S.R. Jacob, Q. Hong, B.A. Coles, R.G. Compton, Variable-temperature microelectrode voltammetry: application to diffusion coefficients and electrode reaction mechanisms, J. Phys. Chem. B 103 (1999) 2963–2969, https://doi.org/10.1021/jp990024w.
[15] F.J. Del Campo, E. Maisonhaute, R.G. Compton, F. Marken, A. Aldaz, Low-temperature sonoelectrochemical processes - part 3. Electrodimerisation of 2-nitrobenzylchloride in liquid ammonia, J. Electroanal. Chem. 506 (2001) 170–177, https://doi.org/10.1016/S0022-0728(01)00501-0.
[16] N.V. Rees, J.D. Wadhawan, O.V. Klymenko, B.A. Coles, R.G. Compton, An electrochemical study of the oxidation of 1,3,5-Tris[4-[(3-*methylphenyl*) *phenylamino*]phenyl]benzene, J. Electroanal. Chem. 563 (2004) 191–202, https://doi.org/10.1016/j.jelechem.2003.08.034.
[17] B.A. Parsons, D.K. Pinkerton, R.E. Synovec, Implications of phase ratio for maximizing peak capacity in comprehensive two-dimensional gas chromatography time-of-flight mass spectrometry, J. Chromatogr. A 1536 (2018) 16–26, https://doi.org/10.1016/j.chroma.2017.07.018.
[18] D.P. Valencia, F.J. González, Understanding the linear correlation between diffusion coefficient and molecular weight. A model to estimate diffusion coefficients in acetonitrile solutions, Electrochem. Commun. 13 (2011) 129–132, https://doi.org/10.1016/j.elecom.2010.11.032.

[19] D.P. Valencia, F.J. González, Estimation of diffusion coefficients by using a linear correlation between the diffusion coefficient and molecular weight, J. Electroanal. Chem. 681 (2012) 121–126, https://doi.org/10.1016/j.jelechem.2012.06.013.
[20] F. Zaccaria, C. Zuccaccia, R. Cipullo, A. Macchioni, Extraction of reliable molecular information from diffusion NMR spectroscopy: hydrodynamic volume or molecular mass? Chem. A Eur. J. 25 (2019) 9930–9937, https://doi.org/10.1002/chem.201900812.
[21] D.M. Duggan, D.N. Hendrickson, Electronic structure of various ferricenium systems as inferred from Raman, infrared, low-temperature electronic absorption, and electron paramagnetic resonance measurements, Inorg. Chem. 14 (1975) 955–970, https://doi.org/10.1021/ic50147a001.
[22] P.N. Bartlett, D. Cook, C.H. (Kees) de Groot, A.L. Hector, R. Huang, A. Jolleys, G. P. Kissling, W. Levason, S.J. Pearce, G. Reid, Non-aqueous electrodeposition of p-block metals and metalloids from halometallate salts, RSC Adv. 3 (2013) 15645–15654, https://doi.org/10.1039/c3ra40739j.
[23] D. Shoup, A. Szabo, Chronoamperometric current at finite disk electrodes, J. Electroanal. Chem. 140 (1982) 237–245, https://doi.org/10.1016/0022-0728(82)85171-1.
[24] M. Zistler, P. Wachter, P. Wasserscheid, D. Gerhard, A. Hinsch, R. Sastrawan, H. J. Gores, Comparison of electrochemical methods for triiodide diffusion coefficient measurements and observation of non-Stokesian diffusion behaviour in binary mixtures of two ionic liquids, Electrochim. Acta 52 (2006) 161–169, https://doi.org/10.1016/j.electacta.2006.04.050.
[25] D.L. Goldfarb, H.R. Corti, Steady-state voltammetric study of the reduction of decamethylferrocenium in dichloromethane at microelectrodes, J. Electroanal. Chem. 509 (2001) 155–162, https://doi.org/10.1016/S0022-0728(01)00530-7.
[26] Y. Marcus, The Properties of Solvents, Wiley, Chichester, 1998.
[27] L. De Lorenzi, M. Fermeglia, G. Torriano, Density and viscosity of 1-methoxy-2-propanol, 2-methyltetrahydrofuran, α,α,α-trifluorotoluene, and their binary mixtures with 1,1,1-trichloroethane at different temperatures, J. Chem. Eng. Data 41 (1996) 1121–1125, https://doi.org/10.1021/je9601220.
[28] O. Ivanciuc, T. Ivanciuc, P.A. Filip, D. Cabrol-Bass, Estimation of the liquid viscosity of organic compounds with a quantitative structure-property model, J. Chem. Inf. Comput. Sci. 39 (1999) 515–524, https://doi.org/10.1021/ci980117v.
[29] R.A. Robinson, R.H. Stokes, Electrolyte Solutions, 2nd ed., Butterworths, London, 1965 revised.
[30] D.M.P. Mingos, A.L. Rohl, Size and shape characteristics of inorganic molecules and ions and their relevance to molecular packing problems, J. Chem. Soc. Dalton Trans. (1991) 3419–3425, https://doi.org/10.1039/DT9910003419.
[31] G.Y. Ahlijah, M. Goldstein, Far-infrared and Raman spectra of tetrahalogeno-complexes of arsenic(III), antimony(III), and bismuth(III), J. Chem. Soc. A Inorg. Phys. Theor. 326 (1970), https://doi.org/10.1039/j19700000326.
[32] F.S.T. Khan, A.L. Waldbusser, M.C. Carrasco, H. Pourhadi, S. Hematian, Synthetic, spectroscopic, structural, and electrochemical investigations of ferricenium derivatives with weakly coordinating anions: ion pairing, substituent, and solvent effects, Dalton Trans. 50 (2021) 7433–7455, https://doi.org/10.1039/d1dt01192h.
[33] Y. Marcus, G. Hefter, Ion pairing, Chem. Rev. 106 (2006) 4585–4621, https://doi.org/10.1021/cr040087x.
[34] Y. Marcus, Ions in Solution and Their Solvation, Wiley, Hoboken, NJ, 2015.
[35] Y. Marcus, Are ionic stokes radii of any use? J. Solut. Chem. 41 (2012) 2082–2090, https://doi.org/10.1007/s10953-012-9922-4.
[36] W. Levason, G. Reid, J.A. McCleverty, T.J. Mayer, The coordination chemistry of arsenic, antimony, and bismuth. Comprehensive Coordination Chemistry II, Elsevier, Amsterdam, 2003, pp. 465–544, https://doi.org/10.1016/B0-08-043748-6/02023-5.
[37] R.G. Lin, G. Xu, G. Lu, M.S. Wang, P.X. Li, G.C. Guo, Photochromic hybrid containing *in situ* -generated benzyl viologen and novel trinuclear [Bi3Cl14]5-: improved photoresponsive behavior by the φ···φ interactions and size effect of inorganic oligomer, Inorg. Chem. 53 (2014) 5538–5545, https://doi.org/10.1021/ic5002144.
[38] C. Ji, Z. Sun, A. Zeb, S. Liu, J. Zhang, M. Hong, J. Luo, Bandgap narrowing of lead-free perovskite-type hybrids for visible-light-absorbing ferroelectric semiconductors, J. Phys. Chem. Lett. 8 (2017) 2012–2018, https://doi.org/10.1021/acs.jpclett.7b00673.
[39] P. Atkins, J. de Paula, Physical Chemistry, 10th ed., Oxford University Press, Oxford, 2014.